UiT
THE ARCTIC
UNIVERSITY
OF NORWAY

Faculty of Science and Technology
Department of Geosciences

Integrated characterization of igneous intrusions in Central Spitsbergen

—

Marte Hergot Festøy
GEO-3900 Master's thesis in geology, May 2017

This document was typeset using the *UiT Thesis LaTeX Template*

Abstract

Igneous intrusions have a strong influence on petroleum systems, groundwater aquifers, and CO_2 storage reservoirs, particularly because they can act as either barriers to, or carriers for fluid flow. This depends on several syn- and post emplacement processes, including fracture development in the intrusion and the host rocks, contact metamorphism of the host rocks, and hydrothermal activity. Especially a highly fractured intrusion-host rock interface can channelize fluids along the intrusion contact. This study integrates outcrop and core data from central Spitsbergen, Arctic Norway, in order to constrain the impact of Lower Cretaceous igneous intrusions on subsurface fluid flow within a siliciclastic reservoir (i.e. the Triassic Kapp Toscana Group), targeted for CO_2 storage. The applied methods include fracture analyses of intrusions and host rocks, partly using digital geology and constructed 3D virtual outcrop models, and porosity analyses of the intrusion-proximal host rocks. At several localities, fracture sets both within the dolerites and the nearby host rocks, reflect the orientation of the intrusions. Fracture frequencies in general increase towards the intrusion contacts. Porosity analyses of host rocks positioned up to 4 m away from the intrusion contact of a 2.28 m thick sill in the DH4 borehole show generally low matrix porosities (on average 0.3%), with calcite cement observed to be the most abundant secondary mineral. In addition, calcite cement is frequently observed in fractures and veins within most intrusions and along the intrusion contacts, but also in intrusion-proximal host rock fractures and in faults that cross-cut the intrusions. In relation to the 2.28 m thick sill, a decrease in the occurrence of precipitated calcite, and an increase in host rock porosity is documented to occur somewhere between 4.82 m and 17.64 m from the intrusion contacts. This is largely attributed to hydrothermal activity occurring both during and after magma cooling. Based on the results from this study, a time transgressive conceptual model for rock evolution and fracture development in and around the igneous intrusions is presented, strongly benefited from 7993 fracture orientation measurements from virtual outcrop analyses. The results suggest that the igneous intrusions in central Spitsbergen primarily act as impermeable barriers to fluid flow. However, they can also provide high-permeability pathways along the highly fractured intrusion-host rock interface. Due to the presence of exceedingly fractured chilled margin of sills, a lack of calcite cement along sill-host rock contacts, no observed chilled margins of dykes, and the observation of thick (up to 10 cm) calcite veins along the dyke contacts, fluid flow is inferred to be higher along the margins of sills than along the margins of dykes. The combination of sills, dykes and other sealing features, can therefore explain why the targeted aquifer has been previously shown to be compartmentalized into several pressure units.

Acknowledgements

- Chrissy McCabe, Lis Allaart and Paul Velsand, for proof-reading this thesis.

- Torgeir Blæsterdalen and Sara Bjørk for support with bugs in LaTeX.

- My family, for always believing in me and supporting me.

Contents

/1

Introduction

1.1   Background and project presentation

Igneous intrusions frequently occur in extensional- (e.g., Jin et al., 1999; Planke et al., 2005; Schofield et al., 2015) and contractional basins (e.g., Witte et al., 2012; Gürer et al., 2016), but also in other settings such as intracratonic sag basins and platform areas (e.g., Senger et al., 2014a; La Terra et al., 2016). During intrusion emplacement, processes associated with the hot (commonly higher than 1100° C, Kjeldstad et al., 2003), overpressured magma (Lister & Kerr, 1991) lead to the formation of a contact aureole (Aarnes et al., 2010) and a complex fracture network in the host rocks proximal to the intrusion (e.g., Delaney et al., 1986; Senger et al., 2013a). Furthermore, complex fracture networks are formed related to cooling of the magma (Hetényi et al., 2012), as the thermal front will be determined by the igneous intrusion geometry (e.g., Spry, 1962; DeGraff & Aydin, 1987; Hetényi et al., 2012). Mafic crystalline igneous rocks typically have a tight matrix, with low permeability and primary porosity (e.g., Petford, 2003; Bermúdez & Delpino, 2008). Fracture networks therefore represent important elements when considering reservoir fluid flow and the sealing capacity of a given intrusion, which may form a barrier to, or a carrier for fluid flow (e.g., Nelson, 2001; Petford, 2003; Rateau et al., 2013). Additionally, an intensely fractured intrusion-host rock interface may channelize fluids along the contact (e.g., Enslin, 1955; Babiker & Gudmundsson, 2004; Matter et al., 2006; Rateau et al., 2013). Depending on several syn- and post-emplacement processes, such as contact metamorphism, hydrothermal activity, diagenesis and tectonic activity, the fractures related to intrusion emplacement can either

be open or closed, making some igneous intrusions permeable and others impermeable (e.g., Petford, 2003; Rateau et al., 2013).

Igneous activity and associated processes can therefore directly influence the flow of groundwater, hydrocarbons, injected CO_2, or hydrothermal fluids (e.g., Schutter, 2003; Wilkes et al., 2004; Babiker & Gudmundsson, 2004; Rateau et al., 2013; Senger et al., 2013a; Gudmundsson & Løtveit, 2014; Comte et al., 2017; Gao et al., 2017). In Svalbard, Early Cretaceous igneous intrusion are found emplaced within Permian to Jurassic siliciclastic and carbonate strata (e.g., Nejbert et al., 2011; Senger et al., 2013a) of the uplifted and subaerially exposed north-western corner of the Barents shelf. This also includes the Upper Triassic to Middle Jurassic Kapp Toscana Group, which is currently being investigated as a reservoir for CO_2 storage (Longyearbyen CO_2 Lab of Svalbard, Braathen et al., 2012).

Fractures related to intrusion emplacement can be divided into three major groups, as suggested by Senger et al. (2015): emplacement-induced fractures, cooling fractures and tectonic fractures. Emplacement induced fractures occur in the host rocks adjacent to the intrusion during magma emplacement, and the fracture spacing commonly increases with distance to the contact (e.g., Delaney et al., 1986). This is because magma is overpressured when it is emplaced (Lister & Kerr, 1991), and triggers substantial damage in the host rocks (e.g., Delaney & Pollard, 1981; Delaney et al., 1986; Jackson & Pollard, 1990; Schaefer & Kattenhorn, 2004; Kattenhorn & Schaefer, 2008). Cooling fractures are fractures forming within the intrusion, and are related to thermal contraction during cooling of the magma (e.g., Jaeger, 1968; DeGraff & Aydin, 1987; Hetényi et al., 2012). The formation of these can follow a four-step trend related to magma emplacement: formation of a highly fractured chilled margin, column-bounding fractures, column-normal fractures and entablature fractures. Chilled margins form as an initial response to magma emplacement against cold surrounding rock (e.g., Van Wyk, 1963; Huppert & Sparks, 1989; Fialko & Rubin, 1999). Column bounding fractures form and propagate in accordance with the isotherm pattern and the thermal stress within the flow (i.e. columnar joints), and are subdivided by column-normal fractures perpendicular to their lengths (e.g., Schaefer & Kattenhorn, 2004; Bermúdez & Delpino, 2008; Kattenhorn & Schaefer, 2008). Entablature fractures represent the final stage of magma cooling, and are often located slightly below the intrusion center (DeGraff & Aydin, 1987; Grossenbacher & McDuffie, 1995; Schaefer & Kattenhorn, 2004). Tectonic fractures, including compaction, exhumation and fault related fractures, are non-related to the intrusion emplacement, and can be present in both intrusions and the host rocks, depending on the timing of the tectonic activity.

Heat conduction from the intrusion can cause the development of a localized contact metamorphic aureole in the host rock (Jaeger, 1959; Simoneit et al., 1978; Aarnes et al., 2010). Furthermore, the presence of fluids can cause hydrothermal activity (e.g., Einsele et al., 1980; Park & Ripley, 1999; Wolela, 2002). Together, contact metamorphic and hydrothermal processes are shown to alter the properties of porous host rocks adjacent to the intrusion, including dissolution of biogenic material, calcite precipitation and recrystallization, clay crystallization, organic matter decomposition and a decrease in porosity (e.g., Einsele et al., 1980; Wolela, 2002; Aarnes et al., 2010; Magee et al., 2013).

Early Cretaceous intrusions in Svalbard belong to the Diabasodden Suite (e.g., Dallmann, 1999; Maher, 2001; Senger et al., 2014b), and have been mapped in an integrated onshore-offshore study by Senger et al. (2013a). The Permian to Jurassic host rocks are well studied. In particular, the Kapp Toscana Group has been extensively investigated with focus on depositional environment (e.g., Mørk et al., 1982; Mørk et al., 1989), diagenesis (e.g., Mørk, 2013) and fracture development (Wærum, 2011; Ogata et al., 2014, 2014). Studies related to the effects of igneous intrusions on the host rocks in Svalbard have primarily focused on the influence of intrusions on the alteration of organic material (Hubred, 2006; Senger et al., 2014a), while fracture analyses of intrusion-related fractures have only focused on the fractures present within the dolerites (Wærum, 2011; Ogata et al., 2012, 2014). However, while natural fractures are suggested to play a key role in in the reservoir storage capacity (Braathen et al., 2012; Ogata et al., 2014), the intrusion-host rock interface has yet to be investigated.

The understanding of how igneous intrusions affect their host rocks and sub-surface fluid flow has improved during the recent years (e.g., Woodford & Chevallier, 2002; Bermúdez & Delpino, 2008; Witte et al., 2012; Holford et al., 2013; Rateau et al., 2013; Schofield et al., 2015). However, while many studies rely on borehole, core and seismic data (e.g., Planke et al., 2005; Bermúdez & Delpino, 2008; Monreal et al., 2009; Holford et al., 2013; Rateau et al., 2013; Schofield et al., 2015), some field based studies have been conducted in e.g. the Neuquen Basin, Argentina (Witte et al., 2012) and in the Karoo Basin, South Africa (Woodford & Chevallier, 2002; Senger et al., 2013a). Quantitative mapping of fracture patterns (Delaney & Pollard, 1981; Delaney et al., 1986; Senger et al., 2015) in addition to numerical and experimental modeling of host rock deformation during intrusion emplacement (Mériaux et al., 1999; Abdelmalak et al., 2012; Galland & Scheibert, 2013) has only been carried out by only a limited number of studies.

In Svalbard, no study has previously investigated fracture patterns at the intrusion-host rock interface. An understanding of how the igneous intrusions affect the host rocks, and how fractures in and around the igneous intrusions

affect fluid flow, is generally lacking (Braathen et al., 2012; Senger et al., 2013a; Senger et al., 2013b;). In addition, several studies from Svalbard are relying on borehole data and remote sensing (Senger et al., 2013a; Senger et al., 2014a). Therefore, a better semi-regional understanding of the Diabasodden Suite, and what effects the intrusions have on the host rocks, is necessary in order to facilitate CO_2 sequestration. Furthermore, fracture and porosity investigations related to igneous intrusions will improve the knowledge related to petroleum and ground water exploration (Senger et al., 2015; Rateau et al., 2013; Schofield et al., 2015; Comte et al., 2017).

1.2   Aims and objectives

This study integrates outcrop and core data in order to characterize igneous intrusions in central Spitsbergen, and aims at investigating the effect the Early Cretaceous intrusions of the Diabasodden Suite have on local and regional fluid flow. The main objective is to develop a conceptual model of rock evolution and fracture development in and around igneous rocks, which is addressed through the following tasks:

- Test and verify methods related to fracture analyses based on photogrammetry.

- Determine petrography and geochemistry of the investigated intrusions.

- Determine porosity changes in host rocks with distance to intrusion contact.

- Quantitatively investigate fracture patterns in and around igneous rocks.

/2

Geological framework

2.1 The geological evolution of Svalbard

The study area is located in central Isfjorden, Spitsbergen. It comprises localities in the Rotundafjellet-Studentdalen area, the Hatten-Botneheia area and Wallenbergfjellet (Figs. 4.1, 3.2), in addition to Adventdalen (cores from the DH4 borehole, Figs. 3.3, 2.7c). This chapter introduces the tectonic setting of Svalbard, the Early Cretaceous igneous rocks of Svalbard and the Arctic, lithostratigraphy and host rock geology, and the major tectonic events that the strata have experienced.

2.1.1 Tectonic setting

The Svalbard archipelago comprises all islands from 74 to 81°N and 10 to 35°E (Fig. 2.1), including Bjørnøya in the south, Kvitøya in the east, and Spitsbergen, which is the largest island, in the west. Currently, Svalbard is bordered to the north by a passive continental margin towards the Arctic Ocean and to the west by a sheared margin (Sundvor & Eldholm, 1979; Faleide et al., 1984). In the north-west, the spreading axis of the transformly segmented Knipovich Ridge (Talwani & Eldholm, 1977) truncates the continental slope of the Barents Shelf. The history of plate tectonics in the Arctic is highly debated (e.g., Vogt et al., 1979; Saltus et al., 2011; Tegner et al., 2011; Døssing et al., 2013), and the remoteness, the prevailing sea ice cover and general harsh conditions makes the Arctic underexplored.
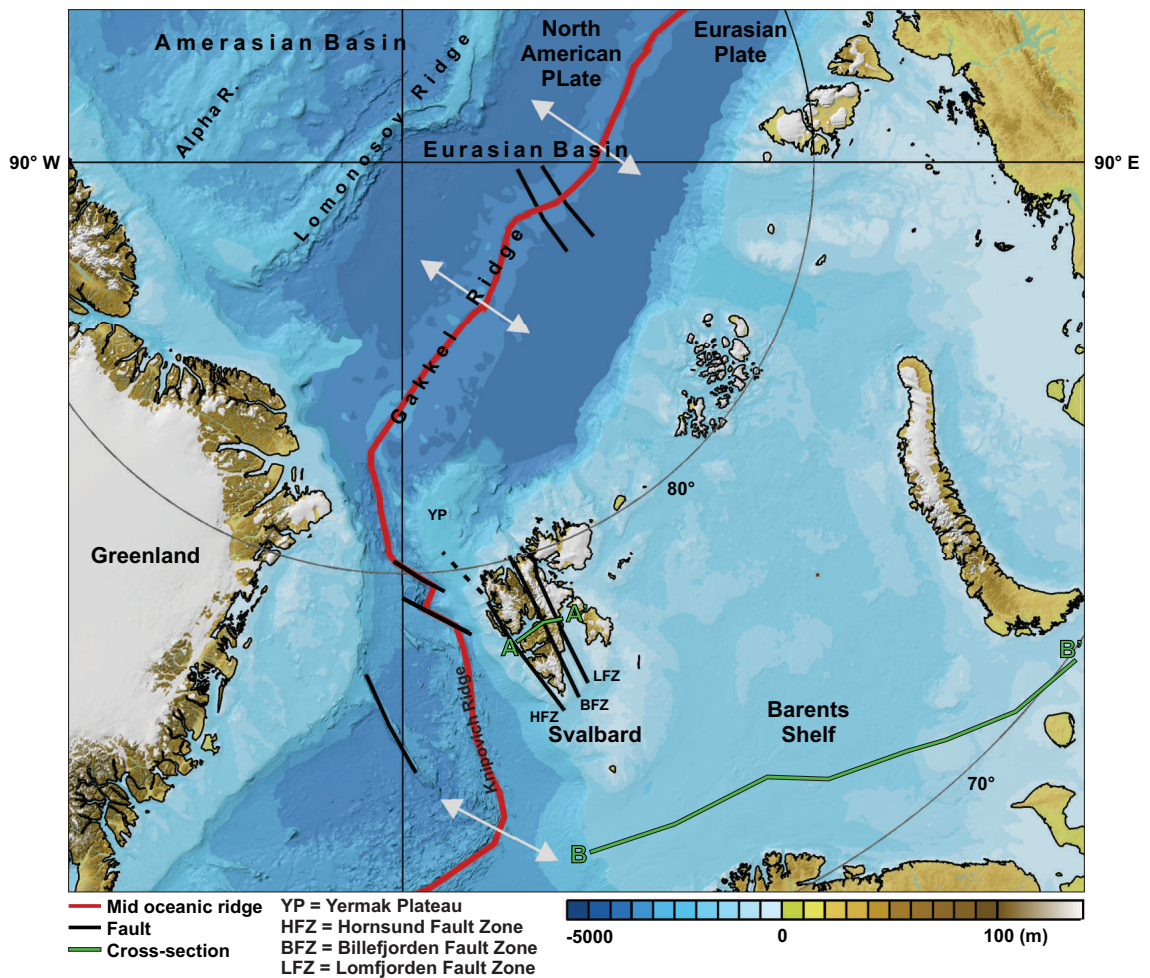
Figure 2.1: Arctic bathymetry (IBCAO v3 dataset) with present tectonic setting. Profiles A-A' and B-B' are displayed in Fig. 2.8. Map modified from Jakobsson et al. (2012)), and tectonic setting details are added from Dallmann (2015).

2.1.2 Lithostratigraphy and host rock geology

Svalbard's sedimentary record is characterized by a continuous northern drift from sub-equatorial latitudes in the Devonian to its present location at 80°N (Fig. 2.2, Worsley et al., 1986). The geological evolution of the lithostratigraphic units in the study area (Fig. 2.2), from Permian to Early Cretaceous, is outlined below. For a more complete overview of the entire stratigraphy, refer to Steel & Worsley (1984) and Dallmann (1999, 2015).
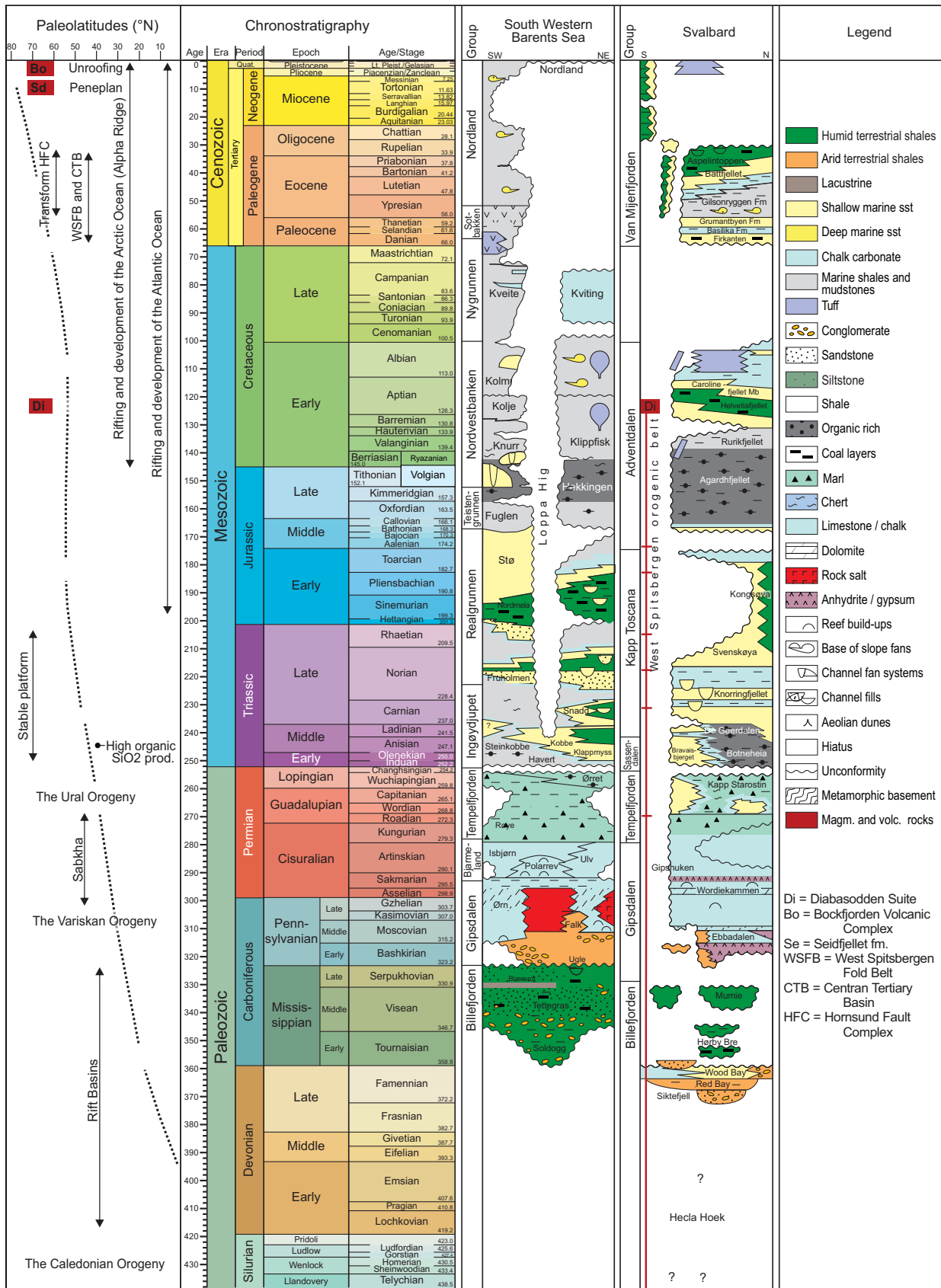
Figure 2.2: Lithostratigraphic chart (modified from Gradstein et al., 2010) with paleo-latitudes estimated from paleomagnetic records (modified from Worsley et al., 1986) and major tectonic events (Dallmann, 2015).

Permian

During the Late Carboniferous, a regional transgression led to development of a warm water carbonate platform (Fig. 2.3a), later resulting in the deposition of carbonates, mudstones and evaporites of the Lower Permian Gipsdalen Group (Fig. 2.2, e.g., Stemmerik & Worsley, 2005). These sediments represent an open- to marginal marine shelf setting with warm and dry conditions (e.g., Hüneke et al., 2001). The climate gradually cooled in concert with a new regional transgression, forming a hiatus that marks the boundary between the Gipsdalen Group and the overlying Upper Permian Tempelfjorden Group (Dallmann, 2015). The Tempelfjorden Group is primarily characterized by biogenic chert (mainly from siliceous sponge spicules) and fossiliferous cool-water limestone, reflecting an open-marine setting with changing temperatures (Fig. 2.3b,c, Blomeier et al., 2011). In Spitsbergen, the Tempelfjorden Group is mainly represented by the cliff-forming Kapp Starostin Formation. The movement of Sibiria towards Euramerica resulted in the formation of the Ural mountain chain and the final development of Pangea at the end of the Permian (Dallmann, 2015).
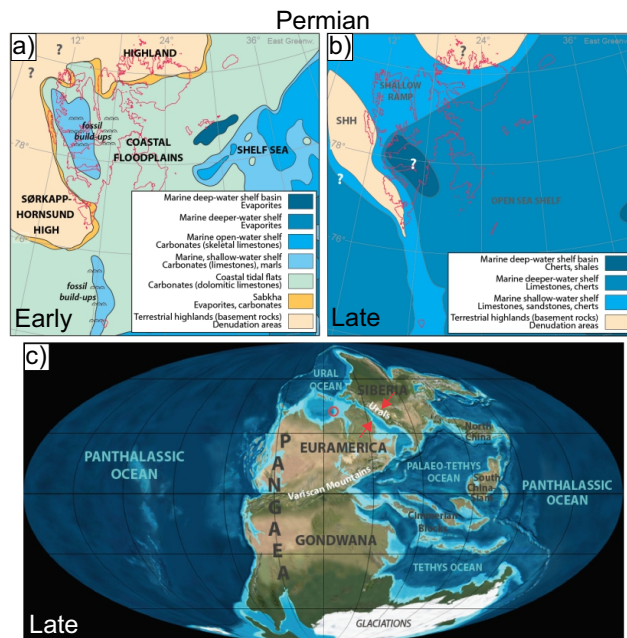
Figure 2.3: Geological setting, Permian. Paleogeographic reconstruction of Svalbard's sedimentary basins during (a) Early and (b) Late Permian. (c) Global paleogeographic reconstruction. Figures modified from Dallmann (2015), see references therein for further details.

Triassic

The Permian-Triassic boundary is marked by a mass extinction (e.g., Cuvier, 1825; Newell, 1967; Baresel et al., 2017), with 90-95 % of all marine species and around 70 % of all terrestrial species being lost (Dallmann, 2015). The mass extinction has, since the early days, been linked to sea level changes (e.g., Cuvier, 1825). More recently, it was placed during a global regression (Newell, 1967), which is suggested to have been caused by an eruptive phase and an associated, short-lived ice age (Baresel et al., 2017). In Svalbard, the boundary between the Kapp Starostin Formation and the overlying Early to Middle Triassic Sassendalen Group is marked by an abrupt occurrence of shales and sandstones (Fig. 2.2), suggested to reflect transgression, and an abrupt shut-down of the silica and cool-water carbonate factories (Fig. 2.4a, b, Worsley, 2008). During the Triassic, Svalbard experienced stable shelf conditions with repeated sea level changes (Fig. 2.4, Faleide et al., 1984; Stemmerik & Worsley, 2005). The Sassendalen Group in central Spitsbergen is primarily represented by the Vikinghøgda Formation (mainly mudstones with sand- and siltstone beds, Mørk et al., 1999) and the Botneheia Formation (mainly organic rich mudstones, e.g., Worsley, 2008).
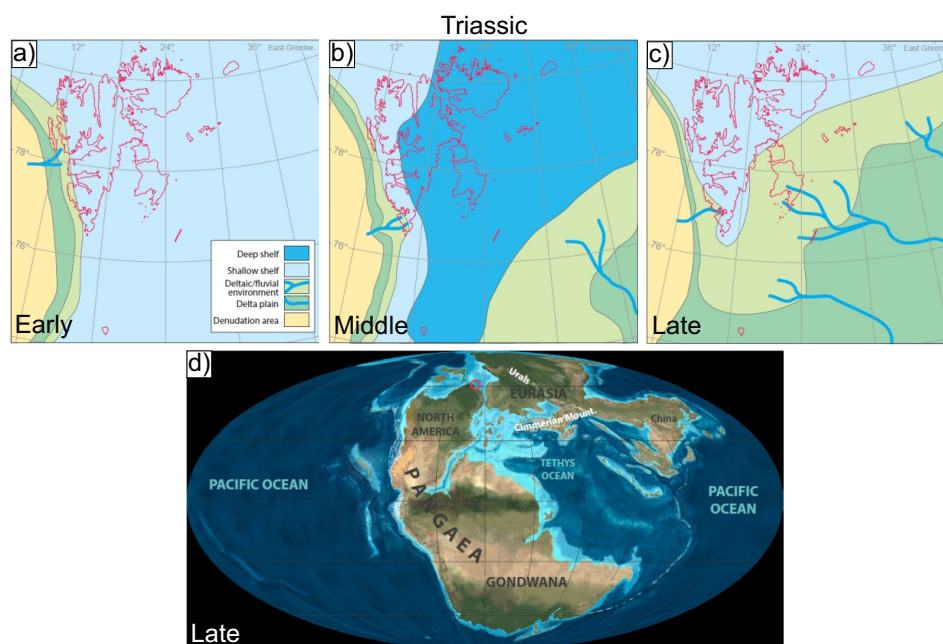
Figure 2.4: Geological setting, Triassic. Paleogeographic reconstruction of Svalbard's sedimentary basins during (a) Early, (b) Middle and (c) Late Triassic. (d) Global paleogeographic reconstruction. Figures modified from Dallmann (2015), see references therein for further details.

The Upper Triassic to Lower Jurassic Kapp Toscana Group marks a considerable change in sedimentation pattern from the Sassendalen Group. The sediment source, previously from the North America and Greenland in the west, was now accompanied by a new sediment source from the Ural Mountains in the east (Fig. 2.4c, d, e.g., Riis et al., 2008; Lundschien et al., 2014). The lower part of the Kapp Toscana Group is comprised of upwards coarsening, deltaic sequences, where the lower mudstones are classified as the Tschermakfjellet Formation, and grade upwards into the De Geerdalen Formation (Fig. 2.2, Dallmann, 2015). The boundary between these two formations is defined by the first resistant sandstone bed (Flood et al., 1971). The two formations make up the Storfjorden Subgroup, and represent the distal equivalent of the Snadd Formation in the Barents Sea (Riis et al., 2008; Lundschien et al., 2014). Further transgression initiated the deposition of the Wilhelmøya Subgroup, (i.e. Knorringfjellet Formation in central Spitsbergen). Uplift and erosion during Late Triassic to Early Jurassic (Fig. 2.9) resulted in reworking and mixing of sediments, and a condensed, quartzitic sandstone unit, represented by the Wilhelmøya Subgroup (e.g., Mørk et al., 1982; Mork, 1999; Riis et al., 2008). The Wilhelmøya Subgroup comprises Late Triassic to Middle Jurassic sediments, and is time-equivalent to the Realgrunnen Subgroup in the Barents Sea (Riis et al., 2008).

Jurassic

During the Early Jurassic, Pangea started to break up as a result of tensile forces, forming an early stage of the Atlantic Ocean between Gondwana and North America (Fig. 2.5a, Dallmann, 2015). In the Late Jurassic (Fig. 2.5b, c), Svalbard was located at 60 °N (Dallmann, 2015). A transgression resulting in deep-marine conditions paired with a relatively high atmospheric CO_2 content and high temperatures are reflected by deposits of organic rich shales defined as the Agardhfjellet Formation of the Adventdalen Group (Fig. 2.2, Ramberg et al., 2007).

Cretaceous

The Lower Cretaceous strata in Svalbard also belong to the Adventdalen Group (Fig. 2.2), and represent a deep to inner shelf setting with a warm and humid climate (Dallmann, 2015). The basal Rurikfjellet Formation was deposited from the Berriasian to the Hauterivian (Fig. 2.6a), and consists primarily of shales and shallow-marine sandstones representing less stagnant conditions than the deposits of the Agardhfjellet Formation (Dypvik, 1984). In central Spitsbergen, a regional unconformity separates the Rurikfjellet Formation from the overlying Barremian to Early Aptian Helvetiafjellet Formation (Fig. 2.6b, Gjelberg &

Steel, 1995). Opening of the Canada Basin during the Early Cretaceous (Tegner et al., 2011; Døssing et al., 2013) led to volcanic activity (Fig. 2.6b, c) and the emplacement of the High Arctic Large Igneous Province during the Barremian, Aptian and Albian (Section 2.1.3, e.g., Maher, 2001), an increased heat flux, and global sea level rise (Dallmann, 2015). This resulted in the fluvial deposits of the Helvetiafjellet Formation alternating with extrusive basalt flows on Kong Karls Land in the east (Smith et al., 1976). The overlying Aptian to Albian Carolinefjellet Formation (Fig. 2.2) consists of shallow marine shales and sandstones (Nøttvedt & Kreisa, 1987), and has a transitional boundary to the underlying Helvetiafjellet Formation (Dallmann, 2015).
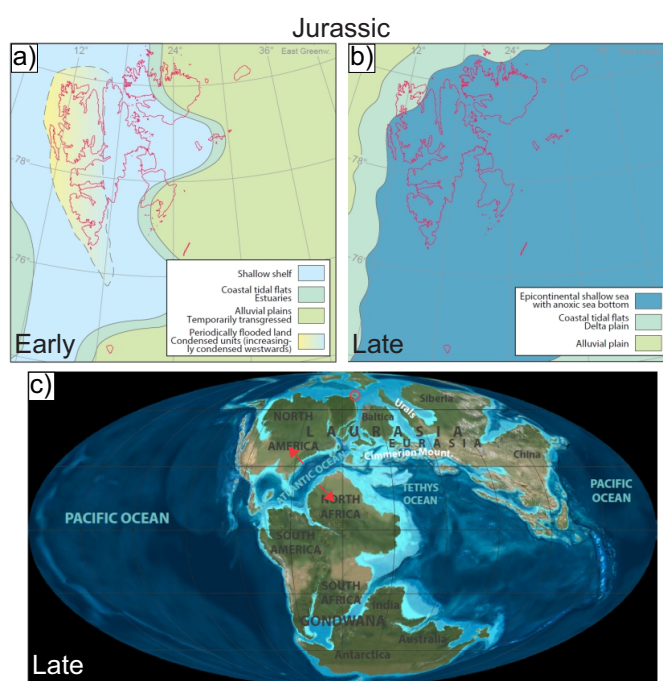
Figure 2.5: Geological setting, Jurassic. Paleogeographic reconstruction of Svalbard's sedimentary basins during (a) Early and (b) Late Jurassic. (c) Global paleogeographic reconstruction. Figures modified from Dallmann (2015), see references therein for further details.

2.1.3 High Arctic Large Igneous Province

Widespread Cretaceous igneous activity in the Arctic has been classified as a Large Igneous Province (LIP, see Bryan & Ernst, 2008 for the definition), collectively referred to as the High Arctic Igneous Province (HALIP, Tarduno et al., 1998). The HALIP covers several hundred thousand square kilometers and includes several areas of volcanics and related hypabyssal intrusives. The areas

include Svalbard, Franz Josef Land, the Canadian Arctic and North Greenland (Fig. 2.7d, Maher, 2001).
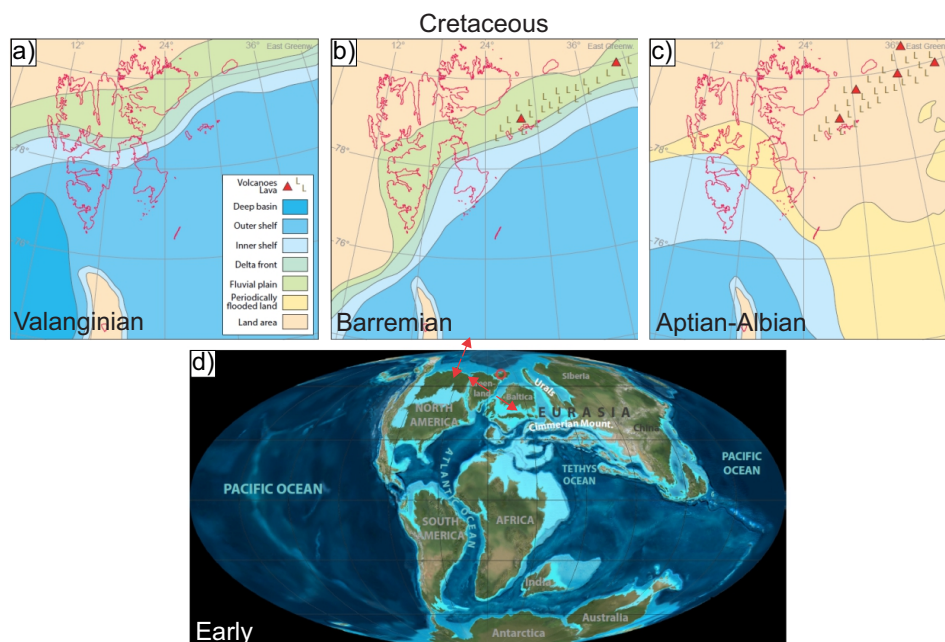
Figure 2.6: Geological setting, Early Cretaceous. Paleogeographic reconstruction of Svalbard's sedimentary basins during (a) the Valangian, (b) the Barremian and (c) the Aptian-Albian. (d) Global paleogeographic reconstruction. Figures modified from Dallmann (2015), see references therein for further details. Tectonic setting of the High Arctic from (Tegner et al., 2011).

Recently, there has been an increased interest in understanding the HALIP due to its important implications for petroleum geology and maturation of host rocks. In addition, host rock maturation and the release of thermogenic gas was possibly also a trigger for the paleoenvironmental changes during the Early Cretaceous (e.g., Grogan et al., 2000; Polteau et al., 2016). Several authors have proposed the origin of the HALIP to be related to the opening of the Canada Basin and subsequent formation of the Alpha Ridge (e.g., Grogan et al., 2000; Tegner et al., 2011). However, large age spans of the HALIP (e.g., 160-80 Ma, Grogan et al., 2000, 120-130, 80-90 Ma, Polteau et al., 2016) from several dating methods are suggested to have been caused by hydrothermal alteration, although several authors also agree that the igneous intrusions in the Barents Sea are of an older age than the volcanics dominantly found in the Arctic Canada and Northern Greenland (e.g., Grogan et al., 2000; Corfu et al., 2013; Polteau et al., 2016). Therefore, the accumulation of the HALIP may either be considered bimodal, as the composition has shifted from tholeiitic towards alkaline (Bailey & Rasmussen, 1997; Estrada & Henjes-Kunst, 2004), or, the two

different compositions, from two different age spans, represent two unrelated events (e.g., Tegner et al., 2011; Thórarinsson et al., 2015). The emplacement of the HALIP is also suggested to have happened independently from the rifting (Schiffer et al., 2017). The processes that caused the opening of the Amerasia and Canada Basins are still highly debated (Schiffer et al., 2017).

2.1.4 Diabasodden Suite

The Diabasodden Suite (defined by Dallmann, 1999) is a complex of basaltic, intrusive and extrusive rocks belonging to the HALIP (Fig. 2.7a, b, c), and are exposed all across Svalbard. In central Spitsbergen, the rocks occur mainly as sills, with thicknesses ranging from 1 m to over 100 m (Maher, 2001; Senger et al., 2014b). Dykes are less common, and have thicknesses up to 15 m (Senger et al., 2014b). In addition, extrusive lava flows are as mentioned exposed on Kong Karls Land in the east ('Kong Karls Land Flows', Smith et al. 1976). In central Spitsbergen, host rocks are commonly comprised of Triassic shale and sandstone successions and Jurassic to Cretaceous shales (Senger et al., 2014b). However, the doleritic intrusions are also present in Devonian-Permian strata, within the Hecla Hoek basement (Birkenmajer & Morawski, 1960), and in unconsolidated sandstones of the Helvetiafjellet Formation on Kong Karls Land (Fig. 2.7, Smith et al., 1976). The emplacement of the Diabasodden Suite has been dated to occur at c. 124.5 Ma (Corfu et al., 2013).

Samples from the Diabasodden Suite are normally medium- to fine-grained, tholeiitic, ophitic and olivine/quartz basalts (Senger et al., 2014b), and are commonly referred to as dolerites (e.g., Grogan et al., 2000; Senger et al., 2014a; Polteau et al., 2016). According to total alkalis versus silica diagrams, all Mesozoic dolerite samples reported from Svalbard have a basaltic composition, including the extrusives on Kong Karls Land. Their geochemical signature is consistent with the HALIP igneous rocks throughout the Arctic, and differs from both older and younger magmatic provinces on Svalbard (Senger et al., 2014b).

For a more complete overview of the HALIP and the Diabasodden Suite, see Maher (2001) and Senger et al. (2014b).
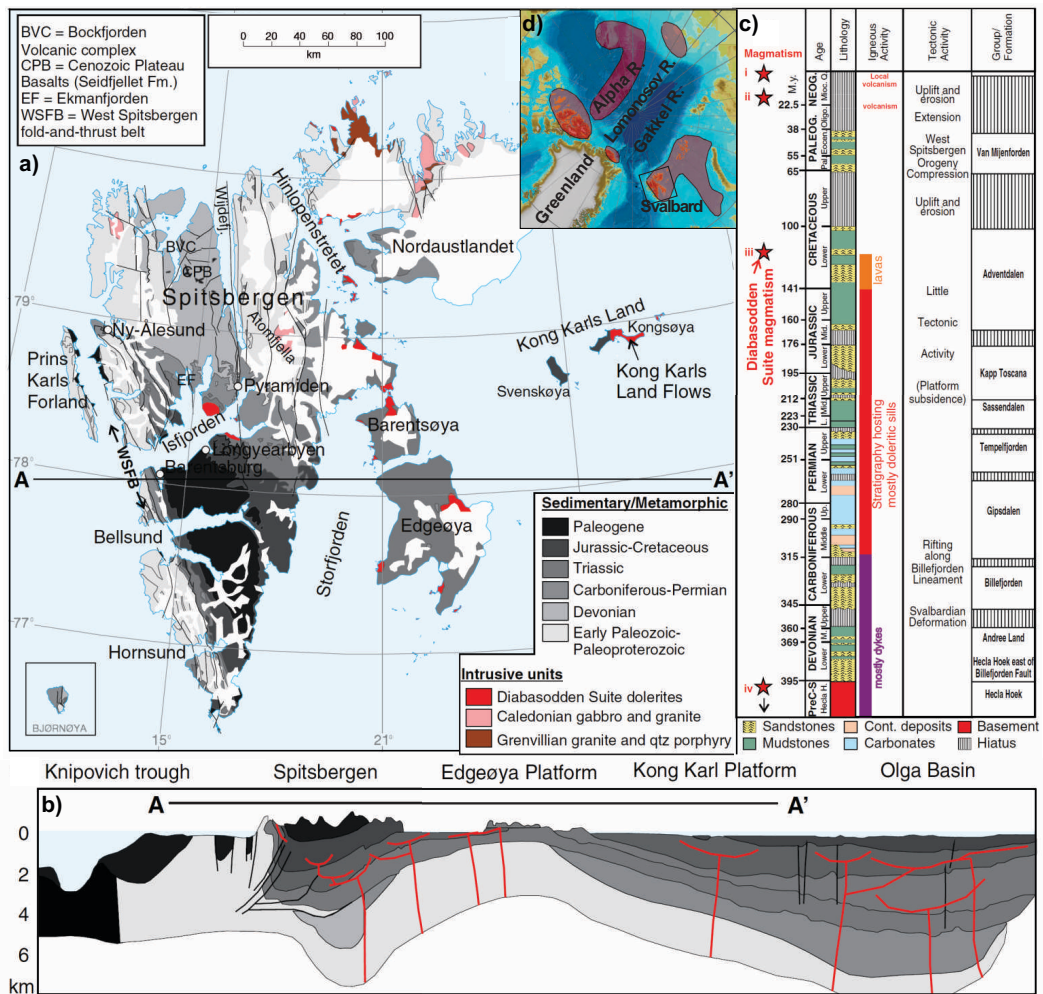
Figure 2.7: (a) Geological map of Svalbard. (b) West-east cross-section, with schematically represented dolerites (red). (c) Stratigraphic column of Svalbard, including magmatic events. (d) Arctic bathymetry (IBCAO v3 dataset) and extent of main igneous provinces classified as part of the High Arctic Large Igneous Province (red area). Figures modified from Senger et al. (2014b), Elvevold et al. (2007), Nøttvedt et al. (1993), Tegner et al. (2011), Shipilov & Karyakin (2010) and Nejbert et al. (2011).

2.1.5 Tectonic evolution

Paleogene

In the Paleogene, the Early Cretaceous intrusions and their host rocks were influenced by compressional tectonics to the west and extensional tectonics to the north (Sundvor & Eldholm, 1979; Tegner et al., 2011; Døssing et al.,

2013). In Early Paleocene, transpression related to rifting in the Labrador Sea caused Greenland and Svalbard to move along the Wegener Fault Zone against the Barents Shelf (Dawes, 2009). This resulted in the formation of the West Spitsbergen fold-and-thrust-belt (WSFB), with major thrust sheets soled in décollement zones along layers of mechanically weak shale and evaporite (e.g., Bergh et al., 1997). In addition, the strata were locally uplifted and tilted (Figs. 2.8a, 2.9), causing steeply dipping beds in the east and gently tilted beds in the west. Some of the intrusions are exposed in the strata folded as part of the WSFB (Birkenmajer et al., 2010). The tilted strata formed a foreland basin in Spitsbergen, collectively referred to as the Central Tertiary Basin (CTB, e.g., Bergh et al., 1997; Braathen et al., 1999; Dörr et al., 2012).

Preexisting N-S striking fault zones, such as the Billefjorden Fault Zone (BFZ) and the Lomfjorden Fault Zone (LFZ), were also reactivated in association with the Paleogene transpression (e.g., Harland et al., 1974; Andresen et al., 1992; Haremo et al., 1993). The BFZ is suggested to have originated as a strike-slip fault zone in connection with the Caledonian Orogeny, and later been reactivated as a normal fault during the Carboniferous (e.g., Johannessen & Steel, 1992; Bælum & Braathen, 2012). South of Isfjorden, east of Botneheia (in Flowerdalen), a reverse fault of the BFZ cuts through the Mesozoic succession, juxtaposing Permian and Triassic strata (Fig. 2.8a, Haremo & Andresen, 1988). The long-lived, presently N-S trending fault zones may have also had implications for magma emplacement during the Early Cretaceous, as weak zones are preferable pathways for magma flow. The study area is located just west of the BFZ.

In the Early Eocene, rifting decreased in the Labrador Sea, oppositely to the North Atlantic where rifting increased (e.g., Skogseid et al., 2000; Jones et al., 2016). The Barents Shelf and Greenland experienced transtension as they moved past each other along the Hornsund Fault Zone (HFZ, Fig. 2.1, Dallmann, 2015). At the end of the Eocene, the continental connection between Greenland and the Barents Shelf was broken, and the former transform HFZ experienced tension (e.g., Dallmann, 2015). This formed a series of major graben formations (e.g., the Forlandsundet graben, e.g., Gabrielsen et al., 1992; Blinova et al., 2009). Sea-floor spreading in the North Atlantic initiated sea-floor spreading along the Gakkel Ridge (Moran et al., 2006). Svalbard migrated further away from Greenland (Faleide et al., 1984), and erosion and subsequent deposition of material from the WSFB created nearly flat-lying strata and peneplaining of the CTB (Fig. 2.8a, e.g., Livsic, 1974; Steel et al., 1985; Grundvåg et al., 2014).
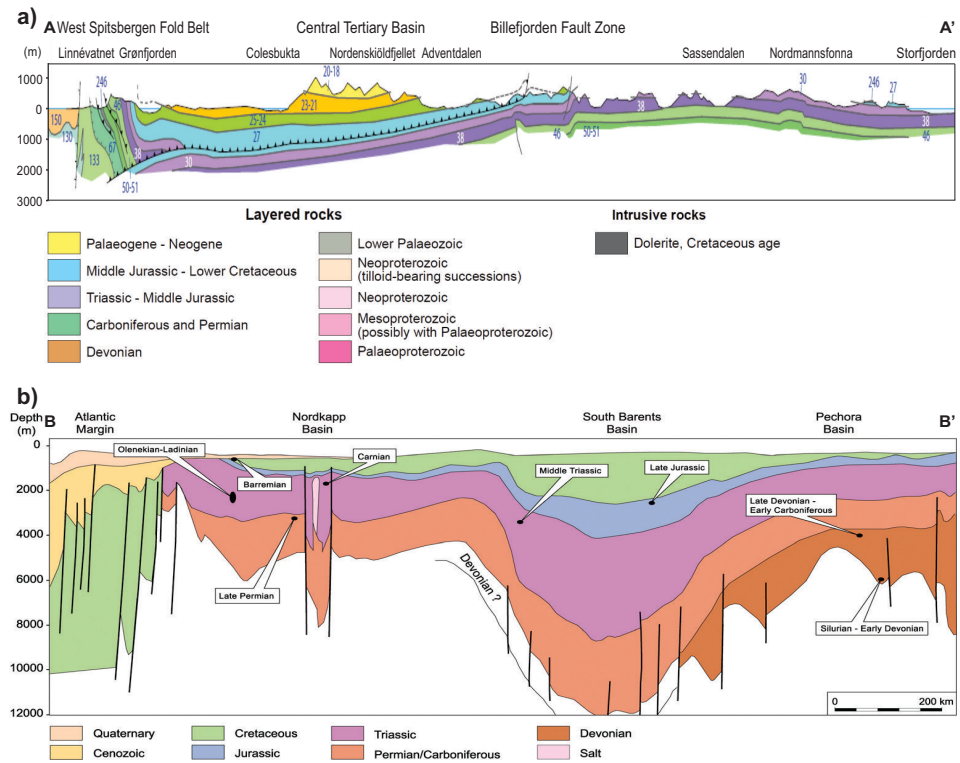
Figure 2.8: (a) Cross section through Nordenskiöld Land, Spitsbergen, modified from Dallmann (2015). (b) Regional cross section of the Barents Shelf, from Henriksen et al. (2011), modified from Johansen et al. (1992). Cross sections are vertically exaggerated. For locations of the cross sections, see Fig. 2.1.

Neogene-Quaternary

During the Miocene and the Pleistocene, northern Svalbard experienced local volcanism (Figs. 2.2, 2.7a, c), i.e. the Seidfjellet Formation (e.g., Prestvik, 1982; Feden et al., 1979; Crane et al., 1982) and the Bockfjorden Volcanic Complex (e.g., Hoel, 1914; Harland & Ay, 1997 Ladygin et al., 2003). The volcanism is suggested to have been related to hot spot activity on the Yermak Plateau (e.g., Prestvik, 1982; Feden et al., 1979; Crane et al., 1982; Dallmann, 1999). Finally, the strata was partly eroded and uplifted during and after the Quaternary glaciations (Dallmann, 2015).

The Cretaceous to Cenozoic regional uplift and tilting of Svalbard (Fig. 2.9, e.g., Vågnes & Amundsen, 1993; Dimakis et al., 1998; Knies et al., 2014) has made it possible to investigate the entire rock succession (Figs. 2.2, 2.8), including the Hecla Hoek basement in the northern and western regions of Spitsbergen, the Devonian in the northern and central part, and the Upper Paleozoic to

Paleogene platform- and foreland basin strata from central Spitsbergen to the easternmost regions of Svalbard (Worsley, 2008). The strata crop out along coastal cliffs as well as valley and fjord sides. The thin vegetation cover and the well preserved outcrops makes the rock succession easy to study, and can be used as a good analogue to subsurface successions in the Barents Sea (Fig. 2.8b).
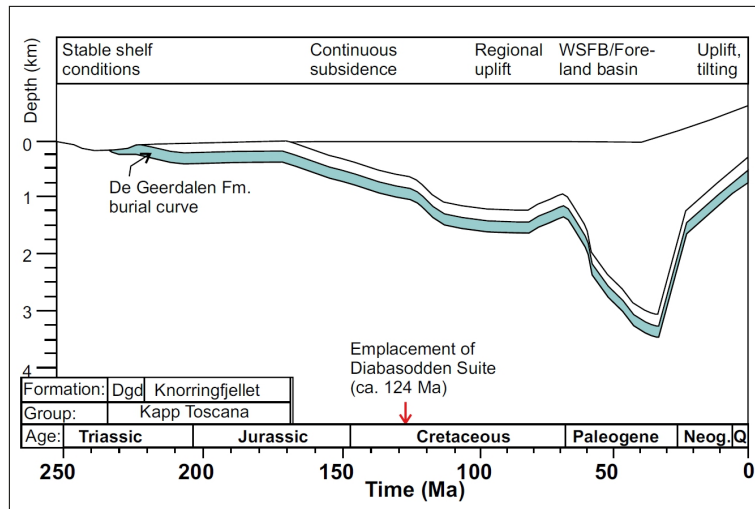
Figure 2.9: Burial curve of the Kapp Toscana Group since its deposition in Late Triassic-Middle Jurassic. DGD = De Geerdalen Formation (see Section 2.1.2). Figure from Senger et al. (2014a), based on vitrinite reflectance of Devonian-Cenozoic coals from Michelsen & Khorasani (1991). The timing of the Diabasodden Suite was constrained from Corfu et al. (2013). The overall tectonic regimes were based on Dallmann (1999).

/3

Data and methods

The proposed target for CO_2 storage, The Kapp Toscana Group (Braathen et al., 2012), is located 700 m below Adventdalen and is cropping out in the Deltaneset-Botneheia area (Fig. 3.2a). Igneous intrusions within the targeted reservoir unit (i.e. the De Geerdalen Formation) may affect the reservoir properties as they can act as both barriers to or carriers for fluid flow (e.g., Rateau et al., 2013). This study primarily uses outcrop data, in addition to cores from the DH4 borehole (Fig. 3.3) which vertically covers the target unit 672-970 m below Adventdalen (Senger et al., 2013b).

The methods used in this study are summarized in Fig. 3.1 and Table 3.1. Data from field methods were comprised of digital photos (Section 3.1.1), fracture zone analyses (Section 3.1.2), structural orientation data and scan lines (Section 3.1.3), lithological logs (Section 3.1.4) and dolerite samples (Section 3.1.5). High-resolution outcrop photos from the field were used to construct virtual outcrop models (e.g., Savary-Sismondini et al., 2008; Gillespie et al., 2011; Casini et al., 2016), and the models were used for further fracture analyses (Section 3.2). Thin sections of the dolerite samples were created, and the observations of these were compared to X-ray fluorescent scanning data of dolerite samples from the Rotundafjellet sill (R_b_01) and the Botneheia dyke (B_01, Section 3.3).

Sixteen m of the DH4 cores (from 942-958 m depth) were logged (Section 3.1.4) and sampled (Section 3.1.5). Thin sections (30 μm thick) were made from the samples, and mineralogical analyses were preformed using scanning electron microscopy and energy dispersive spectroscopy (Section 3.3).
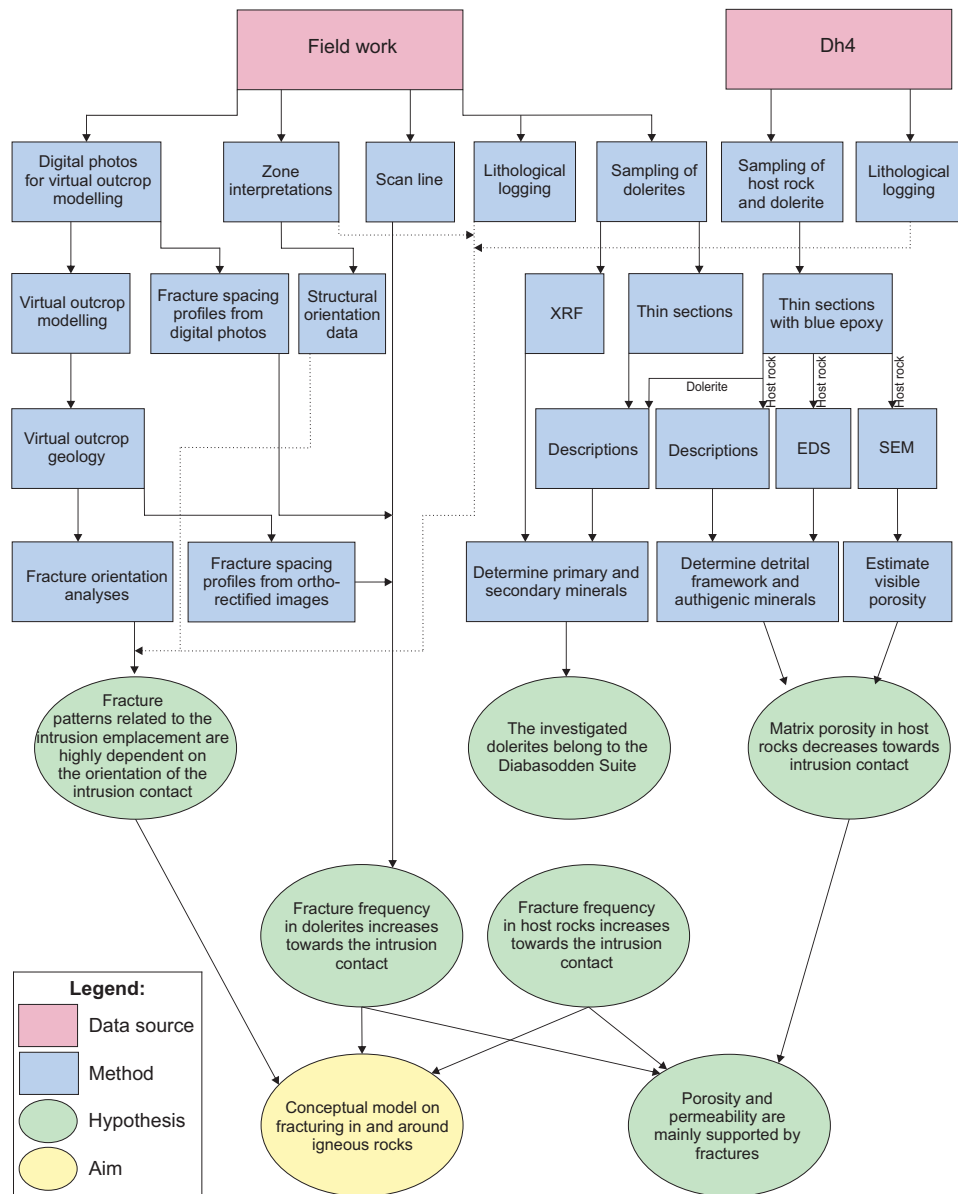
Figure 3.1: Flow chart illustrating the relation between the data source, methods, aims and hypothesises of this thesis.

3.1   Field work and the DH4 cores

Field work (Fig. 3.2) was conducted in central Isfjorden during three day trips in April and a 12 days field campaign in August. Snow mobiles were used for transportation in April, while Polar Circles were used in August. Both a tent

camp and cabins were used as a base during summer, and Longyearbyen was used as a base during spring. DH4 (Fig. 3.3) was studied during a two weeks long stay in Longyearbyen, December 2015.

Table 3.1: Summary of methods and data types used.

Data type	Method	Purpose	Quantity (n)	Comments
Geological map	Visualization	Field campaign planning		
Digital photos	Virtual outcrop modeling	Fracture analyses and outcrop visualization	1823	Digital photos used for virtual outcrop modeling
Digital photos and virtual outcrop models	Fracture spacing analyses	Fracture spacing in and around igneous intrusions	>1897	Mapped fractures
Virtual outcrop model	Fracture orientation analyses	Fracture orientation in and around igneous intrusions	6	Virtual outcrops
Dolerite samples	XRF	Dolerite geochemistry, tectonic setting during intrusion emplacement	2	Samples analysed by XRF
Dolerite samples	Thin sections	Determine petrography of dolerites	12	Samples used for thin section production
Dolerite thin sections	EDS	Determine mineralogy of dolerites	1	Thin sections analyzed by EDS
Host rock samples	Thin sections	Estimate porosity and determine mineralogy in host rocks	26	Samples used for thin section production
Host rock thin sections	SEM	Estimate porosity in host rock	3	Thin sections analyzed by SEM
Host rock thin sections	EDS	Determine primary and secondary minerals in host rocks	3	Thin sections analyzed by EDS
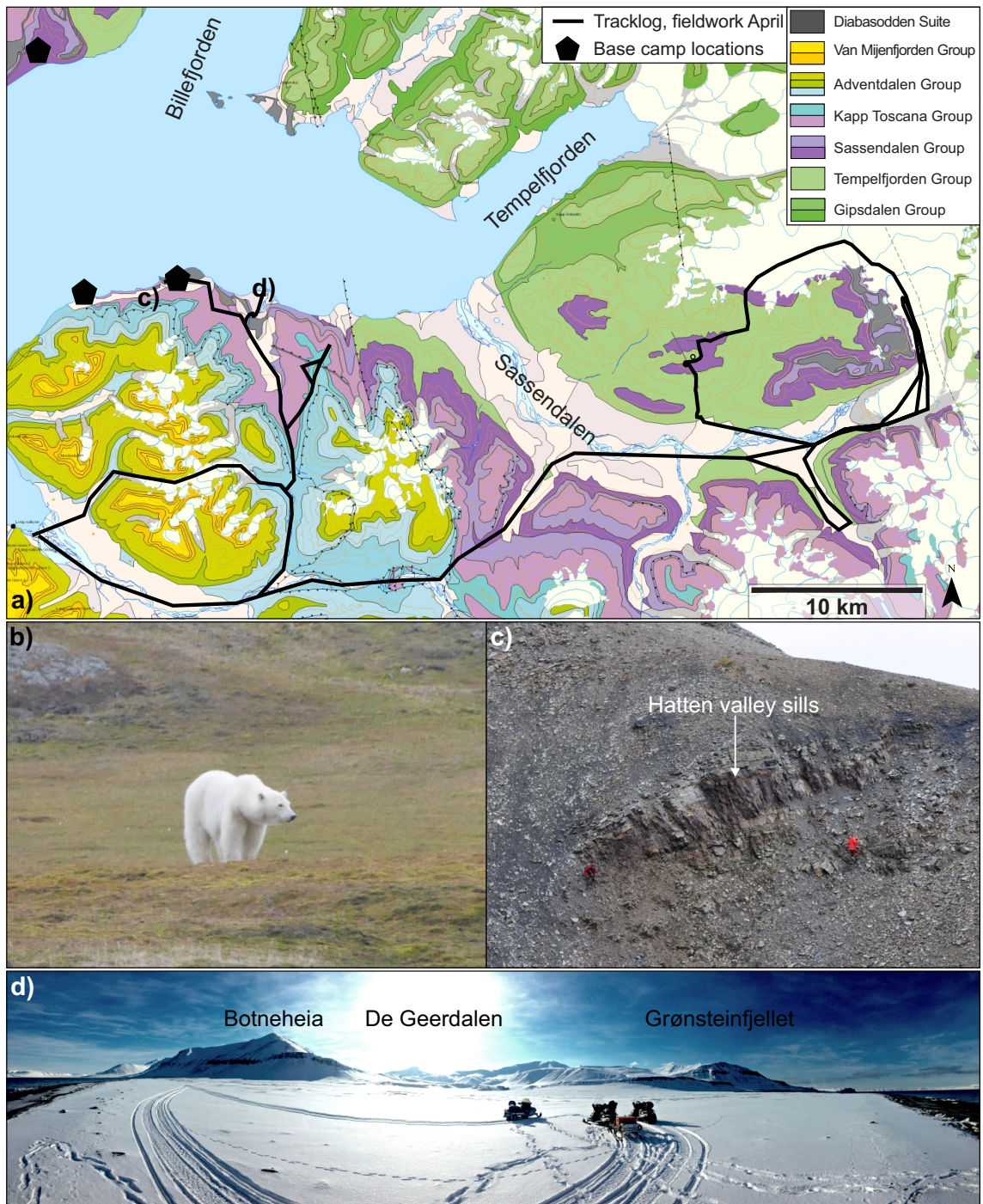
Figure 3.2: (a) Map of study area with April snowmobile tracklog and August base camp locations. (b) Photo of one of two polar bears that stayed in the Diabasodden area for three days in August. Photo by Niklas Schaaf. (c) Photo of the steep terrain in the Hatten valley (Hv, Section 4.1.3). People for scale. Photo by Kim Senger. (d) Panorama photo taken southwards from Elveneset. (a) Map adapted from a Norwegian Polar Institute geological map.
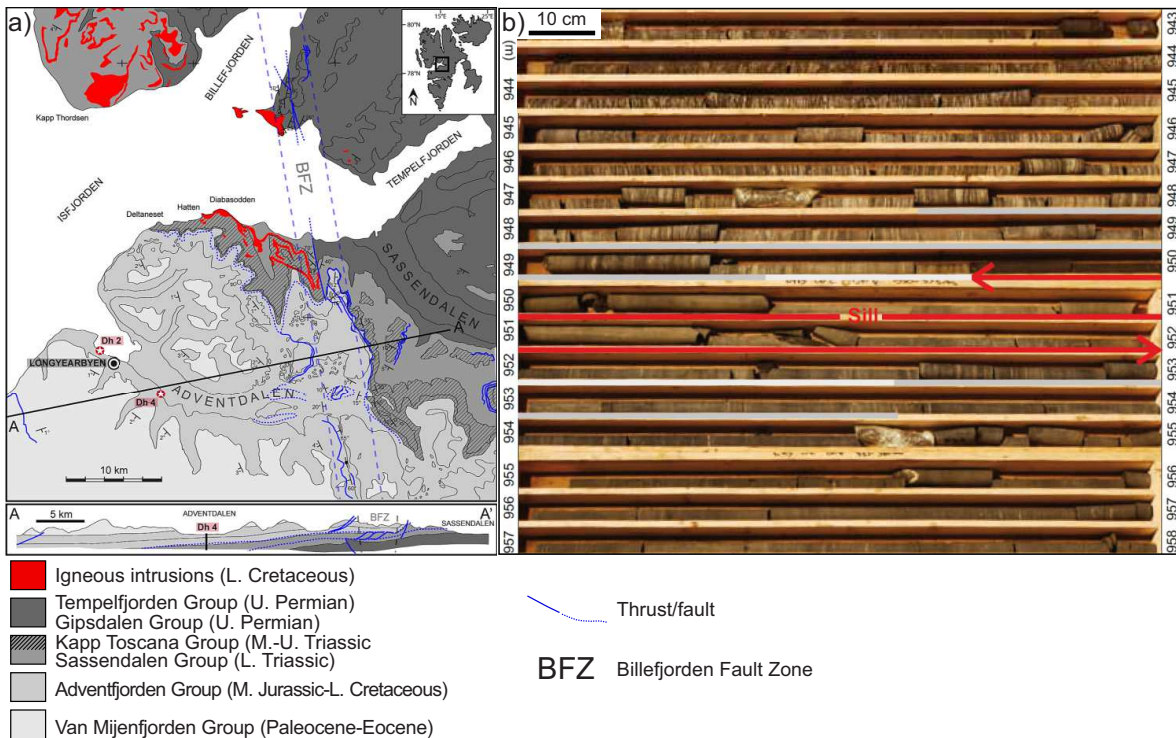
Figure 3.3: (a) Map and cross section illustrating the position of the DH4 borehole. (b) Drill cores from 942-958 m depth. The intrusion is highlighted in red. BFZ=(a) and (b) modified from Senger et al. (2014a).

Several dolerite outcrops in the Isfjorden area, central Spitsbergen, are situated in steep and inaccessible terrain (e.g. Fig. 3.2c). Therefore, many of the visited localities are located along coastal cliffs. Despite the higher accessibility of these sections, they proved to be problematic for data collections due to tides and the preference of polar bears to be walking along beaches (Fig. 3.2b). Data were collected from 18 localities, including amongst others the Rotundafjellet-Studentdalen area, the Hatten-Botneheia area and Wallenbergfjellet (see Fig. 4.1 for location).

3.1.1 Capturing photos for 3D modeling

A total of 2932 high-resolution, digital photos were captured of the outcrops for photogrammetry (e.g., McGlone et al., 1980; Lillesand et al., 2014), including 3D modeling and photo based fracture profiles, as described in Section 3.5. The majority of the photos were captured using a Canon Powershot G16 (12 MP) with a standard lens, and the remainder using a Nikon D90 (12.3 MP)

with a 50 mm Sigma lens and an Ipad camera (8 MP). Photos captured for 3D modeling were taken at slightly different angles every 3third meter along the outcrop. Details on camera settings for quality optimization for 3D modeling are listed in Agisoft (2014). Further workflows on 3D modeling and virtual outcrop geology are described in Section 3.2.

Geographic position for each photo were obtained using several methods. For the Canon Powershot G16, geographic photo positions were automatically estimated using a GPS track log (with the software Garmin Basecamp) following the camera at all times. The Nikon D90 had a GPS mounted on the camera, resulting in precise coordinates for each photo. The Ipad was automatically saving geographic positions through an embedded GPS.

3.1.2   Zone interpretations

In order to characterize fractures within the dolerite and the host rocks, the rocks at each locality were interpreted and classified into a maximum of four different zones in the field, primarily based on spatial changes in the following parameters:

- Mineralogy
- Crystal size
- Color
- Observed fracture pattern
- Sedimentary structures
- Massiveness and resistance to erosion

The zonation and the fracture patterns within these are partly based on the conceptual model proposed by Senger et al. (2015) based on outcrops in the Karoo Basin of South Africa, in addition to several other previously published studies (see Chapter 1). Color changes, i.e. bleaching of shales in proximity to intrusions, a result of total organic carbon (TOC) reduction, are previously described by e.g., Aarnes et al. (2010) and Senger et al. (2014a). Additional parameters, including mineralogy, crystal size, sedimentary structures, massiveness and resistance to erosion, were observed in the field and used to more accurately distinguish one zone from another. Changes in texture and mineralogy, in addition to sedimentary structures were used to differentiate between igneous and sedimentary rocks. Locally, relative changes in rock density and hardness were assessed by hammering in order to divide one lithology into more zones with respect to the distance to the intrusion contact.

The zone classification in this study comprises (listed outwards from the center of the igneous intrusion), zone "A": central dolerite, "B": contact-proximal dolerite, "C": contact-proximal sedimentary rocks affected by intrusion emplacement and "D": contact-distal sedimentary rocks less affected by intrusion emplacement (e.g., Fig. 4.3). Dolerite and sedimentary rocks are relatively easy to differentiate based on texture and fabric. However, internal changes in the sedimentary host rocks or in the dolerite themselves are not always observed. Therefore, if no changes are observed across the intrusion, the entire intrusion is classified as zone "A", and if no changes are observed within the host rocks, and the host rocks are located in proximity to the intrusion, they are attributed to zone "C".

The spatial variations in the intrusions and the host rocks vary from outcrop to outcrop, as the parameters described above, depend on the local history of each outcrop and the intrusion geometry (e.g., Huppert & Sparks, 1989; Senger et al., 2015). The interpretation of each outcrop was based on the following trends: Zone "A" was distinguished by generally larger crystals, a distinct ping sound when hammering, and longer spacing between the fractures than "B". Thin, fine grained dolerite zones dominated by contact-parallel fractures were classified as zone "B". Dolerite zones not dominated by contact-parallel fractures were classified as zone "A". For some intrusions, no obvious fracture pattern was separating contact-proximal dolerite from central dolerite. Here, the separation between zone "A" and "B" are based on changes in colors and crystal sizes (e.g., Winkler, 1949) from the intrusion contact and towards the intrusion center. Zone "C" was distinguished from zone "D" by color, different hammer sound and closer spaced fractures. The boundary between zone "C" and "D" was typically comprised of gradual changes, and can therefore be diffuse.
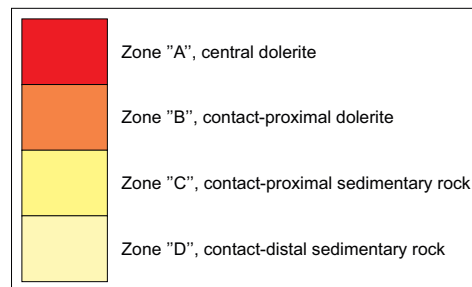
Figure 3.4: Color legend for the interpreted zones. The colors transparently overlay the outcrop photos and are used to illustrate the interpretations of the outcrops (e.g., Fig. 4.3).

Depending on the geometry of the intrusions, the zones were named by upper/lower (u/l, e.g., Fig. 4.27), or western/eastern (w/e, e.g., Fig. 4.3). Where several sills were forming a complex system, zones were difficult to separate. In these cases, the zones are named by number from top to bottom of the outcrop (e.g., Fig. 4.10). A color legend applicable for all zone interpretation figures is shown in Fig. 3.4.

3.1.3   Structural characterization

In order to identify fracture sets in and around the igneous intrusions, a total of 928 fracture orientations were measured. These were measured using the right hand rule, with an Iphone app called Fieldmove Clino (Vaughan et al., 2014) and a standard compass (Compass Expedition S, Silva) with clinometer. Planes were first measured with the compass, and then with the iPhone. Well correlating plane orientations were saved in the Fieldmove Clino app, with related classification parameters comprising locality, zone and plane category (i.e. joint, fault, bedding, intrusion contact), in addition to geographic position.

For the Grønsteinfjellet dyke (Gf_d) and the Rotundafjellet dyke (R_a, Fig. 4.1), the majority of fractures were measured along scanlines (sensu Singhal & Gupta, 2010a). This method implies characterizing fractures (e.g., fracture orientation and fracture length) along a line, such as an imaginary line being perpendicular to the intrusion contact in the intrusions and bedding parallel in sedimentary rocks. The fractures were characterized as either through-going (TG) or bed-confined (BC) in sedimentary rocks, and as continuous or discontinuous in igneous rocks. The scanlines were plotted as described in Section 3.2.5.

Magnetic declination (Table 3.2) was corrected for post acquisition. The data was plotted using the software Stereonet (version 9.9) by Allmendinger (2005).

3.1.4   Lithological logging

One section (6 m) was logged in the field using a meter stick. The sedimentary log was drawn at decimeter-scale and included descriptions of rock type, grain size, sorting, sedimentary structures, and focused particularly on lithology and color changes. A 16 m long section of the DH4 core (from 942-958 m depth, Fig. 3.3) was also logged. Due to the high resolution and the quality offered by the core, the data collected from the core aided in the interpretation of features recorded in the outcrops.

Table 3.2: Magnetic declination corrections applied to orientation data from the field. The values were automatically obtained using the Fieldmove Clino app. The geographic corrections are given in decimal degrees in the WGS84 system.

Locality	Declination applied to	Declination correction (+°)
Hatten	H, Hv, Bc	8,8
Botneheia	B	8,6
Grønsteinfjellet	Gf_a, b, c, d	9,0
Rotundafjellet	R_a	8,7
Studentdalen	Sd_w	8,8
Wallenbergfjellet	Wf_a, b, c, d	10,0

3.1.5   Rock sampling

Rock sampling of dolerites in the field

Rock samples of dolerites were collected in order to determine petrography and geochemistry through thin section observations and XRF scans (Section 3.3). One sample was collected from the center of selected intrusions (Table 4.13), as the crystal sizes increase towards the center of the intrusion (e.g., Winkler, 1949), making the mineralogy easier to determine here than at the margins.

Rock sampling of the DH4 cores

A total of 25 samples (Table 4.12) were collected from DH4, comprising 23 samples of the host rocks and two samples from the intrusion. The samples were collected in order to produce thin sections, where the samples of the intrusion allowed for comparison to dolerites from the field. Sedimentary thin sections were produced in order to determine host rock matrix porosity (Section 3.3) with varying distance to the intrusion contact. These samples were collected as close as possible to the samples analyzed for geochemistry (i.e. Rock-Eval) in Senger et al. (2014a).

3.2   3D virtual outcrop geology

The following section describes the workflows related to the virtual outcrop models from input data (i.e., digital photos), through pre-processing and processing, to output data and analyses of the 3D model.

Field work in Svalbard is demanding because of the harsh climate with snow cover for up to 10 months of the year (e.g., Boike et al., 2003), at times challenging weather conditions, and polar bears. Many outcrops are steep, with

demanding approaches, and can only be efficiently accessible in late winter on snowmobile, by boat during summer or by helicopter at all times of the year (Senger et al., 2016b). Virtual outcrop models constructed by ground based photogrammetry have a much higher spatial resolution (e.g., Kurz et al., 2008) and are significantly cheaper and more user friendly than lidar scans (e.g., Pringle et al., 2006). In addition, virtual outcrop analyses can efficiently provide data that is time consuming to obtain in the field. E.g., during this study, virtual outcrop models constructed from photos collected during 15 days in the field, resulted in 7993 fracture orientations (Table 4.1), many of which were from unaccessible parts of the outcrops.

3.2.1   3D virtual outcrop modeling

3D virtual outcrop modeling was done using the software Agisoft Photoscan Professional (version 1.2). High resolution, digital photos captured in the field (Section 3.1.1) were put into the workspace in the program. Ungeotagged photos were geotagged using the tracklog from the GPS and the software Garmin Basecamp.

Pre-processing

In order to obtain a clean and noise-free finished model, unwanted areas (i.e. foreground and background features, sky and ocean) were deselected in AgiSoft on each photo either manually or by using the "smart wand" tool that automatically deselects grouped, unwanted pixels.

Processing

For the processing steps that follow (Fig. 3.5), recommended settings described in Agisoft (2014) were used. Medium quality was used as higher quality options require a processing time up to several days and weeks during each step.

The first step of the processing was to align photos (Fig. 3.5c) based on geographic references (Fig. 3.5b). Aligning photos implies building a sparse point cloud (Fig. 3.5a) by finding common points in at least two photos. When this step was completed, one could see whether the set of photos were worth further processing. If the aligned photos were not correctly placed in space, further processing was not continued as the model could not be used for orientation data analyses.

The next three processing steps were completed solely by the program, and involved building a dense point cloud (Fig. 3.5e), mesh (Fig. 3.5f) and texture

(Fig. 3.5g). The dense point cloud was the result of depth calculations based on photo positions. The mesh, comprising 3D polygonal surfaces that together represent the object, was constructed based on the dense cloud. The texture was built based on the selected photos, and was created in order to visualize the outcrop.

Generated virtual outcrops are summarized in Table 3.3. To view the virtual outcrop models, see Appendix B. For comprehensive reports of the models, see Appendix C.

3.2.2   Position controlling

In order to quality-control the position of the virtual outcrop, the Agisoft model was exported as a .kmz file with global coordinates, then opened in the Google Earth Pro, and correlated with the map.
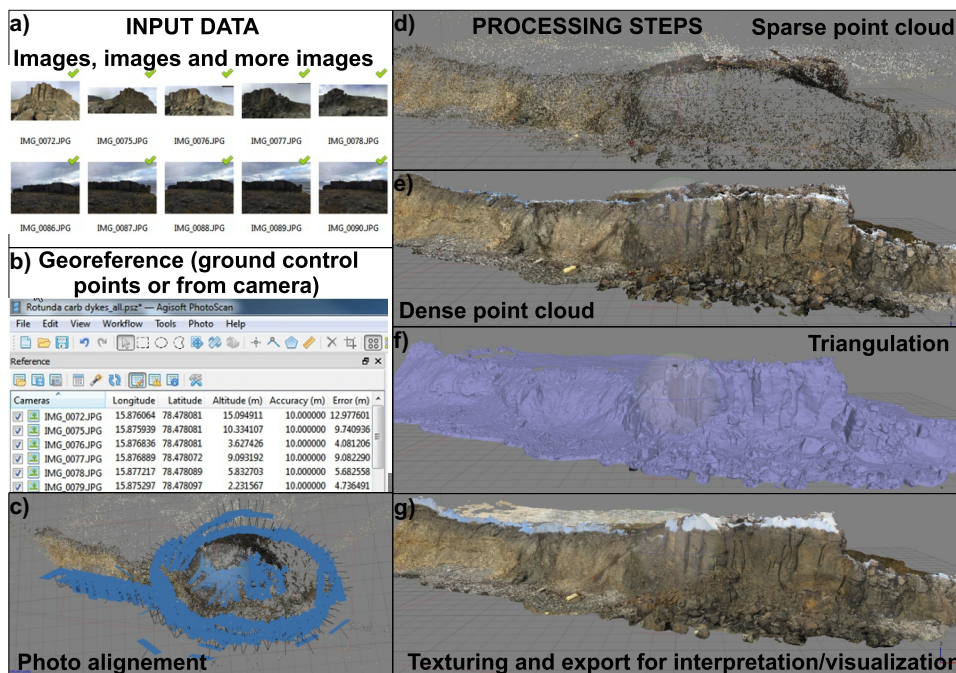
Figure 3.5: From outcrop to virtual outcrop. (a) Input data, comprising photos (b) with georeferences were processed during 4 steps, including (c) photo alignment, (d) generation of a sparse point cloud, (e) dense point cloud, (f) mesh and (g) texture. The virtual outcrop was constructed by the author (Studentdalen dyke east, Section 4.1.7). Figure from Senger et al. (2016b).

Table 3.3: Summary of the virtual outcrops.

Abbrevation	Study site	Outcrop length (m)	Lithology
Bc	Beach c	110	Mixed
Gf_c	Grønsteinfjellet	117	Mixed
Hv	Hatten valley	22	Mixed
R_a	Rotundafjelelt	69	Mixed
Sd_e	Studentdalen	34	Dolerite
Sd_w	Studentdalen	25	Mixed
Wf_e	Wallenbergfjellet	1352	Dolerite

3.2.3   Virtual outcrop visualization

The software LIME (version 1.0, Buckley et al., 2008) was a helpful tool for visualizing the studied outcrops. Distances, outcrop- and plane orientations were also measured using this software. As LIME does not function with 3D models with high coordinates (i.e., global), the 3D models in Agisoft were exported with local coordinates in .ply or .obj format before they were imported into LIME. When viewing 3D models with a local coordinate system in LIME, the outcrop is not correctly referenced in space. Despite its incorrect position in the global positioning system, the outcrop was still situated correctly with respect to orientation, meaning that the software could be used for orientation measurements.

3.2.4   Fracture orientation analyses

In order to strengthen the data set from the field, the software PlaneDetect was used to map fractures. The software automatically detects and analyses local planarity on a meshed surface model (Lato & Vöge, 2012), and gives more precise output data than previously used algorithms that operate with raw point cloud data (e.g., Olariu et al., 2008).

In order to import a file into PlaneDetect, the Agisoft model had to be exported as a .ply file (which required local coordinates). The first step in PlaneDetect was model smoothing, which implies smoothing small scale surface roughness due to artifacts. The second step was the plane mask calculation, which masked regions set by user defined plane radius (m) and the threshold normal vector variation (degrees). The third step was the joint identification, which analyzed the masked regions. This implies that each non-connected masked zone was processed individually, based on the user defined minimum area (m²) and

the overall surface orientation variability (degrees). When an area was larger than the minimum area and the mean normal vector was within a certain threshold, the surface was masked as a plane on the model. Planes analyzed by PlaneDetect are illustrated in Appendix D. After the joint identification, the orientation data was exported as a .txt file. All fracture orientation data was then plotted using the software Stereonet (version 9.9) by Allmendinger (2005).

3.2.5   Virtual fracture spacing profiles

Virtual fracture spacing profiles were analyzed in order to examine changes in fracture spacing along a line. The fracture spacing profiles were carried out using ortho-rectified images and digital photos from the field, and were analyzed and plotted by the following steps. For fracture spacing profiles from digital photos, the workflow starts at step three (fracture mapping).

1. Generate ortho-photo: Virtual spacing profiles were obtained by analyzing ortho-rectified images of the outcrop. Ortho-rectified images are geometrically corrected images with a uniform scale, and were created in Agisoft by the process that makes texture. Thereafter, ortho-rectified images were exported as .tif. This texture process was repeated several times in order to get ortho-rectified images of the outcrop from several angles.

2. Set scale: ArcMap (version 10.4.1) was used to set the correct scale on the image.

3. Fracture mapping: Fracture mapping implies mapping out fractures on an image, and was done using the software CorelDRAW X8. The desired profiles were drawn on the image, and fractures which intersected these lines were mapped out. Then, the image was removed, leaving only fractures, profiles and the scale (with white background), and the fracture map was exported as .png.

4. Analyze profile: In ImageJ, the scale was set, and all lines were made 1 pixel wide by using the macro Jazy_erodilate ("skeletonize"). The profile line was drawn across the image, and the line was analyzed using "analyze profile", and the data was saved as a .txt. The output file contained two columns, including distance along profile and a pixel value. Here, pixel values >0 represented intersected fractures, while values=0 represented empty pixels. The .txt file was opened in Excel, and all values except the peak values were removed. Thereafter, the data was binned using the software KaleidaGraph (version 4.5.3), and finally, binned data were plotted in Excel as histograms with the number of cumulative fractures. This process was preformed for each profile

line. All profiles were analyzed from right to left (horizontal profiles) or top to bottom (vertical profiles). Where the thickness of zones were low, fracture frequency histograms were plotted with a lower bin width than 1 m, and the fracture frequencies were therefore multiplied in order to obtain a comparable designation (fractures/m).

3.3   Laboratory work and chemistry calculations

Laboratory work was carried out at the Department of Geosciences, UiT - The Arctic University of Norway.

3.3.1   Thin section production

A total of 37 thin sections were produced, including 8 thin sections of outcrop dolerites, and 28 thin sections from the DH4 cores. Samples of sedimentary rocks from DH4 were cut in layer-parallel orientation and stained blue with epoxy in order to show porosity. For the samples of the dolerites, weathering surfaces were avoided. All samples were cut into cubes (c. 1.5 x 2 x 3 cm) and were polished prior to thin section production that was completed by the laboratory staff.

3.3.2   Optical microscopy

Thin sections were examined in order to describe the detrital framework and authigenic minerals in sedimentary samples, as well as primary and secondary minerals in doleritic samples. Observations were conducted by using the Leica DMLP petrographic microscope. Images of the thin sections were obtained with a Leica DFC 450 camera mounted on the microscope.

3.3.3   SEM

Scanning electron microscope (SEM) backscatter electron images (BSE) were obtained with the purpose of determining porosity of the sedimentary rocks. Using a SEM is a non-destructive method for determining the elemental composition of a surface. A BSE is based on backscattered electron intensities (x-rays) that reflect the average atomic number of a phase (Reed, 2005). The higher the atomic number of a phase, the brighter the phase is on the output micrograph. Porosity is thereby represented as a black area in the BSE images.

Two thin sections (MF_2015_21, 28) from DH4 were chosen in order to compare the porosity between rocks from the De Geerdalen Formation which were affected and unaffected by igneous intrusions. MF_2015_28 was located 8 cm from the lower contact, within the contact aureole, while MF_2015_21 was located 2,62 m from the upper contact as a sample representative for the rock outside the contact aureole (Section 4.2).

Since the sedimentary rocks consisted of variable proportions of sandstone and mudstone (Section 4.2.2), the thin sections were chosen based on the rock type, as porosity reduction is more important in sandstones, i.e., reservoir rocks, than in mudstones. Additionally, smaller grains are difficult to see on a SEM micrograph. Therefore, the two samples are unfortunately not from the same side of the sill. In total, only three samples (Table 4.12) were analyzed by the SEM due to time limitations.

The porosity of the two samples was determined using the software ImageJ. The percentage of black pixels, representing porosity, was determined using the threshold function.

Energy dispersive spectroscopy (EDS) was used as a qualitative supplement to the optical microscopy in order to determine the mineralogy of thin sections. The EDS system is an integral part of the SEM, and allows point analysis of phases (Reed, 2005).

3.3.4   X-ray Fluorescence

Two dolerite samples (B_01 and R_b_01) were analyzed by X-ray fluorescence (XRF) in order to qualitatively determine composition and discuss whether the investigated dolerites belong to the Diabasodden Suite. The two samples were analyzed for major- (using glass beads) and minor elements (using pressed powder pellets). As for a SEM, the XRF uses x-rays to determine the chemistry, but uses a sample size that makes the results representative for a larger volume of rock.

The number of samples analyzed by XRF was limited due to some samples collected were too small and thus not representative. The samples were not ignited prior to analysis.

3.3.5   CIPW norms

CIPW norms, which show the normative mineral compositions of the analyzed rock, were calculated from the major elemental results for the two samples using the software by Kelsey (1965).

3.3.6 Mg number

The Mg number was calculated for the two samples using Formula 3.3.1. The calculated value was used to determine whether the rock represents a primary melt or not (Hofmann, 1988).

$$Mg\# = \frac{MgO}{MgO + FeO^*} * 100\% \qquad (3.3.1)$$

4

Results

This chapter starts with presenting the different localities and summarizing the new data acquired in this study (Table 4.1). It continues by presenting the virtual outcrops, zone interpretations and structural analyses, organized by each locality. Thereafter, a contact metamorphic study of the DH4 cores and geochemistry and petrography data of selected dolerites are presented. The chapter finishes off by summarizing observations from the different localities, forming the main basis of the discussion in Chapter 5.

4.1   Field localities

This section presents the virtual outcrops and describes each outcrop with focus on zone interpretations and structural analyses of the intrusion-host rock interface. The positions of the studied localities are illustrated in Fig. 4.1.

The orientation data is plotted with a lower hemisphere stereographic projection and are presented as planes, poles to planes with contours (1% area) and rose diagrams (data treated as axes, bin size of 5°). Results from scanlines and virtual profiles are compiled in Table 4.2.
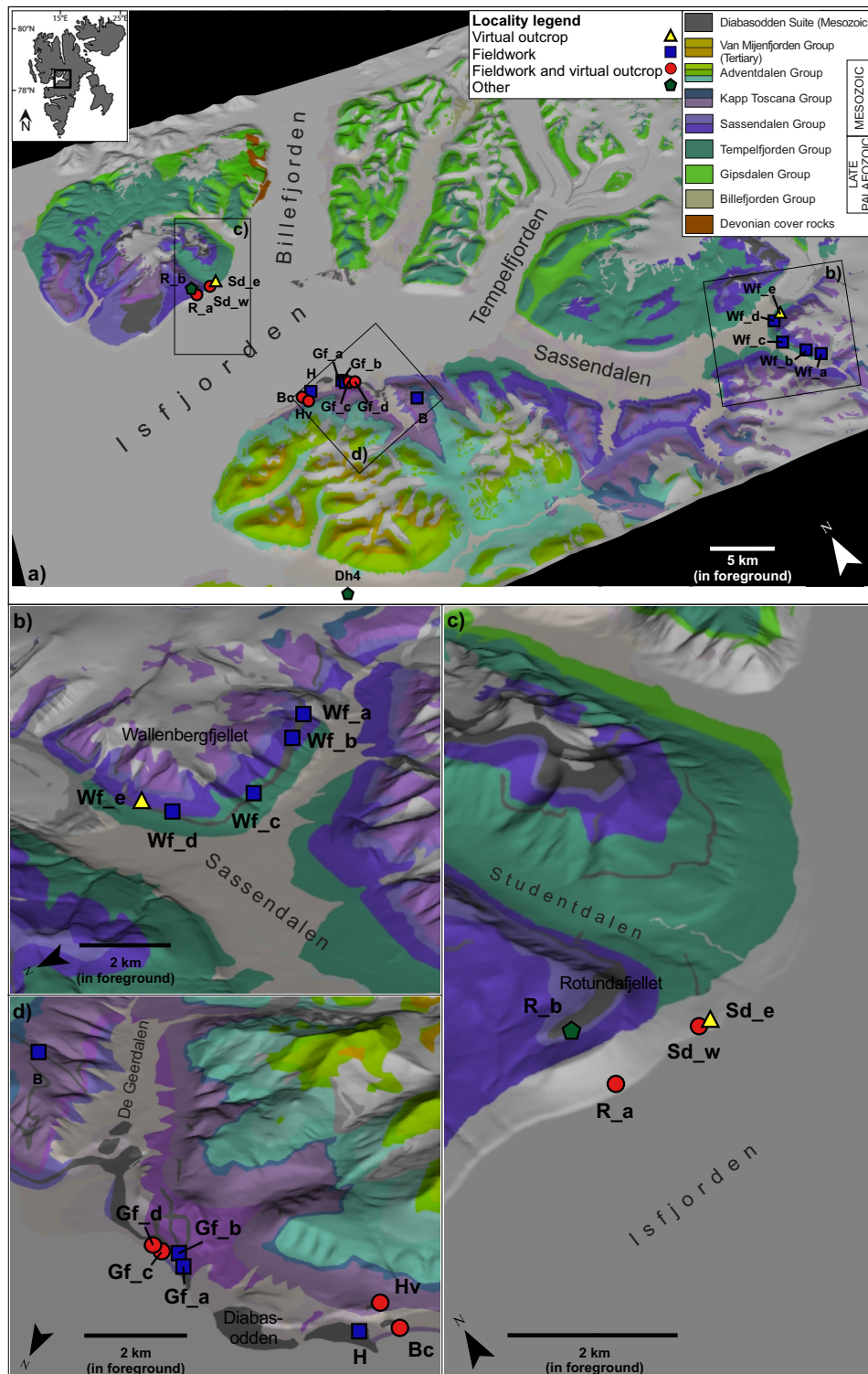
Figure 4.1: Geological maps of the study localities, (a) large scale map of central Isfjorden, and detailed maps of (b) the Wallenbergfjellet area, (c) the Rotundafjellet-Studentdalen area and (d) the Hatten-Botneheia area. See Tab. 4.1 for abbreviations. Map adapted from a Norwegian Polar Institute geological map.

Table 4.1: List of study localities, as well as the location of both previous and new data acquisition. The abbreviations are the names of each locality and are used in the following figures. All data was collected during this study unless references are listed. Geographic locations are given in decimal degrees in the WGS84 system.

Locality abbreviation	Study site	Igneous features (thickness)	Structural data from	Host rock	Longitude	Latitude	Outcrop orientation	Fieldwork	Virtual outcrop extent (m)	Photos taken	Structural field data (n)	Structural virtual data (n)	Scanline m (classic)	Scanline m (virtual)	XRF scan	Thin section description
B	Botneheia	Thin dyke (2 m)	Dolerite	De Geerdalen fm.	16.419733	78.312711	Strike of dyke: 112/292	Yes	0	82	61	0	0	0	Yes	Yes
Bc	Beach c	Thin sills (<2 m)	Dolerite, host rock	De Geerdalen fm.	16.029744	78.354225	062/242	Yes	110	429	79	2160	0	73,5	No	Yes
Dh_4	LYB_CO2_DH4, Adventdalen	Thin sill (2,28 m)	Dolerite, host rock	De Geerdalen fm.	15.827445	78.2024947		No	0	207	0	0	0	0	Senger et al. (2014a)	Yes
Gf_a	Grønnsteinfjellet	Thick sill (c. 30 m)	Dolerite	De Geerdalen fm. Botneheia fm.	16.197708	78.352881		Yes	0	0	50	0	0	0	Nejbert et al. (2011)	Nejbert et al. (2011)
Gf_b	Grønnsteinfjellet	Thick sill (c. 30 m)	Dolerite	De Geerdalen fm. Botneheia fm.	16.192019	78.354697		Yes	0	0	51	0	0	0	Nejbert et al. (2011)	Nejbert et al. (2011)
Gf_c	Grønnsteinfjellet	Thin sill (1,8 m)	Dolerite, host rock	Botneheia fm.	16.227064	78.350097	134/314	Yes	117	411	60	32	0	0	No	Yes
Gf_d	Grønnsteinfjellet	Thin dyke (1,5 m)	Dolerite, host rock	Botneheia fm.	16.222681	78.350656	130/310	Yes		254	81	0	3,75	27,5	Nejbert et al. (2011)	Nejbert et al. (2011)
H	Hatten	Massive feeder complex	Dolerite	De Geerdalen fm.	16.059736	78.356747		Yes	0	0	18	0	0	0	Nejbert et al. (2011)	Nejbert et al. (2011)
Hv	Hatten valley	Thin sills (<2 m)	Dolerite, host rock	De Geerdalen fm.	16.049589	78.350239	98/278	Yes	22	259	102	257	0	36	No	Yes
R_a	Rotundafjellet	Thick dyke (8 m)	Dolerite, host rock	Vikinghøgda fm.	15.807447	78.475008	86/266	Yes	69	815	212	1420	16	176	No	Yes
R_b	Rotundafjellet	Thick dyke (c. 100 m)	None	Vikinghøgda fm.	78.4784	15.7911	86/266	No	0	0	0	0	0	0	Yes	No
Sd_e	Studentdalen east	Thick dyke (c. 25 m)	Dolerite	Kapp Starostin fm.	15.877369	78.478092	93/273	No	34	339	0	396	0	0	No	Yes
Sd_w	Studentdalen west	Thin dyke (1 m)	Dolerite, host rock	Kapp Starostin fm.	15.875653	78.478208	150/330	Yes	25	84	46	89	0	0	No	Yes
Wf_a	Wallenbergfjellet	Thick sill (c. 40 m)	Dolerite	Vikinghøgda fm.	17.899219	78.214236		Yes	0	169	55	0	0	0	No	No
Wf_b	Wallenbergfjellet	Thick sill (c. 40 m)	Dolerite	Vikinghøgda fm.	17.856869	78.221958		Yes	0	9	31	0	0	0	No	No
Wf_c	Wallenbergfjellet	Thick sill (c. 40 m)	Dolerite	Kapp Starostin fm.	17.813947	78.237486		Yes	0	32	39	0	0	0	No	No
Wf_d	Wallenbergfjellet	Thick sill (c. 40 m)	Dolerite	Kapp Starostin fm.	17.842886	78.253467		Yes	0	0	43	0	0	0	No	No
Wf_e	Wallenbergfjellet	Thick sill (c. 40 m)	Dolerite	Vikinghøgda fm.	17.8708	78.2612		No	1352	49	0	3639	0	0	No	No
SUM									1729	3139	928	7993	19,75	313		

Table 4.2: Summary of scanlines and virtual profiles with related parameters.

Profile ID	Locality	Locality abbreviation	Vertical/horizontal	Lithology	Length (m)	Number of fractures	Fractures/m (mean)
Scanlines							
Gf_d_01	Grønsteinfjellet dyke	Gf_d	Horizontal	Mixed	3,8	97	25,9
R_a_01	Rotundafjellet dyke	R_a	Horizontal	Mixed	15,3	193	12,6
Virtual profiles							
R_a_w01	Rotundafjellet dyke	R_a	Horizontal	Host rock	15,6	28	1,8
R_a_w02	Rotundafjellet dyke	R_a	Horizontal	Host rock	16,2	41	2,5
R_a_w03	Rotundafjellet dyke	R_a	Horizontal	Host rock	5,1	12	2,3
R_a_w04	Rotundafjellet dyke	R_a	Horizontal	Host rock	9,9	18	1,8
R_a_w05	Rotundafjellet dyke	R_a	Horizontal	Host rock	4,2	19	4,5
R_a_w06	Rotundafjellet dyke	R_a	Horizontal	Host rock	3,4	19	5,6
R_a_w07	Rotundafjellet dyke	R_a	Horizontal	Host rock	4,5	29	6,4
R_a_w08	Rotundafjellet dyke	R_a	Horizontal	Host rock	3,3	15	4,6
R_a_w09	Rotundafjellet dyke	R_a	Horizontal	Host rock	2,2	11	5,0
R_a_w10	Rotundafjellet dyke	R_a	Horizontal	Host rock	2,4	12	4,9
R_a_w11	Rotundafjellet dyke	R_a	Horizontal	Host rock	2,5	8	3,2
R_a_d01	Rotundafjellet dyke	R_a	Horizontal	Dolerite	11,1	65	5,8
R_a_d02	Rotundafjellet dyke	R_a	Horizontal	Dolerite	11,7	80	6,8
R_a_d03	Rotundafjellet dyke	R_a	Horizontal	Dolerite	11,8	72	6,1
R_a_e01	Rotundafjellet dyke	R_a	Horizontal	Host rock	5,7	28	4,9
R_a_e02	Rotundafjellet dyke	R_a	Horizontal	Host rock	2,3	23	10,0
R_a_e03	Rotundafjellet dyke	R_a	Horizontal	Host rock	15,3	97	6,3
R_a_e04	Rotundafjellet dyke	R_a	Horizontal	Host rock	7,7	36	4,7
R_a_e05	Rotundafjellet dyke	R_a	Horizontal	Host rock	10,2	37	3,6
R_a_e06	Rotundafjellet dyke	R_a	Horizontal	Host rock	3,6	38	10,6
R_a_e07	Rotundafjellet dyke	R_a	Horizontal	Host rock	6,0	26	4,3
R_a_e08	Rotundafjellet dyke	R_a	Horizontal	Host rock	2,6	16	6,3
R_a_e09	Rotundafjellet dyke	R_a	Horizontal	Host rock	4,2	29	7,0
Bc_h_01	Beach c	Bc	Horizontal	Host rock	6,4	30	4,7
Bc_h_02	Beach c	Bc	Horizontal	Dolerite	7,3	31	4,2
Bc_h_03	Beach c	Bc	Horizontal	Dolerite	6,5	34	5,2
Bc_h_04	Beach c	Bc	Horizontal	Host rock	8,4	53	6,3
Bc_h_05	Beach c	Bc	Horizontal	Dolerite	7,6	49	6,4
Bc_h_06	Beach c	Bc	Horizontal	Dolerite	8,1	30	3,7
Bc_v_01	Beach c	Bc	Vertical	Mixed	2,5	21	8,4
Bc_v_02	Beach c	Bc	Vertical	Mixed	2,7	16	5,9
Bc_v_03	Beach c	Bc	Vertical	Mixed	2,2	23	10,5
Bc_v_04	Beach c	Bc	Vertical	Mixed	2,5	22	8,8
Bc_v_05	Beach c	Bc	Vertical	Mixed	2,6	20	7,7
Bc_v_06	Beach c	Bc	Vertical	Mixed	2,9	29	10,0
Bc_v_07	Beach c	Bc	Vertical	Mixed	2,9	23	7,9
Bc_v_08	Beach c	Bc	Vertical	Mixed	3,0	27	9,0
Bc_v_09	Beach c	Bc	Vertical	Mixed	2,9	25	8,6
Gf_d_02	Grønsteinfjellet dyke	Gf_d	Horizontal	Mixed	6,1	59	9,7
Gf_d_03	Grønsteinfjellet dyke	Gf_d	Horizontal	Mixed	6,5	59	9,1
Gf_d_04	Grønsteinfjellet dyke	Gf_d	Horizontal	Mixed	7,1	70	9,9
Gf_d_05	Grønsteinfjellet dyke	Gf_d	Horizontal	Mixed	7,8	85	10,9
Gf_d_06	Grønsteinfjellet dyke	Gf_d	Horizontal	Dolerite	1,5	13	8,7
Gf_d_07	Grønsteinfjellet dyke	Gf_d	Horizontal	Dolerite	1,5	14	9,3
Gf_d_08	Grønsteinfjellet dyke	Gf_d	Horizontal	Dolerite	1,5	15	10,0
Gf_d_09	Grønsteinfjellet dyke	Gf_d	Horizontal	Dolerite	1,5	18	12,0
Gf_d_10	Grønsteinfjellet dyke	Gf_d	Horizontal	Dolerite	1,5	14	9,3
Gf_d_11	Grønsteinfjellet dyke	Gf_d	Horizontal	Dolerite	1,5	11	7,3
Gf_d_12	Grønsteinfjellet dyke	Gf_d	Horizontal	Dolerite	1,5	17	11,3
Gf_d_13	Grønsteinfjellet dyke	Gf_d	Horizontal	Dolerite	1,5	7	4,7
Gf_d_14	Grønsteinfjellet dyke	Gf_d	Horizontal	Dolerite	1,5	12	8,0
Gf_d_15	Grønsteinfjellet dyke	Gf_d	Horizontal	Dolerite	1,5	7	4,7
Hv_h_01	Hatten valley sills	Hv	Horizontal	Host rock	5,0	29	5,8
Hv_h_02	Hatten valley sills	Hv	Horizontal	Dolerite	8,4	27	3,2
Hv_h_03	Hatten valley sills	Hv	Horizontal	Dolerite	8,7	43	4,9
Hv_h_04	Hatten valley sills	Hv	Horizontal	Dolerite	5,3	23	4,4
Hv_h_05	Hatten valley sills	Hv	Horizontal	Host rock	6,3	20	3,2
Hv_v_01	Hatten valley sills	Hv	Vertical	Mixed	1,3	26	20,0
Hv_v_02	Hatten valley sills	Hv	Vertical	Mixed	1,5	28	18,7
Hv_v_03	Hatten valley sills	Hv	Vertical	Mixed	1,4	16	11,4

4.1.1   Rotundafjellet dyke

The outcrop exposed at the beach below Rotundafjellet (R_a, Fig. 4.1) consists of interbedded shale and sandstones belonging to the Vikinghøgda Formation, intruded by a c. 8 m wide, sub-vertical dyke (Fig. 4.3a). Each side of the intrusion center is divided into 4 different zones (Fig. 4.3b).

Virtual outcrop

A part of the virtual outcrop of Rotundafjellet dyke (R_a) is displayed in Fig. 4.2.

Zone interpretations

Zone "A", the center of the dyke, stands out and is less eroded than the rest of the outcrop. Zone "B_w", has closely spaced, highly cemented fractures compared to zone "A". At the margins of the intrusion, zone "B_w" and "B_e" both terminate by calcite filled veins, which mark the contacts between the intrusion and the host rocks.

The host rocks on each side of the intrusion are darker proximal to the contact. By the western contact, the contact-proximal host rocks (zone "C_w") are more brownish than the distal host rocks (zone "D_w"), which are light gray. A transition was observed approximately 1 m from the contact between the intrusion and the host rocks. Relatively few fractures (compared to zone "C_e", see below) forming an irregular fracture pattern are present within zone "C_w".
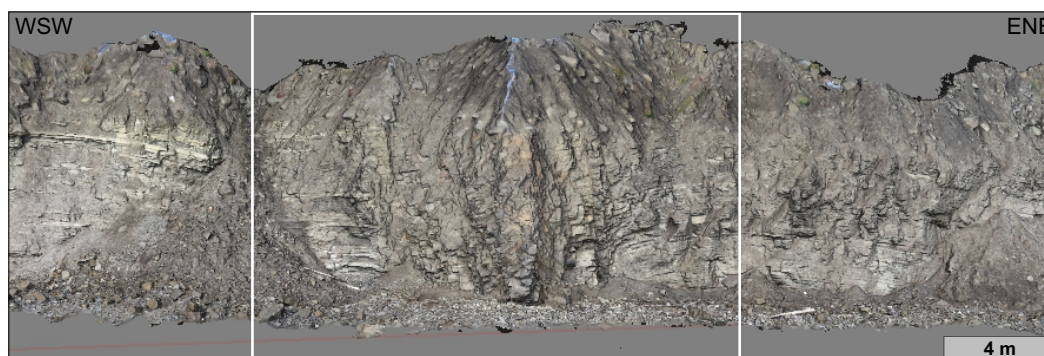
Figure 4.2: Rotundafjellet dyke (R_a). Parts of the virtual outcrop (shaded view). The white box marks the extent on the outcrop displayed in Fig. 4.3.
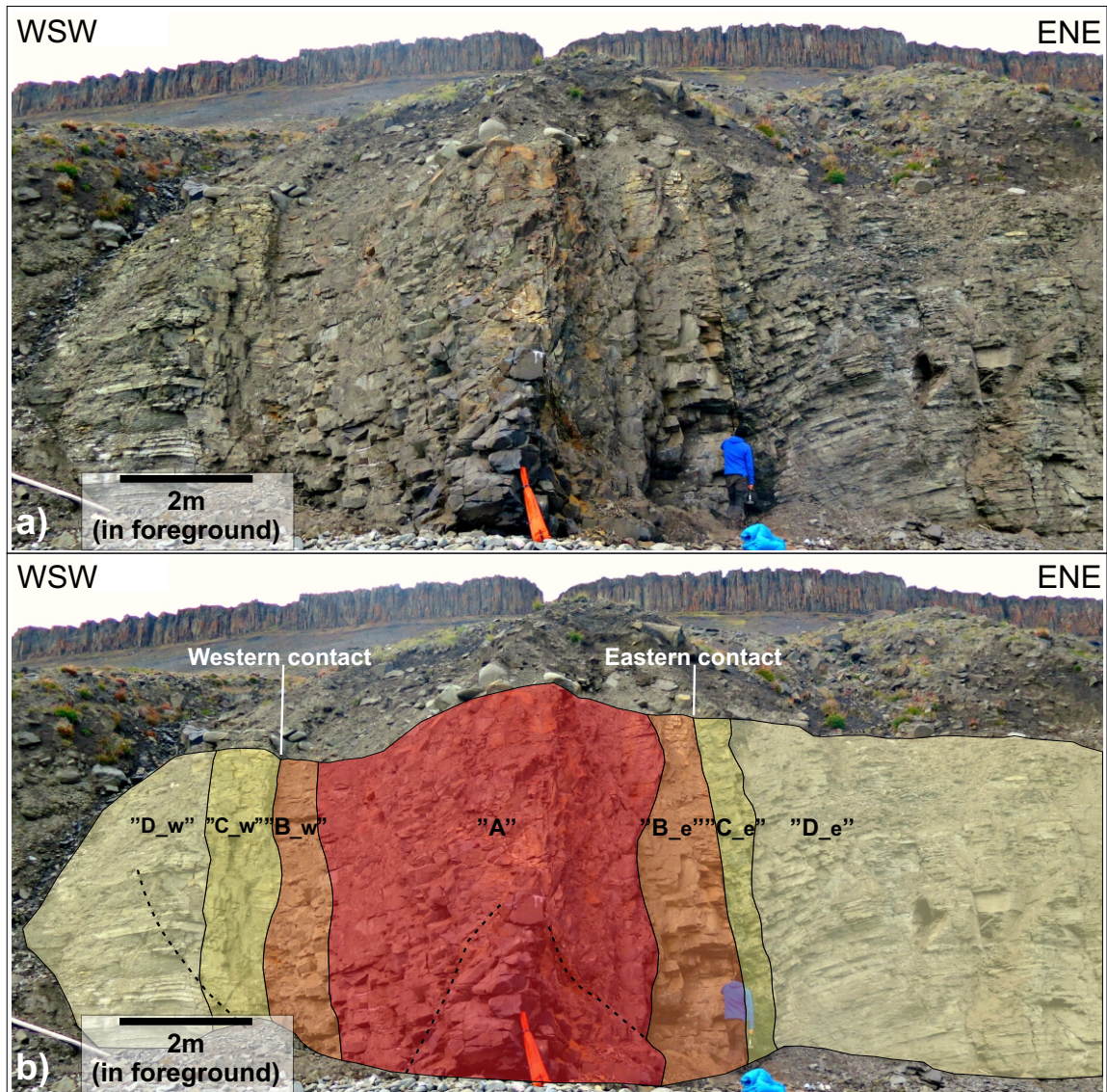
Figure 4.3: Rotundafjellet dyke (R_a). (a) Outcrop photograph, and (b) interpretation of (a). The sill in the background of the photos is the Rotundafjellet sill (R_b). Zone "A" = central dolerite, "B_w", "B_e" = contact-proximal dolerite, "C_w", "C_e" = contact-proximal sedimentary rocks, "D_w", "D_e" = contact-distal sedimentary rocks. Black, dotted lines mark faults. For color legend, see Fig. 3.4.

On the eastern side of the intrusion contact, the proximal host rocks (zone "C_e") are darker gray than the distal host rocks (zone "D_e"). This defines the border between zone "C_e" and "D_e", marked by a distinct color change 60 cm from the intrusion contact. Zone "C_e" is highly fractured (typically every

second cm) perpendicular to the bedding of the host rocks. The bedding is slightly folded downwards towards the intrusion approximately 2 m from the eastern dolerite-host rock contact (Fig. 4.3a).

A normal fault dipping towards east with minimal displacement (a few cm) is observed within zone "D_w" and "C_w" (Fig. 4.3b). In addition, a fault dipping towards north (unknown displacement) is cross cutting the dolerite (Figs. 4.3 and 4.6a). As fracture formation around faults is not within the scope of this study, and as the known displacement of the faults is minor, the effect of the faults on fracture formation has not been taken into consideration.

Carbonate veins frequently occur in and around the dyke. These are observed along the intrusion contacts (up to 10 cm thick), and in the fault dipping towards north. In addition, carbonate coated planes are common in the dolerite (Fig. 4.5b), and are observed in the host rocks up to 30 m from the intrusion contact.

Fracture orientation

Orientation data from Rotundafjellet dyke is partly from the field and partly from virtual outcrop analyses. Most of the structural orientation data from the field were collected along a scanline (R_a_01, Fig. 4.6) across the dyke. The orientation data from the field and from the virtual outcrop analyses (Figs. 4.4a, b and c) correspond well with respect to direction, however, the dip differs slightly (see Fig. 4.4b), suggesting that the virtual outcrop is slightly tilted towards SSE. The data indicates 5 main fracture sets that are listed and presented in Table 4.3.

Stereoplots of field data (Fig. 4.4a), indicate that zone "A" is comprised of intrusion contact-parallel F1 (strike/dip angle: 000/78) fractures, intrusion contact-perpendicular F2 (strike/dip angle: 266/70) fractures and F3 (strike/dip angle: 099/57) fractures. F1, F2 and F3 create a symmetrical fracture pattern, where F2 and F3 are perpendicular to the intrusion contact (F1) and oriented at 45° to each other. F6 fractures (strike/dip angle: 291/04) are also present as can be observed in Fig. 4.3a, but are underrepresented in the data, as they did not intersect the scanline (Fig. Fig. 4.6b.

The orientation data from the contact-proximal dolerite vary between the two sides of the intrusion. On the western side (zone "B_w"), F4 fractures (strike/dip angle: 027/59) are N-S striking and have a lower dip than the F1 fractures. In addition, F2 and F3 (both perpendicular to the intrusion contact) fractures are present here. F3 and the F4 fractures are oriented with 60° to each other, while F2 and F4 fractures are oriented sub-perpendicular to

each other (see Fig. 4.5b for photo). On the eastern side (zone "B_e"), F1, F5 (strike/dip angle: 064/78) and F6 fractures are present, where F1 and F6 are perpendicular to each other, and F1 and F5 are oriented at 60° to each other. However, no contact-perpendicular fractures intersected the scanline (4.5b), meaning that F2 fractures are present in the zone but were not measured in the field. In addition, more F1 fractures are present in the zone that were possible to measure along the scanline, as can be seen in Fig. 4.5b.
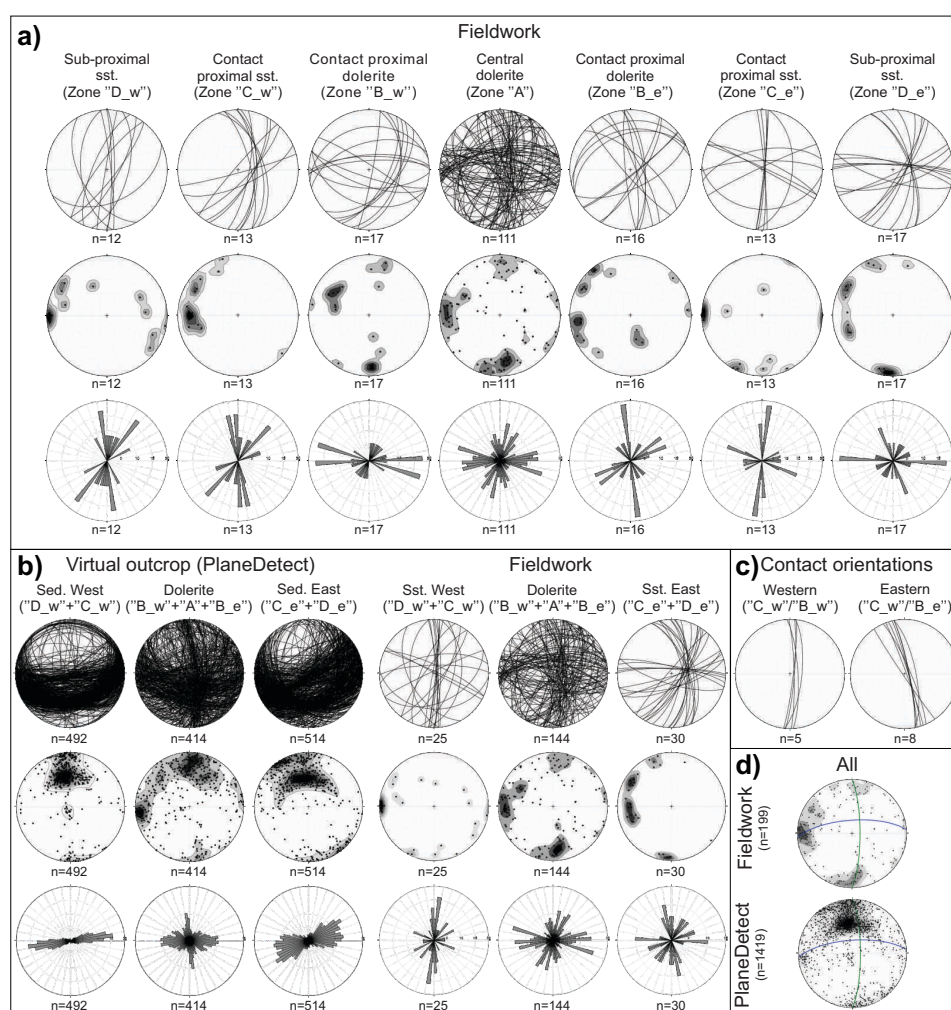
Figure 4.4: Rotundafjellet dyke (R_a). Orientation data from virtual outcrop model analyses and from fieldwork. (a) From each of the 7 interpreted zones, (b) the 7 interpreted zones in (a) summarized as dolerite, western sandstone and eastern sandstone, and compared to data from virtual outcrop analyses, (c) the orientation of the western and the eastern contact (fieldwork). (d) All fractures plotted as poles with contours, averaged intrusion contact (green great circle) and outcrop orientation (blue great circle). Sed. = sedimentary rocks, sst. = sandstone. For zone definitions, see Fig. 4.3.

As the scanline followed sedimentary layers within the sandstone, F2 fractures and fractures that are bedding parallel (which are not included as a set) are underrepresented in the field data. However, these are detected and analyzed by PlaneDetect (Fig. 4.4b). Therefore, fracture orientation data from the contact-proximal sedimentary rocks (zones "D_e" and "D_w" show similar trends as the central dolerite, comprising F1 and F2 fractures. In addition, F5 fractures are identified within the western contact-proximal sandstone (zone "D_w"). It should also be noted that the F1 fractures within the contact-proximal sandstone have a slightly different strike on each side of the intrusion, corresponding well with the intrusion contact on each side.

The orientation data from the field (Fig. 4.4a) within the distal sandstone varies from west to east, however, the two sides correspond well in the virtual outcrop data. F1 and F2 fractures are present on both sides, however, F5 fractures are measured in the field in the distal western sandstone (zone "D_w") and not in the distal eastern sandstone (zone "D_e").

In summary, intrusion contact-parallel and perpendicular (F1 and F2 respectively) fractures are present in all the zones except the western contact-proximal dolerite (zone "B_w"). There, the fractures are inclined, and do not show an obvious fracture pattern. F1 fractures in both the distal and the proximal sandstone are oriented parallel to the intrusion contacts on their respective sides.
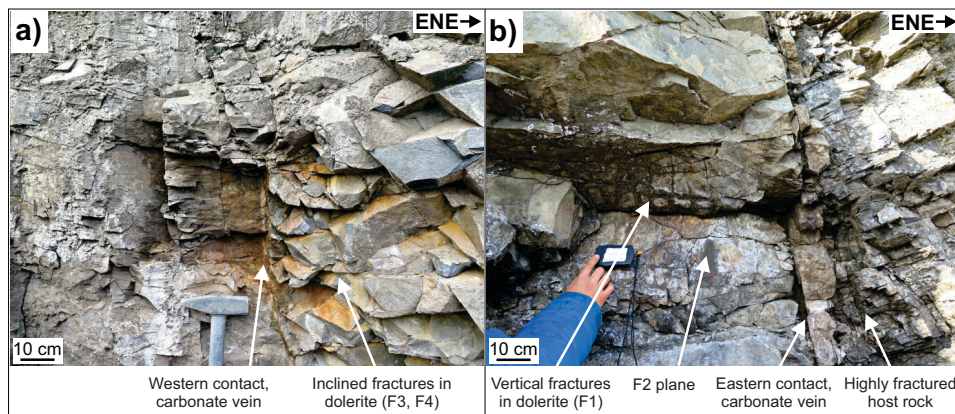
Figure 4.5: Rotundafjellet dyke (R_a). (a) Western contact. Thin carbonate vein in the contact, contact-parallel fractures in the contact-proximal host rocks and inclined fractures within the contact-proximal dolerite. (b) Eastern contact. A c. 10 cm thick carbonate vein in the contact, carbonate cemented contact-parallel and perpendicular fractures, forming a grid. The contact-proximal host rocks in (b) are highly fractured (typically every second cm).

Table 4.3: Rotundafjellet dyke (R_a). Left: Main fracture sets and their presence within each zone. Right: Main fracture sets plotted as planes, all fractures from field work and virtual outcrop plotted as poles.

Set	Orientation	Strike/dip angle	"D_w"	"C_w"	"B_w"	"A"	"B_e"	"C_e"	"D_e"
F1	N-S	000/78	x	x		x	x	x	x
F2	E-W	266/70	x	x	x	x	x	x	x
F3	E-W	099/57			x	x			
F4	NNE-SSW	027/59			x				
F5	ENE-WSW	064/78		x			x		x
F6	WNW-ESE	291/04					x	x	

n=1618
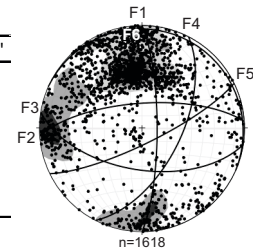
Fracture spacing

Fracture spacing results from within and around the Rotundafjellet dyke are based on analyses of ortho-rectified photos (Fig. 4.6) of the virtual outcrop model, and a 15 m long scanline from the field. The exposure of both the dyke and the host rocks at the beach allows for studying the fracture spacing laterally within the host rocks for several kilometers, following the shore line. The limited virtual outcrop model allowed for fracture spacing analyses of 67 m of the outcrop, including the 8 m thick intrusion, and 24 m and 31 m of host rocks on the western and eastern side, respectively. As previously described, the dyke stands out, making the profiles around the dyke longer than its 8 m width. A total of 23 profiles were analyzed (Fig. 4.7) and the average and the median of the fracture frequency of each meter are plotted in Fig. 4.8a. The scanline from the field is plotted in Fig. 4.8b.

Scanline results show a distinct increase in the fracture frequency (Fig. 4.8b) at 11 m (31 fractures/m, f/m) and 13 m (24 f/m, F1 fractures). These peaks are located within the eastern contact-proximal dolerite (zone "B_e") and sandstone (zone "C_e"), respectively. Generally, the scanline indicates an increase in fracture frequency around the eastern contact and within the dolerite, compared to the sandstones on both sides.

The fracture frequency histogram summarizing the 23 virtual profiles (Fig. 4.8a) has a maximum fracture frequency at 29 and 37 m. The 29 m peak (average fracture frequency of 9.3 f/m) is from the western half of the central dolerite, while the 37 m peak (average fracture frequency of 9.8 f/m) represents the highly fractured contact-proximal host rocks on the eastern side (zone "B_e", F1 fractures). Around 64 m, in the contact-distal part of the eastern sandstone (zone "D_e"), 26 m from the intrusion contact, a relatively high fracture frequency (average fracture frequency of 5,5-9 f/m) is present.
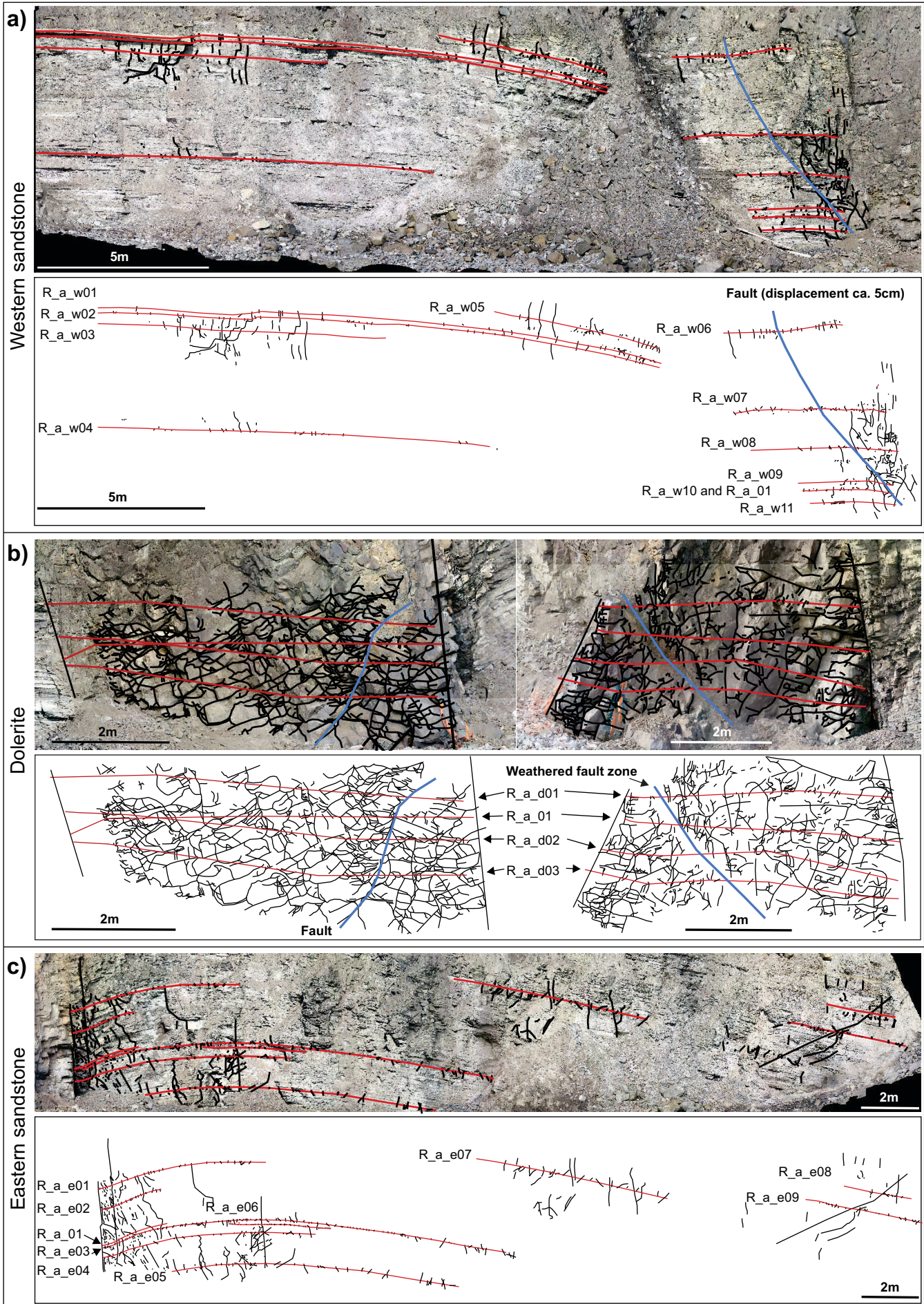
Figure 4.6: Rotundafjellet dyke (R_a). Analyzed fracture frequency profiles (red) of (a) western host sandstone, (b) dolerite, and (c) eastern sandstone. Blue lines mark faults. R_a_w06-09 are following individual beds through the fault. Histograms representing each profile are presented in Fig. 4.7.

Within the dolerite, some values do not correspond between 4.8a and b. This yields especially the area located at 35-36 m (average fracture frequency of 4 f/m) in Fig. 4.8a and at 11-12 m (average fracture frequency of 30 f/m) in Fig. 4.8b. In addition, some areas have very low fracture frequency. The low fracture frequency within the eastern contact-proximal dolerite (zone "B_e) is largely attributed to the fact that the highly fractured area (Fig. 4.5b) did neither intersect the scanline, nor was detected on the ortho-rectified images due to limited resolution. Therefore, the fracture frequency within zone "B_e" is presumably higher than what the two histograms illustrate, meaning that the zone possibly should have a fracture frequency similar to what is observed at 11 m (average fracture frequency of 31 f/m) in Fig. 4.8b.

The contact-proximal dolerite on the western side (zone "B_w") has an average fracture frequency of 7 f/m (Fig. 4.8a) similar to what can be observed in the central dolerite (average fracture frequency of 6.1 f/m). However, the area with the highest fracturing (approximately the first 30 cm of this zone) is in the fracture frequency histogram plotted within the same bin as the poor quality area of the contact-proximal sandstone. Therefore, the area is not included in the summary histogram. The next 50 cm of the area is plotted at 25 m (Fig. 4.8a), in the same interval as the central dolerite, and shows a relatively high fracture frequency. The fracture frequency is also relatively high in the scanline (at 2 m, 13 f/m), however, it is also plotted next to the western contact-proximal sandstone, which is described below.

The western contact-proximal sandstone (zone "C_w") differs from the rest of the outcrop. Compared to the rest of the sedimentary rocks at the outcrop, the zone is brown, diffuse and weathered, and as the fracture frequency plots have no data from this zone, the fracture frequency within this specific zone is not considered.

In the western, distal host rocks (zone "D_w"), the fracture frequency varies between 1 to 6 f/m, notably lower than for the dolerite. In the eastern, distal host rocks, the fracture frequency is relatively steady around 4 f/m at 38-58 m. However, the section from 63 to 67 m (Fig. 4.8a) shows an increase in fracture frequency. This increase differs from the rest of the histogram which shows a general increase in fracture frequency towards the intrusion. In addition, the area is located around 30 m from the intrusion contact. This increase in fracture frequency is considered to be unrelated to the intrusion emplacement, but rather to local sedimentological and/or structural changes, and is therefore not discussed further.
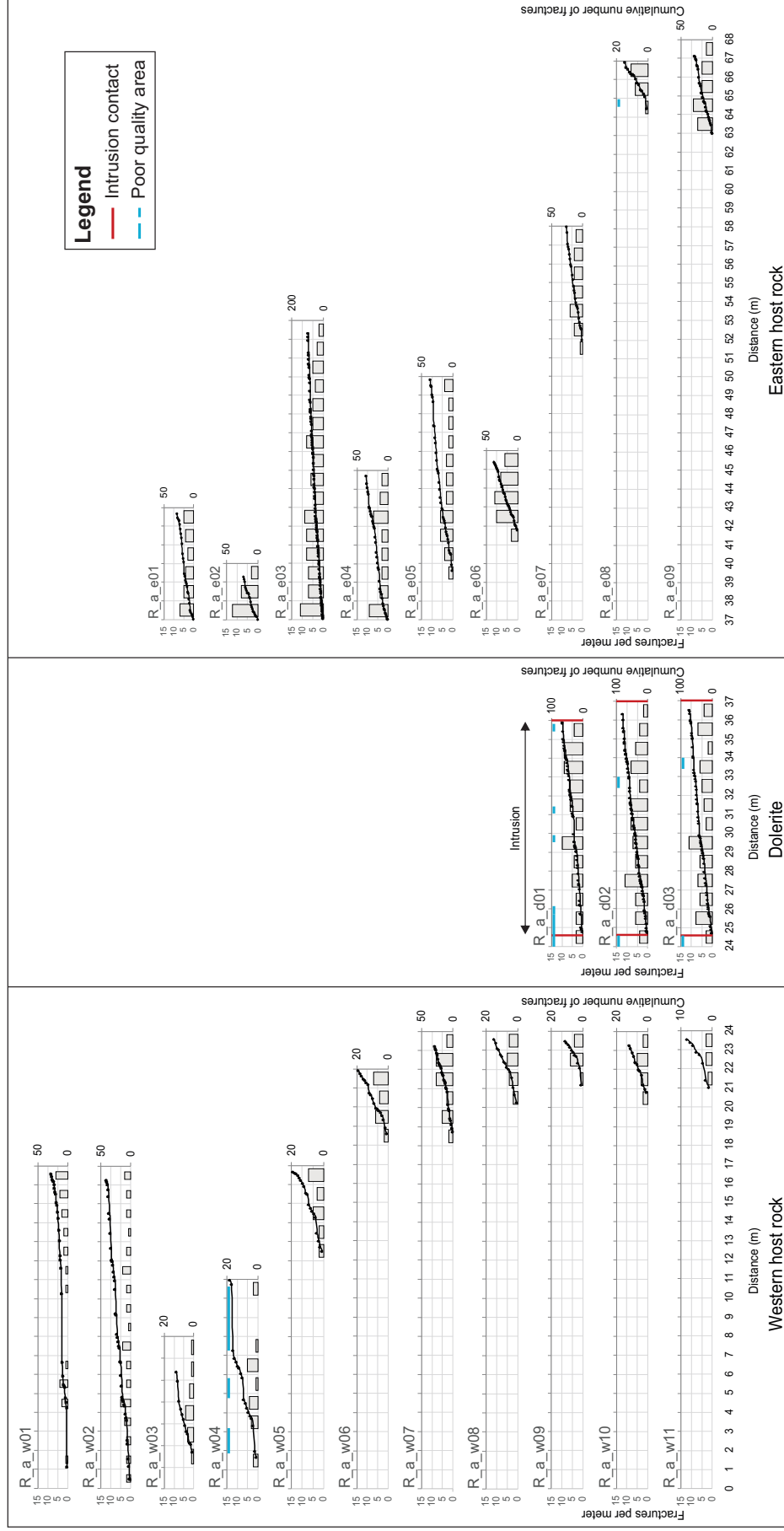
Figure 4.7: Rotundafjellet dyke (R_a). Histograms (left axis) and cumulative frequency (right axis) of the horizontal fracture frequency profiles displayed in Fig. 4.6. The red lines mark the intrusion contacts, while blue lines mark low quality areas. R_a_w1-11 are from the western sandstone, R_a_d1-3 are from the dolerite, while R_a_e1-9 are from the eastern sandstone. Average and median fracture frequencies are plotted in Fig. 4.8a.
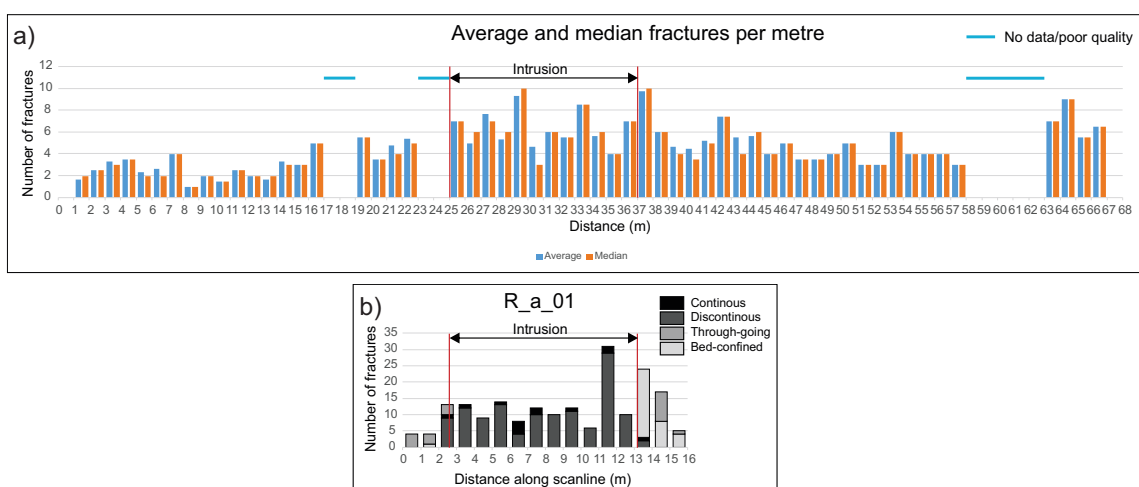
Figure 4.8: Rotundafjellet dyke (R_a). (a) Histogram with median and average values of the 23 profiles from Fig. 4.7. (b) Histogram of the scanline across the dyke.

Overall, the fracture frequency from the virtual profiles (Fig. 4.8a) increases from 1 m on the western side and towards the western intrusion contact. It is high through the intrusion, decreases from the eastern intrusion contact to 58 m, and increases again in the area from 63-67 m.

Comparing the results from the field and the ortho-rectified images (Fig. 4.8), both have a general higher fracture frequency within the dolerite and a high fracture frequency within the contact-proximal sandstone on the eastern side. As observed in Fig. 4.5b, the fractures have a spacing around 2 cm. These are counted as a part of the scanline, but many of these were not detectable on the ortho-rectifies image due to limited resolution. Additionally, as the fracture frequency is based on 1 m intervals, the fracture frequency within the contact-proximal sandstone is presumably higher than what can be seen in both histograms, as this zone (Fig. 4.3) is defined as only 60 cm wide.

4.1.2   Beach c sills

Beach c (Bc, Fig. 4.1) is the third and last beach counting from Deltaneset and eastwards towards Hatten. Several igneous sills are exposed at the beach, within shales and sandstones belonging to the De Geerdalen Formation. Two of these sills are investigated in this study. The regional dip of the bedding around Deltaneset is towards South-West (see Fig. 23 in Senger et al., 2013b), however, the local dip of the bedding at this outcrop is towards east. This makes the sills at Beach c exposed for only a limited distance. The sills are mostly layer

parallel, however, small scale transgressive segments are observed within the study area (e.g., Fig. 4.10b).

Virtual outcrop

A part of the virtual outcrop of the Beach c (Bc) sills is displayed in Fig. 4.9.
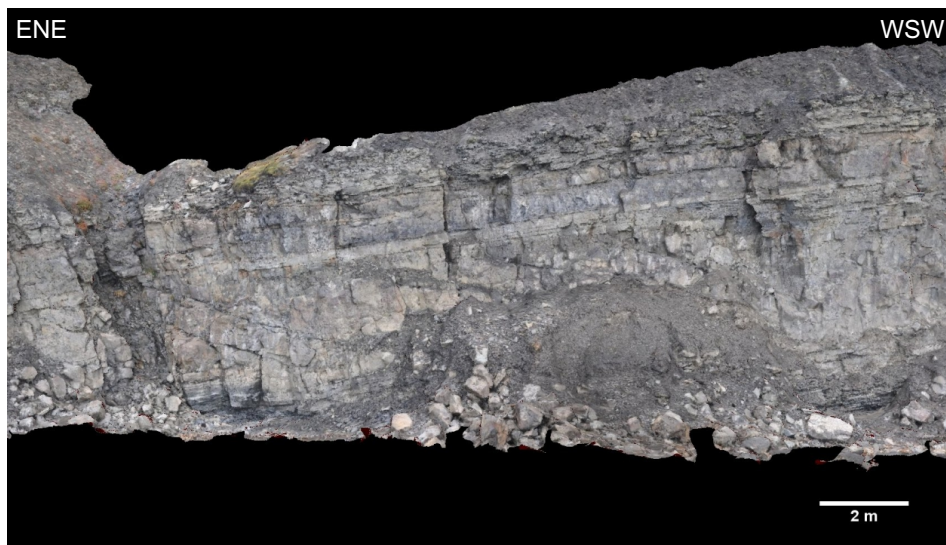
Figure 4.9: Beach c (Bc). Parts of the virtual outcrop.

Zone interpretations

The interpretation of the zones is illustrated in Fig. 4.10 and 4.11. Zone "A_1" and "A_2" consist of brown dolerite. Zone "C_1" and "C_2" show layering, and are therefore classified as contact-proximal sedimentary rocks. No sedimentary layers are observed within zone "B_1", and as the fracture pattern is different than for zone "A_1" and "A_2", this zone is classified as contact-proximal dolerite.

In addition, three more zones were studied and classified outside the image presented in Fig. 4.10a. Between zone "C_2" and "A_2", a relatively thin, brown zone with a lack of sedimentary structures is observed, classified as zone "B_2". Zone "B_3" is located below zone "A_2", and has characteristics similar to zone "B_1" and "B_2". Zone "C_3" is located below zone "B_3", and consists of gray rocks with layering and other sedimentary structures, and is therefore classified as contact-proximal sedimentary rocks. Zone "C_3" has a partly transgressive contact to zone "B_3".
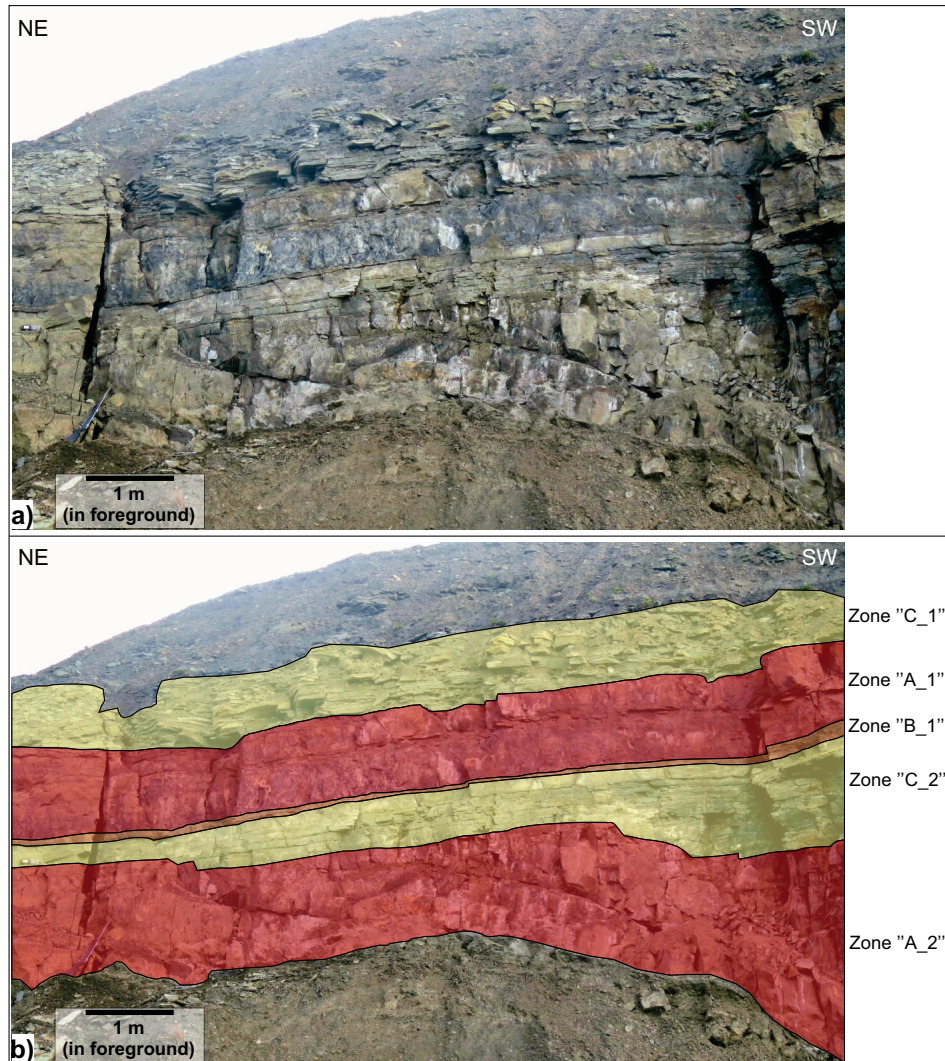
Figure 4.10: Beach c (Bc). (a) Outcrop photograph, and (b) interpretation of (a). Note
the sandwiched sandstone between the two dolerite sills and the small
scale transgressive segments within the lower sill (zone "A_2"), that can
be spotted by following the contact between zone "A_2" and "C_2". See
Fig. 4.11 for a close up picture of zone "B_1". Zone "A_1" and "A_2" =
central dolerite, "B_1" = contact-proximal dolerite, "C_1" and "C_2" =
contact-proximal sedimentary rocks. For color legend, see Fig. 3.4.
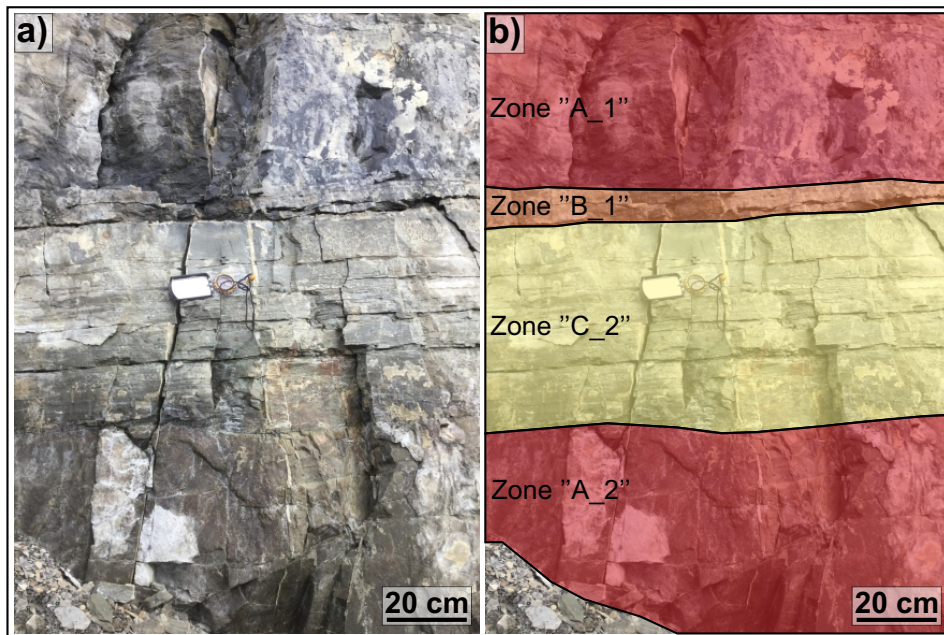
Figure 4.11: Beach C (Bc). (a) Outcrop photograph, and (b) interpretation of (a). Zone "A_1" and "A_2" = central dolerite, "B_1" = contact-proximal dolerite, "C_2" = contact-proximal sedimentary rocks. For color legend, see Fig. 3.4.

Fracture orientation

Structural orientation data (for stereoplots, see Fig. 4.12) is partly obtained from the virtual outcrop model and partly from the field. Data from the two methods correspond relatively well.

The orientation data indicate 4 main fracture sets (Table 4.4). All the studied zones are characterized by vertical F1 (strike/dip angle: 062/86) fractures, F2 (strike/dip angle: 157/88) fractures and F3 (strike/dip angle: 103/89) fractures. F1 is parallel to the outcrop orientation and sub-perpendicular to the intrusion contact (F4, strike/dip angle: 027/12), while F3 is perpendicular to the intrusion contact (F4). F4 fractures are only visible in the field data in zone "B_1", "C_2" and "A_2", but is possibly also present in the other zones.
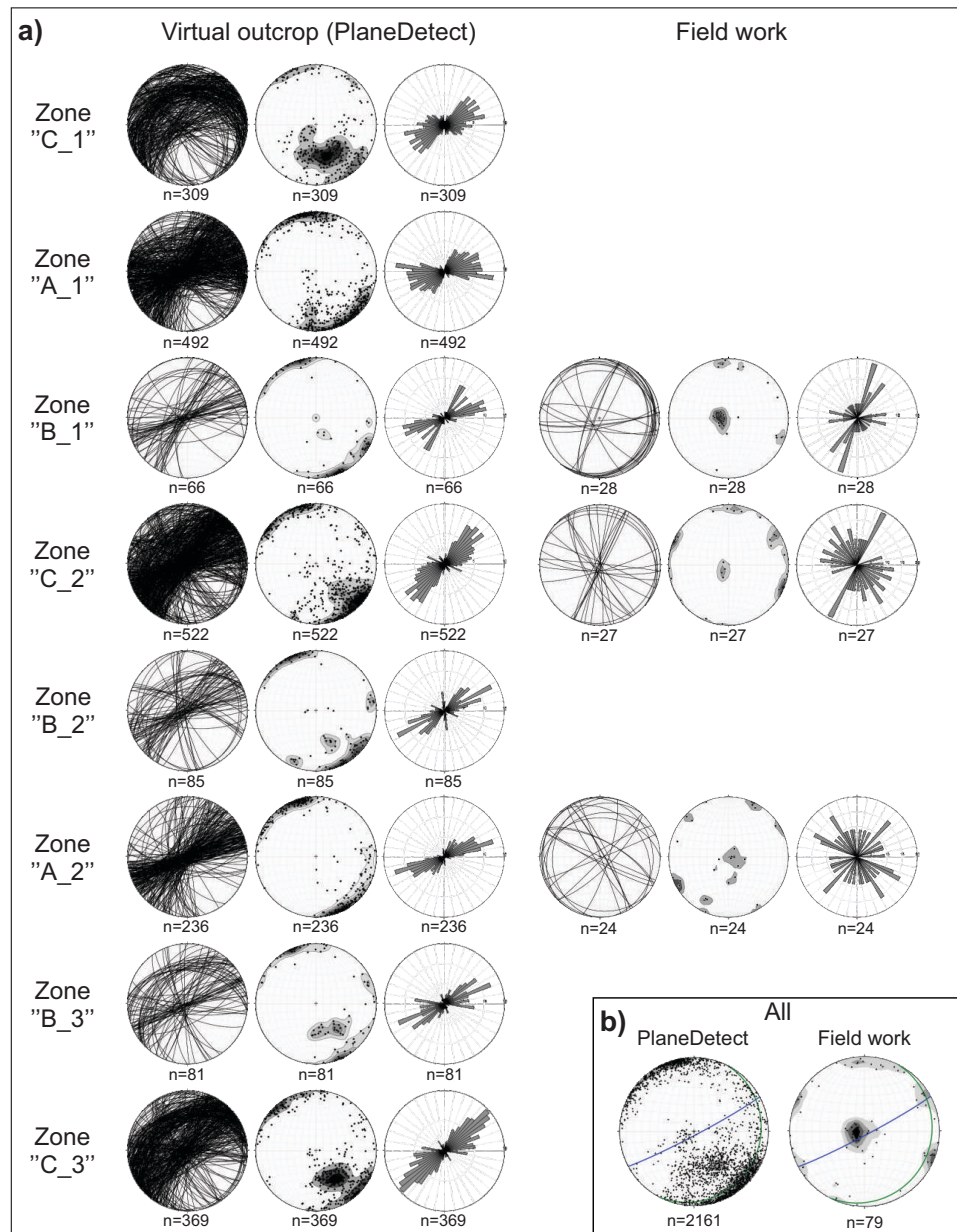
Figure 4.12: Beach c (Bc). (a) Orientation data from virtual outcrop analyses and from the field. (b) All fractures plotted as poles with contours, averaged intrusion contact (green great circle) and outcrop orientation (blue great circle). Zone "A_1" and "A_2" = central dolerite, "B_1", "B_2" and "B_3" = contact-proximal dolerite, "C_1", "C_2" and "C_3" = contact-proximal sedimentary rocks.

F2 is identified in all the zones, however, it is underrepresented in the central dolerites ("A_1" and "A_2"), as few fractures other then F1 fractures (meaning outcrop orientation parallel planes) are present in these zones (see Fig. 4.10a for photo). F1 planes create solid, vertical walls in zone "A_1" and "A_2". F2 is perpendicular to the outcrop orientation (F1) and to the intrusion contact (F4). F4 fractures within zone "B_1", which are parallel to the intrusion contact, can be seen in Fig. 4.11a.

F4 fractures are only measured in the field and were not identified by PlaneDetect due to limited resolution of the virtual outcrop. As this set is contact- and bedding-parallel, the set is likely present in all the sedimentary zones ("C_1", "C_2" and "C_3"). The sedimentary zones are therefore characterized by all the detected fracture sets at the outcrop.

Table 4.4: Beach c (Bc). Left: Main fracture sets and their presence within each zone. Right: Main fracture sets plotted as planes, all fractures from field work and virtual outcrop plotted as poles with contours.

Set	Orientation	Strike/dip angle	"C_1"	"A_1"	"B_1"	"C_2"	"B_2"	"A_2"	"B_3"	"C_3"
F1	NE-SW	062/86	x	x	x	x	x	x	x	x
F2	NW-SE	157/88	x	x	x	x	x	x	x	x
F3	WNW-ESE	103/89	x	x	x	x	x	x	x	x
F4	NNE-SSW	027/12			x	x		x		
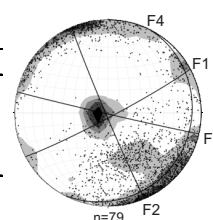
Fracture spacing

The horizontal profiles follow specific contact-parallel heights of the different zones, while the vertical profiles are perpendicular to these. The profiles follow the F1 planes and partly F3 planes, which together make the outcrop orientation, This makes F1 and F3 planes underrepresented in the fracture frequency profiles.

Horizontal profiles
Bc_h_04 (Fig. 4.13a), which follows the sandwiched sandstone (zone "C_2") between the two sills, has the highest maximum fracture frequency (17 f/m, Fig. 4.13b). However, its mean value (5.9 f/m) and interquartile range (2 f/m) is relatively low in comparison. Bc_h_01, which follows the uppermost sandstone layer (zone "C_1"), has a mean value of 4.3 f/m, slightly lower than the mean value of Bc_h_04, and a interquartile range of 5 f/m, indicating that the fracture frequency is changing throughout the profile. Except the higher interquartile range for Bc_h_01, the two profiles have a similar fracture pattern, that mostly comprises F2 (intrusion contact-perpendicular) and F4 fractures (outcrop perpendicular).
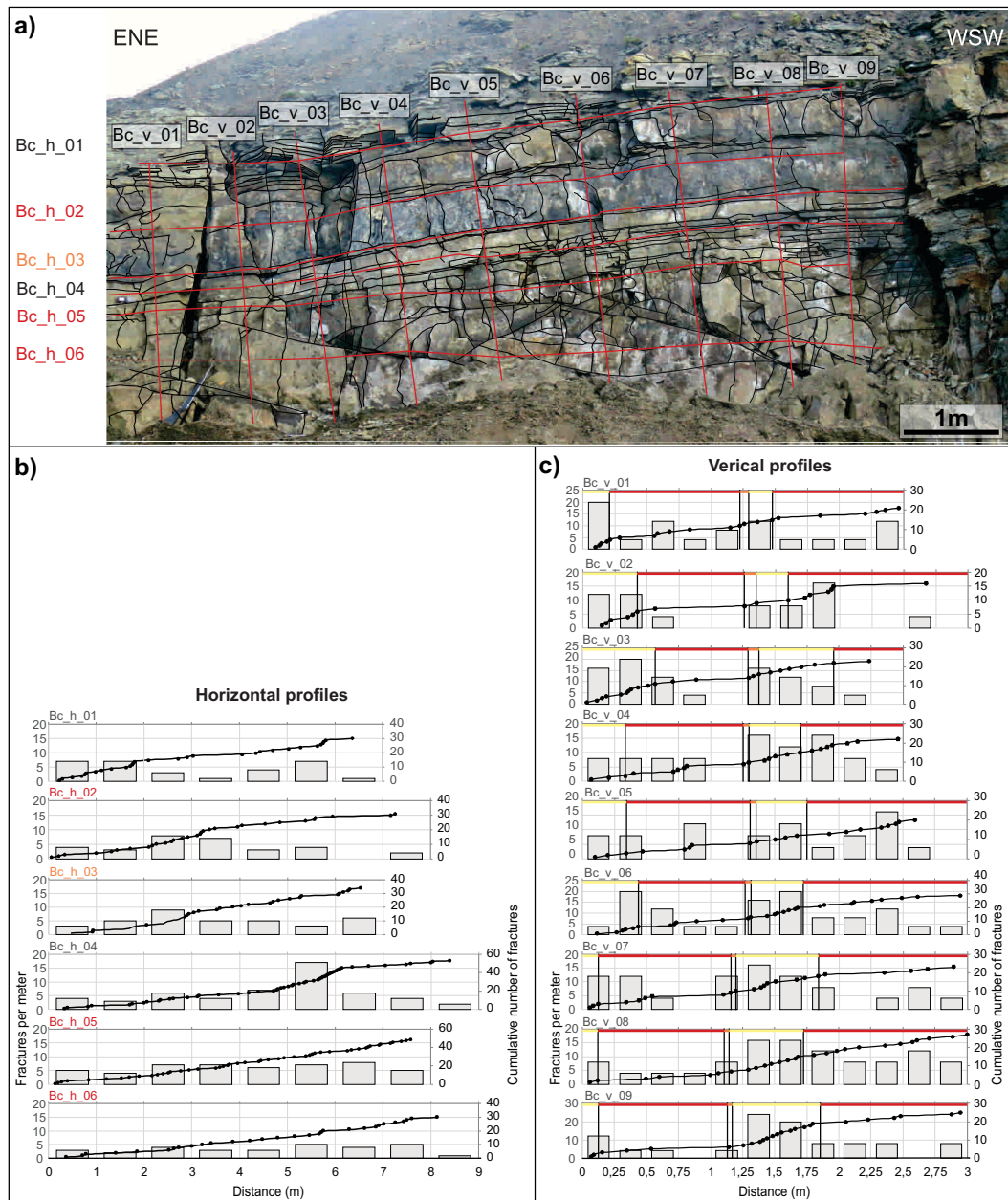
Figure 4.13: Beach c (Bc). (a) The analyzed fracture frequency profiles (red lines) overlaying the mapped fractures (black). (b) and (c) Histograms (left axis) and cumulative frequency (right axis) of the (b) horizontal and the (c) vertical fracture frequency profiles displayed in (a). The black lines in (c) represent the zone contacts, and the colored lines in (c) and the profile names in (a) and (b) represent zones, where red = zone "A" (central dolerite), orange = zone "B" (contact-proximal dolerite), and yellow and black= zone "C" (contact-proximal sedimentary rocks). Horizontal profiles have a bin with of 1 m, while the vertical profiles have a bin with of 0.25 m.

Bc_h_02 (Fig. 4.13b) follows zone "A_1", while Bc_h_05 and Bc_h_06 follow the very upper and the lower part of zone "A_2", respectively. The fracture frequency plots from these zones are dominated by F4 fractures (perpendicular to the outcrop orientation). Comparing these three profiles, Bc_h_05 has the highest mean value (6.1 f/m), while Bc_h_02 and Bc_h_06 have similar mean values of 3.9 and 3.3 f/m respectively. The interquartile range is <2 f/m for these three profiles, indicating that the fracture frequency is relatively constant through the profiles.

Bc_h_03 (Fig. 4.13b) has a maximum and mean fracture frequency of 9 f/m and 5 f/m, respectively. This profile has no values that are obviously differing from the four other horizontal profiles.

In summary, the horizontal fracture frequency is relatively constant for all the zones, except from the sedimentary zones ("C_1" and "C_2") that have a fracture frequency that is changing from low to high through the profile.

Vertical profiles
The fracture spacing of the vertical profiles (Fig. 4.13) is strongly influenced by the fractures within the sandstone that reflect the bedding of the host rocks (F4 fractures). This due to the parallelity of the intrusion and the sedimentary bedding, which especially can be seen in Bc_v_07-09. All profiles, except Bc_v_05, have the highest fracture frequencies within the sedimentary zones (up to 24 f/m). Generally, the fracture frequency within the dolerites is spanning from 0-16 f/m, however, most bins within the dolerite have a fracture frequency between 4-8 f/m. The cumulative plots show the spacing between the analyzed fractures, where the dominating fractures are contact-parallel (F4 fractures). Some F4 fractures are separating one zone from another. In addition, enhanced fracturing is present in the middle of zone "A_1", as also can be observed in Fig. 4.10a.

The mean fracture frequency of the whisker plots (Fig. 4.14) for the vertical profiles, are similar for all profiles, ranging from 6.7-9.6 f/m. However, the interquartile range has a rather great span, ranging from 3 to 11 f/m, indicating that the vertical fracture frequency also changes laterally. This is discussed below.

The interquartile range (Fig. 4.14) is highest for Bc_v_03 (11 f/m) and lowest for Bc_v_04 (3 f/m). Bc_v_03 (Fig. 4.13a) has a higher fracture frequency in the top of the profile (through zone "C_1"), and a lower fracture frequency in both zone "A_1" and "A_2" than Bc_v_04. The difference in fracture frequency within zone "C_1" is likely a result of a shorter profile through this zone due to weathering in the top of the outcrop by Bc_v_04, meaning that the vertical fracture frequency through zone "C_1", at a given height, probably is constant

laterally. Fractures within zone "A_2" are mostly low angeled fractures that are thought to not be related to the intrusion emplacement (the orientation of these is not measured), and are locally present on the outcrop. This results in Bc_v_04 having a low interquartile range, explained by the medium fracture frequency throughout the profile, and Bc_v_03 having a high interquartile range due to the high fracture frequency in the top and a low fracture frequency in the bottom. In addition, the bin width of 25 cm implies multiplying the number of fractures within each bin with 4 to obtain a comparative value (f/m). This implies, that the interquartile range would be 1/4 lower for all profiles if the fracture frequency had the relation f/25 cm instead of f/m.

The mean interquartile range for all the profiles is 7.1 f/m, which is similar to the values for all the profiles except Bc_v_03 and 04. This suggests that the contact-perpendicular fracture frequency is changing through the different zones, and more specifically is higher through the contact-proximal sandstones and the contact-proximal dolerite, and lower through the central dolerites.
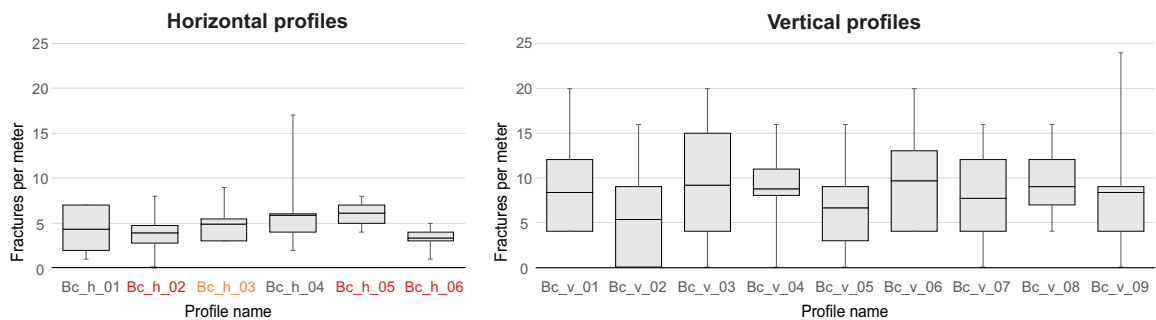
Figure 4.14: Beach c (Bc). Whisker plots (minimum, lower quartile, mean, upper quartile, maximum) of the horizontal (left) and vertical (right) profiles. The color of the horizontal profile names illustrate zone "A" (red), zone "B" (orange) and zone "C" (black).

4.1.3   Hatten valley sills

The Hatten valley sills (Hv, Fig. 4.1) are exposed in an unnamed valley approximately 500 m south of Hatten. The outcrop shows a complex system of several sills within shales and sandstones belonging to the De Geerdalen Formation. Two of these, and their surrounding sedimentary rocks are interpreted in this study (Fig. 4.16). The sills are layer parallel within the studied area, but are transgressive in the western part, as can be seen on the virtual outcrop (Fig. 4.15, western side). Four faults (Fig. 4.15, displacement <2 m) are present on the eastern side of the outcrop. Structural analyses of the outcrop are carried out west of the faulted area, as the faults seemingly did not affect the fracture patterns here.

Virtual outcrop

Parts of the virtual outcrop of Hatten valley sills (Hv) are displayed in Fig. 4.15.
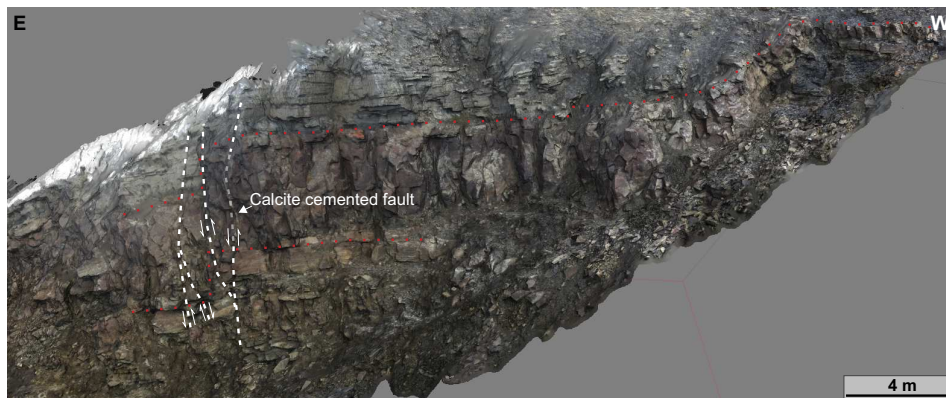
Figure 4.15: Hatten valley sills (Hv). Parts of the virtual outcrop (shaded view). The red, dotted lines illustrate the upper and the lower contact of the dolerite, which is offset by four faults (white, dotted lines) in the eastern part, and is transgressive in the western part. Structural analyses of the outcrop are carried out west of the faulted area. For detailed zone interpretations, see Fig. 4.16.

Zone interpretations

Starting from the top of the outcrop (Fig. 4.16b), zone "C_1" consists of layered, gray, sandstone, with a relatively thin layer (15 cm) of black shale at the base. Zone "A_1" is c. 20 cm thick and has a brown to reddish weathering color on the outside. A fresh surface shows a gray to brown, highly weathered rock, with identifiable crystals of plagioclase. Interpretation of this zone is further based on a thin section (MF_2016_2), which is further described in section 4.3.2. This zone is above respectively zone "B_1" and "A_2", where descriptions and comparison of these that follows below, is the base of the separation of these three zones.

See Fig. 4.17a, b for the descriptions that follow. The three zones have the same weathering color, but fresh surfaces of samples from the zones are differing from each other. Zone "B_1" is c. 10 cm thick, is very fine grained with an aphantic texture, and looks similar as what has earlier been interpreted as contact-proximal dolerite. The fresh surface color is darker and less red compared to zone "A_1". Based on colors and observed fractures, the zone is interpreted as contact-proximal dolerite. Zone "A_2" is c. 2 m thick, has a gray to black fresh surface color and an aphantic texture. Due to its thickness, it is interpreted as

central dolerite. Zone "A_1" is dominated by contact-perpendicular fractures, and based on this and thin section descriptions (Section 4.3.2), the zone is interpreted as central dolerite. The interpretations of these three zones are further discussed in Section 5.4.3.
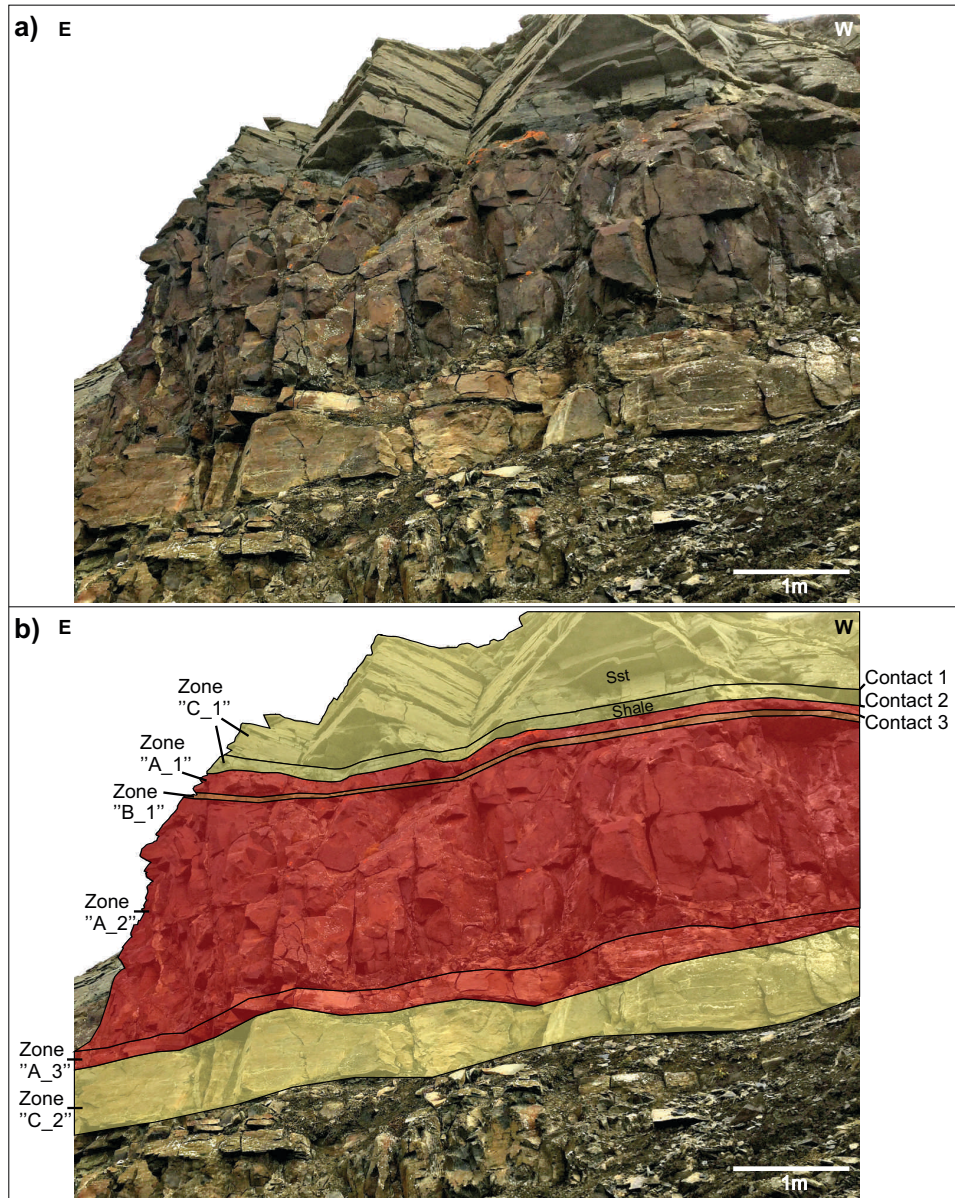
Figure 4.16: Hatten valley (Hv). (a) Outcrop photograph, and (b) interpretation of (a). Zone "C_1" includes both shale and sandstone. Contact 1, 2 and 3 mark measured contacts that are plotted in Fig. 4.18. Zone "A_1", "A_2" and "A_3" = central dolerite, "B_1" = contact-proximal dolerite, "C_1" and "C_2" = contact-proximal sedimentary rocks. For color legend, see Fig. 3.4.
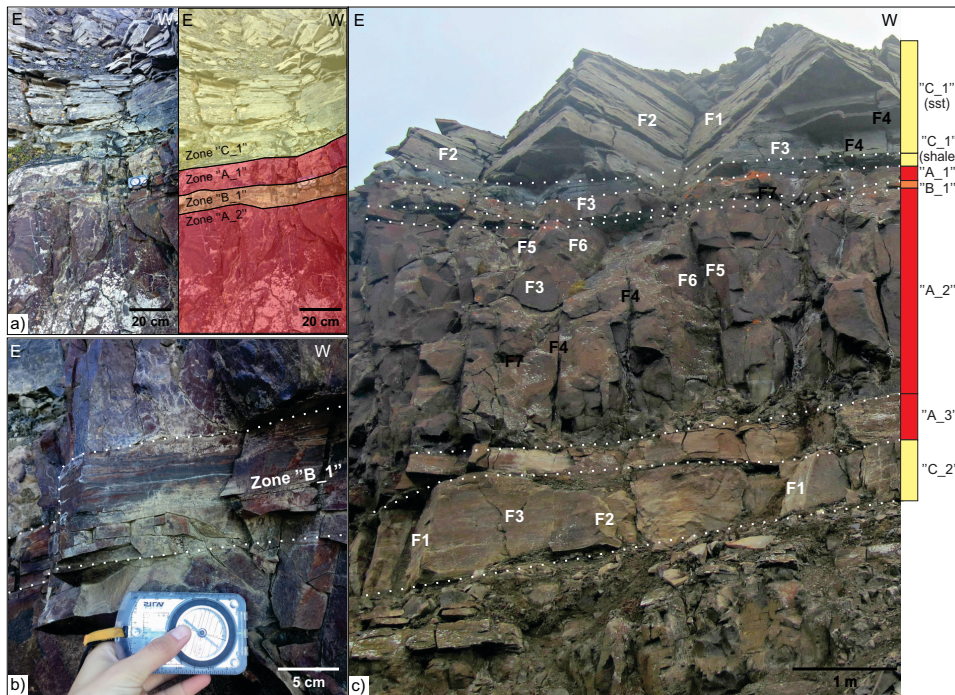
Figure 4.17: Hatten valley (Hv). (a) Outcrop photograph with interpretation. The shale at the base of zone "C_1" is not present at this specific spot. (b) Close up photo of zone "A_1" , "B_1" and "A_2", illustrates the contact-parallel fractures in zone "B_1". (c) Photo with the main fracture sets. Black labels represent fractures intersecting the outcrop, while white labels represent visible fracture planes. The dotted lines illustrate the borders between zones. Zone "A_1", "A_2" and "A_3" = central dolerite, "B_1" = contact-proximal dolerite, "C_1" and "C_2" = contact-proximal sedimentary rocks. For color legend, see Fig. 3.4.

Below zone "A_2" (Fig. 4.16), there is a c. 20 cm thick zone with a reddish brown weathering surface color. Fresh surface colors of this zone are slightly brownish, dark gray, and shows small to medium sized crystals of plagioclase and pyroxene. The fractures within the zone are contact-perpendicular. Based on these descriptions, the zone is interpreted as central dolerite. The lowermost interpreted zone is zone "C_2". This zone has a reddish light brown weathering surface. On fresh surfaces, the rock is slightly brownish, light gray, and sand grains are visible. The zone is therefore interpreted as contact-proximal sedimentary rocks, more specifically a massive sandstone layer. A fourth sill (c. 50 cm thick) is present below zone "C_2". This zone is partly buried and is therefore not investigated.

Carbonate veins are common at the outcrop, particularly along the faults in the eastern part of the outcrop (Fig. 4.18), but also within fractures in the dolerite.

Fracture orientation

Orientation data from the field and from virtual outcrop analyses (Fig. 4.18 correlate well for all zones. However, zone "B_1" is only 10 cm thick, and therefore only 5 planes are analyzed of this zone by PlaneDetect. The field data is therefore the basis for the fracture orientation descriptions for this zone. Zone "C_1" includes both shale and sandstone, where structural orientations from the two lithologies are measured separately in the field, but are merged during virtual outcrop analyses.

The stereoplots indicate 7 main fracture sets all together (Fig. 4.17c, Table 4.5). F1 (strike/dip angle: 302/79), F2 (strike/dip angle: 210/76), F3 (strike/dip angle: 278/88) and F4 (strike/dip angle: 336/85) are present in zones "C_1" (including shale and sandstone) and "C_2". F1 and F2 are oriented perpendicular to each other and sub-perpendicular to the intrusion contact (F7, strike/dip angle: 37/13). F1 and F2 are not present in the dolerites (Fig. 4.17).

F4 is present inn all zones except zone "B_1". F3 and F5 (strike/dip angle: 325/52) are present in zone "A_1", "A_2", "A_3", "B_1" and "C_2". F6 (strike/dip angle: 237/60) is identified in zone "A_1", "A_3" and "C_2". F3, F5 and F6 form a symmetrical pattern, where F3 is perpendicular to the intrusion contact, and F4 and F5 are oriented 45° to the intrusion contact. Zone "B_1" is mainly characterized by fractures oriented parallel to the intrusion contact (F7, for photo see Fig. 4.17b).

In summary, the central dolerites comprise F3-F7 fractures, while zone "B_1" (contact-proximal dolerite) is dominated by contact-parallel fractures (F6, Fig. 4.17b). Zone "C_1", which is >2 m thick and overlying the intrusions, comprises F1-F4 fractures. In contrast, zone "C_2", which is sandwiched between two sills, has the same fracture pattern as zone "C_1" (F1-F4), in addition to the fracture pattern characterizing the overlying intrusions (F5 and F6).
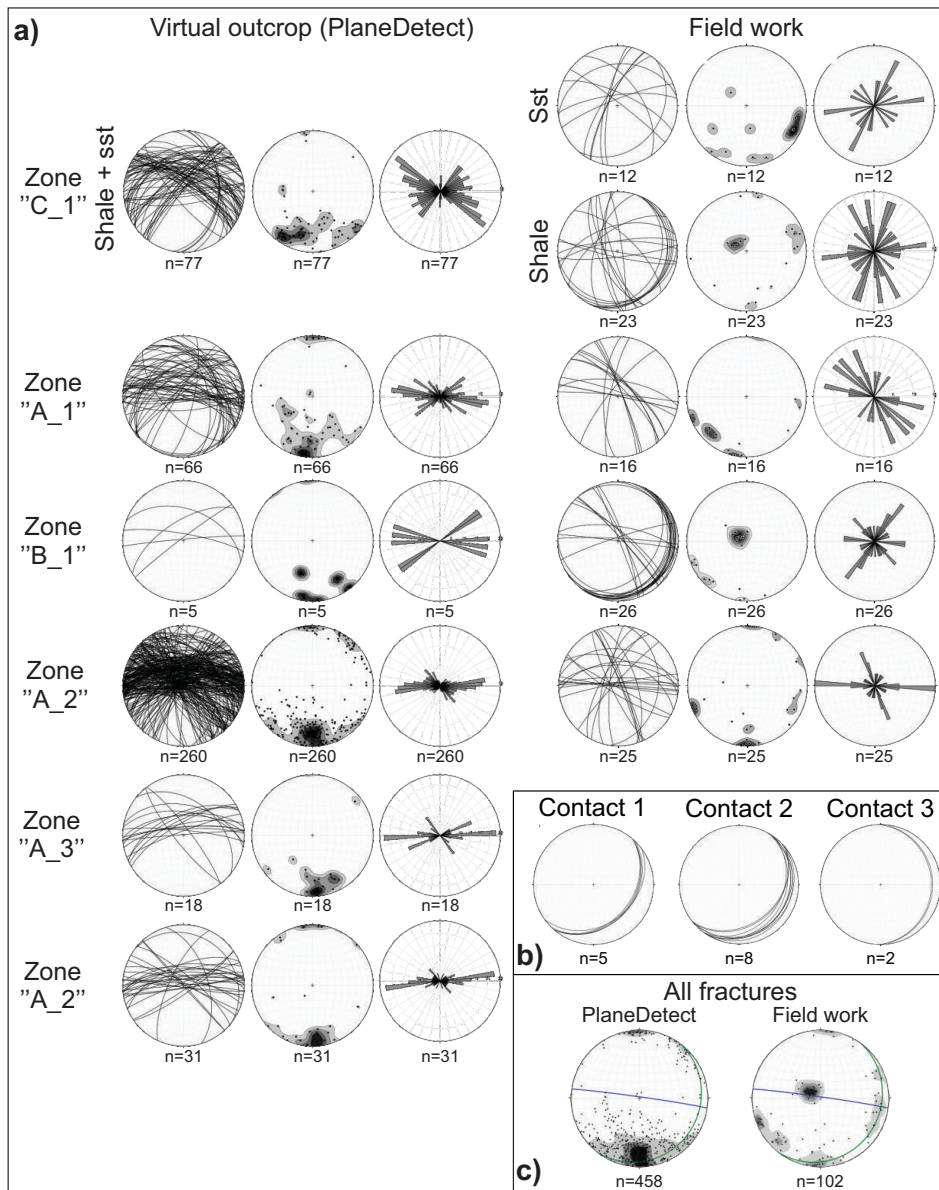
Figure 4.18: Hatten valley (Hv). (a) Orientation data from virtual outcrop analyses and from the field. Zone "C_1" includes both shale and sandstone, where structural data from the two lithologies are measured individually in the field, but are merged during virtual outcrop analyses. (b) Intrusion contact orientations (for location of these, see Fig. 4.16b). (c) All fractures plotted as poles with contours, averaged intrusion contact (green great circle) and outcrop orientation (blue great circle). Zone "A_1" and "A_2" = central dolerite, "B_1" = contact-proximal dolerite, "C_1" and "C_2" = contact-proximal sedimentary rocks. 4.16.

Table 4.5: Hatten valley (Hv). Left: Main fracture sets and their presence within each zone. Right: Main fracture sets plotted as planes, all fractures from fieldwork and virtual outcrop model plotted as poles with contours.

Set	Orientation	Strike/dip angle	"C_1" (shale)	"C_1" (sst)	"A_1"	"B_1"	"A_2"	"A_3"	"C_2"
F1	NW-SE	302/79	x	x					x
F2	NE-SW	210/76	x	x					x
F3	WNW-ESE	278/88			x	x	x	x	x
F4	NNW-SSE	336/85	x	x	x		x	x	x
F5	NNW-SSE	325/52			x	x	x	x	x
F6	NE-SW	237/60			x			x	x
F7	NE-SW	37/13				x	x		
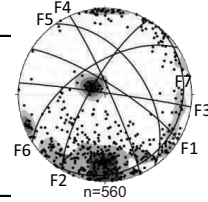
Fracture spacing

Horizontal profiles

Fig. 4.19 illustrates the 5 zone confined (horizontal) profiles, which are plotted in Fig. 4.20. Hv_h_01, which follows the shale in the lower part of zone "C_1", has the highest maximum and mean fracture frequency, of 9 f/m and 5.8 f/m, respectively, dominated by F1, F2 and F4 fractures. Hv_h_05, which follows the sandstone layer that is sandwiched between two sills, has the lowest maximum value (5 f/m) and the lowest mean value (2.9 f/m).

Comparing Hv_h_02-04, Hv_h_03, which follows the lower part of zone "A_2", has the highest fracture frequencies, with a mean value of 4.8 f/m. Hv_h_02 has the lowest interquartile range (1 f/m, Fig. 4.20b) of these three profiles, indicating a constant fracture spacing. No obvious differences can explain why these horizontal fracture frequencies are varying with height.

Fracture frequencies for zone "C_1" (Hv_h_01) and "C_2" (Hv_h_05) are contrasting to each other. This is especially visible in the interquartile range, which is 4 f/m for Hv_h_01, and 1.4 f/m for Hv_h_05 (Fig. 4.20b). The different fracture frequencies can possibly be explained by the composition of the host rocks, as Hv_h_01 follows shale, and Hv_h_05 follows sandstone.

Vertical profiles

For vertical fracture frequency profiles (Fig. 4.21), the highest fracture frequencies are present within the sedimentary rocks (average fracture frequency of 30 f/m) and the contact proximal dolerite (average fracture frequency of 34 f/m). The intervals within the central dolerite has the lowest fracture frequencies (average fracture frequency of 7.5 f/m).
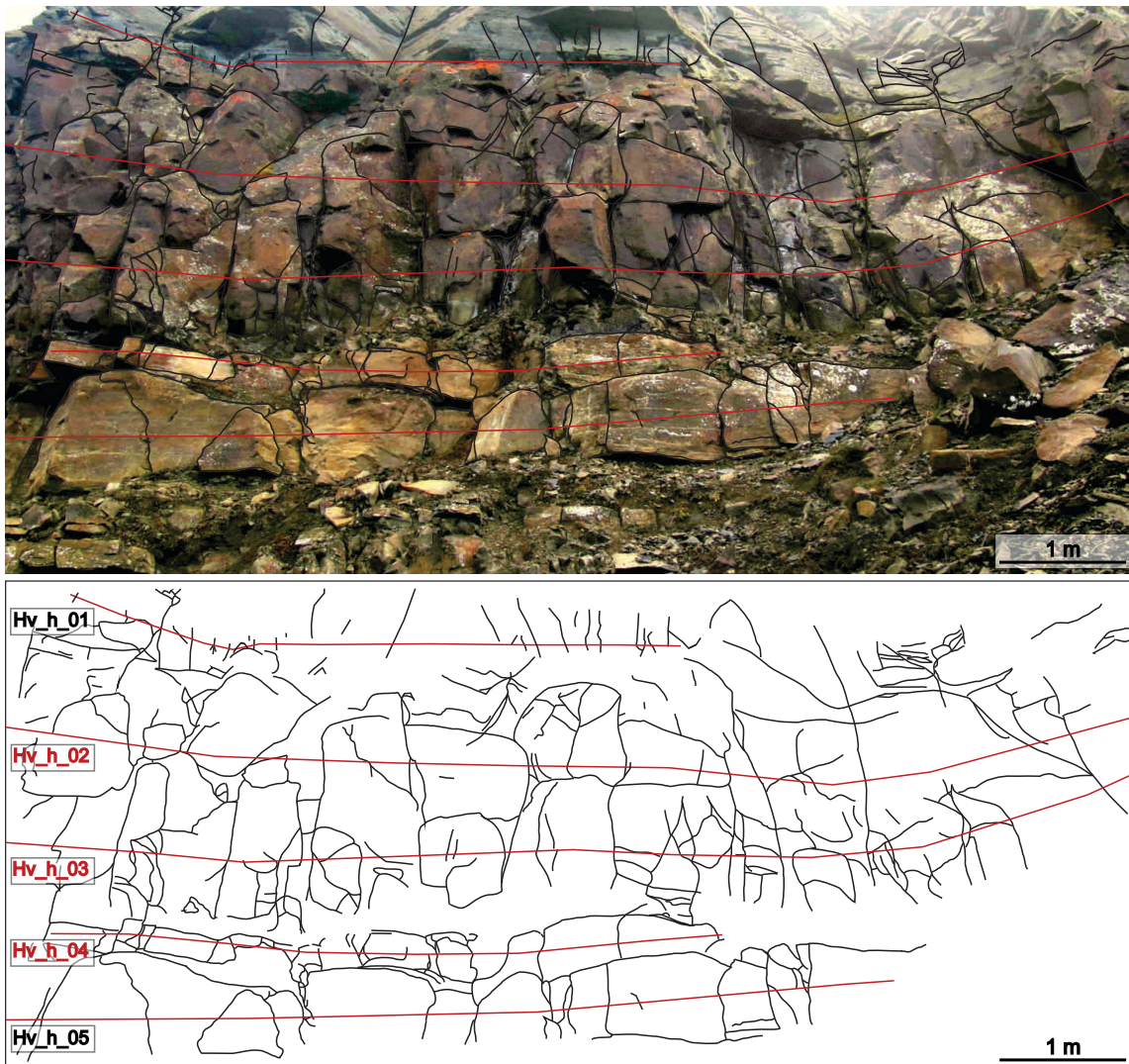
Figure 4.19: Hatten valley (Hv). Analyzed fracture frequency profiles overlaying the mapped fractures. Hv_h_01 follows the shale layer of zone "C_1" (sandstone), while Hv_h_02 and Hv_h_03 follow the upper and the lower part of zone "A_2" (dolerite) respectively. Hv_h_04 follows zone "A_3" (dolerite), and Hv_h_05 follows zone "C_2" (sandstone). The color of the profile names illustrate zone "A" (red) and zone "C" (black).
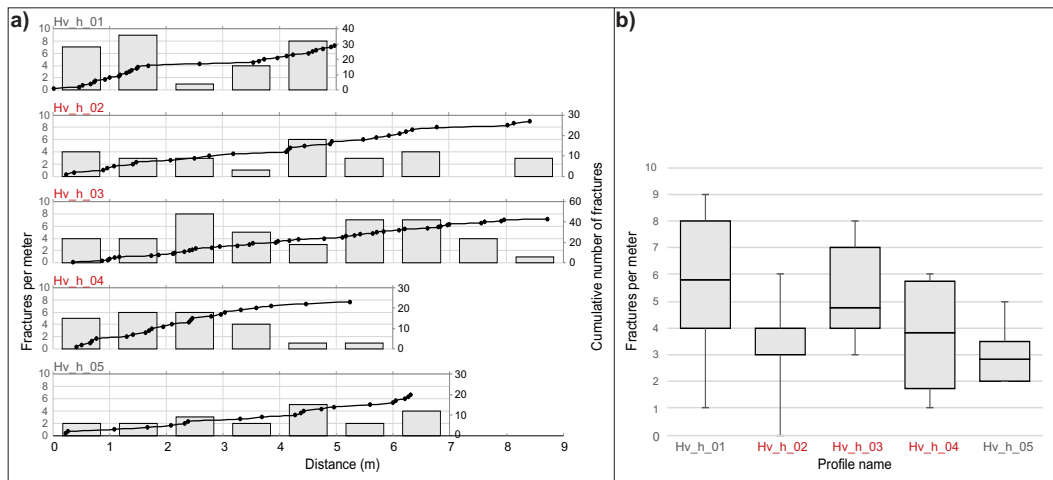
Figure 4.20: Hatten valley (Hv). (a) Histograms (left axis) and cumulative frequency (right axis) of the fracture frequency profiles displayed in Fig. 4.19. (b) Whisker plots (minimum, lower quartile, mean, upper quartile, maximum) of the fracture frequency histograms displayed in (a). Red = zone "A", black = zone "C".
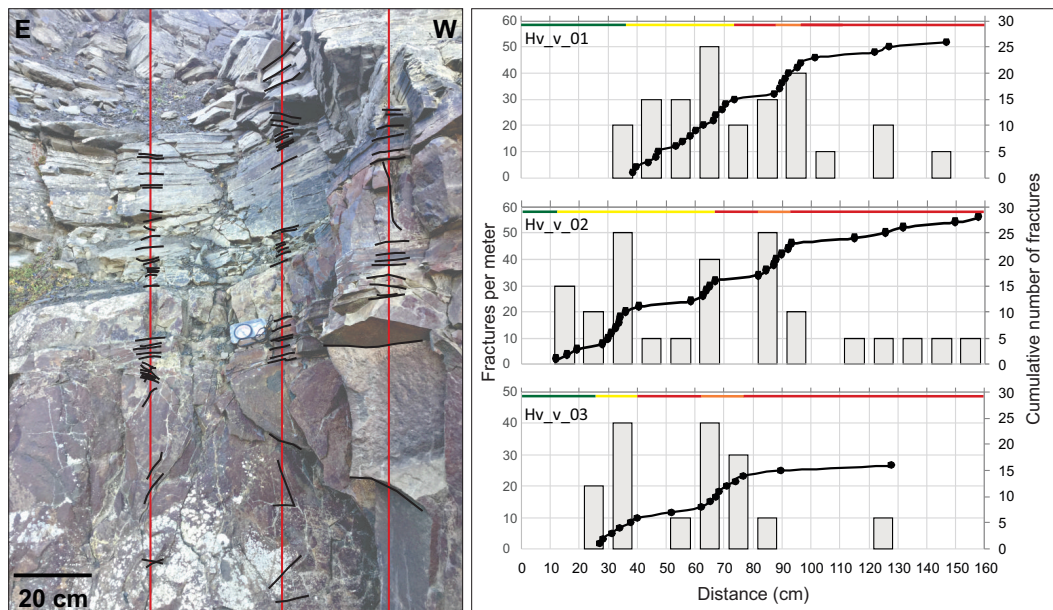
Figure 4.21: Hatten valley (Hv). Left: Analyzed vertical fracture frequency profiles and mapped fractures. The photo is 30% transparent. Right: Histograms (left axis) and cumulative frequency (right axis) of the fracture frequency profiles. Green = unanalyzed areas, yellow = contact proximal sedimentary rocks (zone "C_1"), orange = contact proximal dolerite (zone "B_1"), red = central dolerite (zone "A_1" and "A_2").

4.1.4   Grønsteinfjellet dyke

The Grønsteinfjellet dyke (Gf_d, Fig. 4.1) is the 1.5 m thick, sub-vertical dyke exposed at the beach beneath Grønsteinfjellet, within shales belonging to the Botneheia Formation. The outcrop is well preserved, and extends for several hundred meters. A low angle fault (strike/dip angle: 162/03) with an unknown displacement offsets the dyke at the base of the outcrop (Fig. 4.22), making the dyke only exposed in the hanging wall of the outcrop. A sill is exposed in the footwall, and is further described as Grønsteinfjellet thin sill (Section 4.1.5).

Zone interpretations

On the western side of the intrusion, the distal bedding of the sedimentary host rocks is sub-horizontal, while the three most contact-proximal meters are folded down towards the intrusion (towards east, for stereoplot see Fig. 4.23). The bedding is easily followed laterally on the western side of the intrusion.

In contrast, the structural aspect of the bedding on the eastern side of the intrusion is rather complex. For photo, see Fig. 4.25a. In the lowermost meter of the hanging wall, proximal to the intrusion, the bedding is slightly folded downwards towards the intrusion (this bedding is measured and illustrated in the stereoplot in Fig. 4.23). However, above, the bedding is folded upwards towards the intrusion. Between the two opposite dipping strata, approximately 1.5 m above the major fault, the rocks are highly fractured and fragmented (Fig. 4.24c, d). A 50 cm long fragment of sedimentary rocks with a dip of approximately 80° is observed here (Fig. 4.25a, just below the profile line presenting scanline Gf_d_01). This complex folding may have had a strong influence on the local fracturing, especially within the eastern contact-proximal host rocks.

The interpreted zones in and around the dyke are primarily based on color changes that can be observed in Fig. 4.22a. The dolerite is light brown in the center (zone "A"), and dark brown close to the contacts (zone "B_e" and "B_w"). As the host rocks mainly consist of black shale, the contact-distal sediments on both sides of the intrusion are black, and classified as zone "D_e" and "D_w". Proximal to the intrusion (c. 1,5 m from the intrusion and inwards), the host rocks are light gray (zone "C_e" and "C_w").

Several carbonate veins are observed around the intrusion. One thick vein (7 cm thick) is present along the western contact, while several bedding parallel veins (<3 cm thick) are present in the western contact-proximal host rocks (zone "C_w", Fig. 4.24b).
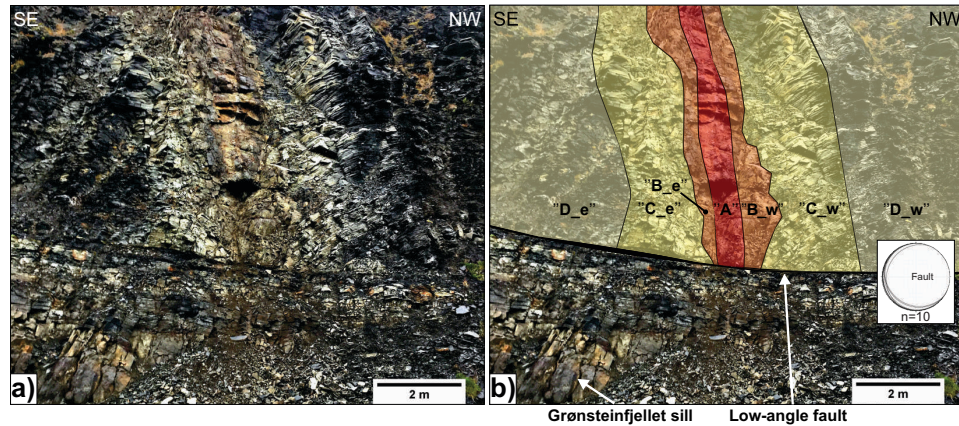
Figure 4.22: Grønsteinfjellet dyke (Gf_d). (a) Outcrop photograph, and (b) interpretation of (a). Zone "A" = central dolerite, "B_e" and "B_w" = contact-proximal dolerite, "C_e" and "C_w" = contact-proximal sedimentary rock, "D_e" and "D_w" = contact-distal sedimentary rocks. Grønsteinfjellet thin sill is visible in th lower, left corner. For color legend, see Fig. 3.4.

Fracture orientation

Most of the structural data were collected along a scanline (Gf_d_01, Figs. 4.25a, d) across the dyke, from the lower part of the intrusion. Structural orientation data from the different zones are presented in stereoplots in Fig. 4.23. Four main fracture sets are detected and are listed in Table 4.6.

Three main sets are identified within the central dolerite (zone "A"). F1 (strike/dip angle: 178/90) is oriented parallel to the intrusion contact, while F2 (strike/dip angle: 273/85) and F3 (strike/dip angle: 176/25) are oriented sub-perpendicular to the intrusion contact (see Fig. 4.24a for photo). F1 is also identified in the western and eastern contact-proximal dolerite (zone "B_w" and "B_e"), while F2 is identified in the western contact-proximal dolerite (zone "B_w"). However, both F2 and F3 fractures are present in contact-proximal dolerite in the upper part of the dolerite (Fig. 4.24a), which is presumably less affected by the local folding.

F4 (strike/dip angle: 012/81) is only identified within the host rocks, and is on average oriented perpendicular to the sedimentary bedding. F1 fractures in the contact-proximal host rocks were not measured in the field, but can be observed on the photo in Fig. 4.24a.
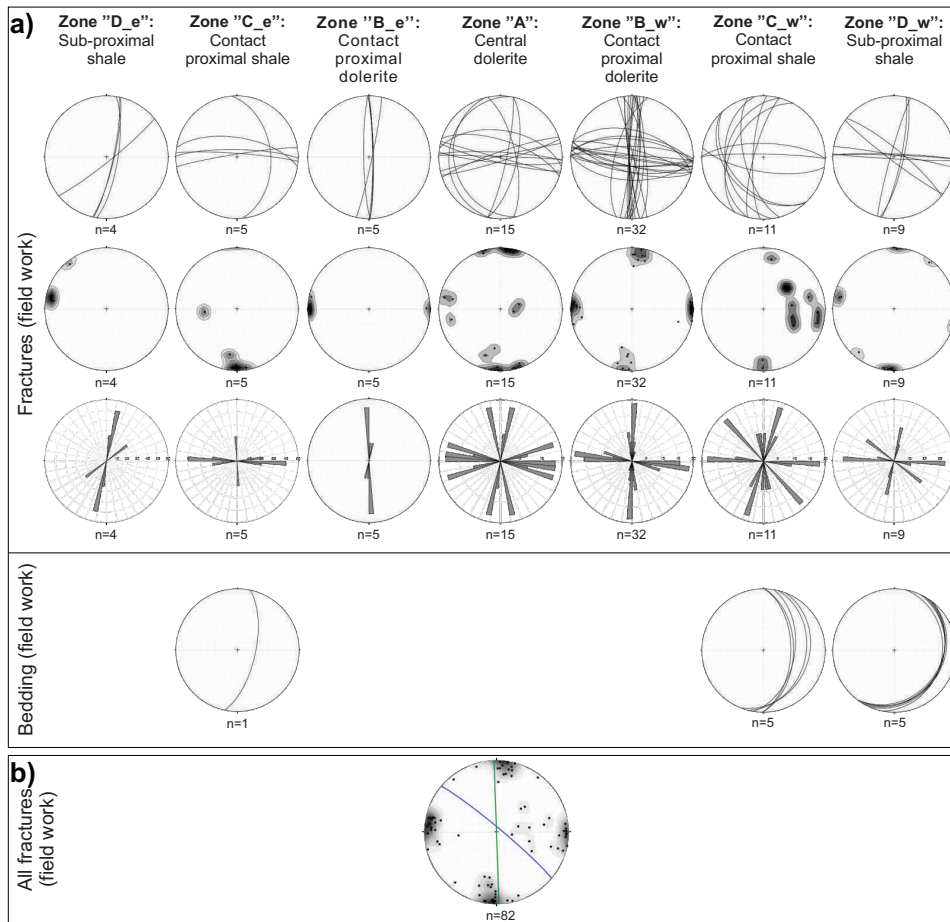
Figure 4.23: Grønsteinfjellet dyke (Gf_d). (a) Fracture orientation, and bedding orientation data from each interpreted zone. (b) All fractures plotted as poles with contours, averaged intrusion contact (green great circle) and outcrop orientation (blue great circle). Zone "A" = central dolerite, "B_e", "B_w" = contact-proximal dolerite, "C_e", "C_w" = contact-proximal sedimentary rocks, while "D_e", "D_w" = contact-distal sedimentary rocks.

Table 4.6: Grønsteinfjellet dyke (Gf_d). Left: Main fracture sets and their presence within each zone. Right: Main sets plotted as planes, all fractures plotted as poles with contours.

Set	Orientation	Strike/dip angle	"D_e"	"C_e"	"B_e"	"A"	"B_w"	"C_w"	"D_w"
F1	N-S	178/90		x	x	x	x	x	
F2	E-W	273/85		x		x	x	x	x
F3	N-S	176/25				x			
F4	NNE-SSW	012/81	x						x
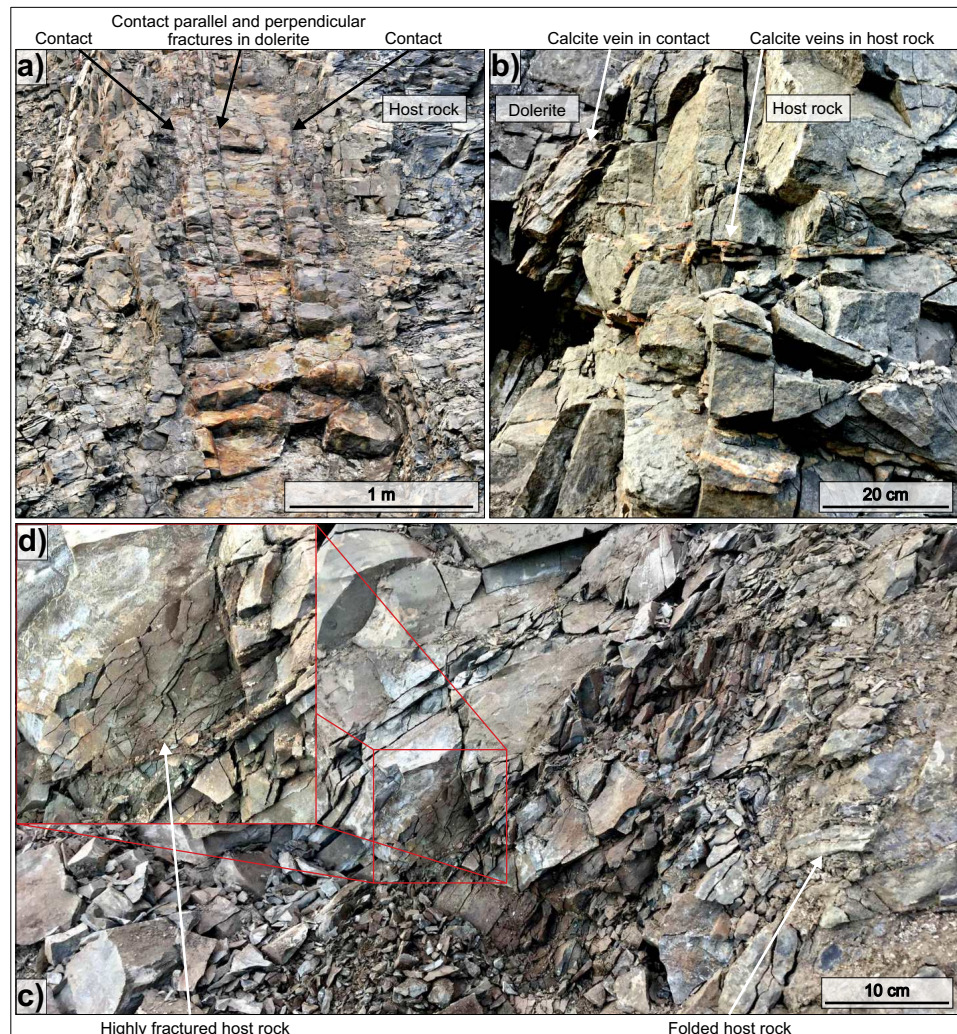
Figure 4.24: Grønsteinfjellet dyke (Gf_d). (a) Contact parallel and perpendicular fractures in the dolerite from the upper part of the dyke. (b) A 7 cm thick carbonate vein in the western contact, and several carbonate veins within the western contact-proximal host rocks (zone "C_w"). (c) Highly fractured area and a folded fragment within the eastern contact-proximal host rocks (zone "C_e"). (d) Zoom in of (c) of the highly fractured area with an average fracture spacing 1 cm.

Fracture spacing

The high quality of the outcrop serves excellent opportunities for studying the sedimentary rocks with varying distance to the dyke. Unfortunately, poor data from this area, partly due to poor weather, did not allow for virtual outcrop modeling. Therefore, in addition to one scanline conducted in the

field (Gf_d_01), 14 contact-perpendicular profiles are analyzed based on digital photos. Gf_d_02-05 (Fig. 4.25a, b) are from the lower part of the dyke, and intersect the 1.5 m thick dyke and 2-3 m of the host rocks on each side of the dyke. Gf_d_06-15 (Fig. 4.26a) are only covering the dyke in the upper part of the outcrop. Each profile is following a sandstone layer within the sedimentary rocks, and is horizontal through the dyke.

Fig. 4.25d displays a histogram of the scanline. A distinct peak is present at 1-1,5 m, which represents the highly fractured area previously mentioned within the eastern contact-proximal sedimentary rocks (Figs. 4.24c and d). The fractures in this area are plotted as bed-confined fractures, however, the rocks are fragmented and crushed in this area, making the actual bedding orientation ant thickness uncertain, except for the fragment mentioned above. Therefore, orientation data was not collected within this area, as the fractures likely are a result of the complex folding. Except the peak at 1-1,5 m, the fracture frequency is stable at 10 f/m within the dolerite, and 8 f/m within the host rocks (Fig. 4.25d). A decrease in bed-confined and an increase in through going fractures is observed from 0,5-1 m to 0-0,5 m (Fig. 4.25c). The end of the profile is at 3.75 m, making the fracture frequency for the last bin (3,5-4 m) possibly twice as high as the histogram illustrates.

Fig. 4.25c presents histograms of Gf_d_02-05. Gf_d_02-04 show an enhanced fracture frequency around the contacts, where the peaks are located within the contact-proximal host rock, 0-1 m from the contact. Generally, the fracture frequency within the host rocks is increasing towards the contacts. Within the intrusion, the fracture frequency is decreasing towards the center, where the fractures are oriented parallel to the contacts (F1). However, the intrusion width/bin width ratio is low, making local changes in fracture frequency within the intrusion less visible.

Gf_d_05 (Fig. 4.25c) differs from Gf_d_02-04, and has three peaks. These are located within the eastern contact-proximal host rocks (zone "C_e", at 1.5-2 m), within the western contact-proximal dolerite (zone "B_w", at 4-4.5 m) and within the western contact-distal host rocks (zone "D_w", at 5.5 m). The western contact-proximal host rocks (zone "D_w") have an enhanced fracture frequency in Gf_d_03 and Gf_d_04, while no obvious increase is present in the two other profiles. Within the dolerite, the fracture frequency is between 7 and 12 f/m.

Both the average and the median fracture frequencies for Gf_d_06-15 are increasing towards the contact. This yields especially on the south-eastern side of the dyke, where the overall average fracture frequency is 7.2 f/m at 0.5-0.75 m and 11.2 f/m at 0-0.25 m (for photo, see Fig. 4.26a). The profiles are dominated by contact-perpendicular (F1) fractures.
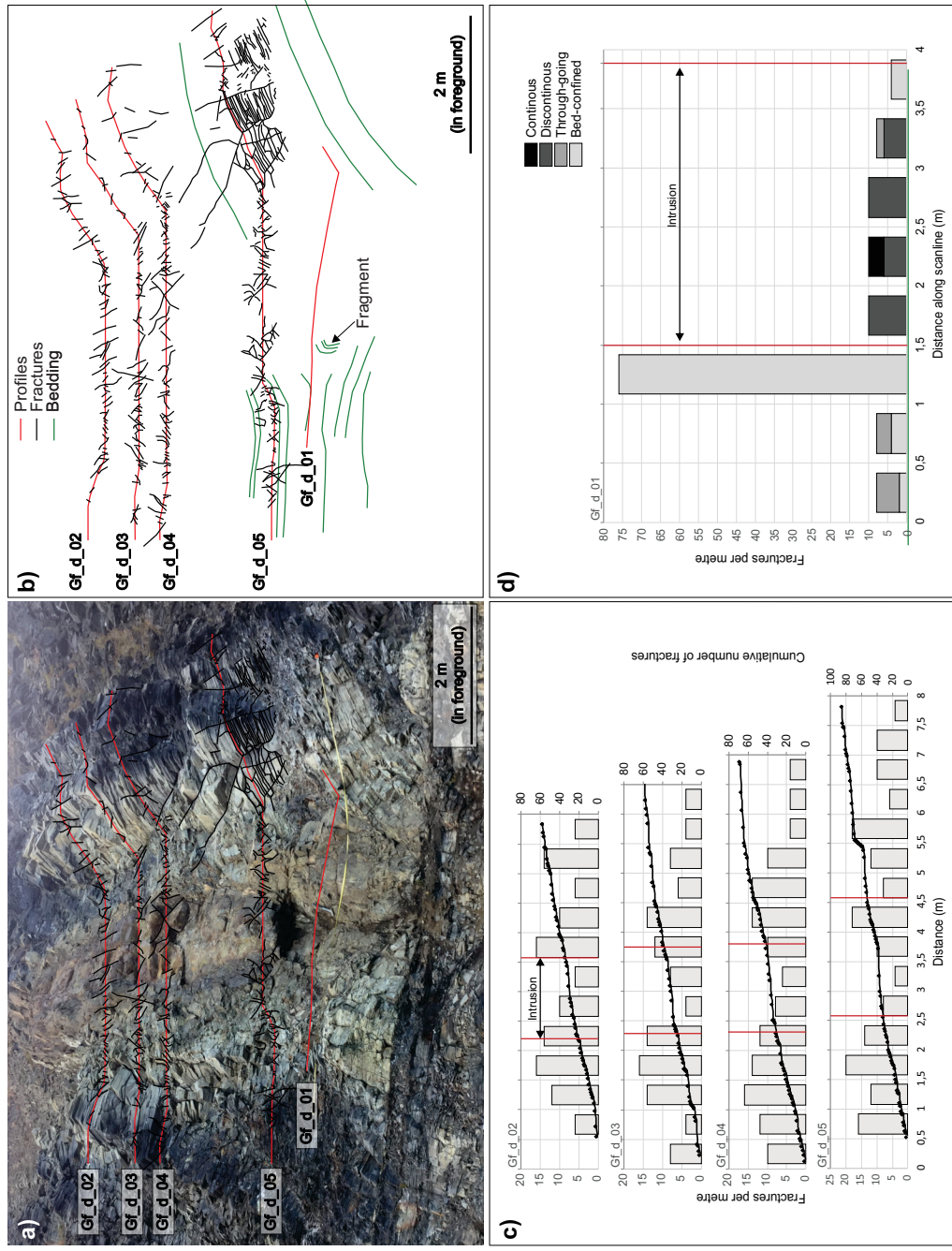
Figure 4.25: Grønsteinfjellet dyke (Gf_d). (a) and (b) illustrate the analyzed fracture frequency profiles from the lower part of the dyke, mapped fractures and bedding indicators. (c) Histograms (left axis) and cumulative frequency (right axis) of the fracture frequency profiles displayed in (a) and (b). (d) Traditional scanline across the dyke, displayed in (a) and (b). The bin width for all histograms is 0.5 m. All profiles are horizontal through the dyke and follow distinct sedimentary layers within the host rocks. The red lines mark the intrusion contact.
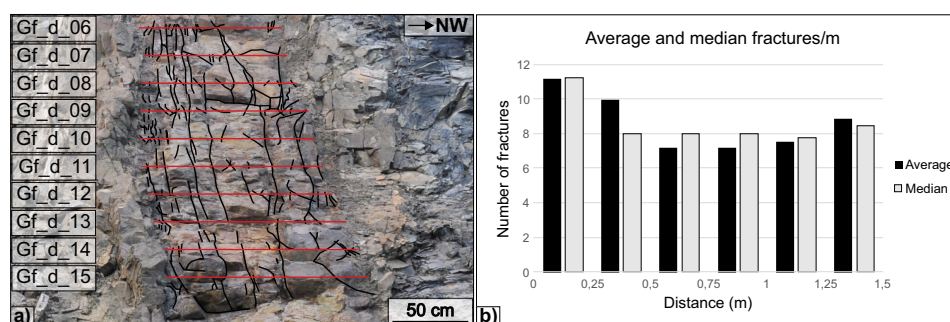
Figure 4.26: Grønsteinfjellet dyke (Gf_d). (a) Mapped fractures and analyzed fracture frequency profiles. (b) Histogram with average and median fracture frequencies for the profiles displayed in (a). All profiles are 1.5 m long, based on the assumption that the dyke has an uniform thickness at this outcrop.

4.1.5 Grønsteinfjellet thin sill

Grønsteinfjellet thin sill (Gf_c, Fig. 4.1) is a 1,75 m thick, layer parallel (within the studied area) sill exposed at the beach beneath Grønsteinfjellet, just east of the Grønsteinfjellet dyke (Fig. 4.22. The sill is exposed at the beach for 165 m.

Virtual outcrop

A part of the virtual outcrop of the Grønsteinfjellet (Gf_c) sill can be view in Appendix B. The texture quality of the virtual outcrop is lower than for the rest of the virtual outcrops, however, the virtual outcrop has a representative mesh and is perfectly oriented.

Zone interpretations

A lithological log (Fig. 4.27), conducted approximately 30 m from the south-eastern end of the sills exposure, illustrates the interpretations of the zones. Starting from the bottom of the log, zone "C_l" (contact-proximal sandstone) consists of 95 cm of laminated black shale, with nodules and clay chunks. The next 120 cm consists of massive, partly normal graded, very fine grained sandstone. The dolerite, comprising zones "B_l" (contact-proximal dolerite), "A" (central dolerite) and "B_u" (contact-proximal dolerite), is characterized by a brown color. Zone "B_l" (25 cm thick) and zone "B_u" (10 cm thick) are differentiated from zone "A" (135 cm thick) by closer spaced contact-perpendicular

fractures. These fractures in zone "B_l" can be observed in Fig. 4.27, however, zone "B_u" is barely visible in this figure. Zone "C_u" consists of 130 cm of laminated shale, 50 cm of very fine grained, red sandstone interbedded with shale layers, and 50 cm of reverse graded sandstone.
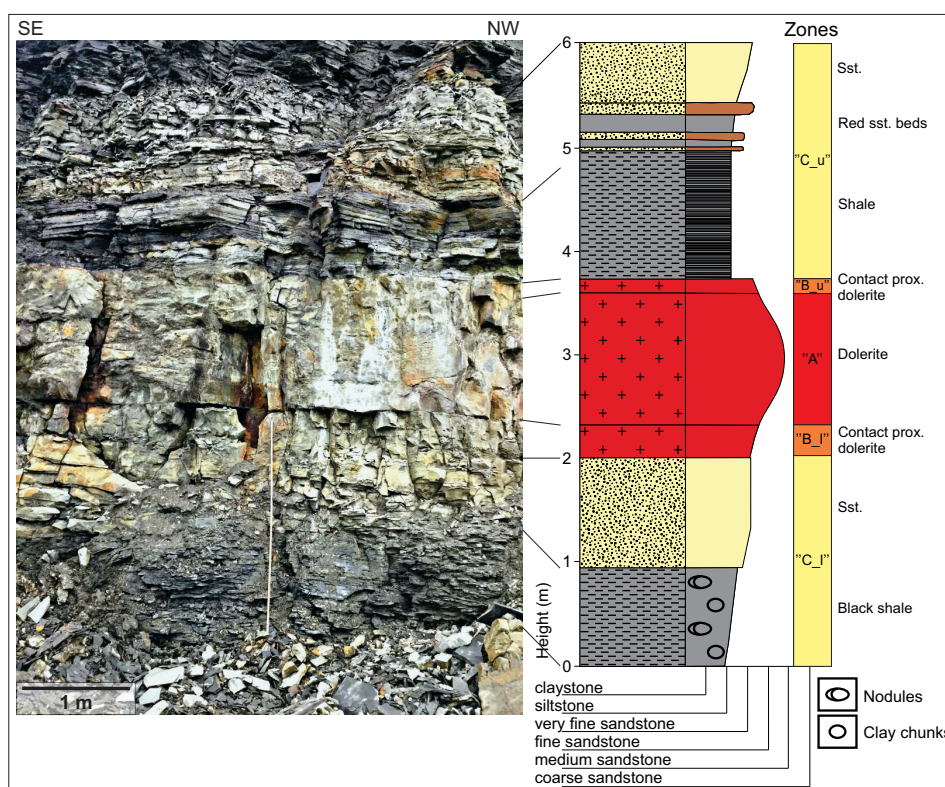
Figure 4.27: Grønsteinfjellet sill (Gf_c). Outcrop photograph and lithological log of the sill and the contact. Zone column represents the interpreted zones. Zone "A" = central dolerite, "B_u" and "B_l" = contact-proximal dolerite, "C_u" and "C_l" = contact-proximal sedimentary rocks.

Fracture orientation

Structural orientation data from in and around Grønsteinfjellet sill is partly from field work in the area of the lithological log (Fig. 4.27), and partly from virtual outcrop model analyses. Unfortunately, only three zones were measured in the field as a result of lack of time due to polar bears in the area. The orientation data is presented in Fig. 4.28. 5 main sets were identified and are listed in Table 4.7.
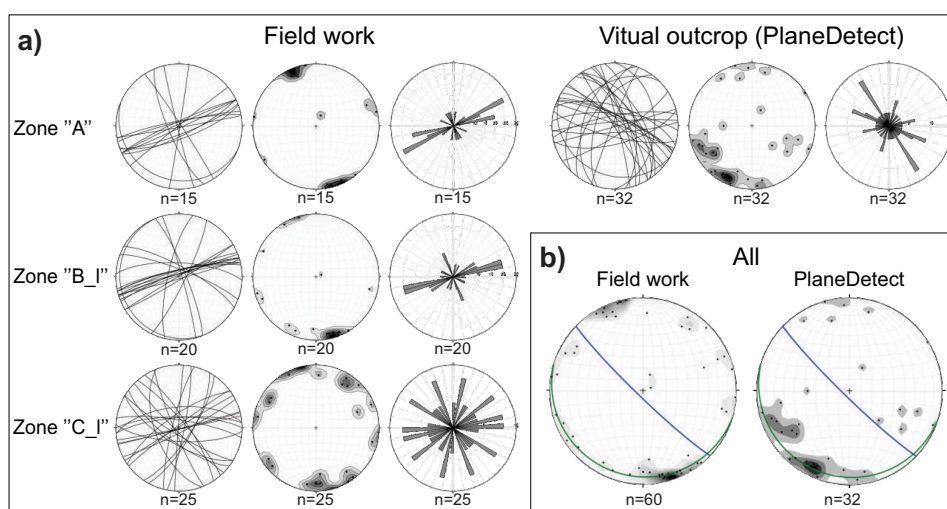
Figure 4.28: Grønsteinfjellet sill (Gf_c). (a) Orientation data for three of three zones. (b) All fractures plotted as poles with contours, averaged intrusion contact (green great circle) and outcrop orientation (blue great circle). Zone "A" = central dolerite, "B_l" = contact-proximal dolerite, "C_l" = contact-proximal sedimentary rocks.

Table 4.7: Grønsteinfjellet sill (Gf_c). Left: Main fracture sets and their presence within each zone. Right: Main fracture sets plotted as planes, all fractures from fieldwork and virtual outcrop analyses plotted as poles with contours.

Set	Orientation	Strike/dip angle	"A"	"B_l"	"C_l"
F1	ENE-WSW	251/85	x	x	x
F2	NNW-SSE	166/88	x	x	x
F3	NNE-SSW	028/80			x
F4	WNW-ESE	294/81			x
F5	WNW-ESE	107/09	x	x	

F1 (strike/dip angle: 251/85) and F2 (strike/dip angle: 166/88) are oriented perpendicular to the intrusion contact (F5, strike/dip angle: 107/09), respectively, and are present in all the three measured zones. F5 has limited measurements from the field in zone "A" and "B_l", however, the set can easily be spotted in the three measured zones (Fig. 4.27).

Zone "C_l" displays 4 main sets, comprising F1, F2, F3 (strike/dip angle: 028/80) and F4 (strike/dip angle: 294/81). F3 and F4 are not present in the dolerite.

4.1.6   Studentdalen dyke west

Several dykes are exposed at the beach at the mouth of Studentdalen (Fig. 4.1). Two of these, located approximately 15 m from each other, are investigated in this study, referred to as the Studentdalen dyke west (Sd_w) and the Studentdalen dyke east (Sd_e, Section 4.1.7).

The Studentdalen dyke west is an approximately 1 m wide, inclined dyke within carbonates belonging to the Upper Permian Kapp Starostin Formation.

Virtual outcrop

A virtual outcrop of Studentdalen dyke west (Sd_w) is displayed in Fig. 4.29a.
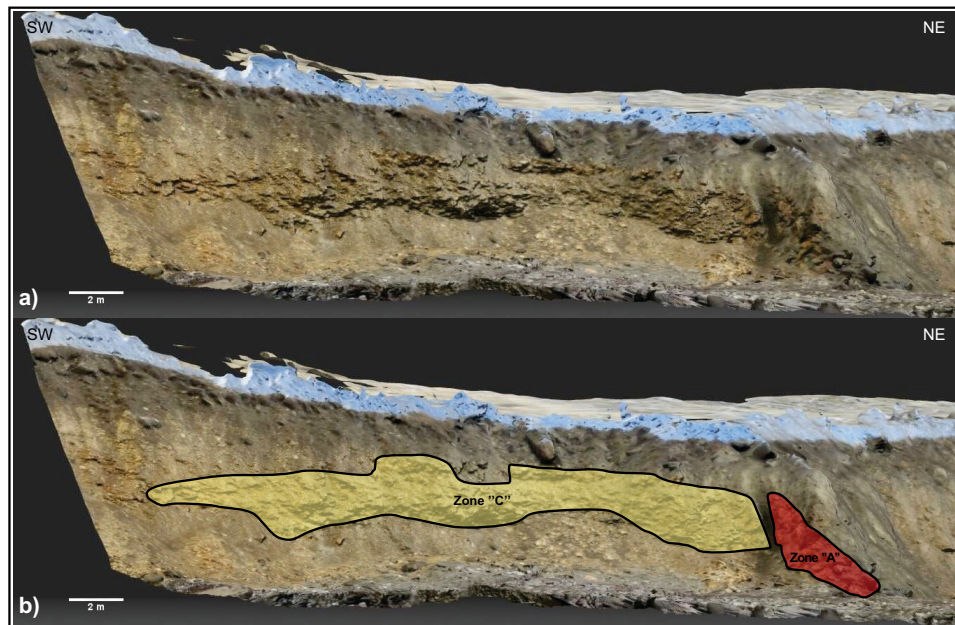
Figure 4.29: Studentdalen dyke west (Sd_w). (a) Virtual outcrop model, and (b) interpretation of (a). Zone "A = central dolerite, "C" = contact-proximal sedimentary rocks. For color legend, see Fig. 3.4.

Zone interpretations

Both the intrusion and the host rocks are highly weathered and fractured (Fig. 4.29a). As a result of the weathering, both the host rocks and the intrusion were buried in scree, making interpretations of zones and defining contacts between

them difficult. Therefore, only two zones have been defined. (Fig. 4.29b). The two zones are primarily differentiated by color. Zone "A" consists of weathered, highly fractured, brown dolerite, while zone "C" consists of weathered, highly fractured, light brown limestone. The contact between the two zones has a dip of approximately 60 degrees (Fig. 4.30).

Fracture orientation

Two main fracture sets (Fig. 4.30, Table 4.8) were identified within zone "C", F1 (strike/dip angle: 95/84) and F2 (strike/dip angle: 355/88), which are perpendicular to each other. For zone "C", the data from the field and the virtual outcrop correspond relatively well, especially when considering that the outcrop has many loose rocks that likely have been analyzed by PlaneDetect, despite that most weathered areas are cropped out and not analyzed.
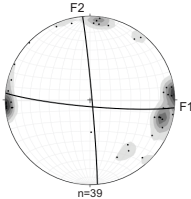
Only one fracture set is identified within zone "A" (F1), which also is present within zone "C". No obvious relation is observed between the fractures within zone "C" and the intrusion contact (strike/dip angle: 037/63).
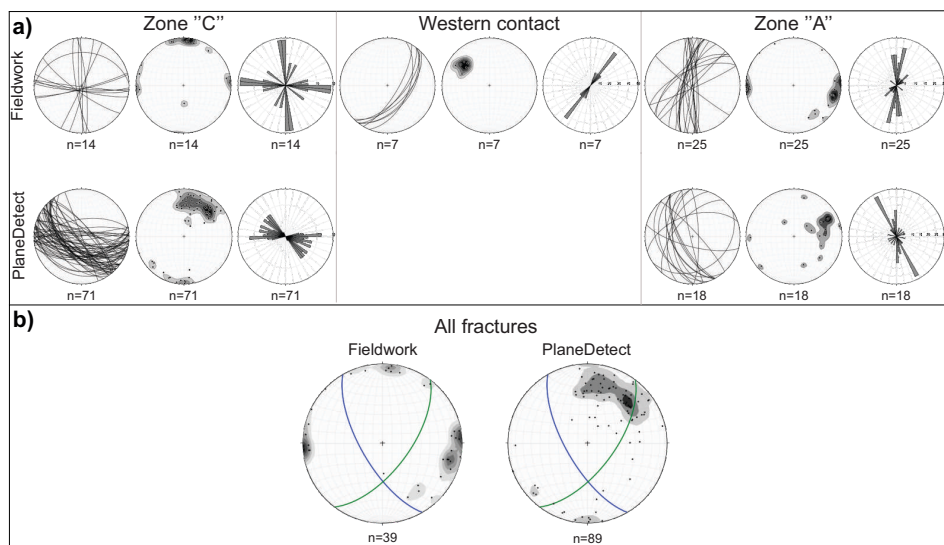
Figure 4.30: Studentdalen dyke west (Sd_w). (a) Fracture orientation data for the two zones and the western intrusion contact. (b) All fractures plotted as poles with contours, averaged intrusion contact (green great circle) and outcrop orientation (blue great circle). Zone "A" = central dolerite, "C" = contact-proximal sedimentary rocks.

Table 4.8: Studentdalen dyke west (Sd_w). Left: Main fracture sets and their presence within each zone. Right: Main fracture sets plotted as planes, all fractures from fieldwork plotted as poles with contours.

Set	Orientation	Strike/dip angle	"A"	"C"
F1	E-W	95/84		x
F2	N-S	355/88	x	x

4.1.7   Studentdalen dyke east

Virtual outcrop

A virtual outcrop of the Studentdalen dyke east (Sd_e, Fig. 4.1) is displayed in Fig. 4.31a.

Zone interpretations

The Studentdalen dyke east is a 25 m thick dyke exposed at the beach in the mouth of Studentdalen (Fig. 4.1).

Starting from the center of the dyke (Fig. 4.31), zone "A" stands out as a large, brown block, characterized by vertical fractures. Zone "B_w" and "B_e" (both have a width of <3 m) symmetrically surround zone "A" and consist of massive, dark brown rocks. These are interpreted to be contact-proximal dolerites due to their massiveness and high resistance to erosion, compared to the weathered down host rocks adjacent to the intrusion. Due to a limited time frame on the project, petrographic observations and analyses of the rocks form the interpreted contact-proximal dolerite was not preformed. It can therefore also be that zones "B_w" and "B_e" have a different origin, such as limestone locally metamorphosed by the heat during intrusion emplacement (contact-proximal sedimentary rocks).

Fracture orientation

Fracture orientation data from virtual outcrop analyses are plotted in Fig. 4.32. The stereoplots from zone "A" indicate 5 main fracture sets (listed in Table 4.9).
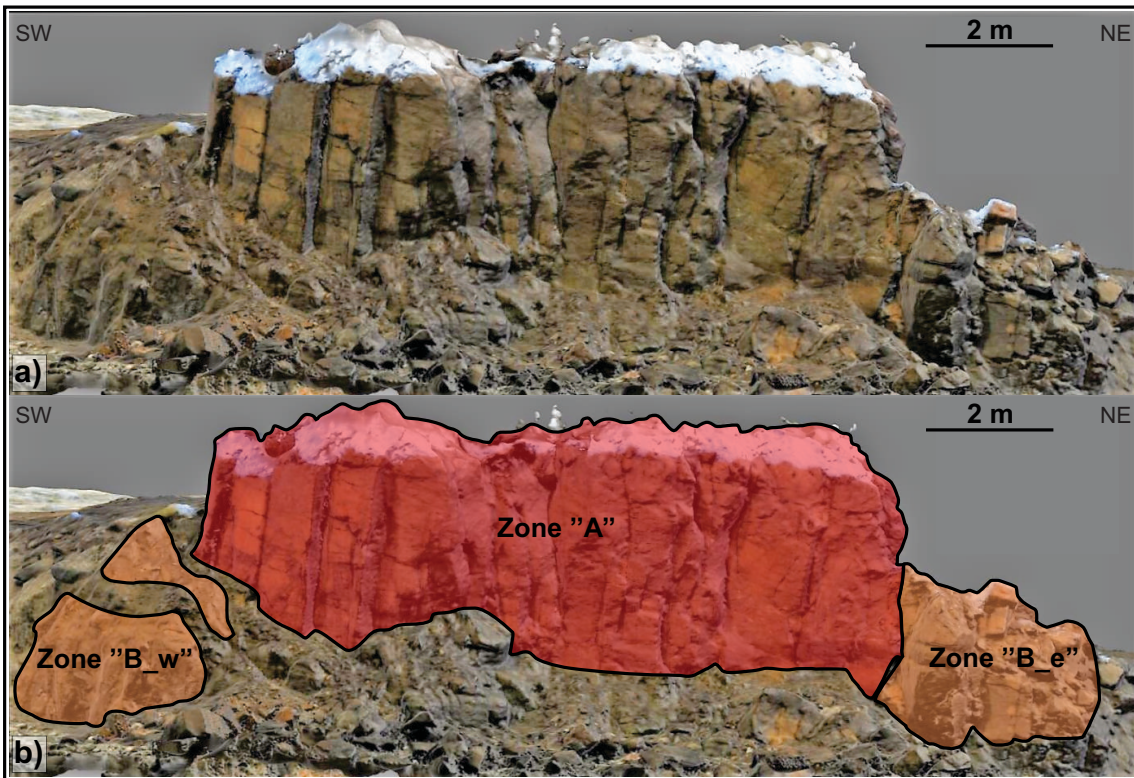
Figure 4.31: Studentdalen dyke east (Sd_e). (a) Virtual outcrop model, and (b) interpretation of (a). . Zone "A" = central dolerite, "B" = contact-proximal dolerite. The virtual outcrop was constructed by the author, but is adapted from Senger et al. (2016b). For color legend, see Fig. 3.4.

Zone "A" is characterized by vertical fractures, comprising F1 (strike/dip angle: 184/82), F2 (strike/dip angle: 234/81) and F3 (strike/dip angle: 288/85), in addition to F4 (strike/dip angle: 076/10), which is horizontal. F1 fractures represent fractures parallel to the interpreted (but not clearly visible) intrusion contact. F2 fractures reflect the outcrop orientation of zone "B_w" and partly zone "A", while F3 fractures reflect the outcrop orientation of zone "B_e" and partly zone "A". F4 reflects the top surface of zone "A".

F5 (strike/dip angle: 141/63) and F6 (strike/dip angle: 017/24) comprise fractures with lower dip angles, striking NW-SE and NNE-SSW respectively, and are both perpendicular to the F2 fractures. F5 fractures are identified in zone "B_w" and "B_e", while F6 fractures are identified within zone "A" and "B_e". F5 is perpendicular to F2, while F6 is perpendicular to F3.

Generally, the three zones show similarities in fracture pattern, where all three are dominated by vertical fractures. However, zone "B_w" and "B_e" have more inclined fractures (F5 and F6) than zone "A".
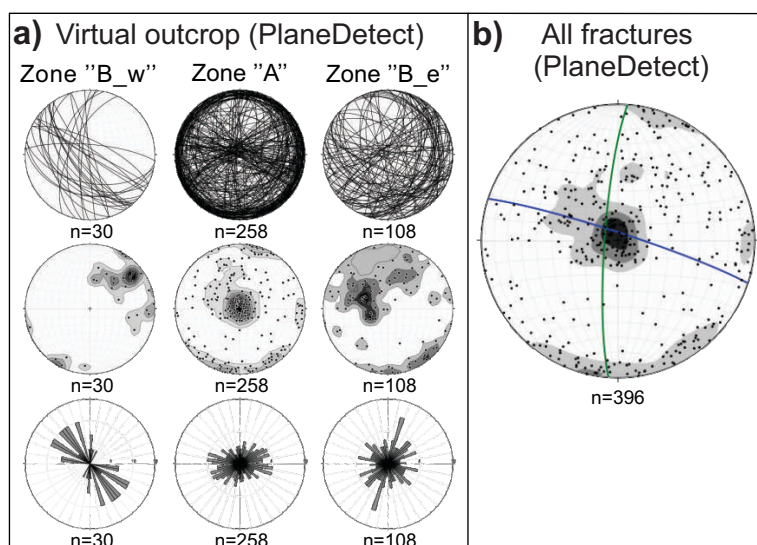
Figure 4.32: Studentdalen dyke east (Sd_e). (a) Orientation data from the three of zones. (b) All fractures plotted as poles with contours, averaged intrusion contact (green great circle) and outcrop orientation (blue great circle). Zone "A" = central dolerite, "B_w" and "B_e" = contact-proximal dolerite.

Table 4.9: Studentdalen dyke east (Sd_e). Left: Main fracture sets within the different zones. Right: Main fracture sets plotted as planes, all fractures plotted as poles with contours.

Set	Orientation	Strike/dip angle	"B_w"	"A"	"B_e"
F1	N-S	184/82	x	x	x
F2	NE-SW	234/81		x	x
F3	WNW-ESE	288/85	x	x	
F4	ENE-WSW	076/10		x	
F5	NW-SE	141/63	x		x
F6	NNE-SSW	017/24		x	x
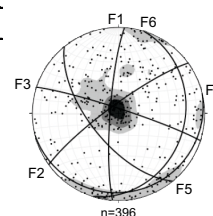
4.1.8　Wallenbergfjellet sill

The Wallenbergfjellet sill (Fig. 4.1) is a c. 40 m thick, layer-parallel to transgressive sill cropping out along the north-northwestern and the west-southwestern side of Wallenbergfjellet. On the western corner of Wallenbergfjellet, the sill is exposed within rocks belonging to the Kapp Starostin Formation (localities Wf_c and d, Fig. 4.35), while on the southern and northern side of the mountain, it is exposed within rocks belonging to the Vikinghøgda fm (Wf_a, b and e). The host rocks were snow covered when the Wallenbergfjellet localities were visited, however, the Kapp Starostin Formation consists mainly of spiculitic

chert (Dustira et al., 2013), while the lower part of Vikinghøgda Formation primarily consists of mudstones (Mørk et al., 1999).

Virtual outcrop

A virtual outcrop of the northwestern side of Wallenbergfjellet (W_e) is displayed in Fig. 4.33b.
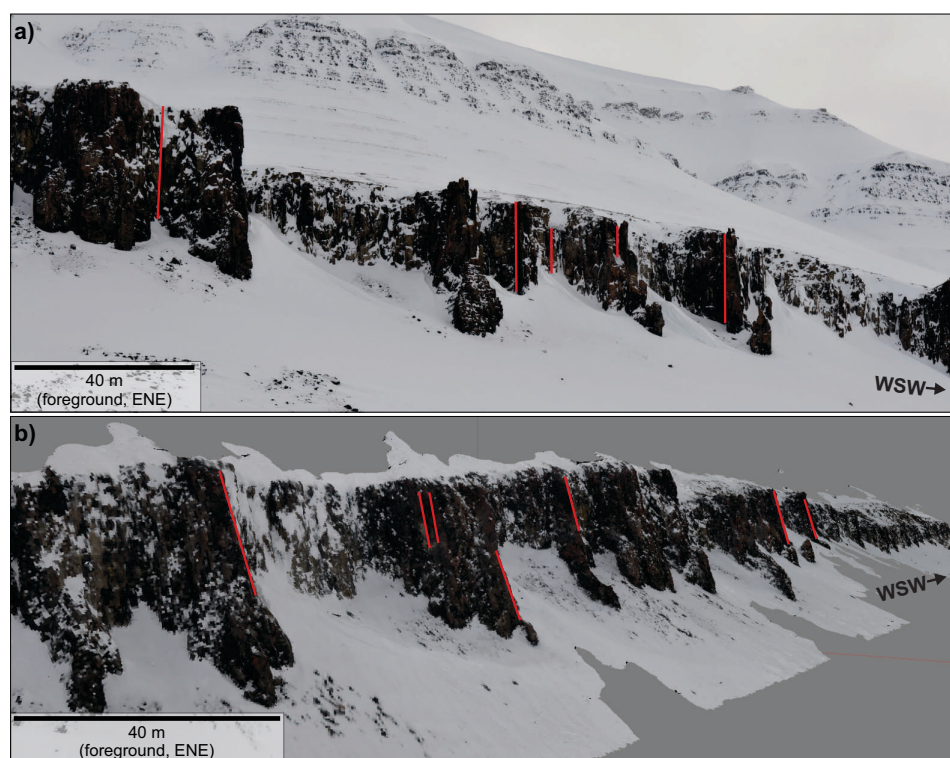
Figure 4.33: Wallenbergfjellet (Wf_e). (a) Photo illustrating the vertical jointing of the sill. (b) Parts of the virtual outcrop (textured view), oriented with z-axis vertical on the image, to illustrate the slightly different dip between (a) and (b). The dip of the fractures is indicated with red lines.

Fracture orientation

Fracture orientation data from five different localities is plotted in Fig. 4.34. The data from Wf_a-d are based on fieldwork, and the data from Wf_e is based on virtual outcrop model analyses.
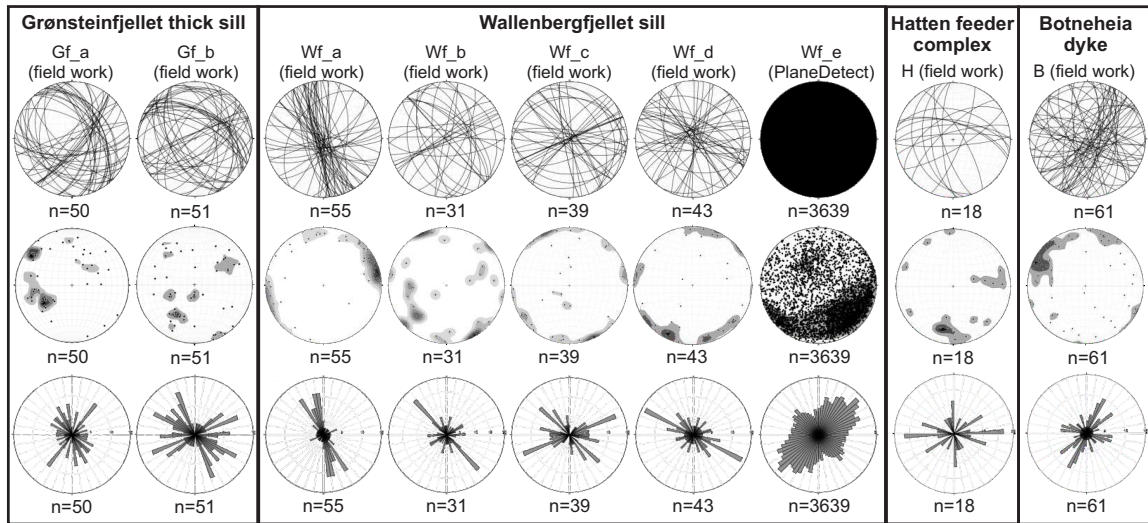
Figure 4.34: Structural orientation data of dolerites, including Grønsteinfjellet thick sill (Gf_a and b), the Wallenbergfjellet thick sill (Wf_a-e), the Hatten feeder complex (H) and the Botneheia dyke (B). All measurements are from field work, except at Wf_e, that are from virtual outcrop analyses.

Wf_a-d are dominated by vertical fractures, where the strike varies between the localities (Table 4.10). In general, the fractures are well correlating with the outcrop at each locality (Fig. 4.35), where the following fracture sets represent the outcrop orientation: F1 (at Wf_a, strike/dip angle: 142/83), F3 (at Wf_b, strike dip angle: 313/79), F5 (at Wf_c, strike dip angle: 169/82), F8 (at Wf_d, strike/dip angle: 230/87) and F9 (Wf_e, strike/dip angle: 23/58). The main fracture sets at localities Wf_a-d comprise F1-F8 fractures (listed in Table 4.10). 2-3 fracture sets are identified at each locality, and are oriented from 30 to 70° relative to each other.

Wf_e is dominated by F3 (strike/dip angle: 313/79), F9 (strike/dip angle: 230/58) and F10 (strike/dip angle: 068/31), that are perpendicular to each other. F9 and F10 have a similar strike as the outcrop orientation, confirming the right orientation of the virtual outcrop, however, the dip of the two sets is slightly lower (approximately 20°) compared to the field data from Wf_a-d. In addition, the photo in Fig. 4.33a, and the image of the virtual outcrop in Fig. 4.33b, indicate that the dip angle of the columns at the virtual outcrop is slightly lower than in the outcrop in the photo. This suggests that the virtual outcrop is somewhat tilted towards SSE, resulting in F9 and F10 having a slightly different dip than what is real, while the vertical F4 fractures, perpendicular to the outcrop orientation, are not affected by the tilting. F9 is therefore likely the same set as F8 (Fig. 4.35). No obvious trend is linking the varying strike of the fractures at the different localities.

Table 4.10: Wallenbergfjellet sill (Wf_a-e). Main fracture sets within the sill and their presence within each locality. See Fig. 4.35 for stereoplots.

Set	Orientation	Strike/dip angle	Wf_a	Wf_b	Wf_c	Wf_d	Wf_e
F1	NNW-SSE	142/81	x				
F2	ENE-WSW	247/89	x	x	x		
F3	NW-SE	313/79		x	x		x
F4	N-S	010/87		x			
F5	N-S	169/82			x		
F6	NNE-SSW	011/84				x	
F7	NW-SE	297/86				x	
F8	NE-SW	230/87				x	
F9	NE-SW	230/58					x
F10	ENE-WSW	068/31					x
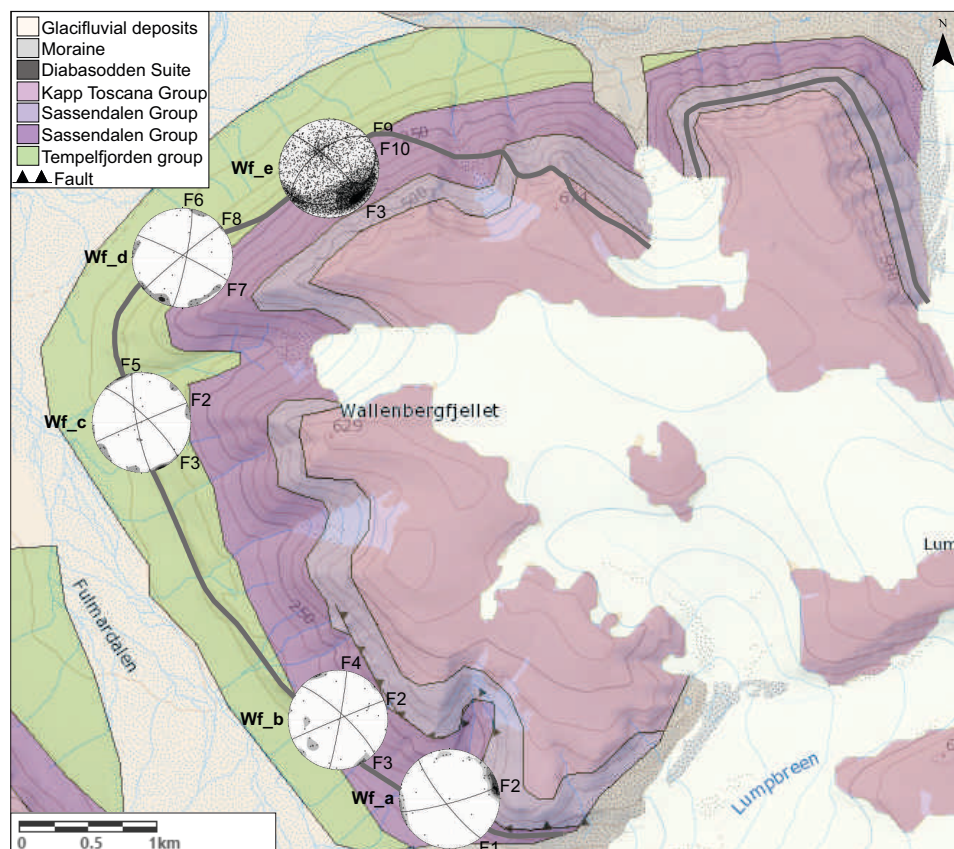
Figure 4.35: Wallenbergfjellet (Wf_e). Geological map with main fracture sets at each locality, illustrate the good correspondence between fracture orientations, intrusion contact (mostly horizontal) and the outcrop orientation at each locality. See Fig. 4.1 for location. Map adapted from a Norwegian Polar Institute geological map.

4.1.9   Orientation data from other intrusions

A short description of the three other igneous features and orientation data from these follows below. The structural orientation data is displayed in Fig. 4.34, and their main fracture sets are listed in Table 4.11.

Table 4.11: Left: Main fracture sets within the intrusions Grønsteinfjellet thick sill (Gf_a and b), Hatten feeder complex (H) and Botneheia thin dyke (B). Right: Main fracture sets plotted as planes, all fractures plotted as poles.

Set	Orientation	Strike/dip angle	Locality abbrevation	
Hatten feeder complex			H	
F1	W-E	268/67	x	
F2	N-S	177/72	x	
Grønsteinfjellet thick sill			*Gf_a*	*Gf_b*
F1	NE-SW	039/80	x	x
F2	NNW-SSE	331/48	x	x
F3	NW-SE	132/33	x	x
F4	E-W	273/14		x
Botneheia dyke			B	
F1	NE-SW	026/73	x	
F2	NW-SE	115/80	x	

Hatten feeder complex

The Hatten feeder complex (H, Fig. 4.1) is a massive system (up to 160 m high), which may represent the feeder of the magmatic system (Senger et al., 2013a). The igneous feature forms the hill called Hatten.

The orientation data (Fig. 4.34) indicate two main fracture sets (Table 4.11), F1 (strike/dip angle: 268/67) and F2 (strike/dip angle: 177/72), oriented perpendicular to each other.

Grønsteinfjellet thick sill

The Grønsteinfjellet thick sill (comprising locality Gf_a and b, Fig. 4.1) is the approximately 30 m thick sill cropping out along Grønsteinfjellet, above the Grønsteinfjellet thin sill (Gf_c) and thin dyke (Gf_d). The intrusion contact of the sill is not measured in the field due to a complex geometry of the intrusion and no exposed intrusion contact in the studied area. The sill is exposed within rocks from the Botneheia Formation and the De Geerdalen Formation.

The stereoplots from Gf_a and Gf_b indicate 4 main fracture sets. F1 (strike/dip angle: 039/80), F2 (strike/dip angle: 331/48) and F3 (strike/dip angle: 132/33) are present at both localities, and are oriented with 60° to each other. F4 (strike/dip angle: 273/14) is only measured at Gf_b.

Botneheia dyke

Botneheia dyke (B, Fig. 4.1) is a c. 2 m thick dyke exposed at the top of Botneheia. In the studied area, the dyke is exposed within rocks belonging to the De Geerdalen Formation. The dyke is striking NW-SE, and has a dip of approximately 80° towards SW.

The stereoplots indicate two main fracture sets. F1 (strike/dip angle: 026/73) is oriented perpendicular to the intrusion contact, while F2 (strike/dip angle: 115/80) is oriented parallel to the strike of the intrusion.

4.2   Adventdalen, DH4 intrusion

The Adventdalen DH4 intrusion (Fig. 3.3) is a 2.28 m thick intrusion from the lower part of the Triassic De Geerdalen Formation (e.g., Braathen et al., 2012). It is located between 949.71-951.99 m depth of the DH4 borehole in Adventdalen (core site located 8 m above sea level).

4.2.1   Zone interpretations

A lithological log of the intrusion and parts of its upper and lower host rocks (7,72 m above the intrusion and 6 m below the intrusion) with interpretations of the zones is presented in Fig. 4.36. For a photo of the cores, see Fig. 3.3 in Chapter 3. From the bottom of the log (at 958 m), the lowermost three meters consist of black shale with sandstone laminas (Fig. 4.36, iiii), overlain by three meters of black shale with sandstone laminas, cross laminas and clusters. The lowermost 6 meters are classified as zone "C_l" and "D_l". The dolerite, classified as zone "A", is not further divided into zones due to a lack of interpretative structures. The host rocks above the intrusion (zone "C_u" and "D_u") consist of black shale with sandstone laminas, crosslaminas and clusters (Fig. 4.36, i).
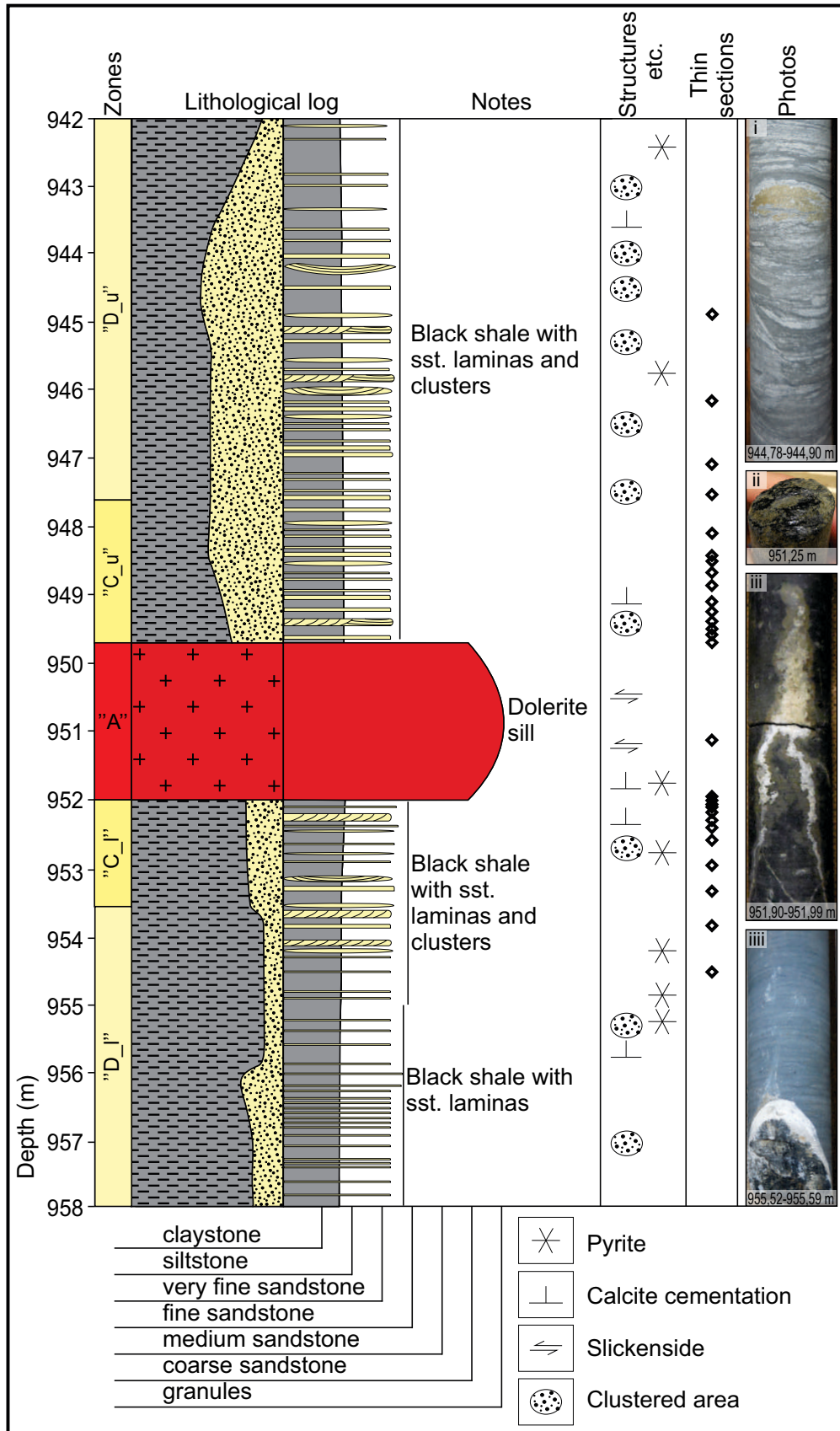
Figure 4.36: DH4. Lithological log, interpreted zones, thin section depth and core photos. i = pyrite lens, ii = surface with slickensides, iii = calcite vein (thin section MF_2015_24, Fig. 4.42b, b*), and iiii = calcite filled fracture. Zone "A" = central dolerite, "C_u" and "C_l" = contact-proximal sedimentary rocks, "D_u" and "D_l" = contact-distal sedimentary rocks. Sst. = sandstone. For color legend, see Fig. 3.4.

The border between the contact-proximal and the contact-distal host rocks on both sides of the intrusion is defined by a bleached color of the contact-proximal host rocks, as can be observed in Fig. 3.3b, Chapter 3. The border between zone "C_l" and "D_l" is defined at 953,60 m, while the border between zones "C_u" and "D_u" is defined at 947,70 m. Surfaces with slickensides (Fig. 4.36, ii) are observed within the dolerite and calcite-filled fractures (e.g., Fig. 4.36, iiii) are observed throughout the studied cores.

4.2.2   Contact metamorphic study

Tab. 4.12 lists the samples from DH4 and their respective thin sections. As the main focus of this section is on the change in porosity around the intrusions, and mud can not be diagnostically identified in a petrographic microscope, this section focuses primarily on two thin sections dominated by quartz grains, located 2.13 m from the upper intrusion contact (MF_2015_21, at 947.09 m) and 0.07 m from the lower intrusion contact (MF_2015_28, at 952.07 m).

Table 4.12: Samples from DH4, their respective thin sections and associated parametes.

Thin section ID	Depth (m)	Sample ID	Lithology	Sampled date	Sampled by	SEM analysis	Porosity determination
MF_2015_23	944,89	MF_2015_23	Shale	18.12.2015	MF		
MF_2015_22	946,16	MF_2015_22	Shale	18.12.2015	MF		
MF_2015_21	947,09	MF_2015_21	Shale	18.12.2015	MF	x	x
MF_2015_20	947,58	MF_2015_20	Shale	18.12.2015	MF		
MF_2015_19	948,1	MF_2015_19	Shale	18.12.2015	MF		
MF_2015_27	948,45	MF_2015_18	Shale	18.12.2015	MF		
MF_2015_18	948,47	MF_2015_18	Shale	18.12.2015	MF		
MF_2015_17	948,7	MF_2015_17	Shale	18.12.2015	MF		
MF_2015_16	948,88	MF_2015_16	Shale	18.12.2015	MF		
MF_2015_25	949,12	MF_2015_25	Shale	18.12.2015	MF		
MF_2015_14	949,28	MF_2015_14	Shale	18.12.2015	MF		
MF_2015_26	949,4	MF_2015_14	Shale	18.12.2015	MF		
MF_2015_13	949,51	MF_2015_13	Shale	18.12.2015	MF		
MF_2015_12	949,62	MF_2015_12	Shale	18.12.2015	MF		
MF_2015_29	949,68	MF_2015_12	Shale	18.12.2015	MF	x	
MF_2015_1	951,15	MF_2015_01	Dolerite	18.12.2015	MF		
MF_2015_24	951,98	MF_2015_24	Dolerite	18.12.2015	MF		
MF_2015_10	952,01	MF_2015_10	Shale	18.12.2015	MF		
MF_2015_28	952,07	MF_2015_10	Shale	18.12.2015	MF	x	x
MF_2015_9	952,08	MF_2015_09	Shale	18.12.2015	MF		
MF_2015_11	952,2	MF_2015_11	Shale	18.12.2015	MF		
MF_2015_8	952,3	MF_2015_08	Shale	18.12.2015	MF		
MF_2015_7	952,4	MF_2015_07	Shale	18.12.2015	MF		
MF_2015_6	952,6	MF_2015_06	Shale	18.12.2015	MF		
MF_2015_5	952,94	MF_2015_05	Shale	18.12.2015	MF		
MF_2015_4	953,34	MF_2015_04	Shale	18.12.2015	MF		
MF_2015_3	953,84	MF_2015_03	Shale	18.12.2015	MF		
MF_2015_2	954,49	MF_2015_02	Shale	18.12.2015	MF		

General description

The studied shales are mineralogically immature, and consist primarily of quartz, calcite, clay, organic material and pyrite. Ti-oxides (Fig. 4.37, chlorite and plagioclase with calcite overgrowth are observed in low abundances. The detrital framework is largely dominated by quartz in the sandstone laminas, and clay in the shale laminas. The origin of the clay minerals is not considered, as the clay minerals could not be diagnostically identified neither in the microscope, nor on the SEM images.
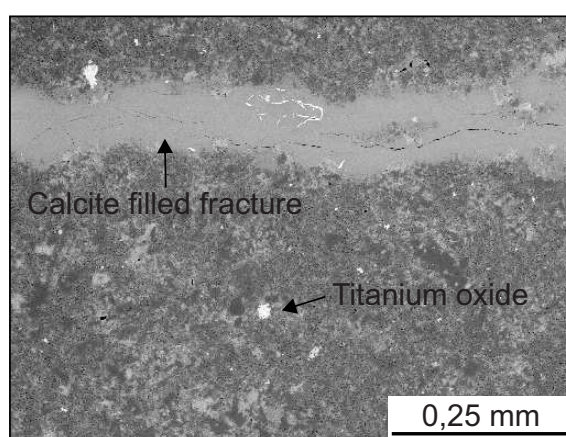
Figure 4.37: DH4. Thin section of a shale lamina with Ti-oxides and a calcite filled fracture, sample MF_2015_29.

Low-grade metamorphic minerals

Chlorite is observed in very low abundances in all the studied thin sections, and is most prominent proximal to the intrusion (MF_2015_28). The chlorite occurs as quartz coating, as authigenic cement in the matrix and as small crystals.

Authigenic minerals

Observed authigenic minerals comprise calcite and pyrite (in addition to minor amounts of chlorite). Within the sandstone laminas, the calcite represents up to 70% of the rock (Fig. 4.38a, a*) and is infilling voids (Fig. 4.38c), fractures (Fig. 4.36, iii) and small cracks. In addition, calcite is seen to replace detrital feldspar. In the laminas that consist of clay and organic material, (Fig. 4.38b, b*), calcite is exclusively present within fractures and small cracks (Fig. 4.37). Pyrite is frequently occurring in the studied cores (Fig. 4.36), and is present primarily within the sandstone laminas.
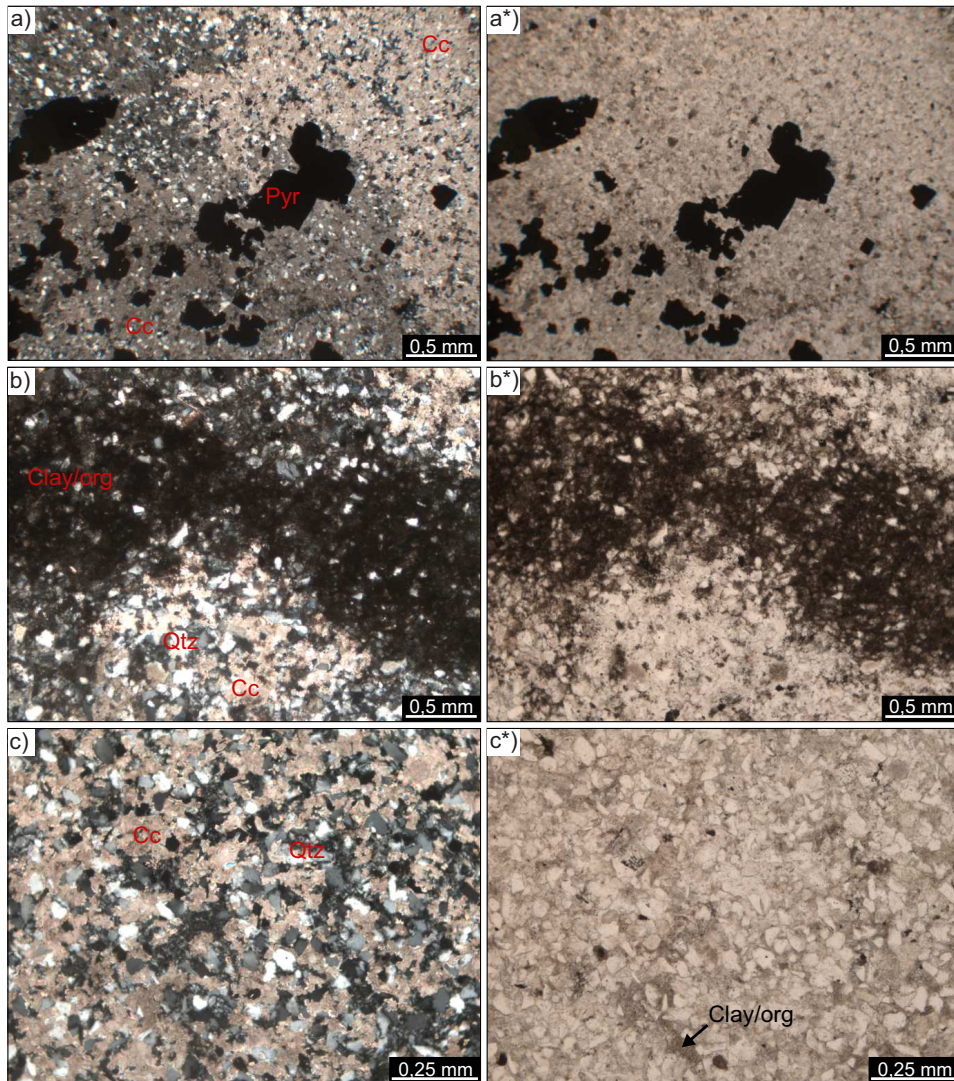
Figure 4.38: DH4. (a, a*) Calcite-cemented sandstone with pyrite overgrowth, sample MF_2015_27. (b, b*) Clay-rich lamina within calcite-cemented sandstone, sample MF_2015_21. (c, c*) Calcite cemented sandstone, sample MF_2015_28. Qtz = quartz, Cc = calcite, Pyr = pyrite, Clay/org = clay and organic material. Images on the left are in cross polarized light, while images on the right (*) are in plane polarized light.

Porosity and permeability

The blue epoxy, which the thin sections were stained with to show porosity, did only percolate through the outer rim (maximum 1 mm) of the thin sections, indicating low permeability. Several fractures are filled with calcite (Fig. 4.36, iiii).

SEM micrographs of a contact-proximal (MF_2015_28) and a contact-distal (MF_2015_21) thin section from DH4 are displayed in Fig. 4.39. Their respective visible porosities are displayed below the backscatter images, and estimated to be 0,33% for the contact-distal micrograph, and 0,26% for the contact-proximal micrograph. Both micrographs have low porosities, however the porosity for the contact-proximal sample is slightly lower than for the contact-distal sample. Observations of the 28 thin sections infer that the estimated porosities are representable for the host rocks in the investigated section (at 942-958 m depth).
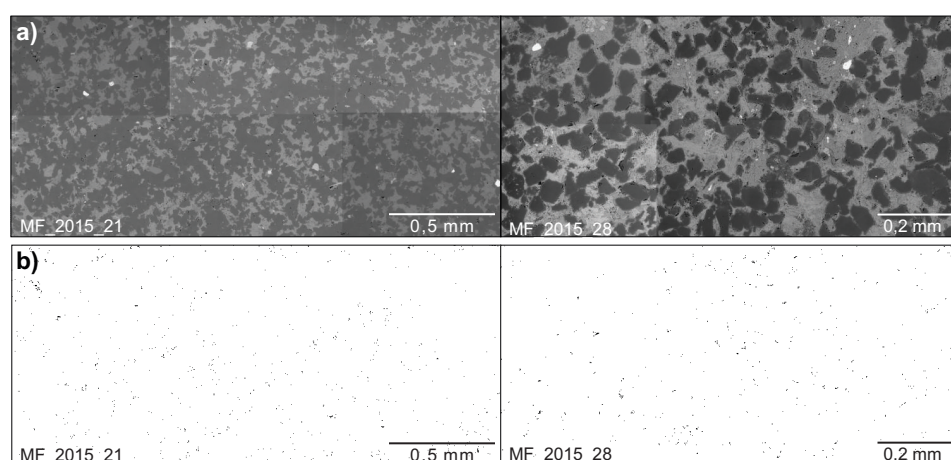
Figure 4.39: (a) Backscatter images of the host rocks of the DH4 intrusion. Upper: sample MF_2015_21 (2.13 m from upper contact). Lower:sample MF_2015_28 (0.07 m from lower contact). (b) Threshold images that illustrate visible porosity of the images in (a).

4.3 Geochemistry and petrography of dolerite intrusions

4.3.1 Field descriptions

The dolerites in the field have a brown weathering surface. Hand samples from the center of the intrusions are generally dark gray to black, and consist of plagioclase and clinopyroxene, with a grain size varying from fine to medium. Exceptions among the investigated intrusions is the Botneheia dyke and a Hatten valley sill (zone "A_2", Fig. 4.16). Both these intrusions have multiple amygdales (up to 1,5 cm in diameter) with white mineral infill and a brown rim. The Hatten valley sill has a color similar to the color of the sandstone.

4.3.2 Petrography

Table 4.13 lists the doleritic samples from the field and from DH4. The studied dolerites are mostly fine to medium grained with a plagioclase crystal diameter up to 5 mm. The texture varies between porphyritic and ophitic.

The 20 cm thick intrusion at Hatten valley has a porphyritic texture (Figs. 4.42a, a*), comprising plagioclase phenocrysts (diameter up to 3,5 mm) altered by white micas (seritization), primarily surrounded by a matrix of fine-grained material. Porphyritic texture is also present at the margin of the DH4 sill. The center of the 25 m thick Studentdalen dyke east and the 8 m thick Rotundafjellet dyke show ophitic texture (Figs. 4.40).

Visible primary minerals (Fig. 4.40) comprise clinopyroxene (up to 40%) plagioclase (up to 40%), oxides (up to 10%) and locally present olivine (up to 7%). Some orthopyroxene (up to 5%) is also present.

Table 4.13: Dolerite samples from the field and the DH4 cores, and their respective thin sections. Fm = Formation.

Thin section ID	Sample ID	Locality	Locality abbreviation	Zone name (if interpreted)	Sample represents	Intrusion thickness (m)	Lithology	Host rock	Sampled date	Sampled by
MF_2015_01	MF_2015_1	DH4	DH4		Sill, central part	1,28	Dolerite	De Geerdalen Fm.	Dec., 2015	MF
MF_2015_24	MF_2015_24	DH4	DH4		Sill, margina	1,28	Dolerite	De Geerdalen Fm.	Dec., 2015	MF
MF_2016_01	MF_2016_1	Hatten valley	Hv	"A_1"	Sill, central part	0,2	Dolerite	De Geerdalen Fm.	Aug., 2016	MF
MF_2016_02	MF_2016_2	Hatten valley	Hv	"A_2"	Sill, central part	2	Dolerite	De Geerdalen Fm.	Aug., 2016	MF
MF_2016_05	MF_2016_5	Rotundafjellet	R_a	"A"	Dyke, marginal part	8	Dolerite	Vikinghøgda Fm.	Aug., 2016	MF
MF_2016_07	MF_2016_7	Studentdalen W	Sd_w	"A"	Dyke, marginal part	1	Dolerite	Kapp Starostin Fm.	Aug., 2016	MF
MF_2016_08	MF_2016_8	Studentdalen E	Sd_e	"A"	Dyke, marginal part	25	Dolerite	Kapp Starostin Fm.	Aug., 2016	MF
MF_2016_12	MF_2016_12	Beach c	Bc	"A_2"	Sill, central part	2	Dolerite	De Geerdalen Fm.	Aug., 2016	MF
MF_2016_15	MF_2016_15	Grønsteinfjellet	Gf_c	"A"	Sill, central part	1,8	Dolerite	Botneheia Fm.	Aug., 2016	MF
MF_2016_16	MF_2016_16	Botneheia dyke	B		Dyke, margin	2	Dolerite	De Geerdalen Fm.	Apr., 2016	MF
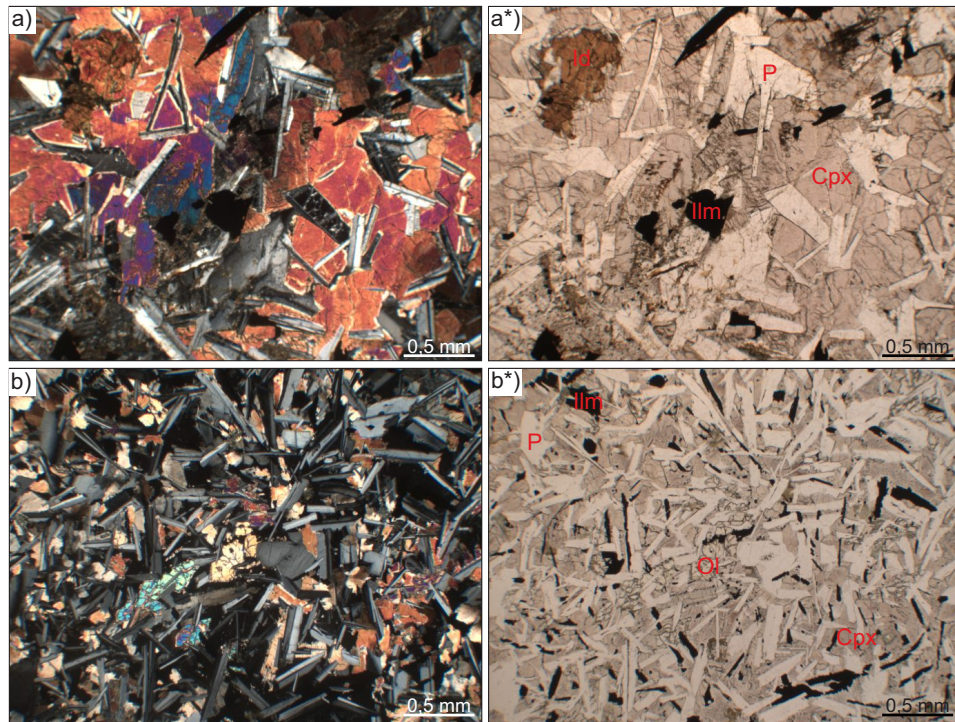
Figure 4.40: Dolerite texture. (a) Ophitic texture, sample MF_2016_08. Primary minerals comprise plagioclase (P), clinopyroxene (Cpx), and ilmenite (Ilm), while iddingsite (Id) is a pseudomorph. (b) Ophitic texture, sample MF_2016_05. Primary minerals comprise plagioclase and olivine (Ol), clinopyroxene and ilmenite. Images on the left are in cross polarized light, while images on the right (*) are in plane polarized light.

Phenocrysts are mainly represented by plagioclase (Figs. 4.42a, a*, 4.40b, b*). Generally, the plagioclase phenocrysts are enclosed in clinopyroxene, with varying amounts of smaller plagioclase crystals, oxides and some olivine.

Several thin sections are dominated by secondary minerals, reflecting later alteration processes. These secondary minerals primarily comprise white micas (Figs. 4.42a, a*) and stilpnomelane (Figs. 4.42c, c*, d, d*). Iddingsite is present (up to 7%, Figs. 4.40a, a*) in the central part of the Studentdalen dyke east. In addition, alteration minerals such as calcite, prehnite and quartz are observed. Amygdales are frequently occurring in the samples (up to 1.5 cm in diameter, Fig. 4.41). These are filled with secondary stilpnomelane, calcite, prehnite and quartz. Prehnite and quartz are only identified within these amygdales, while quartz also is present in a vein (Figs. 4.42b, b*). Stilpnomelane is frequently occurring as fine grained material between plagioclase phenocrysts (Fig. 4.42d, d*), but does also occur as larger crystals (Fig. 4.42c, c*). The white micas and the iddingsite are pseudomorphs after respectively plagioclase and olivine.
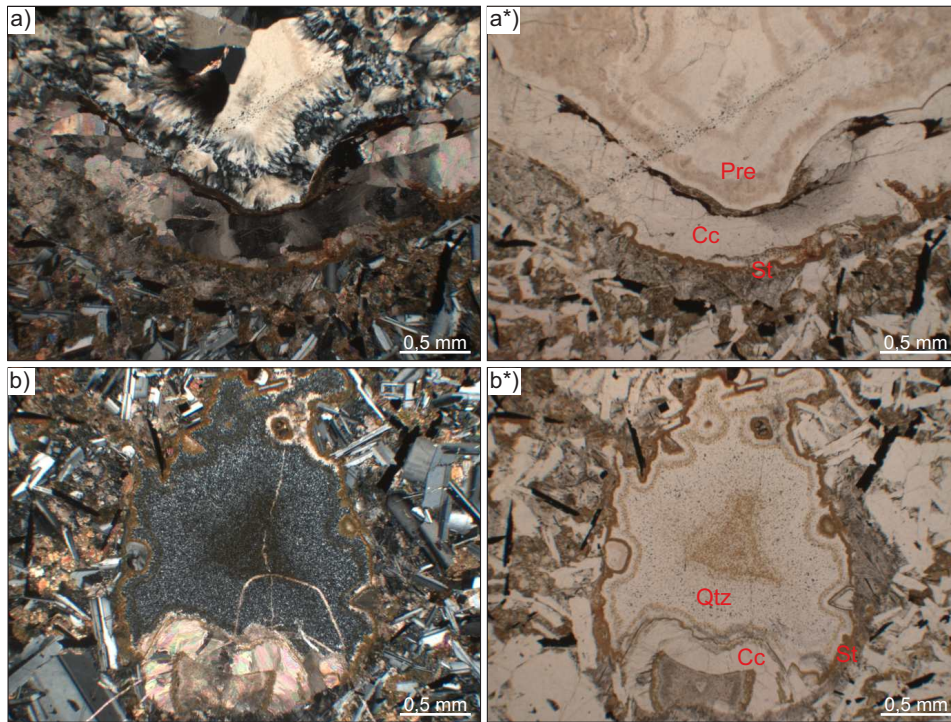
Figure 4.41: Amygdales, sample MF_2016_16, filled with (a and a*) stilpnomelane (St, on the rim), calcite (Cc) and prehnite (Pre), (b and b*) stilpnomelane (on the rim), calcite and quartz (qtz). Images on the left are in cross polarized light, while images on the right (*) are in plane polarized light.

The grain size of plagioclase varies from very fine grained to 4 mm (Fig. 4.42a, a*). The plagioclase phenocrysts (including sericite alterations) have an euhedral shape, while fine grained plagioclase is anhedral and needle-shaped (Fig. 4.42a, a*). Visible clinopyroxene grains vary in size from very fine grained (porphyritic, Fig. 4.42d, d*) to large and surround the plagioclase, Fig. 4.40a). Their shape is primarily anhedral. The oxides were analyzed with an EDS, indicating a mineralogy dominated by ilmenite. These crystals are anhedral and seemingly occupy the space between the plagioclase and clinopyroxene (Fig. 4.40b, b*). Olivine is represented by crystal sizes between 0.5 and 2 mm and is anhedral.

The euhedral shape of plagioclase phenocrysts in the samples from the center of thicker intrusions (Fig. 4.40a, a*) indicates that these crystallized first. As clinopyroxene is surrounding the plagioclase, forming an ophitic texture, these are thought to be crystallized secondly. Olivine and ilmenite are anhedral, occupying spaces between plagioclase and clinopyroxene, and is therefore inferred to be the final minerals to crystallize.
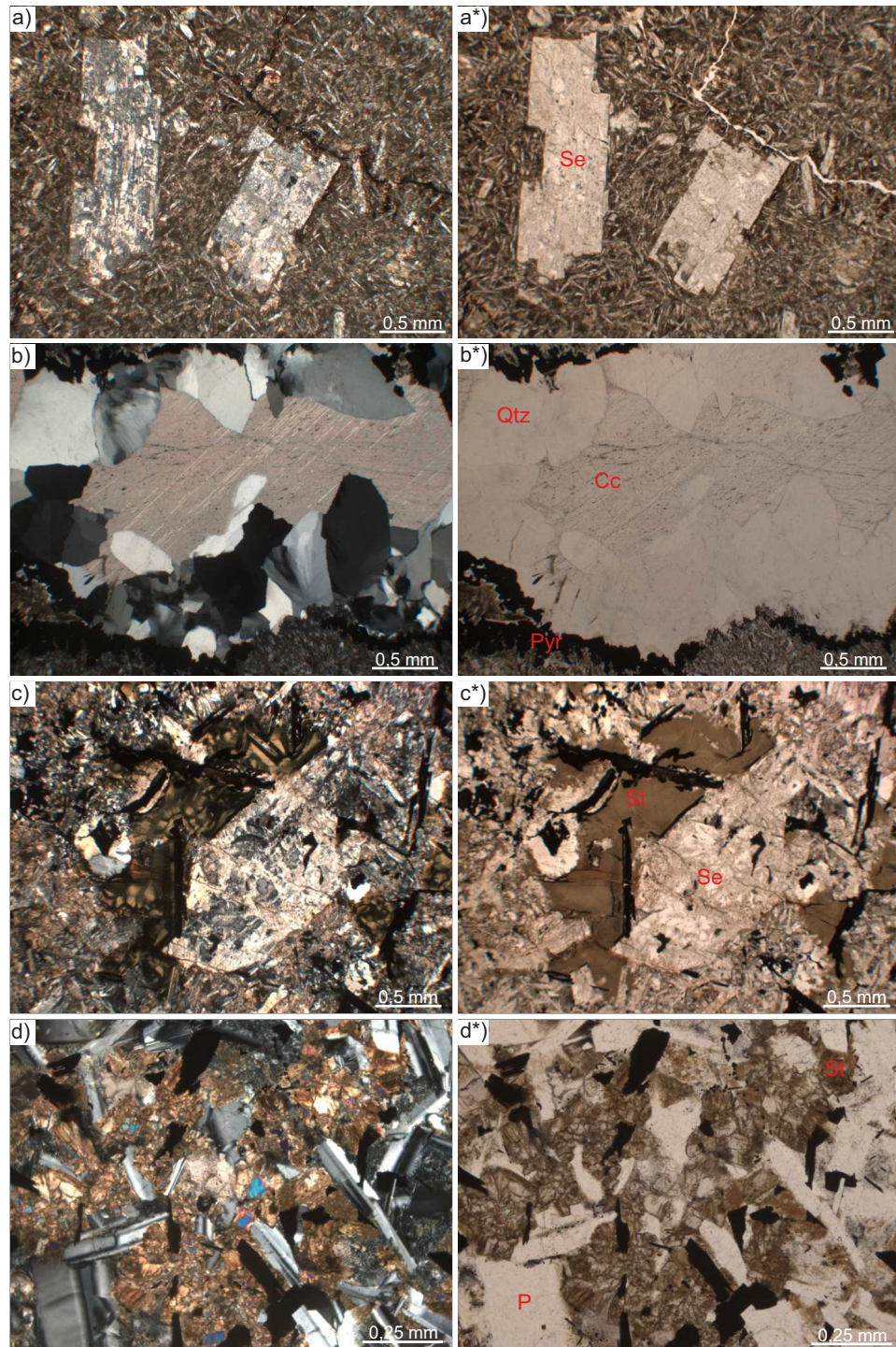
Figure 4.42: Dolerite petrography. (a, a*) Porphyritic texture, sample MF_2016_1.
Sericite (Se) overgrowth of plagioclase (P) phenocrysts in a fine grained
matrix. (b and b*) Sample MF_2015_24, vein consisting of pyrite (Pyr),
calcite (Cc) and quartz (Qtz). (c and c*) Sample MF_2016_15, alteration
minerals comprising stilpnomelane (St) and sericite. (d and d*) Sample
MF_2016_16, plagioclase phenocrysts in a fine grained matrix mostly con-
sisting of stilpnomelane. Images on the left are in cross polarized light,
while images on the right (*) are in plane polarized light.

The most altered samples are represented by MF_2015_24, MF_2016_1, MF_2016_2, MF_2016_16, while the least altered samples comprise MF_2015_1, MF_5016_5 and MF_2016_8. The three latter are plotted in a gabbro tetrahedron from Yoder & Tilley (1962) in Fig. 4.43, where they are classified as olivine- and quartz tholeiites.

Comparing fresh surfaces of hand samples of the two studied sills at Hatten valley, the sample from the 20 cm thick intrusion is brown, with plagioclase phenocrysts. The sample from the 2 m intrusion is gray and has an aphantic texture. The 20 cm thick intrusion has a porphyritic texture (Figs. 4.42a, a*), with plagioclase phenocrysts (diameter up to 3,5 mm) overgrown with white micas (seritization). The phenocrysts are surrounded by a matrix of brown, fine grained material, possibly stilpnomelane. In contrast, the center of the 2 m thick sill at Hatten valley has an aphantic, intergranular texture, no plagioclase overgrowth, with several small quartz-filled amygdales (up to 0.3 mm in diameter) present.

Figs. 4.42b, b* illustrate the mineralogy of the vein shown in Fig. 4.36, iii. This vein consists of calcite, quartz and pyrite, which all except quartz are common authigenic minerals in the shale proximal to the intrusion in DH4 (Section 4.2.2).
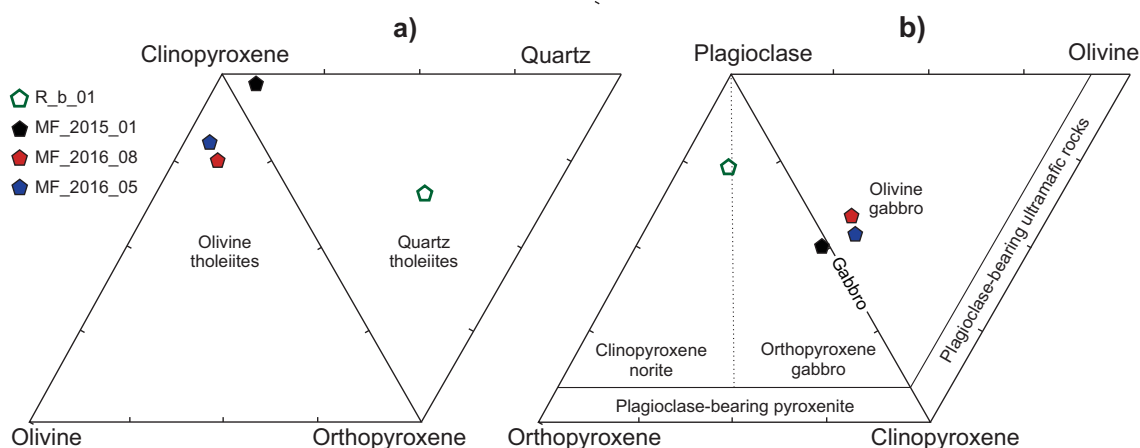
Figure 4.43: Gabbro tetrahedron classification. Diagram from Yoder & Tilley (1962).

4.3.3 Whole rocks geochemistry

Major elements

The Botneheia dyke (B_01, intrusion margin) and the Rotundafellet sill (R_b_01, intrusion center) have respective SiO_2 contents of 44 and 49.27 wt%, Al_2O_3 of 12.81 and 13.11 wt%, FeO · of 13.19 and 13.26 wt%, CaO of 10.46 and 9.58 wt%, MgO of 5.36 and 6.17 wt%, TiO_2 of 3 wt%, Na_2O of 1.92 and 2.31 wt%, P_2O_5 of 0.32 wt%, MnO of 0.18 and 0.21 wt% and K_2O of 0.15 and 0.77 wt% Table (4.14).

Table 4.14: Major (wt%) concentrations of samples from Botneheia sill and Rotundafjellet dyke.

Sample	SiO2	TiO2	Al2O3	FeO*	MnO	MgO	CaO	Na2O	K2O	P2O5	Sum
				Major elements (wt%)							
B_01	44,00	3,00	12,81	13,19	0,18	5,36	10,46	1,92	0,15	0,32	91,39
R_b_01	49,27	3,00	13,11	13,26	0,21	6,17	9,58	2,31	0,77	0,31	97,99

The sum of major elements in the Botneheia and Rotundafjellet sample is 91.39 wt% and 97.99 wt%, respectively. The sum from Botneheia is very low, and as the sample is not ignited (Section 3.3), the low sum may be the result of both volatiles released during preparation of the sample for XRF analysis, and water content in the sample (e.g., Lechler & Desilets, 1987). In contrast, the sum from Rotundafjellet is close to 100 wt%. As described in section 4.3.2, the margin of the Botneheia dyke is highly altered, with amygdales frequently occurring. The analyzed Rotundafjellet sample had in hand sample no signs of alterations. Therefore, the low sum of the Botneheia sample is likely related to the content of alteration minerals (Tugrul & Gürpinar, 1997).

Whole rock compositions of the two samples are plotted in the total alkali versus silica (TAS) classification diagram (Fig. 4.45). The Rotundafjellet sample is classified as a basalt, however, the Botneheia sample is according to the classification a picrite. This is likely due to strong alteration of the rock, as picrite is defined as a basalt with MgO > 12 wt% (Le Bas, 2000).

The Mg number (Equation 3.3.1, Chapter 3) for R_b_01 is calculated to be 45.35, meaning that the olivine is mostly represented by fayalite. The value is lower than the critical value of 68,8 (Roeder & Emslie, 1970), that represents the least magnesian melt that can coexist with mantle olivine. This implies that the sill at Rotundafjellet did not crystallize from a primary melt, but has been fractionated. The Mg number for B_01 is 42.01. This low value illustrates the low MgO content and supports the explanation of a highly altered sample originating from a non-picritic composition

CIPW norms (Section 3.3) were calculated for both samples, and the values for R_a_01 (as B_01 is heavily altered) are plotted in a $(Na_2O + K_2O)$ - FeO^* - MgO diagram (AFM, Fig. 4.44) and in a gabbro tetrahedron classification (Fig. 4.43). The AFM diagram indicates that the rock is a tholeiite, while in the gabbro tetrahedron diagram, the rock is classified as a gabbronorite quartz tholeiite.
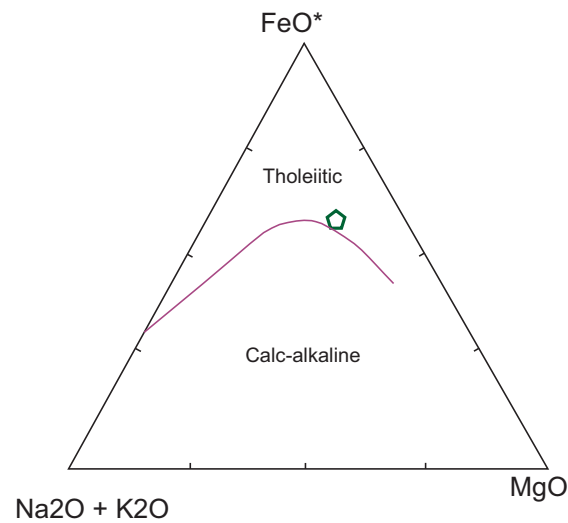
Figure 4.44: R_a_01 plotted in a $(Na_2O + K_2O)$ - FeO^* - MgO (AFM) diagram used to differentiate thoeliitic rocks from calc-alkaline rocks, separated by the solid line. Diagram and solid line criteria from Irvine & Baragar (1971).
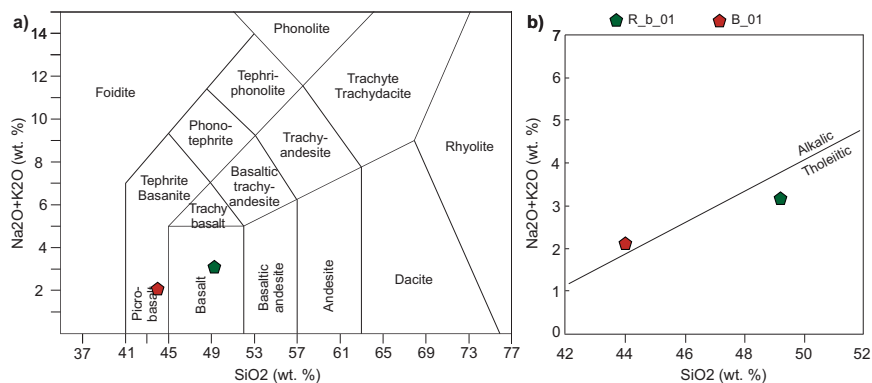
Figure 4.45: Total alkali versus silica (TAS) diagram. Normative composition of magmatic rocks. (a) Diagram after Le Bas et al. (1986), dividing line in (b) from Le Maitre et al. (1989).

Trace elements

Results from trace element analyses are limited both in number of samples and number of elements analyzed. Therefore, trace elements from the two samples are listed and plotted in a primitive mantle normalized trace element diagram in Appendix A.

4.4 Linkage of observations from different localities

4.4.1 Virtual outcrops

The virtual outcrops are generally correctly placed with respect to orientation, while the dip of the outcrops at some localities is slightly off (with up to 20°) perpendicular to the outcrop orientation compared to the field data.

4.4.2 Zone interpretations

Host rocks consisting of sandstones are characterized by a slightly darker gray color proximal to the contact than distal to the contact (the Rotundafjellet dyke). Host rocks consisting of black shales are characterized by a bleached zone proximal to the contact (the Grønsteinfjellet dyke, Fig. 4.22a, and the DH4 intrusion, Fig. 3.3).

Sills tend to appear layered, making the separation between individual sills and thereby their possible zonation challenging.

The weathering surface of Grønsteinfjellet dyke is dark brown proximal to the contact and light brown in the center (Fig. 4.22a). However, these color changes are not observed in other intrusions in this study.

For the Studentdalen dyke east, the dark rocks present on each side of the central dolerite are primarily interpreted as contact-proximal dolerites (zone "B") as their lithology differs from the surrounding carbonates.

4.4.3   Structural analyses

Intrusion geometry

4 of the 6 investigated dykes are striking N-S (Fig. 4.46). Two exceptions include the Botneheia dyke and the Studentdalen dyke west, which are striking WNW-ESE and NE-SW, respectively. The investigated sills are layer-parallel to transgressive, where the sills at Beach c (Fig. 4.10a) and Hatten valley (Fig. 4.15) are locally rising towards W, while the sill at Wallenbergfjellet is rising towards SW (Fig. 4.35).

Fracture orientation

Zone "A" of the studied sills is dominated by two to three contact-perpendicular (vertical) fracture sets (Fig. 4.46). In addition, one set is aligned parallel to the intrusion contact. These planes are often out of range in the field and therefore not measured (e.g. the Wallenbergfjellet sill).

Zone "A" of the studied dykes have a similar fracture pattern as the sills, dominated by two to three vertical fracture sets (Fig. 4.46). In relation to the intrusion geometry, one of the sets is contact-parallel, while one set is contact-perpendicular. The best example of a dyke that has two vertical sets is the Grønsteinfjellet dyke (photo in Fig. 4.24a). The only dyke with three vertical fracture sets is the Studentdalen dyke east (Fig. 4.46). This feature is further discussed in Section 5.4.3.

Where rocks locally are interpreted as contact-proximal dolerites (zone "B"), these are primarily dominated by contact-parallel fractures, in addition to minor amounts of contact-perpendicular fractures (Fig. 4.46). The fracture pattern in the western contact-proximal dolerite at the Rotundafjellet differs from the other interpreted contact-proximal dolerites, as none of the main fracture sets are contact-parallel, but rather inclined.

Fractures in the contact-proximal host rocks are overall parallel to the intrusion contacts (Fig. 4.46). This yields also for layer parallel sills, despite that layer-parallel fractures in the host rocks usually are not measured. The Hatten valley and the Beach c sills have several sets that are identified within both the host rocks and the dolerite, in addition to several sets that are only identified in the host rocks. For Grønsteinfjellet sill, different sets are present in the host rocks and the dolerite.
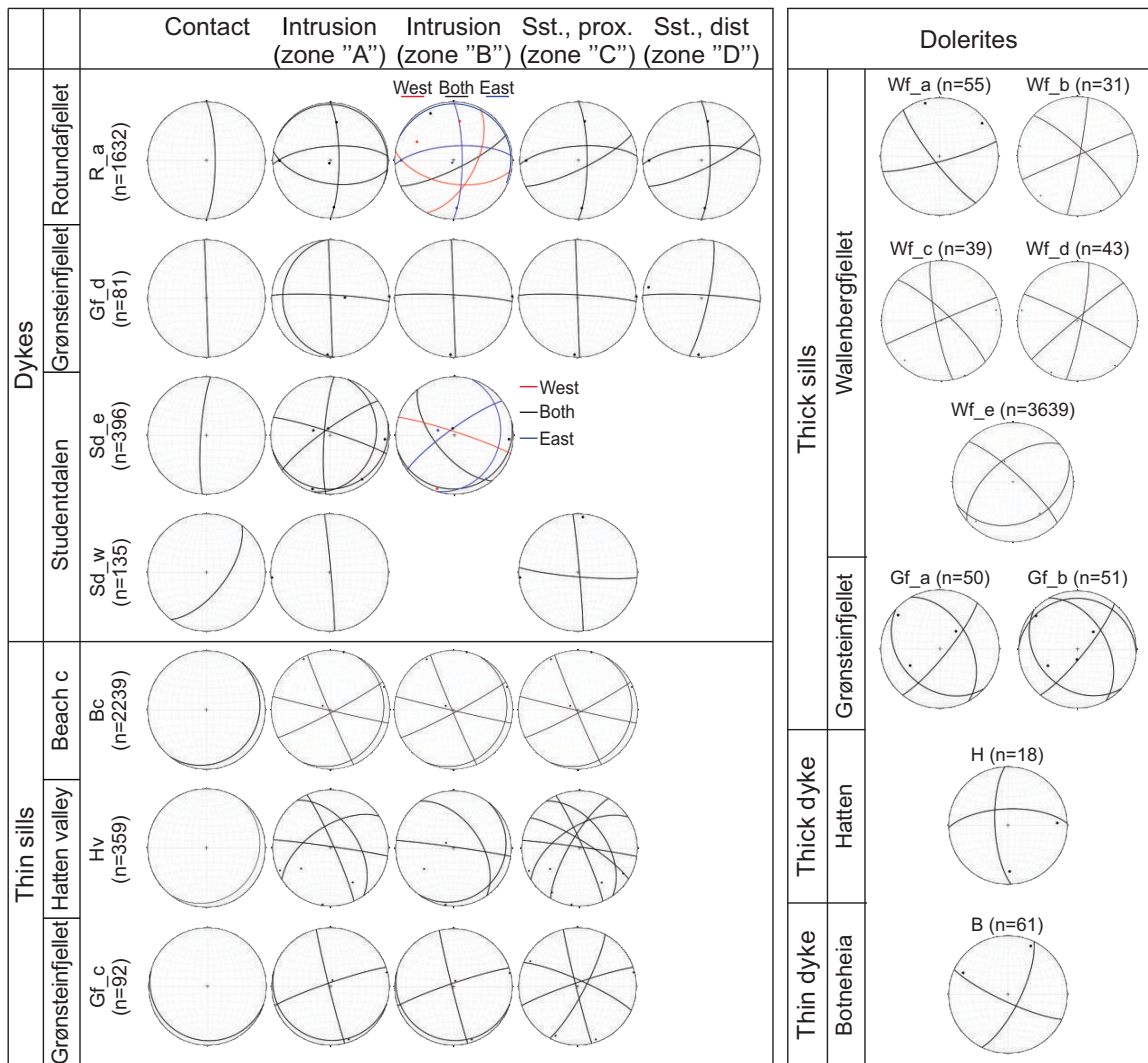
Figure 4.46: Left: Intrusion contact and main fracture sets in the different zones within and around dykes and sills. Right: Main fracture sets in the dolerites. No separation is made between zone "A" and "B" in the dolerites presented on the right.

For Rotundafjellet dyke, where fracture sets are studied extensively up to 30 m from the intrusion contact, the contact-distal host rocks are characterized by the same fracture sets as the contact-proximal host rocks, and are parallel to the intrusion contact (Fig. 4.46).

No obvious trend is observed when comparing the fracture sets in sills and dykes with intrusion thickness (Fig. 4.47). This is further discussed in Section 5.4.
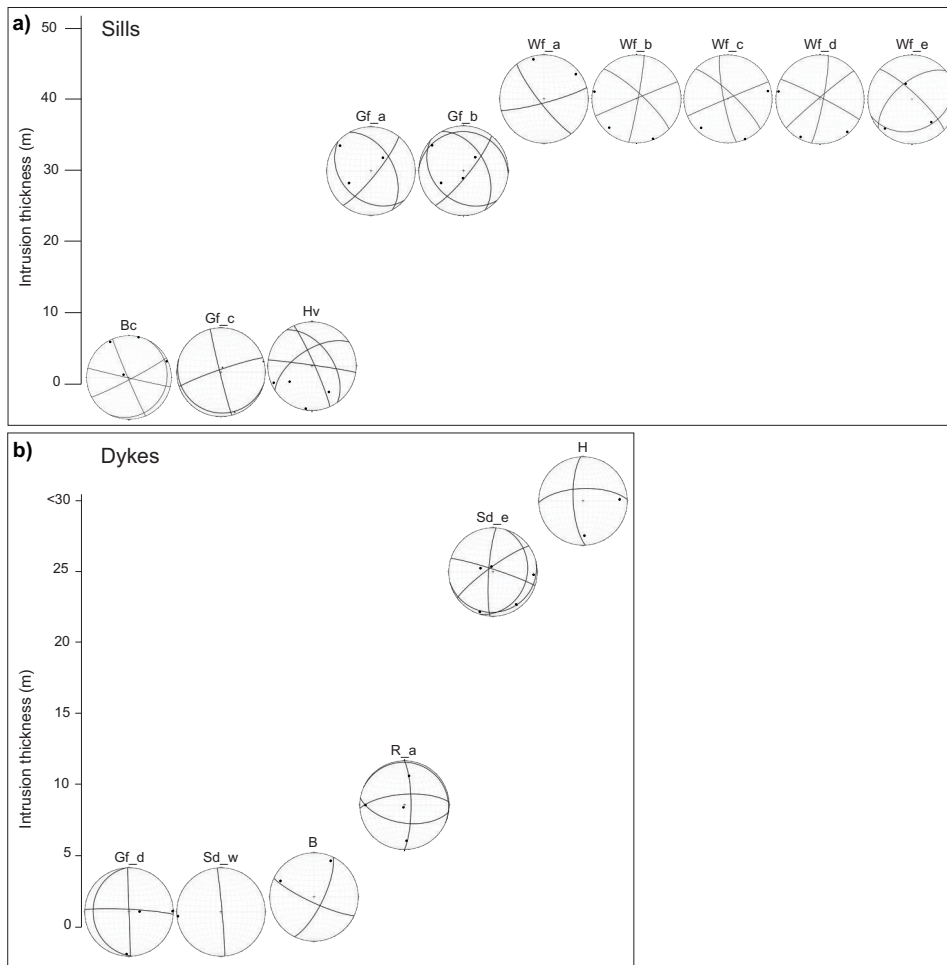
Figure 4.47: Main fracture sets in the central dolerites plotted against intrusion thickness in (a) sills and (b) dykes.

Fracture spacing

Whisker plots of fracture spacing for all analyzed profiles are displayed in Fig. 4.48. The lowest mean spacing is present in the mixed, horizontal profiles (comprising scan lines and virtual profiles) through dykes and their host rocks, where the fractures primarily are vertical. The mean fracture spacing is also low for the mixed, vertical profiles through the sills and the host rocks, where the fractures primarily are oriented parallel to the intrusion contact and the bedding (Hv_v_01-02). The high interquartile range for the scanline through Grønsteinfjellet dyke (Gf_d_01) is mainly a result of the highly fractured area, believed to be fold related.
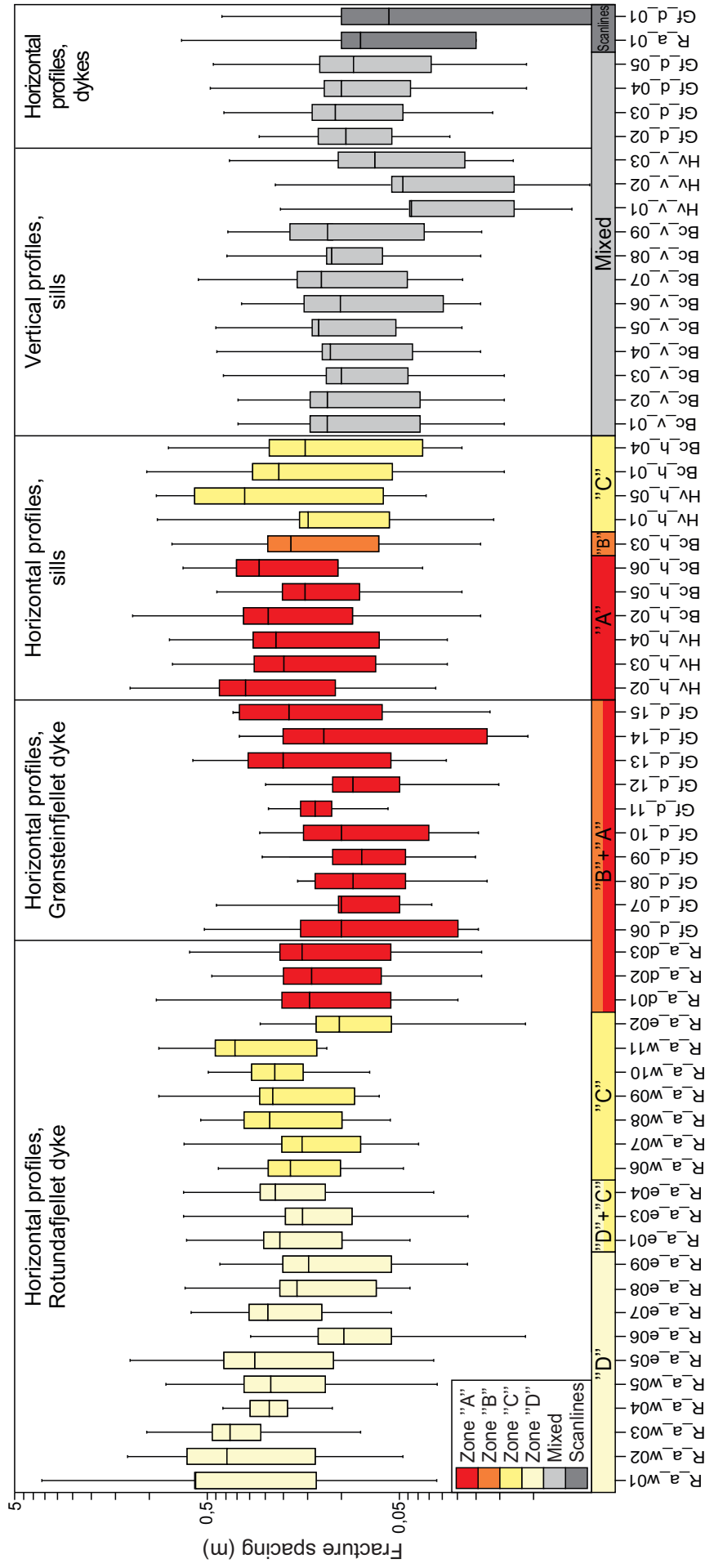
Figure 4.48: Whisker plots (minimum, lower quartile, mean, upper quartile and maximum) of fracture spacing for all profiles and scanlines, subdivided based on intrusion geometry (dyke/sill) and profile direction (horizontal/vertical). In addition, the profiles are sorted by zone, where "D + C" refer to contact-distal and proximal host rocks, and "B + A" refer to central and contact-proximal dolerite, where a profile crosses several zones. For the Rotundafjellet dyke, each profile is plotted with an increased distance to the contact towards left. Zone "A" = central dolerite, "B" = contact-proximal dolerite, "C" = contact-proximal sedimentary rocks, and "D" = contact-distal sedimentary rocks. Poor quality areas are excluded. Note the logarithmic scale.

Horizontal profiles through the sills or their host rocks (Fig. 4.48) indicate similar fracture spacing through the different zones. However, the interquartile range is slightly higher for the contact-proximal sandstones than for the dolerites, indicating that the fracture spacing varies more laterally within the host rocks of sills than within the sills.

The profiles through and around the Rotundafjellet dyke (Fig. 4.48) indicate a generally higher mean fracture spacing for the host rocks than for the dolerites. For the host rocks, the mean fracture spacing decreases slightly from zone "D" to zone "C". This decrease is better illustrated in Fig. 4.49a (left), where the fracture spacing for the host rocks is separated into eastern and western host rock, and the mean fracture spacing for each meter from the contact is plotted against distance to intrusion contact. Fig. 4.49b, (left), show the same plot for the host rocks around the Grønsteinfjellet dyke. This plot illustrates the same trend as for the Rotundafjellet dyke, where the fracture spacing in the host rocks increases with distance to the intrusion contact.

Horizontal profiles through the Grønsteinfjellet dyke (Fig. 4.48) have a varying interquartile range between the profiles. The higher interquartile range values represent a spatial change in fracture spacing (e.g., Gf_d_14). Fig. 4.49b suggests that the high interquartile range for these profiles represents a decrease in fracture spacing in both the dolerite and the host rocks towards the contact. The lower interquartile range values represent a more consistent fracture spacing through the dyke (e.g., Gf_d_11), attributed to a limited resolution of the analyzed photo (Fig. 4.26a).

The fracture spacing in the dolerites is generally higher contact-parallel to the sills than contact-perpendicular to the dykes (Fig. 4.48). Comparing the fracture spacing in the host rocks, no distinct change is observed between the contact-perpendicular profiles of the Rotundafjellet dyke and the contact-parallel profiles of the sills.

For the dolerites, a decrease in fracture spacing towards the contact is present at the Grønsteinfjellet dyke (Fig. 4.49b, right). The best-fit curves correlate well with the data (i.e. high R^2 values). For the Rotundafjellet dyke (Fig. 4.49a, right), the mean fracture spacing versus distance to contact varies between the eastern and the western side. The best-fit curves do not correlate well with the data (i.e. low R^2 values). No obvious trend is observed in this plot.

Mean fracture spacing of all profiles through dolerites is plotted against intrusion thickness in Figs. 4.49c-f, and illustrates the relation between contact-parallel profiles, contact-perpendicular profiles, all horizontal profiles and intrusion thickness. The contact-parallel profiles (Fig. 4.49c, following individual zones), have a consistent mean fracture spacing (between 21.5 and 24 m). The linear best fit for this curve is negative, and indicates a decrease in mean fracture spacing against thickness. However, the curve does not correlate well with the data (low R^2 values). The mean fracture spacing for contact-perpendicular profiles (Fig. 4.49d, that cross cut both sills and dykes), is decreasing with intrusion thickness, illustrated by the linear best fit. Fig. 4.49e illustrates the mean fracture spacing in all horizontal profiles, including dykes and sills, and indicates a similar negative trend as Fig. 4.49d. For all profiles (Fig. 4.49f), including contact-parallel and perpendicular profiles, the trend is also negative.

4.4.4 Petrography, geochemistry and porosity of dolerites and host rocks

The investigated dolerites are classified as olivine- and quartz-thoelittes (excluding the XRF data from the altered sample B_01). Primary minerals comprise mainly clinopyroxene, plagioclase and olivine, however, calculated CIPW norms for R_b_01 also show that the rock contains 10% quartz. The low Mg number of the sample R_b_01 (45.35) indicates that the rock did not crystallize from a primary melt, but has been fractionated.

Most dolerite samples are heavily altered, where white mica and iddingsite are common pseudomorphs after plagioclase and olivine, respectively. Field observations show that calcite is common in and around the intrusions, and is exclusively present at the intrusion/host rock interface and in faults. This is also confirmed by the thin sections, where calcite in addition to other secondary minerals are common in veins, fractures, small cracks and amygdales. Thin sections from the host rocks of the DH4 intrusion also have high amounts of secondary calcite, which occupies all pores, resulting in low porosity (<0.33%) of the host rocks located within 2.13 m from the intrusion contact.
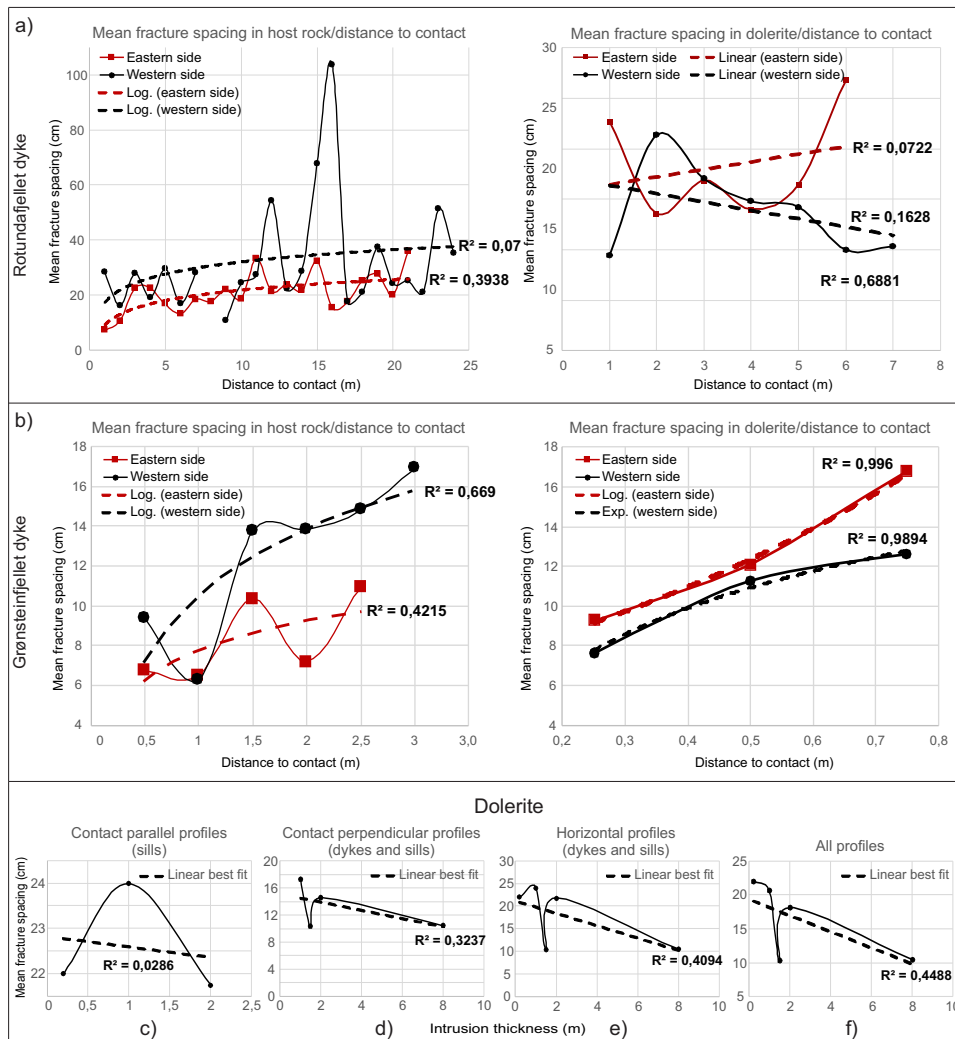
Figure 4.49: (a) and (b) left: Mean fracture spacing in host rocks versus distance to contact. Right: Mean fracture spacing in dolerite versus distance to contact. (c-f) Fracture spacing in dolerite versus intrusion thickness for (c) contact-parallel profiles, (d) contact-perpendicular profiles, (e) horizontal profiles and (e) all profiles. The dotted lines represent best-fit curves, and are provided with R^2 values (i.e. correlation values for the curves with the data). All profiles illustrate the mean fracture spacing of both scanlines and virtual profiles, except from (b) left, where the scan line data is excluded due to the highly fractured area in the eastern contact-proximal host rocks (Fig. 4.24c, d), interpreted to be strongly affected by the local, complex folding. Poor quality areas are excluded. Each sub-figure represent all suitable profiles, however, neither the profiles Hv_v_01-03 nor Gf_d_06-15 are included as these were analyzed after the formation of figure, which was a rather complicated process.

/5

Discussion

This chapter discusses the results presented in Chapter 4. First, digital geology and dolerite petrology are briefly discussed. However, the main body of the chapter focuses on how igneous intrusions affect subsurface fluid flow, including fracture development, contact metamorphic processes and hydrothermal activity. In addition, schematic wireline logs are presented based on the properties of the investigated intrusions and their host rocks, to better be able to identify igneous features in the subsurface.

5.1   Digital geology

In this study, digital geology has enabled assessment of much more data than would have been possible during traditional field work only. Advantages and disadvantages for the use of digital methods are summarized in Table 5.1.

Table 5.1: Advantages and disadvantages for the use of digital methods.

Digital method	Advantages	Disadvantages
Fieldmove Clino	• Can measure strike and dip of planes • Can save digital photos, notes and drawings • Data automatically saved with geographic locations • Data easily imported into 2D map-view and 3D software	• Measured strike not reliable and needs to be corrected with a compass • Digital devices need extra power sources, especially in cold, Arctic conditions
3D modeling by photogrammetry	• Acquiring digital photos is cheap and user friendly • Acquiring digital photos is done in a sparse amount of time, an advantage if one has limited time in the field • Allows for structural analyses • Allows for exporting ortho-rectified images • Allows for studying an outcrop after fieldwork (e.g. using the software LIME)	• 3D modeling software is expensive • Processing time may take days to weeks for each model
Fracture orientation analyses of 3D virtual outcrop models	• Allows for reliable fracture orientation results if the virtual outcrop is correctly oriented • Using the software PlaneDetect, analyses are quick and easy, compared to doing measurements in the field •Allows for measurements of inaccessible parts of outcrops • Gives a strong dataset in combination with measurements from the field	• Results are incorrect if the outcrop is not correctly oriented • Results are dominated by outcrop-parallel measurements
Fracture spacing analyses from ortho-rectified images	• Fracture spacing analyses are time consuming to do in the field • Ortho-rectified images have an uniform scale • Ortho-rectified photos can cover the whole outcrop extent	• Ortho-rectified images have a lower quality than the input-photos, and can easily hide details
Fracture spacing analyses from digital photos	• Fracture spacing analyses are time consuming to do in the field • Fracture spacing analyses from digital photos will have a more correct scale than similar analyses conducted in the field • Digital photos have a higher quality than ortho-rectified images, allowing for detailed analyses	• Digital photos do not have a uniform scale, making areas in the foreground appear larger than they are • Digital photos do only cover a limited part of the outcrop

Using the app Fieldmove Clino (Section 3.1.3, Vaughan et al., 2014), field data, including digital photos, orientation measurements and notes, are automatically saved with geographic coordinates, making the data easily imported into 3D software, such as Google Earth Pro. This is especially useful, as one can correlate

the orientation data with location and topography, and possibly also other digital datasets, such as geological maps, virtual outcrop models and digital elevation models. The app is additionally able to measure plane orientations. However, during this study, strike measurements clearly needed to be controlled with measurements from a compass, both of host rocks and dolerites. This is in fact supported by Novakova & Pavlis (2017), who investigated the precision of smart phones and tablets for measurement of planar orientations, including Fieldmove Clino, and concluded that the magnetic sensors are unacceptably unstable.

Virtual outcrop modeling by the use of photogrammetry (Section 3.2.1, e.g., McGlone et al., 1980; Lillesand et al., 2014) is cheap and user friendly. Acquiring digital photos for virtual outcrop modeling is done in sparse amount of time, an advantage when the time in the field is limited. The processing of the data in Agisoft Photoscan Professional may take several days for each model, dependent on the wanted quality. However, the method provides several opportunities for analyses that otherwise would be time-consuming to do in the field, as described below.

A correctly oriented virtual outcrop model allows for reliable fracture orientation results by the use of algorithms in PlaneDetect (Lato & Vöge, 2012). In this study, fracture analyses of one virtual outcrop (Wf_e) resulted in 3639 fracture orientation measurements, contrasting to the total sum from the field of 928 measurements (Table 4.1). Certainly, the results from the analyses are dominated by outcrop-parallel measurements (i.e. planes with a larger diameter), in contrast to scanlines that will be biased by planes oriented perpendicular to the outcrop orientation, as pointed out by Senger et al. (2015). Together, field work and virtual outcrop analyses give a strong dataset, where the virtual outcrop analyses provide an objective dataset, and field work provides data that always, to some degree, will be subjective.

From what has been experienced during this study, it is clear that fracture spacing analyses based on digital photos always will have a higher quality and will therefore be more precise than similar analyses of secondary ortho-rectified images. However, ortho-rectified images give the opportunity to analyze larger areas with a uniform scale. Dependent on the wanted rate of details to be analyzed, high resolution, close-up, overlapping photos are needed for detailed analyses of fractures. In contrast, digital photogrammetry from distance, e.g. from a boat, will be sufficient for interpretations of large-scale structures, such as igneous intrusion geometries and faults.

A final advantage with digital geology is the possibility to continue the survey of an outcrop also after fieldwork. During this study, several uncertainties regarding the interpretations have been checked by visualizing the virtual

outcrop models in LIME (Buckley et al., 2008), that give an overall better visualization than the digital photos. In addition (as described in Section 3.2) the no-snow cover field season is limited to approximately 2 months, and inaccessibility, weather and polar bears, generally challenges fieldwork in Svalbard. Winter darkness and high logistical costs further limit fieldwork campaigns in time. From the discussion of the advantages and disadvantages of digital geology, the complications regarding field campaigns in Svalbard and my own experience from working with this project, it is clear that a dataset based on fieldwork strongly will benefit from virtual outcrop models.

5.2   Dolerite petrology

In this section, the investigated dolerites are placed into a larger context, addressed through the hypothesis:

- The investigated dolerites belong to the Diabasodden Suite.

Results from the petrographic and geochemical analyses show that the unaltered samples are basaltic gabbro olivine/quartz tholeiites (Figs. 4.43, 4.44, 4.45). One exception is the unaltered sample (R_b_01) that was analyzed by the XRF, which is a basaltic gabbronorite quartz tholeiite. The classification of the rocks, including the TAS diagram in Fig. 5.1, corresponds to similar studies of the Diabasodden Suite (Holmes, 1918; Tyrrell & Sandford, 1933; Dypvik, 1979; Weigand & Testa, 1982; Dahlgren et al., 1992; Bailey & Rasmussen, 1997; Shipilov & Karyakin, 2010; Nejbert et al., 2011) and rocks of the tholeiitic suite of the HALIP (e.g., Ntaflos & Richter, 2003; Estrada & Henjes-Kunst, 2004; Drachev & Saunders, 2006). In addition, the investigated dolerites show the same alteration pattern as dolerites of Svalbard reported by Shipilov & Karyakin (2010) and Nejbert et al. (2011), comprising white micas and iddingsite pseudomorphs, carbonates, and multiple minerals that have in-filled vesicles (amygdales). The limited number of samples that have been analyzed for a restricted number of trace elements (Appendix A) show a pattern that is in good agreement with the results from Bailey & Rasmussen (1997), Shipilov & Karyakin (2010) and Nejbert et al. (2011), reflecting their continental intra-plate setting.

On the basis of the rocks stratigraphic presence within Permian to Jurassic rocks (e.g., Senger et al., 2014a; 2014b), their geographic location (e.g., Senger et al., 2013a), the presence of similar alteration minerals (e.g., Nejbert et al., 2011; Shipilov & Karyakin, 2010) and the limited petrographic and geochemical results, the investigated dolerites are inferred to belong the Diabasodden Suite.

Diabasodden Suite:
✖   Holmes (1918)
▲   Tyrell and Sandford 1933 (n=12)
✚   Dypvik 1979 (n=4)
▼   Weigand and Testa 1982 (n=11)
★   Dahlgren et al., 1990 (n=29)
▶   Bailey and Rasmussen 1997 (n=9)
◆   Shipilov and Karyakin 2010 (n=14)
●   Nejbert el al., 2010 (n=8)

Quaternary Volcanic Complex:
▽   Skjelvåle et al., 1989 (n=9)

Cenozoic Plateau Basalts:
◇   Presvik 1978 (n=15)
▲   Tebenkov and Sirotkin., 1990 (n=4)

Lower Pliocene Submarine Volcanism:
✿   Mørk and Duncan 1993 (n=5)

Pre-Mesozoic Magmatism:
◈   Ohta 1985a (n=20)
▣   Murashov et al., 1983 (n=2)

This study
⬟   R_b_01
⬠   B_01

Figure 5.1: Major element results from this study plotted together with geochemical data from the major magmatic pulses of Svalbard described in the literature (Holmes, 1918; Tyrrell & Sandford, 1933; Prestvik, 1978; Dypvik, 1979; Weigand & Testa, 1982; Murashov et al., 1983; Ohta, 1985; Skjelkvåle et al., 1989; Tebenkov & Sirotkin, 1990; Dahlgren et al., 1992; Bailey & Rasmussen, 1997; Mørk & Duncan, 1993; Shipilov & Karyakin, 2010; Nejbert et al., 2011) in a total alkali versus silica (TAS) diagram after Le Bas et al. (1986). The black line marks the geochemical signature of the Diabasodden Suite, while the dotted lines mark the geochemical signature of the HALIP rocks in Franz Joseph Land, Arctic Canada, North Greenland and De Long Islands. For references on the basis for these lines, see Senger et al. (2014b). Modified from Senger et al. (2014b).

The crystal sizes are generally corresponding well to the sample distance to the contact (i.e. larger crystal sizes towards the center, e.g., Winkler, 1949. This is illustrated by e.g. the ophitic texture in the center of the 8 m thick Rotundafjellet dyke (Fig. 4.40b, b*) and the porphyritic texture of the margin of the DH4 sill. The observations do also correlate with descriptions by Nejbert et al. (2011). However, the dolerites at the Hatten valley locality (Section 4.3.2) differ from this pattern. Here, the sample from the center of the 0.2 m thick sill (zone "A_1", Section 4.1.3) has a porphyritic texture, and is dominated by plagioclase phenocrysts, up to 4 mm in diameter. In comparison, the sample from the center of the 2 m thick sill (zone "A_2") has an aphantic, intergranular texture, where plagioclase crystals are only 0.5 mm in diameter. Both when assuming that the two zones represent two individual sills, or are a part of the same sill, the textures are contrasting to what one would expect. The porphyritic texture of zone "A_1" corresponds with observations by Nejbert et al. (2011) for thin sills or intrusion margins. Nonetheless, one would expect similar sized or larger plagioclase crystals, and larger clinopyroxene crystals in the center of the 2 m thick zone "A_2", due to a generally longer cooling time of thicker sills (Winkler, 1949). In addition, the two samples show different alteration minerals, as described in Section 4.3.2. These observations infer that the two zones are from two different episodes of intrusion emplacement, i.e., represent two stacked sills. Nejbert et al. (2011) reported two different K-Ar dates with a large age span from the margins (115.8 and 117.3 Mya) and the center (78.6 Mya) of the 30 m thick Grønsteinfjellet sill. Nejbert et al. (2011) suggested that the thick sill may represent a group of composite, stacked sills, developed during different episodes of intrusion emplacement, which they based on conclusions by Menand (2008). The study by Nejbert et al. (2011) thereby supports that several magma emplacement episodes might have occurred, and is further discussed in Section 5.4.3.

5.3   Contact metamorphic and hydrothermal processes

In order to facilitate a discussion on contact metamorphic and hydrothermal processes, this section starts with a comparison of sedimentology, porosity and mineralogy between the investigated intrusion-proximal section, and intrusion-distal sedimentary rocks within the Kapp Toscana Group. Secondly, TOC and Rock-Eval data from the investigated section (Senger et al., 2014a) is integrated and discussed, as a supplementary indication on the extent of the contact aureole of the DH4 intrusion. Finally, processes that have contributed to changes in mineralogy, porosity and Rock-Eval data with distance to the intrusion contact are discussed. The section is addressed through the following hypotheses:

- Matrix porosity in the host rocks decreases towards the intrusion contact.

- Porosity and permeability in host rocks are mainly supported by fractures.

5.3.1   Sedimentology

The studied section of DH4 (Fig. 3.3, Chapter 3) comprises black shales with a general increasing amount of laminated sandstone towards the top (Fig. 4.36, Chapter 4). The shales and sandstones reflect hemipelagic sedimentation in a shallow marine environment (Section 4.2).

The increased flux of sand towards the top of the section, indicates a shallowing-up system in an open marine environment, possibly from offshore to offshore transition. The sedimentological descriptions and interpretations of the investigated section correspond with rocks of the lower part of the De Geerdalen formation in the DH4 cores (e.g., Braathen et al., 2012, Senger et al., 2013b and Rød et al., 2014). The rocks described by e.g. Rød et al. (2014) of similar depths of the De Geerdalen Formation comprise mudstones interbedded with hummocky cross stratified sandstone beds, which likely gives a larger perspective on the cross-laminas observed in the 3 cm thick core. Furthermore, the lithological log corresponds to the general description of the lower part of the De Geerdalen Formation (Section 2.1.2).

5.3.2   Porosity

Sandstones tend to have high porosities, often due to the preservation of primary porosity (e.g., O'Brien et al., 1986; Zhang et al., 2016). Measured porosities of the DH4 section(Figs 4.39, 5.4) are 0.33% 2.13 m from the upper contact (MF_2015_21, at 947.09 m depth) and 0.26% 0.07 m from the lower contact (MF_2015_28, 952.07 m depth). The values strongly contrast to porosity data from elsewhere in the Kapp Toscana Group (Fig. 5.3, Farokhpoor et al., 2010; Orchard et al., 2010; Mørk, 2013). Farokhpoor et al. (2010) measured porosities of the Kapp Toscana Group in DH4 using helium porosimetry and brine saturation. Farokhpoor et al. (2010) report a porosity of 5.93% 17.64 m from the lower intrusion contact (at 969.64 m depth). In addition, measured porosities of the De Geerdalen Formation from Farokhpoor et al. (2010) range from 2.31% (at 920.70 m depth) to 16.1% (at 857.50 m depth). Supplementary porosity data of the Kapp Toscana Group by Mørk (2013), carried out using modal analyses, confirm this range in porosities, with an average value of 8 % modal porosity, with the lowest value of 2% porosity (at 718.5 m depth). Porosity data from Orchard et al. (2010) from DH2 (Fig. 3.3a), Adventdalen, obtained using mercury porosimetry, is slightly lower than the data from Farokhpoor

et al. (2010). However, their mean porosity value of the samples from the Kapp Toscana Group is 6,3%. Neither of these three studies calculated porosities in proximity to the investigated intrusion, which is the thickest intrusion cored from the DH4 borehole. Although the lithology slightly changes with depth, and different methods are used in Farokhpoor et al. (2010), Orchard et al. (2010), and Mørk (2013) compared to this study, the decrease in porosity towards the intrusion contact is considerable, as illustrated by Fig. 5.2. A subtle decreasing trend can be observed towards the intrusion in Fig. 5.3. Furthermore, Fig. 5.3 indicates that the thinner intrusions apparently have had have a limited effect on host rock porosity.

5.3.3   Mineralogy

The rocks of the De Geerdalen Formation are classified as arenites, and are considered texturally and mineralogically immature (e.g., Flood et al., 1971; Mork, 1999; Mørk, 2013). Studied thin sections from this study consist primarily of detrital quartz, organic material, and secondary calcite, pyrite and chlorite. In contrast, thin sections from the De Geerdalen Formation described by e.g. Mørk (2013) and Støen (2016) consist additionally of detrital k-feldspar, albite, mica and other lithic fragments, secondary quartz and less abundant secondary calcite and pyrite. Additionally, porosity is visible on the thin section images on a larger scale in these two studies (Fig. 5.2). The causes of the differences in mineralogy and porosity are discussed in Section 5.3.5.

5.3.4   Rock-Eval

TOC and Rock-Eval data from Senger et al. (2014a) from selected shale laminas from the same section of DH4 that is investigated in this study, are plotted in Fig. 5.4. Rock-Eval parameters are used for source rock discrimination in the petroleum industry, and are obtained from pyrolysis (e.g., McCarthy et al., 2011; Selley & Sonnenberg, 2014). The technique involves heating up samples under an inert atmosphere of helium or nitrogen, where detectors measure the release of hydrocarbon gases at progressively higher temperatures. The S1 peak represents free hydrocarbons that are expelled under lower temperatures of pyrolysis. The T_{max} is the temperature at which maximum hydrocarbon generation (S2) occurs, where S2 corresponds to the hydrocarbons that still may be produced if thermal maturation continues. The hydrogen index (HI) is a measure of how much hydrogen which is present, and is derived from the ratio of hydrogen to TOC (McCarthy et al., 2011).

Figure 5.2: Comparison of cementation and porosity of the lower part of the De Geerdalen Formation, (a) adjacent and (b) distal to the intrusion contact. (a) From Sample MF_2015_28, at 952.07 m depth, 0.07 m from the lower intrusion contact. (b) From Mørk (2013), from 901 m depth, 49 m from the upper intrusion contact. Cc = calcite, Qtz_p = primary quartz, Qtz_s = secondary quartz, Clay/org = clay and organic material. Note the dissolution porosity (Di, stained blue with epoxy) in (b) and the lack of porosity in (a), despite the different scale. (a) In crossed polarized light, (b) in plane polarized light.

Figure 5.3: Porosities of the De Geerdalen Formation and the Wilhelmøya Subgroup (W.S.) from DH2 and DH4, compiled from Farokhpoor et al. (2010), Orchard et al., 2010 and this study.

The TOC, the hydrogen index (HI; mg HC/g TOC) and the S2 (mg HC/g dry rock) decrease symmetrically towards the intrusion contacts on either side of the intrusion (Fig. 5.4). In addition, the host rock is bleached on either side of the intrusion. Yet, the background host rock data suggests a high background variability for these parameters (Senger et al., 2014a). The T_{max} data do not show a clear trend towards the intrusion, however, there are predominantly higher T_{max} values within 1 m from the intrusion contact. From 946.2 to 943.5 m there is a decrease in TOC, HI and S2, which Senger et al. (2014a) have attributed to the heterogeneity within the background TOC content.
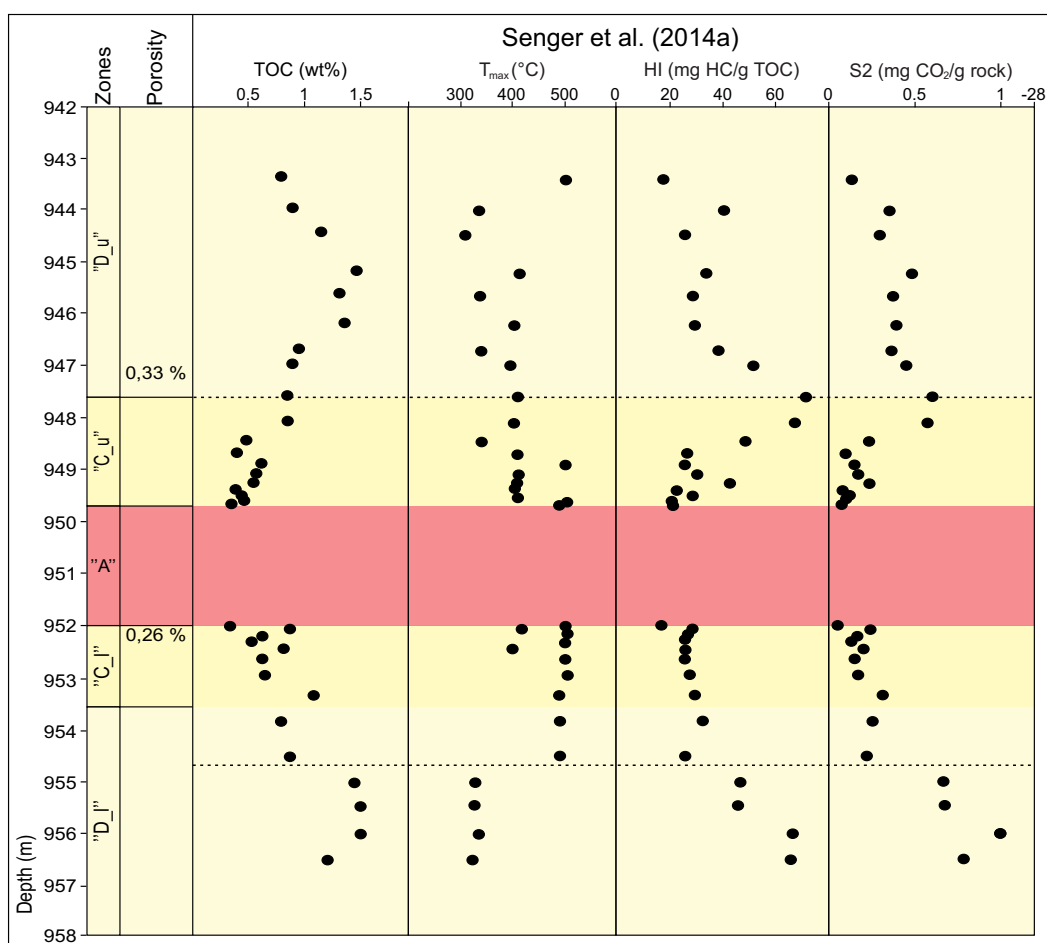
Figure 5.4: DH4. Zone interpretations and results of estimated host rock matrix porosity integrated with total organic carbon (TOC) and Rock-Eval data from Senger et al. (2014a). The stipple line represents the thickness of the metamorphic aureole, defined by their geochemical analyses. Zone "A" = central dolerite, "C_u" and "C_l" = contact proximal sedimentary rocks, "D_u" and "D_l" = contact distal sedimentary rocks, HI = hydrogen index. Refer to text for details.

TOC and Rock-Eval data are also obtained by Koevoets et al. (2016) from the DH2 and the DH5R cores (Adventdalen) of the organic rich Agardhfjellet Formation (from 410-740 m depth, Chapter 2), which stratigraphically overlies the Kapp Toscana Group. For these samples, the T_{max} and the HI are respectively progressively increasing and decreasing with depth. TOC and S2 show overall stable trends. In contrast, the TOC and Rock-Eval data from the deeper, intrusion-proximal section in the De Geerdalen Formation from Senger et al. (2014a) in Fig. 5.4 are obviously changing towards the intrusion contact, both on the upper- and lower side of the intrusion.

5.3.5 Causes of the differences from the contact-proximal to the contact-distal host rocks

The decrease in porosity, TOC, HI, S2 and secondary quartz, and the increase in secondary calcite towards the contacts evidences that the host rock was affected by process related to the emplacement of the igneous intrusion (e.g., Einsele et al., 1980; Wolela, 2002; Aarnes et al., 2010). This is also supported by the DH4 study by Senger et al. (2014a). Furthermore, assuming a similar mineralogical of thin sections in this study and the other mentioned studies of the De Geerdalen Formation, a lack of k-feldspar, albite and mica within the studied section indicates that the sedimentary rocks in proximity to the intrusion have experienced different processes post deposition than rocks of the De Geerdalen formation not in proximity to igneous intrusions.

Common processes related to the interaction between hot intrusions and porous, wet, host rocks include devolatilization and large changes in pore fluid composition, related to alteration of organic material, dissolution of biogenic material and possibly elements introduced during the magmatic activity (e.g., Wolela, 2002; Aarnes et al., 2010; Magee et al., 2013). Furthermore, precipitation of hydrothermal minerals, low-grade metamorphism of preexisting minerals and a reduction in porosities in the intrusion-adjacent host rocks may occur (e.g., Einsele et al., 1980; Wolela, 2002; Magee et al., 2013). Possible processes related to mineralogy changes and a reduction in porosity towards the intrusion contact are discussed below.

Diagenesis is primarily a chemical process controlled by temperature (Bjørlykke, 2015). The lower part of the De Geerdalen Formation, i.e. from 760-970 m depth (unit A in Braathen et al., 2012) is generally strongly influenced by compaction and cementation of quartz, calcite and pyrite, where quartz is the most abundant diagenetic mineral. Assuming a geothermal gradient of 30°C and a maximum burial of more than 3 km, the rocks not affected by the emplacement of igneous intrusions may have experienced temperatures higher than 90°C (Mørk, 2013). The source of silica in unit A has been attributed to dissolution of feldspar and

other labile, silica rich grains, forming dissolution porosity. Dissolution porosity is the main porosity type in unit A (except fracture porosity), and is commonly cemented with clay-minerals, which are suggested to have a positive impact on preserving porosity by limiting quartz cement growth (Mørk, 2013). Comparing the suggested diagenetic processes of unit A with the studied section, the most important differences appear to be the presence of dissolution porosity and the dominance of quartz cementation elsewhere in unit A, which are lacking within the studied section.

First of all, dependent on the rate of lithification and burial of the sedimentary host rock, emplacement of igneous intrusions can spatially be accommodated by surface uplift and/or a decrease in the host rock volume (e.g., Galland & Scheibert, 2013). The latter results in a decrease in porosity in the host rock adjacent to the intrusion as a result of expulsion of pore fluids and fluids related to the alteration of organic matter (e.g., Aarnes et al., 2010 Magee et al., 2013) and possible solution creep from intrusion parallel mineral boundaries to intrusion perpendicular mineral boundaries (Twiss & Moores, 1992). Considering an estimated emplacement depth of 1 km (Senger et al., 2014a), and the sill thickness of 2.28 m, a volume reduction is more plausible. However, compaction of the host rock can not be confirmed from the thin sections in this study, as these are cut in a layer-parallel orientation.

Secondly, cooling of the magma was followed by extensive alteration of labile detrital minerals, such as k-feldspar, plagioclase and micas, and possibly biogenic material. Partly dissolved labile minerals such as k-feldspar and mica are generally observed in unit A (Mørk, 2013), and are seemingly lacking in the studied section. This indicates that, if previously present, labile grains are either fully dissolved and later cemented by calcite, or replaced by calcite. A process which may have contributed to the dissolution of feldspar is an introduction of organic acids or CO_2 from alteration of organic material (Barclay et al., 2000), which is evidenced by Senger et al. (2014a) in Fig. 5.4 to have occurred.

Finally, the most important factor for reducing porosity adjacent to the intrusion appears to be the presence of secondary calcite, which is seen to occupy most spaces between quartz- and clay-minerals and organic matter (Figs. 4.38, 4.39). In addition, calcite is observed in thin and thicker fractures, respectively 0.1 mm (Fig. 4.37) and 0.5 cm (Fig. 4.36iiii) in diameter. Calcite cementation is common at elevated temperatures (Einsele et al., 1980), and the high amounts of calcite adjacent to the intrusion therefore indicate local hydrothermal activity, which is supported by Mørk (2013).

The only higher-temperature mineral observed in the investigated thin sections is chlorite. Chlorite coated quartz grains may prevent quartz overgrowth and may therefore increase preservation of porosity (Bjørlykke & Jahren, 2010). However, chlorite is also present in the matrix, which may be a result of the

transformation of clay minerals (e.g. smectite), that were detrital or formed during dissolution of detrital feldspar. Clay minerals in general are common as pore-filling cement (e.g., Wolela, 2002), and therefore, chlorite can be observed within the calcite cementation. However, chlorite may also have formed as a metasomatic mineral, partly sourced from magnesium and iron ions from the igneous intrusion (Wolela, 2002). Chlorite cement is also observed elsewhere in unit A (Mørk, 2013), and may form in sediments at shallow depths (Bjørlykke & Jahren, 2010). Magnesium-rich chlorites are typical of high temperature metamorphic rocks, while iron-rich chlorites may form as authigenic cement in sediments at shallow depths (Bjørlykke & Jahren, 2010). As chlorite primarily is observed as cement, and the composition of the chlorite observed in this study is not known, the chlorite does not indicate the temperatures of which it was formed.

Precipitation of secondary quartz is primarily controlled by the concentration of SiO_2 in the fluids and the temperature (Simpson et al., 2015). One explanation for the lack of secondary quartz adjacent to the intrusion can therefore be too high temperatures (Simpson et al., 2015). If this was the case, it can have implied that the secondary quartz reported by e.g. Mørk (2013) elsewhere in unit A (if precipitation occurred during and/or after magma cooling), is partly sourced by the silica rich fluids adjacent to the intrusion. This because the concentrations of SiO_2 may have increased due to dissolution of labile, SiO_2 rich grains proximal to the intrusion, and fluids rich in SiO_2 may therefore have been transported away from the intrusion as a result of hydrothermal convection (e.g., Taylor, 1974), and precipitated elsewhere in the De Geerdalen Formation where the temperatures are lower. The theory of precipitation of quartz and calcite elsewhere in unit A during and after magma cooling is in fact supported by Ogata et al. (2012), who investigated fracture systems, including calcite-filled fractures, of the Mesozoic succession in central Spitsbergen. Ogata et al. (2014) observed calcite veins within and around dolerites, and calcite and subordinate quartz veins within and in close proximity to carbonate layers, sandstones and conglomerates.

The general convection of fluids away from intrusions is evident around the Rotundafjellet dyke (Section 4.1.1), where calcite coated planes in the host rocks are observed up to 30 m away from the contact (Section 4.1.1, p. 41). However, the presence of up to 10 cm thick calcite veins along the contacts of dykes (e.g., Fig. 4.5a) does also indicate that fluid flow has been focused along the intrusion contacts of dykes during initial stages of hydrothermal activity. This has also been observed by Einsele et al. (1980) for intrusions in the Guaymas Basin, California. Calcite veins along the contacts of sills are not observed.

Calcite coated fracture planes are also observed within dolerite sills (e.g. Fig. 4.16a) and dykes (e.g., Fig. 4.5b). In addition, the amygdales at the margin of the Botneheia dyke (Fig. 4.41) and the vein at the margin of the sill in DH4 (Figs. 4.36iii, 4.42b, b*), indicate that hydrothermal activity has also occurred after cooling of the intrusions. The vein has a symmetrical texture, comprising, from the rim and inwards, pyrite (FeS_2), quartz (SiO_2) and calcite ($CaCO_3$). The order of these minerals indicates the order of cementation of the different minerals, which likely is caused by a gradual decrease in temperature. Augite ($CaFeSi_2O_6$) is the predominant clinopyroxene of the Diabasodden Suite (e.g., Nejbert et al., 2011). It is therefore possible that the minerals in the vein are a result of a chemical reaction between augite and hydrogen sulfide (H_2S). Hydrogen sulfide can be sourced by either the magma or alteration of organic matter. As alteration of organic matter has been suggested to occur in proximity to the intrusion (Fig. 5.4, Senger et al., 2014a), the latter is more likely.

The source for carbonate and pyrite in the studied section can therefore partly be related to later stages of hydrothermal alteration of the cooled magma, as suggested by Wolela (2002) for the Ulster Basin, UK. However, unit A of the De Geerdalen Formation is characterized by calcite cementation throughout. Cementation is often local in origin (Einsele et al., 1980), and the main source of carbonate in the De Geerdalen Formation has therefore been suggested to be related to high amounts of carbonate grains and bioclastic fragments in the Formation (Mørk et al., 1982). Furthermore, extensive calcite cementation and an absence of quartz cementation is observed in all the investigated thin sections of the host rocks in the DH4 (up to 4.82 m away from the contact), indicating that also the host rocks outside the contact aureole (defined by the dotted lines in Fig. 5.4, Senger et al., 2014a) have suffered from extensive calcite cementation. The higher porosities at 969.64 m (5.93%, 17.64 m from the lower intrusion contact) in Farokhpoor et al. (2010) indicate that a decrease in precipitated calcite (from intrusion-related hydrothermal activity), and an increase in porosity occurs somewhere between 4.82 m (sample MF_2015_23) and 17.64 m (Farokhpoor et al., 2010) from the intrusion contacts, assuming a symmetrical cementation pattern on either side of the sill.

Despite the presence of calcite in and around the intrusions, indicating hydrothermal activity during and possibly after cooling of the magma, calcite cemented faults, cross-cutting dolerites, are observed at the Hatten valley locality (Fig. 4.15). This indicates that the faults, hence the calcite veins, are of a younger origin, and implies that calcite cementation also has occurred after the final cooling, meaning that calcite coated planes within the dolerites also can be a result of later cementation. The major tectonic event Spitsbergen experienced post emplacement of the Diabasodden Suite in Early Cretaceous was the transpression in Paleogene and formation of the WSFB (Chapter 2). According to the burial curve in Fig. 2.9, maximum burial of the De Geerdalen

Formation has been suggested to occur in Late Paleogene, associated with the WSFB and the CTB. It is therefore likely that the faults are related to Paleogene transpression, and that calcite cementation also occurred associated with related burial in Late Paleogene.

Permeabilities of the host rocks adjacent to the intrusion in DH4 are not investigated in this study. However, low percolation rates of blue epoxy (maximum 1 mm of the thin section boundaries) in the investigated thin sections indicate low permeabilities. This observation is supported by the low porosities of the investigated thin sections, where the limited amount of pores appear to be unconnected with each other. In addition, low permeabilities (from no flow to 0.126 md) of the De Geerdalen Formation from the DH4 cores are previously documented by Farokhpoor et al. (2010). Even though several fractures are cemented with calcite, some are not. Porosity, and hence also the permeability, is therefore suggested to be restricted to fractures in the host rocks adjacent to the intrusion, and possibly also elsewhere in the De Geerdalen Formation, which is previously suggested by Ogata et al. (2012).

5.3.6 Extent of contact aureole

A contact aureole is defined by Aarnes et al. (2010) as the intrusion-proximal host rock zone of elevated metamorphism relative to the background level. The extent of a contact aureole is usually expressed as the percentage of the distance from the intrusion margin divided by intrusion thickness (e.g., Aarnes et al., 2010; Senger et al., 2014a). The metamorphic aureole of the DH4 sill is defined by Senger et al. (2014a) to be 4.47 m (195% of the sill thickness), based on geochemical data. In contrast, a 30 m thick sill at Botneheia is shown to have a contact aureole of 100% of the sill thickness, based on geochemical data (Hubred, 2006). Furthermore, experimental modeling of contact aureoles by Aarnes et al. (2010) show that aureole thicknesses can vary from c. 30% to 200%, on the basis of vitrinite reflectance. The extent of the contact aureole is dependent on several parameters, e.g., intrusion thickness, magma temperature host rock temperature and emplacement duration (Aarnes et al., 2010). The contact aureoles of both the DH4 sill and the Botneheia sill therefore fall within the range proposed by Aarnes et al. (2010), however, the large span in contact aureole thickness for the two localities suggest that local differences in the parameters mentioned above have occurred. Another factor that can control the extent of a contact aureole is the rate of burial of the host rocks prior to intrusion emplacement. This is illustrated by Barker & Bone (1995), who investigated contact metamorphism around a 2.2 m thick dyke in the Devonian limestones, and concluded that the limited contact aureole was caused by heating of the host rocks prior to intrusion emplacement. Since both the DH4 sill and the Botneheia sill are located in the lower part of the De

Geerdalen Formation (for burial curve, see Fig. 2.8), this option is excluded. It is therefore suggested that the difference in contact aureole is mostly related to sill thickness and emplacement duration. In addition, as no chilled margin of the DH4 sill is observed, a lack of chilled margins can make heat more effectively conducted through the host rocks, resulting in a thicker contact aureole. This is supported by (Huppert & Sparks, 1988), who experimentally studied heat transfer processes and host rock melting related to intrusion emplacement.

In relation to the DH4 sill, and the fact that extensive calcite cement (i.e. low porosities) is observed 2 m outside the contact aureole, the area of the host rocks that has been affected by the intrusion emplacement has been subdivided into three zones, further explained in Section 5.4.5. This is supported by Haave (2005) for the Karoo Basin, South Africa. Haave (2005) found decreased porosities up to 35 m away from a 15 m thick sill, attributed to hydrothermal activity, which included 15 m of the host rocks outside the contact aureole that was defined based on measured organic parameters.

5.4 Fracturing patterns in and around igneous rocks

This section starts with a brief discussion on the geometries of the intrusions investigated in this study and other mapped intrusions in central Spitsbergen (Senger et al., 2013a), since fracturing related to igneous intrusions is suggested to be highly dependent on the geometry of the igneous feature (e.g., Bermúdez & Delpino, 2008; Hetényi et al., 2012; Senger et al., 2015). The main body of the section is related to mechanisms that can have caused the formation of the fracture sets presented in Sections 4.1 and 4.4. As a summary, the section finishes of with presenting a conceptual model with three scenarios (Figs. 5.7, 5.8, 5.9) on fracturing patterns and rock evolution in and around igneous intrusions in central Spitsbergen. The discussions are addressed through the following hypotheses:

- Fracture patterns related to the intrusion emplacement are highly dependent on the orientation of the intrusion contact.

- Fracture frequency in dolerites increases towards the intrusion contact.

- Fracture frequency in host rocks increases towards the intrusion contact.

- Porosity and permeability are mainly supported by fractures.

In this study, fractures in and around igneous rocks are divided into three major fracture types, (introduced in Chapter 1): emplacement-induced fractures in host rocks, cooling fractures in the igneous intrusions and tectonic fractures in either only the host rocks or in both host rocks and igneous intrusions. The different fracture sets are defined based on the following: Emplacement-induced fractures, forming in the host rock as magma is overpressured when it is emplaced (Lister & Kerr, 1991), are defined as parallel to the intrusion contact, as described by Delaney et al. (1986) and Woodford & Chevallier (2002). Cooling fractures, being only present in the intrusion due to thermal contraction of magma, are defined as contact-perpendicular and contact-parallel (e.g., Bermúdez & Delpino, 2008; Kattenhorn & Schaefer, 2008, Hetényi et al., 2012). Tectonic fractures, including all fractures that are not related to intrusion emplacement, are either only present in the host rocks or present in both host rocks and intrusions, dependent on the timing of tectonic activity. Surfaces with slickensides are clear indicators for the presence of tectonic fractures. However, such surfaces were not studied in detail due to limited time in the field. Therefore, the results are primarily interpreted based on orientation in relation to the intrusion contact, and the zone they are present in (Fig. 5.5).

5.4.1 Intrusion geometries

Most of the investigated dykes are vertical to sub-vertical, oriented N-S, striking parallel to sub-parallel to the BFZ (Chapter 2). Two exceptions include the Botneheia dyke and the Studentdalen dyke west, which are striking WNW-ESE and NE-SW, respectively. The orientation of the Botneheia dyke is evident, as the dyke is well exposed and previously mapped, (Fig. 3.2a for map), and runs along a normal fault dipping towards NNE. However, the orientation of the Studentdalen dyke west may be a source of error, as the contact was buried in scree and therefore challenging to measure.

For the thin sills, the 1.5 m thick Grønsteinfjellet sill is layer parallel over longer distances (165 m), while others show small-scale, transgressive segments rising towards E (at the Hatten valley and the Beach c localities). The thicker sills are previously well mapped, with the Wallenbergfjellet sill transgressing upwards towards SE, and the Rotundafjellet thick sill transgressing upwards towards W. The Grønsteinfjellet thick sill is connected with a complex system of sills and dykes in the Hyperittfossen-Botneheia area (Senger et al., 2013a). The lowest stratigraphic point where this network of dolerites is exposed, is in the middle of De Geerdalen, within unconsolidated marine and glaci-fluvial Quaternary deposits.

The most striking result is that several fracture sets are identified both within the dolerites and within the host rocks, at several localities, reflecting the orientation of intrusions. Therefore, interpreting the fractures has admitably been a challenging task. Rather than creating zones of weakness in order to transgress, it is likely that the dykes have intruded into preexisting weak zones (e.g., Delaney et al., 1986), either aligned with (i.e. the N-S striking dykes), or related to (i.e. the Botneheia dyke) the BFZ. This is in accordance with Senger et al. (2013a), who mapped igneous intrusions in central Isfjorden based on seismic, magnetic, lidar, borehole, topographic and multibeam bathymetric data, and Schiffer et al. (2017), who evaluated potential stress fields in the Arctic. One possibility is that the N-S striking dykes are associated with a giant radiating dyke swarm, centered on a mantle plume at the southern end of the Alpha Ridge (Embry & Osadetz, 1988; Buchan & Ernst, 2006; Jackson et al., 2010; Døssing et al., 2013; Thórarinsson et al., 2015). According to plate tectonic reconstructions in the Arctic by Døssing et al. (2013), the proposed mantle plume was located north of Svalbard in the Early Cretaceous. One of these major dykes is located in the northern Barents Sea, and is suggested to be a result of lateral magma propagation by Minakov et al. (2017). For an illustration of a radiating dyke swarm, see Fig. 6 in Minakov et al. (2017).

Interpreting zonation of thin sills has been difficult in the field, as multiple sills clearly are emplaced above each other (Beach c, Fig. 4.10), and are mostly bedding-parallel. In contrast, dykes are easily identified in the field as they cross-cut sedimentary layers, and therefore serves good opportunities in order to study spatial changes in the host rock with distance to the contacts. In addition, they can have contacts to several sedimentary lithologies, making it possible to study how the intrusion has affected host rocks within different lithologies, both with respect to fracture development and contact-metamorphism. An example is the Rotundafjellet dyke (Fig. 4.3) that contacts both shale and sandstone beds. Therefore, the zonation one otherwise can observe around dykes, can easily be misinterpreted around sills. This is especially the case for fine-grained sills that show no evidence of mineral crystals (i.e. a magmatic origin in this specific tectonic setting), and can easily be confused with red, contact-metamorphosed sandstone beds, such as at the Hatten valley locality (Fig. 4.16). The zonation interpretations of the Hatten valley outcrop are discussed in Section 5.4.3.

5.4.2   Emplacement-induced fractures

Magma propagation will theoretically cause the formation of emplacement-induced fractures related to host rock deformation (Delaney & Pollard, 1981; Delaney et al., 1986; Mériaux et al., 1999; Kattenhorn & Schaefer, 2008), which in turn will lead to enhanced fracturing in the host rock in vicinity to the

intrusion. The large-scale end member scenario of host rock deformation is the formation of forced folds, i.e. folds where the final overall shape and trend are dominated by the shape of a forcing member below (Stearns, 1978), such as a laccolith or a sill (Jackson & Pollard, 1990; Hansen & Cartwright, 2006). In addition, folds may occur in the host rock proximal to dykes (e.g., Grasemann & Stüwe, 2001). The emplacement of large intrusions may even force surface deformation, as modeled by e.g. Abdelmalak et al. (2012) and Galland & Scheibert (2013). Emplacement-induced fractures in the host rock of dykes and sills are discussed below.

Dykes
Generally, the host rocks are observed to be folded in proximity to the dykes (e.g. Figs. 4.3a, 4.25a, b). Measured fractures in the host rocks of dykes are, both proximal and distal to the intrusion contact, predominantly oriented either parallel to the intrusion contact or parallel to the outcrop orientation (Fig. 5.5). However, this is not the case for Studentdalen dyke west. Here, fractures in the host rock, up to 38 m away from the intrusion contact, are vertical and parallel to fractures measured in the dyke, but not parallel to the measured contact. As the fractures in the dyke are neither parallel nor perpendicular to the intrusion contact, this indicates either that the dyke is massive (i.e. a lack of cooling fractures), and characterized by tectonic fractures, or that the measured contact is a source of error. The dyke is not previously mapped.

This study has documented an enhanced fracturing in the host rock in proximity to igneous dykes (Figs. 4.48 and 4.49a, b), best illustrated by the host rocks on the eastern side of the Rotundafjellet dyke (Fig. 4.49a, left). Enhanced fracturing in proximity to dykes is also present around the Grønsteinfjellet dyke (Fig. 4.25), however, the horizontal extent of the profiles is limited (up to 3.5 m on each side of the dyke). These results are in good agreement with Delaney et al. (1986), who studied emplacement-induced fractures around dykes. An enhanced fracturing in proximity to the dykes, and similar fracture orientations within the proximal and distal host rocks, strengthen the theory of which the dykes in central Spitsbergen were emplaced within preexisting weak zones.
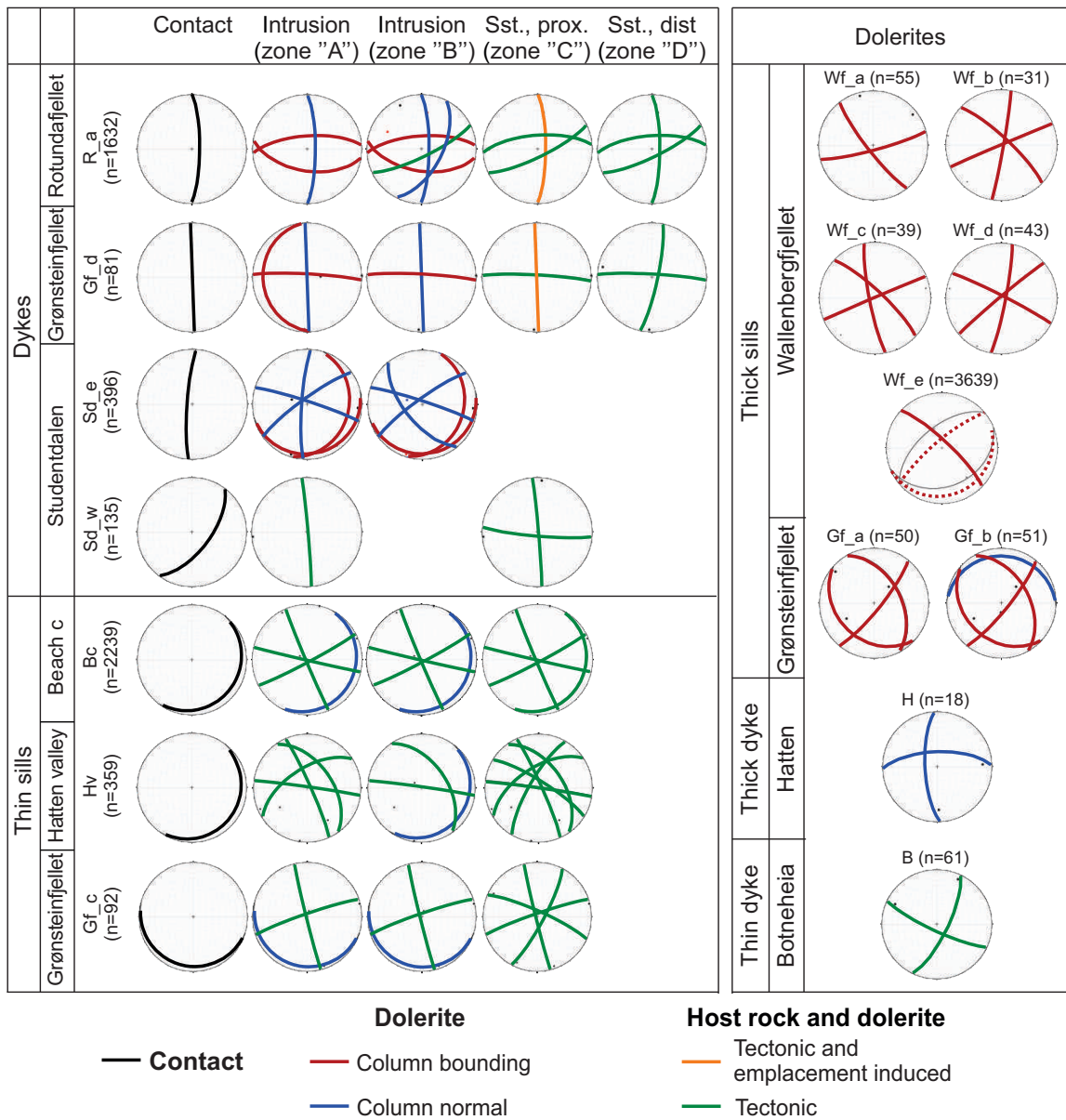
Figure 5.5: Interpretation of the fracture sets displayed in Fig. 4.46. The fractures are divided into column-bounding, column-normal, emplacement-induced and tectonic. The dotted lines represent fracture sets where corrections have been applied due to tilting of the analyzed virtual outcrop.

Sills

Two of the host rock zones measured in this study are sandwiched between a complex network of sills (at the Beach c and Hatten valley localities, Sections 4.1.2 and 4.1.3). This has apparently caused rather complex fracture patterns

within these zones. Data on changes in fracture frequency and orientation with distance to intrusion contact of sills is restricted due to a limited vertical extent of the outcrops. Not least, if the emplacement of sills forms contact-parallel fractures in host rock (Delaney et al., 1986), these fractures will be parallel to fractures along the bedding planes in the sedimentary host rock.

Horizontal fracture profiles of contact-proximal sandstones from the De Geerdalen Formation in this study show that the average horizontal fracture frequencies are in the range of 3.2 f/m to 6,3 f/m (bedding thicknesses range from 0.6->2 m, Table 4.2). The values are similar to values from the the Kapp Toscana Group reported by Wærum (2011, sandstones from similar stratigraphic levels, bedding thickness unknown) and Ogata et al. (2012, 0.4-3 m thick silt- and sandstone beds), where the fracture frequencies range from 1.1 f/m to 6.1 f/m and 3 f/m to 8 f/m, respectively. This indicates that emplacement of sills have not contributed to the formation of fractures in the host rock that are nonparallel to the sill contact.

Vertical fracture frequency plots from the Beach c locality show that the presence of contact-parallel fractures is enhanced within the contact-proximal sandstones (zone "C_1" and "C_2", Fig. 4.13). For the Hatten valley locality, contact-parallel fracturing is evident in the profiles in Fig. 4.21 in the upper shales and sandstones (zone "C_1"), but not in the intrusion-sandwiched sandstone layer (zone "C_2, Fig. 4.16). Based on (the limited number of) fracture frequency profiles and observations, it appears unlikely that emplacement of thin (<2 m) sills do induce intrusion-parallel fractures, neither in fine-, nor coarse-grained sedimentary host rocks. This because the layer-parallel fractures within fine-grained rocks can be fabric-related (Grasemann et al., 1999) and a result of loading and uplift, as similar fractures are observed at e.g. the Rotundafjellet and Grønsteinfjellet localities (Figs. 4.3a, 4.22a) in intrusion-distal host rocks.

5.4.3   Cooling fractures

Fractures related to cooling will clearly be controlled by intrusion geometry and thickness (Senger et al., 2015), as cooling occurs from the cooler host rock interface and propagates inwards (Hetényi et al., 2012). Additionally, the orientation of cooling fractures in sills has been suggested to be related to the regional paleostress during cooling (Maher et al., 2016).

Dykes
Cooling fractures within the investigated dykes are primarily equally dominated by contact-parallel and contact-perpendicular fractures, best illustrated by the Grønsteinfjellet dyke (Fig. 4.24a). The dyke is characterized by two

vertical fracture sets and one horizontal fracture set (Fig. 4.24a). According to Kattenhorn & Schaefer (2008), column bounding (i.e. contact perpendicular) fractures would form first, and would be bounded by column-normal (i.e. contact parallel) fractures that subdivide columns perpendicular to their lengths. The orientations of the cooling fractures within the dolerites in the present study are therefore in good agreement with e.g. Kattenhorn & Schaefer (2008), Bermúdez & Delpino (2008), Hetényi et al. (2012) and Witte et al. (2012), who investigated jointing in igneous intrusions and lava flows. However, results from the Studentdalen dyke east (Fig. 4.31a) contrast with this pattern, and is discussed below.

The Studentdalen dyke east is characterized by three vertical fracture sets (Fig. 4.46), forming a hexagonal pattern, with only one plane (representing the top surface) that is contact perpendicular. The fractures correspond well with cooling fractures described in e.g. Spry (1962) and Hetényi et al. (2012). The dominance of vertical fractures (and columns, see Fig. 4.31a) indicates that cooling has occurred in a vertical direction. The vertical fractures seem to form a radial pattern, as described by Bermúdez & Delpino (2008) for sills, however, the radial pattern is oriented perpendicular to what one would expect for a dyke. Vertical fractures, independent on geometry, were early described by Fuller (1938) for lava flows in Oregon, USA. Fuller (1938) suggested that joints being independent on intrusion geometry may be a result of the escape of volatiles once the margin has cooled. However, no vesicles are observed along the vertical joints, excluding this explanation. The remnants of the dyke indicate a round to rectangular shape in map-view (see Appendix C), and the dyke is noncontinuous landward. In addition, magnetic anomalies in Senger et al. (2013a) do not indicate that the dyke continues seaward. The best explanation would therefore be that what has until now been interpreted as a dyke, is a thick, noncontinuous sill, that represents the top of a dyke, which has been restricted from further vertical and horizontal movement, and therefore has been cooled in a vertical direction. This is also supported by the fracture patterns in the feature being similar to the fracture patterns present in e.g. the Wallenbergfjellet sill (Fig. 5.5). The feature remains poorly understood to the author.

The fractures within the Botneheia dyke are discussed in Section 5.4.4.

The investigated dykes show no sign of entablature fractures (Kattenhorn & Schaefer, 2008) or cavity zones (Bermúdez & Delpino, 2008; Delpino & Bermúdez, 2009; Witte et al., 2012), which are fractures and vesicles respectively, representing the final portion of magma and lava to cool (Kattenhorn & Schaefer, 2008; Witte et al., 2012). However, entablature fractures are suggested to be common in the center of dykes, as described by e.g. Senger et al. (2013a) for the Karoo Basin, South Africa.

This study has documented that fracture spacing within dykes decreases towards the intrusion contacts, best illustrated by the Grønsteinfjellet dyke (Figs. 4.26, 4.49b, right). For the Rotundafjellet dyke, the fracture spacing in the dolerite is variable (Fig. 4.49a, right), however, enhanced fracturing in the contact-proximal dolerites can be observed in Fig. 4.5b. Despite this, no distinct chilled margins are observed at the margins of the investigated dykes. This is possibly be a result of the remelting of chilled margins due to sufficient internal heat and a prolonged magma flow of dykes (Huppert & Sparks, 1989).

Sills

Cooling fractures within the investigated, thicker sills (>30 m thick) are primarily dominated by three contact-perpendicular fracture sets and one contact-parallel fracture set (Fig. 4.46). For thinner sills (<2 m thick), fracture sets present within the dolerites are also present within the host rocks. The thin sills are therefore interpreted as massive, with a lack of cooling fractures, which in deed is the case for the upper sill at the Beach c locality (zone "A_1", Fig. 4.10). Massive sills are previously described by e.g. Park & Ripley (1999) for Precambrian, basaltic sills in Minnesota, USA. The other investigates sills, including the lower Beach c sill (zone "A_2"), the Grønsteinfjellet sill and the Hatten valley sills, seem to have some degree of columnar jointing in the outcrop photos in Figs. 4.10, 4.27, 4.17c. However, the structural data indicate that the sills are dominated by the same fracture sets as their host rocks. Woodford & Chevallier (2002) documented fractures in the intrusion-proximal host rock being contact-perpendicular and contact-parallel to the intrusion contact. Woodford & Chevallier (2002) interpreted these as cooling joints in the dolerite extending into the host rock. However, Woodford & Chevallier (2002) also described that reactivation faulting had occurred along the strike of the fault, and it is therefore also possible that these fractures are a result of tectonic activity. In fact, the fracture sets within the Hatten valley dolerites are also present regionally (Wærum, 2011; Ogata et al., 2014; Senger et al., 2016a; Schaaf et al., 2017), and are therefore interpreted as tectonic, even though they may look like cooling joints (Fig. 4.16a).

As mentioned in Section 5.4.1, zonation of outcrops with sills, especially where multiple sills form a complex system, is a source of error. Contact proximal dolerites are in this study present at all the visited localities with thin sills, as thinner zones dominated by intrusion-parallel fractures. These are interpreted as chilled margins (e.g., Huppert & Sparks, 1988; Huppert & Sparks, 1989; Woodford & Chevallier, 2002). A chilled margin is best illustrated by the Beach c sills (Fig. 4.11). The zones at the Hatten valley locality, however, show a rather complex system of sills (Fig. 4.17a, b). Here, the chilled margin is located between two central dolerite zones, where the composition of the central dolerites is confirmed by thin-section observations (Section 4.3.2). Since the

two central dolerites are separated by a chilled margin, this indicates two separate episodes of magma emplacement and cooling. One possibility is that zone "A_2" and "B_1" (Fig. 4.16) are the result of either an older or a younger event than zone "A_1", where zone "B_1" represents the chilled margin with contact-parallel fractures. A thin zone that possibly is a chilled margin, is present below zone "A_2", but is not previously interpreted in this study as a separate zone as it is highly weathered (i.e. a lack of interpretative structures). Zone "A_1" is only 15 cm thick, and therefore the formation of a 10 cm thick chilled margin is less likely. The small crystals in zone "A_1" (Section 5.2) also supports this theory of two separate events. Another possibility is that what has been interpreted as individual sills (zone "A_1" and "A_2"), are from one event, where zone "B_1" represents an entablature zone (e.g., Kattenhorn & Schaefer, 2008). This is less likely, as a entablature zone would rather form in the lower part of the sill, as one would expect an enhanced cooling from the top (DeGraff & Aydin, 1987; Grossenbacher & McDuffie, 1995). Furthermore, an entablature zone would form a complex system of fractures (Kattenhorn & Schaefer, 2008), and not contact-parallel fractures as are observed in this zone. Therefore, I argue that the two sills are from two different episodes of intrusion emplacement, evidenced by a chilled margin, i.e. an internal contact between the two sills. This is also supported by Huppert & Sparks (1989), who concluded that chilled margins of sills will be preserved and continue to grow at the floor, but can partly or fully remelt in the roof due to higher convection, forming an internal contact represented by a chilled margin.

In addition, zones "A_3" and "C_2" at the Hatten valley locality have been interpreted as dolerite and sandstone, respectively (Fig. 4.16), despite their similar appearance on the photo. The differentiation between these zones is based on the observations of mineral crystals in zone "A_3", and zone "A_3" is therefore interpreted as a highly altered dolerite. However, it cannot be excluded that both these zones are of a sedimentary origin, as the colors of zone "A_3" clearly show more similarities to the colors of the underlying sandstone zone "C_2" than the overlying dolerite zone "A_2". The outcrop remains poorly understood to the author, and a more detailed study of the locality is needed to resolve these questions.

At the Beach c locality, there are indicators for entablature fractures, dividing the sill into two halves (Fig. 4.10): An upper and a lower part of the sill, comprising 40 % and 60 % of the sill thickness, respectively. The entablature zone was not interpreted as an individual zone in the field, however, the zone has similar characteristics as described by Kattenhorn & Schaefer (2008), such as a complex fracture pattern. This entablature zone is located slightly closer to the top than the bottom of the sill, opposite of what one would expect (DeGraff & Aydin, 1987; Grossenbacher & McDuffie, 1995), and is continuous along strike of the sill across the whole outcrop. However, the dolerites present

on either side of the zone have similar characteristics (e.g. color and a lack of cooling joints), suggesting that they are part of the same sill, separated by an entablature zone nearly at the center.

The present study has documented enhanced fracturing within the chilled margins compared to within the central dolerites of the sills in three high-resolution, close-up profiles (Hv_v_01-03, Fig. 4.21) from the Hatten valley locality. Enhanced fracturing is clearly also present within the chilled margins of the Beach c sills (Fig. 4.11), but it is not well documented in the fracture frequency plots in Fig. 4.13 due to lower resolution of the analyzed photo. The chilled margin here is dominated by approximately three to four intrusion parallel fractures (Fig. 4.11), despite it's thickness of only 10 cm. The presence of chilled margins of the sills, and not of the dykes, correspond to quantitative analyses of chilled margins in igneous rocks by Huppert & Sparks (1989). Huppert & Sparks (1989) concluded that if the magma flow is prolonged and has sufficient internal heat, such as feeding dykes, initially chilled margins can be partly or fully remelted. In contrast, magma flows that are more stagnant will have better preserved chilled margins, which typically is the case for sills, due to lower internal heat (Huppert & Sparks, 1989).

5.4.4   Tectonic fractures

Interpreted tectonic fractures are either present in the intrusions and their host rocks, or only within the host rocks. Overall, 6 fracture sets are interpreted as tectonic, comprising J1-J6 (Fig. 5.6.
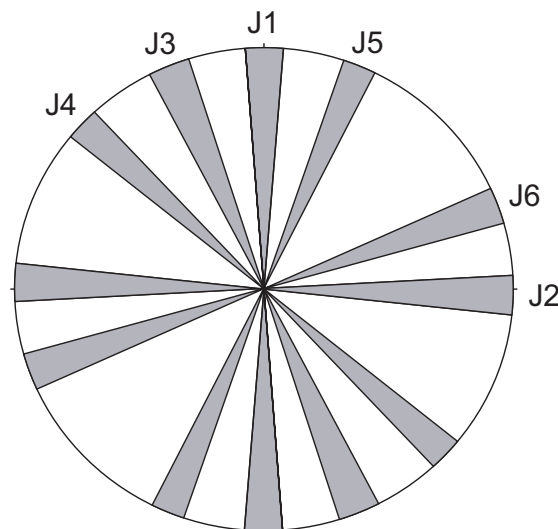
Figure 5.6: Fracture sets present in dolerites and host rock, interpreted as tectonic fractures.

J1 (Fig. 5.6), striking N-S, and J2, striking E-W to ENE-WSW, are present in the the N-S trending dykes and their host rocks. J1 is neither identified in the sills, nor their host rocks, however, J2 is present in the dolerites and the host rocks at most localities. This could indicate that J1 is primarily emplacement induced of N-S striking dykes. However, N-S striking fractures are present in shales of the Agardhfjellet Formation (Schaaf et al., 2017) and in sandstones of the De Geerdalen Formation (Wærum, 2011; Ogata et al., 2014), indicating that this set is present regionally. This means that J1 represents both emplacement induced, column-bounding and tectonic fractures, as best illustrated by the Rotundafjellet and the Grønsteinfjellet dykes (Fig. 5.5). Ogata et al. (2014) pointed out that N-S striking fractures are oriented approximately parallel to the axes of the major folds of the WSFB (Section 2.1.2) in Braathen et al. (1999). J2 is the dominant fracture set the De Geerdalen and the Agardhfjellet Formations (Ogata et al., 2014; Senger et al., 2016a; Schaaf et al., 2017). J2 is also the most abundant fracture set in the present study. The interpretation of J2 as a tectonic set is supported by Ogata et al. (2014), who stated that J2 is present in all litho-structural units of the Mesozoic succession of central Spitsbergen. Ogata et al. (2014) assigned this set to be a product of ENE-WSW transpression, assuming that the main regional joint sets are aligned parallel to the maximum regional horizontal paleostress of the associated WSFB.

J3 (Fig. 5.6), striking NNW-SSE, is present in sills and the host rocks of sills (Fig. 5.5). Regionally, J3 is present in the Agardhfjellet Formation (Schaaf et al., 2017) and in the De Geerdalen Formation (Wærum, 2011; Ogata et al., 2014). J3 may either be a sub-ordinate J1, and/or a shear-fracture set related to clockwise rotation of the horizontal compression from NE-SW to ENE-WSW, as suggested by Ogata et al. (2014).

J4 (Fig. 5.6), striking NW-SE, and J5, striking NNE-SSW, are present in the host rocks of the Hatten valley and the Grønsteinfjellet sills, and within the Botneheia dyke. The Botneheia dyke is oriented along the J4 plane. J4 and J5 are documented elsewhere in the De Geerdalen Formation, the Agardhfjellet Formation and within dolerites (Wærum, 2011; Ogata et al., 2014, Maher et al., 2016). The fractures present within the Botneheia dyke do not form distinct columns in the dyke. The dyke is therefore interpreted as massive dyke characterized by tectonic fractures, with a lack of cooling fractures

J6 (Fig. 5.6), striking ENE-WSW, is present in the sills and their host rocks and within the western contact proximal dolerite and the host rocks of the Rotundafjellet dyke. Regionally, the set is present in the De Geerdalen Formation (Wærum, 2011; Ogata et al., 2014) and in the Agardhfjellet Formation (Ogata et al., 2014). J6 is suggested to represent a sub-ordinate fracture set of the J2 (Ogata et al., 2014).

A lack of cooling fractures within the thin sills (except the upper sill at Beach c, which clearly is massive), should not be completely excluded. Contraction of magma may have caused similar fracture patterns within the host rocks, as described by Woodford & Chevallier (2002). However, as the fractures within these sills also are present regionally, it is possible that cooling fractures within the mentioned dolerites were developed, parallel to sub-parallel to Early Cretaceous (i.e. HALIP-related) tectonic fractures in the host rocks. This is supported by Maher et al. (2016), who investigated fracture patterns within dolerites and the Triassic strata on Edgeøya, Svalbard. Maher et al. (2016) suggested that the interpreted cooling fractures in the dolerites were formed aligned with the regional stress field during the emplacement of the HALIP. Furthermore, Maher et al. (2016) pointed out that the cooling fractures are dominated by E-W, N-S and NNE-SSW striking fracture sets, and inferred these to represent a counterclockwise rotation of the maximum stress field from N-S to NNE-SSW. Since these sets (J1, J2 and J5, Fig. 5.6) also are present within the investigated dolerite and host rocks, it is possible that the fractures originated in the Early Cretaceous, either during or after cooling of the magma.

On Edgeøya, NW-SE striking faults in the Triassic strata are interpreted as being of a syn-sedimentary origin (Maher et al., 2016). The normal fault at the Rotundafjellet locality (Fig. 4.6a) may have such an origin.

In summary, tectonic fractures are striking NW-SE to NNE-SSW, and ENE-WSW to E-W. The N-S (J1), NNE-SSW (J5) and E-W (J2) striking fracture sets are inferred to have formed during and/or after magma emplacement, related to to maximum horizontal N-S to NNE-SSW stress field in the Early Cretaceous (Maher et al., 2016), and were reactivated during transpression in the Paleogene (Ogata et al., 2014). The NW-SE (J4), the NNW-SSE (J3) and the ENE-WSW (J6) fracture sets are suggested to have originated during ENE-SSE transpression in the Paleogene, and may have partly been reactivated as shear-fractures during clockwise rotation of the horizontal compression from NE-SW to ENE-WSW in the Paleogene (Ogata et al., 2014).

5.4.5   Conceptual model

Based on the interpretations of the obtained dataset and the presented state-of-the-art, a conceptual time-transgressive model for rock evolution and fracture development in and around igneous rocks within the Triassic-Jurassic strata in central Spitsbergen is presented. The model includes three different scenarios, including a thin sill (Fig. 5.7), a thick sill (Fig. 5.8) and a dyke (Fig. 5.9). The models assume symmetric cooling of the magma, i.e. a symmetric fracture pattern on each side of the intrusion center. Nevertheless, the fracture pattern will locally depend on several parameters, e.g. magma temperature, host rock

temperature, intrusion geometry, emplacement duration, cooling time, host rock porosity and permeability and the presence of fluids. Based on the processes and structures related to intrusion emplacement as described above, the rocks are divided into five zones (illustrated in Fig. 5.9c), comprising, from the inner part of the intrusion and outwards, a highly fractured entablature zone (zone "1A"), cooling joints parallel and perpendicular to the intrusion contact (zone "1B"), a highly fractured chilled margin (zone "1C"), a highly fractured and baked margin of the host rock (zone "2A") and the unaffected host rock (zone "2B").

The model is improved upon earlier models from e.g. Ogata et al. (2014) for central Spitsbergen and Senger et al. (2015) for the Karoo Basin, South Africa, and contains details from several authors (e.g., Gill (2010), Pollard (1973), Kattenhorn & Schaefer (2008) and Delaney et al. (1986)). The fractures are simplified into three groups dependent on the intrusion-related processes, including emplacement-induced fractures, cooling fractures and fractures that are not related to the intrusion emplacement, as in Senger et al. (2015). In contrast to Senger et al. (2015), the presented model in this study is time-transgressive, and therefore better illustrates when the different processes occur. In contrast to Ogata et al. (2014), the present model illustrates a more detailed fracture development related to intrusion emplacement, as well as it indicates spatial changes in the host rocks, as a result of contact metamorphic and hydrothermal processes, that can be observed in host rock shales in the field. In contrast to the models in Senger et al. (2015) and Ogata et al. (2014), it illustrates zonation that only can be identified in a microscope, i.e. how zone "2A" (contact-proximal host rocks) in principle can be divided into three partly overlapping sub-zones (illustrated in Fig. 5.9c, as a result of three intrusion related processes. These sub-zones comprise the host rock that (1) has been fractured due to the overpressured magma (sub-zone "2A1", e.g., Lister & Kerr, 1991; Delaney et al., 1986), (2) has been metamorphosed during heat conduction (zone "2A2", e.g., Barker & Bone, 1995), and (3) has been hydrothermally altered due to fluid convection away from the intrusion (zone "2A3", Fig. 5.9c, e.g., Einsele et al., 1980; Wolela, 2002). As illustrated in Fig. 5.9c), zone "2A1" is limited to a narrow area proximal to the intrusion, zone "2A2" covers a distance of approximately 100% of the intrusion thickness, and is partly overlapping zone "2A1", while zone "2A3" covers at a minimum 350% of the intrusion thickness away from the intrusion, and is partly overlapping both zones "2A1" and "2A2". Zone "2B" is defined to start where zone "2A3" ends, and is therefore not included in the model.

In addition, the present model indicates how vertical fracture sets present in the intrusions also are present in the sandstones in central Spitsbergen. However, in contrast to the model in Ogata et al. (2014), where vertical fractures in the host rock are not included, despite their presence in their results. The model
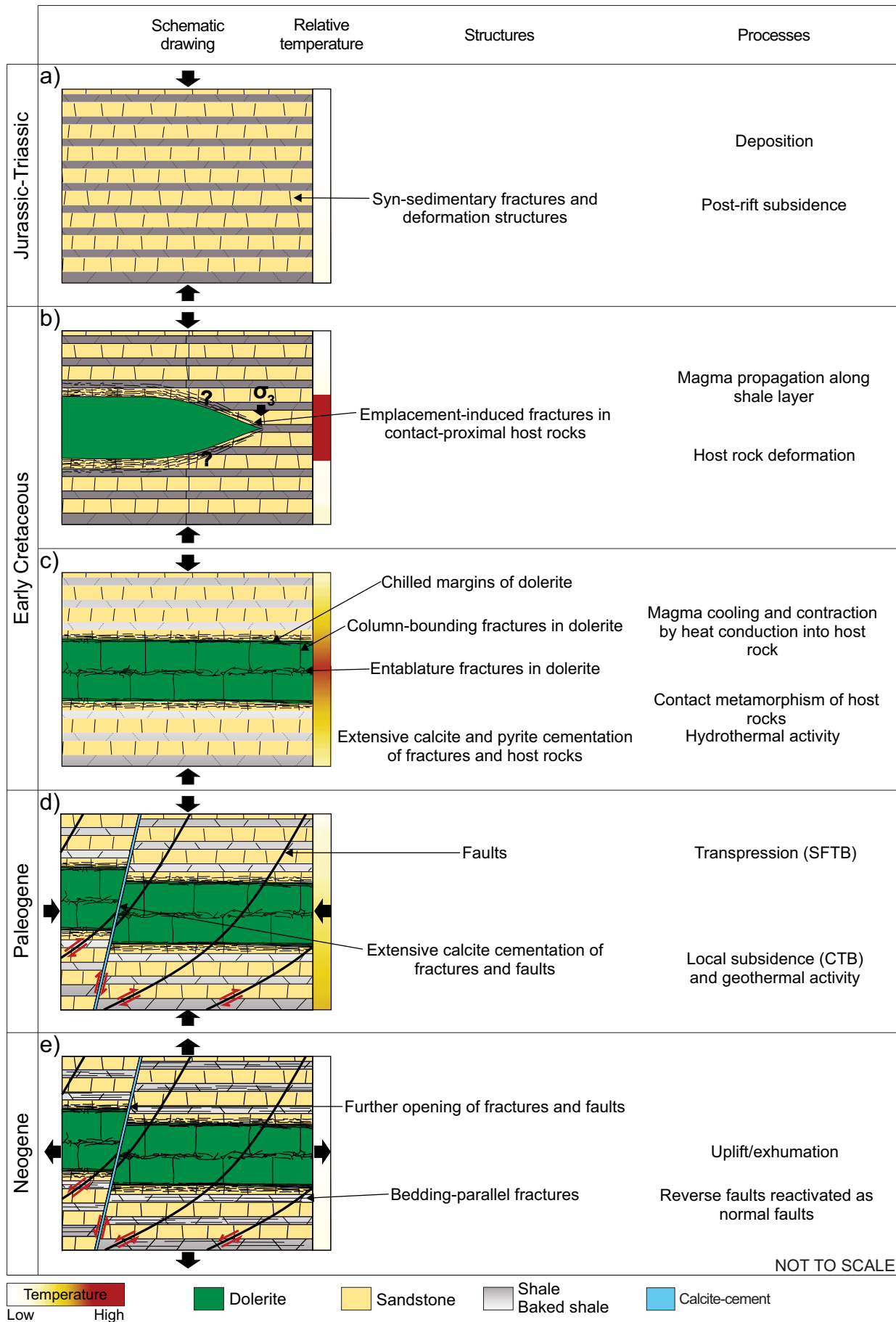
Figure 5.7: Conceptual time-transgressive model for rock evolution and fracture development in a thin sill and its host rocks, from deposition in the Mesozoic until present. The fracture pattern within the sill is based on the thin sills investigated in this study (i.e. <2 m thick). Relative temperatures indicate the rate of burial and how the heat from the intrusion is conducted through the host rock with time. Improved upon earlier models from Ogata et al. (2014) and Senger et al. (2015).
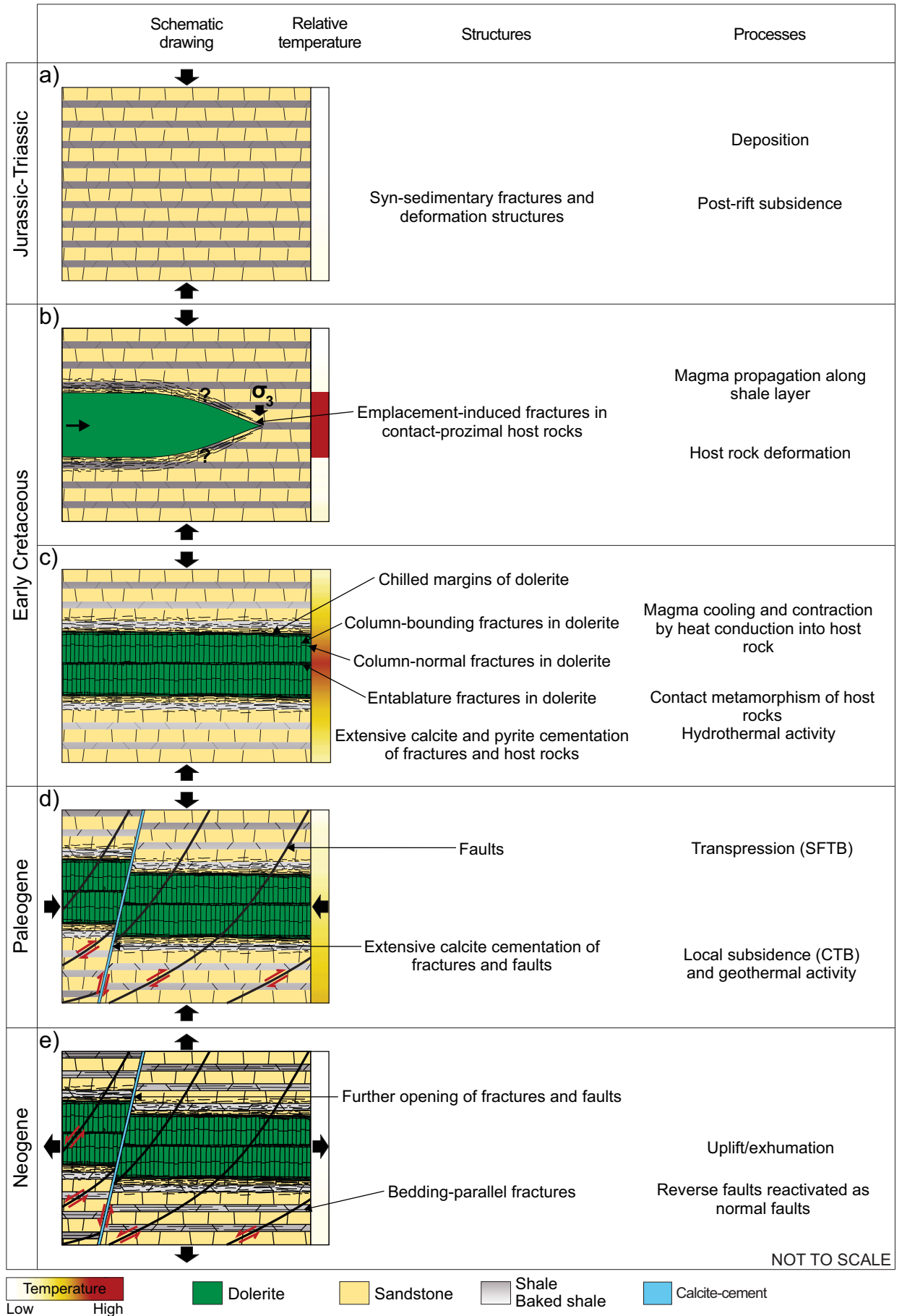
Figure 5.8: Conceptual time-transgressive model for rock evolution and fracture development in a thick sill and its host rocks, from deposition in the Mesozoic until present. The fracture pattern within the sill is based on the thick sills investigated in this study (i.e. >30 m thick). Relative temperatures indicate the rate of burial and how the heat from the intrusion is conducted through the host rock with time. Improved upon earlier models from Ogata et al. (2014) and Senger et al. (2015).

	Schematic drawing	Relative temperature	Structures	Processes

a) Jurassic-Triassic

Syn-sedimentary fractures and deformation structures

Deposition

Post-rift subsidence

Fault reactivation or development

b) Early Cretaceous

σ₃

Emplacement-induced fractures in contact-proximal host rock

Magma propagation along preexisting fault

Host rock deformation

c)

Chilled margins of dolerite

Remelting of chilled margins

Column-bounding fractures in dolerite

Column-normal fractures in dolerite

Extensive calcite and pyrite cementation of contacts, fractures and host rocks

Magma cooling and contraction by heat conduction into host rock

Contact metamorphism of host rocks

Hydrothermal activity

d) Paleogene

Reverse faults

Extensive calcite cementation of fractures and faults

Transpression (SFTB)

Local subsidence (CTB) and geothermal activity

e) Neogene

Further opening of fractures and faults

Bedding-parallel fractures

Uplift/exhumation

Reverse faults reactivated as normal faults

NOT TO SCALE

Legend:
- Dolerite
- Calcite-cement
- Sandstone
- Shale
- Baked shale
- "1A" - entablature zone
- "1B" - columnar joint zone
- "1C" - chilled margin
- "2A1" - empl.-induced fracture zone
- "2A2" - contact-metamorphic zone
- "2A3" - hydrothermally altered zone

Figure 5.9: Conceptual time-transgressive model for rock evolution and fracture development in a dyke and its host rocks, from deposition in the Mesozoic until present. The fracture pattern within the dyke is based on the dykes investigated in this study (i.e. 1-8 m thick). The zonation in (c) approximately indicates where the different intrusion-related processes may occur. Improved upon earlier models from Ogata et al. (2014) and Senger et al. (2015).

also illustrates how igneous intrusions tend to propagate along preexisting weak zones, such as shale layers (Figs. 5.7b, 5.8b) or faults (Fig. 5.9b), how the heat is conducted away from the intrusions with time, and how the dyke intrusion-host rock contact often becomes cemented due to focused fluid flow along the dyke contact during hydrothermal activity (Fig. 5.9c), which are details that are lacking in the models in Ogata et al. (2014) and Senger et al. (2015).

5.5   Characterizing igneous intrusions in the subsurface

In order to better understand how igneous intrusions appear in the subsurface, the properties of the investigated intrusions and host rocks are discussed in relation to previous studies, which furthermore is applied to schematic wireline logs of a hypothetical sill and its host rocks 5.10.

Sills in sedimentary basins are easily mappable on seismic sections, as sills have high P-wave velocities and density values (i.e. high acoustic impedance) compared to sedimentary host rocks (e.g., Planke et al., 2005). However, relatively thin intrusions fall below the typical seismic resolution and are therefore poorly imaged in seismic data (e.g., Senger et al., 2013a; Schofield et al., 2015; Eide et al., 2016). This is illustrated by Eide et al. (2016), who studied deeply emplaced sill complexes in East Greenland, and concluded that sills with thicknesses of 7-12 m generally are to thin to be imaged by seismic survey in kilometer-scale subsurface scenarios. In addition, thick intrusions or extrusives will strongly decrease and disturb the seismic imaging quality of rocks below the basalt. This is especially true for the Møre and Vøring Basins (e.g., Planke et al., 1999) offshore Mid-Norway and the Faroe-Shetland Basin (e.g., Gallagher & Dromgoole, 2008; Schofield et al., 2015). From analyses of well data, Schofield et al. (2015) concluded that up to 88% of the total sills within the sedimentary rocks of the Faroe-Shetland Basin are potentially not clearly imaged in seismic data due to the limitations mentioned above. Coring is relatively expensive (Selley & Sonnenberg, 2014), and therefore, detailed outcrop data can be linked with conventional wireline logs in order to better map and characterize igneous intrusions that are present in the subsurface (e.g., Schofield et al., 2015; Senger et al., 2017).

Wireline logs are logs that represent geophysical properties of the penetrated rocks (e.g., Selley & Sonnenberg, 2014). In Fig. 5.10, the schematic wireline logs represent an impermeable sill (zone "1B") with highly fractured chilled margins (zone "1C") and entablature zone (zone "1A"), in addition to a host rock that is highly fractured (zone "2A1"), with a contact aureole (zone "2A2") and a

highly cemented area (zone "2A3"). The host rocks consist of shales interbedded with sandstones, where the matrix porosity is slightly decreasing towards the intrusion contacts due to high rates of secondary calcite. The schematic logs represent rocks that have salt water as the main fluid.
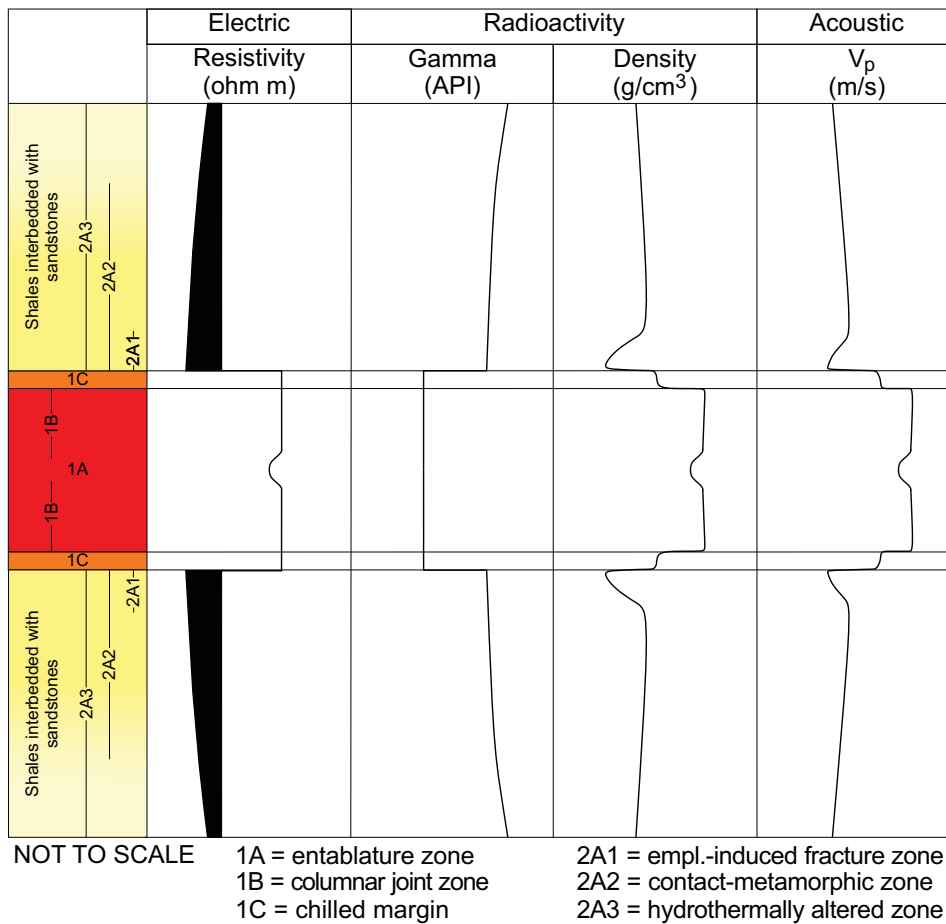
Figure 5.10: Schematic wireline logs of a hypothetical sill and its host rocks. Modified from Planke et al. (1999), Smallwood & Maresh (2002), Jerram et al. (2009), Nelson et al. (2009), Cukur et al. (2010) and Bowman et al. (2012).

An introduction to the parameters presented in Fig. 5.10, following Selley & Sonnenberg (2014) is presented below. P-wave (i.e. acoustic velocity, V_p) logs are used to establish lithology and porosity changes. Electric resistivity logs indicate changes in saturated porosity and fluid type. The radioactivity logs illustrated in Fig. 5.10 comprise gamma ray and density. Gamma ray logs are a result of natural radioactivity of rocks, and are used to differentiate highly radioactive rocks containing clays and organic matter from rocks with a low

content of radioactive elements, such as igneous rocks. Density logs are a result of secondary gamma radiation, which can be related to the electron density of atoms in the rocks, and are in turn directly related to the bulk density. For a more complete introduction to the different parameters, see to Selley & Sonnenberg (2014).

In volcanic basins, V_p and density values tend to be higher in the dolerite compared to sedimentary host rocks (Fig. 5.10, e.g., Planke et al., 1999; Cukur et al., 2010; Smallwood & Maresh, 2002; Senger et al., 2017). In this study, an increase in crystal size is documented for the 2.28 thick DH4 sill (Section 4.2) towards the intrusion center, supported by Winkler (1949). This suggests that a V_p log will slightly decrease from the intrusion contact towards the center of the sill (Fig. 5.10). This is thus supported by Francis (1982) and Smallwood & Maresh (2002), who attributed a decrease in the V_p towards the center off sills to coarser crystals. Highly fractured chilled margins (zone "1C") and entablature zones (zone "1A"), observed in the sills investigated in this study, will lead to a decrease in V_p and density here compared to the rest of the dolerite (zone "1B", Nelson et al., 2009).

A decrease in host rock matrix porosity towards the intrusion contact (in zone "2A3" in Fig. 5.10) is documented for the DH4 sill (Section 5.3.2), and leads to a gradual increase in V_p and density logs (e.g., Smallwood & Maresh, 2002). However, porosity is inferred to be higher in close proximity to intrusions due to the presence of emplacement-induced fractures in the host rocks (zone "2A1"), as documented for the dyke localities (e.g. Fig. 4.49), resulting in a decrease in V_p and density logs immediately adjacent to the intrusion. Despite the lack of documentation of emplacement induced fractures in the host rocks adjacent to sills, the highly fractured area is applied to the illustration in Fig. 5.10. This due to the fact that sills can contribute to damaging adjacent host rocks (e.g., Hansen & Cartwright, 2006). Furthermore, a decrease in V_p in the host rocks towards sills has previously been suggested to be related to microcracks that form due to fluid escape during hydrothermal alteration (Planke et al., 1999), supporting a decrease of P-velocity immediately adjacent to the intrusion.

Gamma ray logs show an abrupt drop within sills due to a lack of radioactive elements, which are present in e.g. clays and k-feldspar in sedimentary host rocks (Fig. 5.10, e.g., Cukur et al., 2010; Smallwood & Maresh, 2002; Senger et al., 2017). In this study, the lack of k-feldspar proximal to the DH4 intrusion, and a presence of k-feldspar elsewhere in the De Geerdalen Formation (e.g., Mørk, 2013) is attributed to hydrothermal activity, i.e. the dissolution and/or replacement of k-feldspar by calcite adjacent to the intrusion (Section 5.3.5). This suggests that changes in mineralogy occur with distance to the intrusion contact (in zone "2A3" in Fig. 5.10). Therefore, a gamma ray log will show

a slightly progressive decrease towards the intrusion, related to the amount of k-feldspar present in the host rocks proximal to the intrusion (Fig. 5.10). Smallwood & Maresh (2002) suggested that the contact aureole cannot be seen in the gamma ray logs, as mineralogical changes during contact metamorphism do not significantly affect the composition of minerals in the host rocks. However, even though contact metamorphism do not significantly change the composition of the host rocks directly, precipitation or alteration of minerals by hydrothermal activity can (e.g., Einsele et al., 1980; Wolela, 2002), suggesting that changes in gamma ray logs can occur with distance to the intrusion contact.

Resistivity values tend to be higher within intrusion than in host rocks (Fig. 5.10, e.g., Smallwood & Maresh, 2002). However, the presence of high amounts of pyrite (i.e. highly conductive iron, Kato et al., 2012) in the host rocks adjacent to the DH4 intrusion (e.g. Fig. 4.36i) suggests that a resistivity log will decrease and be highly variable in the host rocks towards the intrusion contact (in zone "2A3" in Fig. 5.10). Furthermore, high fracture porosity immediately adjacent to the intrusion contact (zone "2A1"), filled will salt water (i.e. low resistivity), will result in lower resistivity proximal to the intrusion (Selley & Sonnenberg, 2014). This is in contrast with Smallwood & Maresh (2002), who suggested that pyrite in host rocks adjacent to intrusions lead to an increased resistivity towards the intrusion contacts. Since iron is highly conductive, the presence of pyrite will lead to a decrease in resistivity (e.g., Kato et al., 2012), and therefore the suggestion by Smallwood & Maresh, 2002 is inferred to incorrect.

5.6   Effect of igneous intrusions on fluid flow

This section applies the previous discussions to highlight the impact that the emplacement of the Diabasodden Suite has on subsurface fluid flow. To be able to understand subsurface fluid flow within the Kapp Toscana Group, an introduction to essential background information follows.

Well data from Adventdalen show that the targeted reservoir has a significant under-pressure, indicating that the reservoir apparently is well sealed (e.g., Braathen et al., 2012; Wangen et al., 2015). The gently dipping reservoir crops out 15 km north-east of the well site, as illustrated in this study, which should allow pressure communication with the surface (Senger et al., 2013a). However, pockmarks in Isfjorden indicate focused fluid flow seepage sites from some layers in the subsurface, along faults (Blinova et al., 2012) and outcropping edges of igneous intrusions (Senger et al., 2013a). Since the reservoir has a significant underpressure, the igneous intrusions present in the reservoir unit and the overlying shales, in combination with sealing shales, permafrost, pinch-

outs and faults, may therefore contribute to the compartmentalization of the reservoir unit (Senger et al., 2013a). This is supported by pressure data in the lower and upper part of the Kapp Toscana Group, that indicate separate pressure cells within the target aquifer, suggesting that vertical pressure barriers do exist within the aquifer (Senger et al., 2013b). Furthermore, it implies that even small-scale intrusions and their contact aureoles, which are shown to have different porosity and permeability than the host rocks (Sections 5.3, 5.4) may locally affect the entire reservoir.

5.6.1   Local effect of igneous intrusions on fluid flow

Cooling joints within dolerites are previously suggested to be poorly connected, and igneous rocks are therefore traditionally viewed as impermeable (e.g., Schutter, 2003; Matter et al., 2006). Igneous intrusions have been shown to act as impermeable barriers in numerous studies, such as the Phetchabun Basin, Thailand, where oil is produced from a reservoir that is sealed by a folded sill (Schutter, 2003). In essence, permeability is suggested to be higher parallel to the intrusion contact (Chevallier et al., 2004). This is also supported by observations by Matter et al. (2006), who studied permeability in and around igneous intrusions in the Newark Rift Basin, USA, and Rateau et al. (2013), who investigated the role of igneous intrusions on hydrocarbon migration in the Faroe-Shetland Basin.

As illustrated in this study, a decrease in porosity and permeability is present in the contact-proximal host rocks, attributed to contact metamorphism and hydrothermal activity related to intrusion emplacement. These results are supported by similar studies, e.g. Einsele et al. (1980) and Wolela (2002), see Section 5.3 for further details. However, a highly fractured intrusion-host rock interface (i.e. chilled margins in dolerite and emplacement induced fractures in host rocks) may allow for channelizing fluids along contacts of the intrusions (e.g., Wilkes et al., 2004; Matter et al., 2006). This is also illustrated by Senger et al. (2013a), who presented a conceptual model of fracturing in and around igneous intrusions. In addition, highly fractured contact zones drive several successful groundwater boreholes in South Africa (Van Wyk, 1963; Woodford & Chevallier, 2002). The presence of an entablature zone (e.g., Bermúdez & Delpino, 2008; Witte et al., 2012), which is interpreted at the Beach c locality (Fig. 4.10a), can also allow for fluid flow parallel to the intrusion. However, entablature zones would require additional contact perpendicular pathways to be functional in a reservoir setting.

As documented in this study, the presence of cemented fractures may partly resist fluid flow along the intrusion-host rock interface. Despite high precipitation rates of secondary minerals during and after cooling of the magma, cementation is also evident from the calcite cemented reverse faults that are

cross-cutting dolerites (discussed in Section 5.3). As previously mentioned, additional cementation is suggested to occur during maximum burial in Paleogene. The degree of secondary minerals present will strongly control whether a fracture is open (permeable) or closed (impermeable). The presence of calcite in fractures of dolerites and host rocks indicates that permeability rates have been high, possibly prior to the intrusion emplacement, but that physical and chemical conditions were facilitated for the precipitation of calcite. It is therefore possible that in similar volcanic basin settings, where the strata containing igneous intrusions have either not undergone deep burial, especially during or after intrusion emplacement, or where fluids have dissolved and removed secondary minerals, porosity and permeability of the intrusion-host rock interface will likely be better preserved, supported by Schutter (2003). In Svalbard, uplift and unloading of the rocks may have led to further opening of cemented fractures, as suggested by Singhal & Gupta (2010b) and Rateau et al. (2013) for similar volcanic basins. However, this was not payed attention to in the field, and is therefore not documented in this study.

In summary, the present study has shown that the emplacement of igneous intrusions may on a local scale reduce porosity of the sedimentary host rocks in vicinity to the intrusion, and create pathways for fluids along the intrusion-host rock interface (e.g., Rateau et al., 2013) . This due to a documented decrease in intrusion-proximal host rock matrix porosity and an increased fracture frequency in both intrusions and host rocks towards the contacts.

5.6.2   Regional effect of igneous intrusions on fluid flow

Regionally, a loss of porosity adjacent to igneous intrusions will have limited implications for reservoir porosities. However, igneous intrusions can control fluid flow, as they can create preferential fluid flow pathways and destroy preexisting traps, or conversely act as seals and traps in combination with other sealing features, and therefore compartmentalize reservoirs (e.g., Cartwright et al., 2007; Schutter, 2003; Holford et al., 2013; Rateau et al., 2013). In a petroleum system, impermeable igneous intrusions can compartmentalize source rocks, leading to low communication rates between source rocks and reservoir rocks (Eide et al., 2016). This will further lead to migration shadows (Rateau et al., 2013), meaning that reservoir rocks located above an impermeable sill will not be charged with hydrocarbons due to a lack of migration pathways into the reservoir rocks. Migration shadows can also be applied to the proposed CO_2 reservoir, as impermeable intrusions will prevent fluid flow from one fully functional reservoir compartment into another.

In contrast, some igneous rocks may even have higher permeability and porosity than the sedimentary host rocks, due to highly connected fractures and a pres-

ence of secondary porosity (Schutter, 2003). Examples of this are commercially-exploitable igneous hydrocarbon reservoirs in e.g. China (Wu et al., 2006), Mexico (Salas, 1968), Venezuela (Mencher et al., 1953), Namibia (Bray et al., 1998), and Argentina (Witte et al., 2012). This is inferred to not be the case for the Kapp Toscana Group, as the fractures within the intrusions have a higher rate of calcite cement than the surrounding rocks, corresponding with the fact that dolerites are particularly reactive with calcaerous liquid (Matter et al., 2011). In addition, the fracture frequency in both the dolerites and their host rocks towards intrusion contacts indicates focused fluid flow along the intrusion-contact interface.

Whether an igneous intrusion acts as a barrier to, or carrier for fluid flow, is as mentioned highly dependent on the geometry and the orientation of the igneous feature, and whether the fractures are open or closed (e.g., Rateau et al., 2013). In Svalbard, dykes are observed to intrude either preexisting faults or along strike of what is interpreted to reflect paleostress, while sills are seen to intrude litholgically weak zones, such as gypsum and organic-rich shales (Senger et al., 2013a). Sills do often create 3D saucer shaped (concave) geometries (e.g., Chevallier & Woodford, 1999; Rocchi et al., 2007; Hansen et al., 2011). Assuming focused fluid flow along the intrusion-host rock interface, fluids will likely be channelized along the margins of transgressive (or saucer-shaped) sills. Saucer-shaped geometries have been proposed for Svalbard by Polteau et al. (2008), while Senger et al. (2013a) identified a probable saucer-shaped sill in 2D seismic data offshore Bjørndalen. In addition, the intrusions on the southern shore of Isfjorden are overall rising towards southeast and northwest on either side of the De Geerdalen (Senger et al., 2013a).

On the basis of the interpretations and the published literature presented above, three possible 2D scenarios of fluid flow related to hypothetical igneous intrusions are presented (Fig. 5.11). The hypothetical fluid-injection point illustrates how the fluids may be distributed within the reservoir. In all scenarios, the reservoir is capped by sealing shales (i.e. the Upper Jurassic Agardhfjellet Formation) and possibly permafrost. The first scenario (Fig. 5.11a) is based on the assumptions in which an intrusion is impermeable, as the fractures, both within the sill and along the intrusion-host rock interface, are impermeable (i.e. closed, cemented or non-connected). Here, both sills and dykes together, or in combination with other sealing features, may compartmentalize the reservoir into smaller units, dependent on their geometries. This is previously schematically illustrated for the Faroe-Shetland Basin (Rateau et al., 2013).

The fractures investigated in this study in and around the igneous intrusions in central Spitsbergen are highly cemented, however, they may have opened up during uplift and removal of overburden loading (Rateau et al., 2013). Assuming that the fractures provide sufficient permeability for fluid flow, the intrusion-

host rock interface may act as a high-permeability pathway, which will have several consequences for CO_2 sequestration, as presented below.
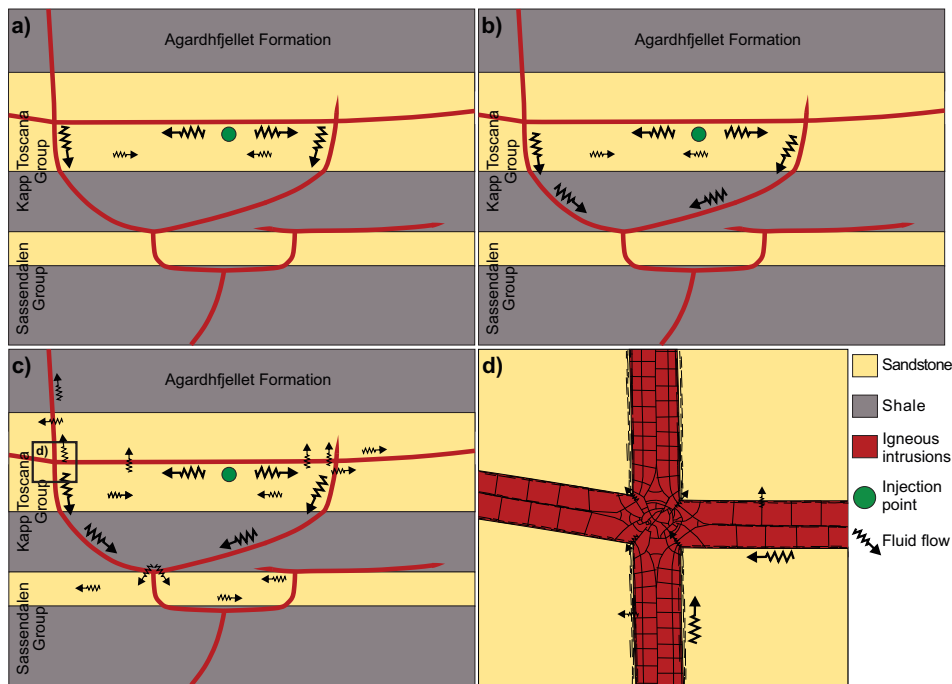
Figure 5.11: Three scenarios of how igneous intrusion in central Spitsbergen can affect subsurface fluid flow, where a) illustrates how intrusions can act as impermeable barriers to fluid flow, and b) how a highly fractured intrusion-host rock interface can act as carriers for fluid flow, and c, d) how intrusions may channelize fluids parallel and perpendicular to their contacts. Not to scale.

The second scenario (Fig. 5.11b) assumes that an intrusion in itself is impermeable, but serves high-permeability fluid flow pathways along the intrusion-host rock interface (i.e. chilled margins and emplacement induced fractures) as previously illustrated by Chevallier et al. (2004) for the Karoo Basin. In this scenario, igneous intrusions can provide connection between otherwise isolated porosity units, such as the coarsening-upwards successions of the De Geerdalen Formation (e.g., Mørk et al., 1989). However, they can also act as a seal bypass system (Cartwright et al., 2007), as fluids may be channelized through otherwise sealing features along dykes or transgressive sills towards the surface. In central Spitsbergen, an example of a dyke that may act as a seal bypass system is the Botneheia dyke, which extends through the entire reservoir unit and partly into the cap-rock shales of the Agardhfjellet Formation (Senger et al., 2014a). However, assuming that the dyke has breached into a sill, which likely is the case for the Botneheia dyke and sill (see Senger et al., 2013a

for map), an injection point below such a sill can prevent fluid flow through the dyke-sill connection. This is the basis for the compartmentalization in the second scenario (Fig. 5.11b).

In the third scenario (Fig. 5.11c, d), both the intrusion and the intrusion-host rock interface are highly permeable, both parallel and perpendicular to the contact. In this case, the igneous intrusions can provide connection between otherwise isolated compartments, store fluids within the fractures and act as seal bypass systems, both vertically and horizontally. Assuming an uniform cooling in the sill and the dyke, where the last magma to cool is located in the dyke-sill meeting point, one would expect a radial an concentric cooling fracture pattern (e.g., Bermúdez & Delpino, 2008) that merges towards a possible entablature zone (Fig. 5.11d, e.g., Kattenhorn & Schaefer, 2008). These fractures may hypothetically also act as preferential fluid flow pathways, dependent on their connectivity, as illustrated in Figs. 5.11c and d.

As noted by Senger et al. (2013b), the exact nature and dimensions of the pressure cells in the subsurface of central Spitsbergen are poorly understood. However, the presence of separate pressure cells indicate that vertical pressure barriers, possibly including igneous intrusions, faults, pinch-outs, sealing shales and permafrost, do exist. Therefore, I suggest that the second scenario provides the best explanation of fluid flow in and around igneous intrusions in the targeted reservoir. This is based on the observations and analyses from this study, and the fact that the targeted reservoir is underpressured (Braathen et al., 2012) and is shown to consist of several pressure compartments, indicating a closed system (Senger et al., 2013b). An increase in fracture frequency towards the contact indicates that fluid flow will be preferential along the intrusion-host rock interface. Furthermore, since calcite is abundant, and no chilled margins, despite an increase in fracture spacing towards the intrusion contact, are observed in the dyke-host rock interface, this indicate restricted vertical fluid flow along the dykes. In contrast, an absence of calcite and a presence of chilled margins in the sill-host rock interface, indicate that fluid flow is more efficient horizontally along the margins of sills. Impermeable sills and dykes, in combination with each other and/or other sealing features, can therefore provide 3D compartments within the reservoir.

5.6.3   Implications for CO$_2$ storage within the Kapp Toscana Group

Fluid flow is in this study suggested to be higher along the margins of sills than along the margins of dykes, related to the presence of chilled margins and the rate of calcite cementation. Especially the highly fractured sill-host rock inter-face can therefore connect lithology-dependent compartments where sills are

transgressive. Injection of CO_2 in the underpressured reservoir will likely cause fractures to open up (Senger et al., 2013b), and therefore, the injection needs to be stopped at a certain overpressure in order to maintain the sealing properties of fractures and faults that are present in the sealing features. Dependent on the chemical and physical conditions within the reservoir, injection of CO_2 can have several implications for the sequestration: (1) CO_2 can dissolve calcite cement within the fractures and matrix due to its acidity, as calcite cement is thermodynamically unstable in CO_2 rich environments (Barlet-Gouédard et al., 2007), resulting in the fluids migrating out of the reservoir. (2) pressurized calcaerous liquid caused by the dissolution of calcite can cause further cementation of fractures in the intrusions (Senger et al., 2013b), as dolerites are particularly reactive with calcaerous liquid (Matter et al., 2011), increasing the sealing properties of the intrusions. Or (3) the permeable pathways remain open due to very slow geochemical reactions, which are shown to be slow in wet supercritical CO_2 settings (Machel, 2005; Barlet-Gouédard et al., 2007). This results in preserved connectivity between compartments and hence successful CO_2 sequestration.

This study has contributed to the knowledge of the impact that igneous intrusions emplaced within the Kapp Toscana Group have on fluid flow, which furthermore can be applied to similar volcanic basin systems where exploration for petroleum, ground water or CO_2 storage occurs.

/6

Future research

- It is evident that porosity and permeability both within the igneous intrusions, the adjacent host rock and the intrusion-distal host rock is restricted to fractures, as matrix porosities and permeabilities in general are low. This study has contributed to the overall understanding of fracture connectivity in and around igneous intrusions, however, a better database on cementation rates of fractures, faults and the host rocks in proximity to the intrusions within the Kapp Toscana Group is necessary in order to predict weather igneous intrusions in central Spitsbergen are compartmentalizing or channelizing injected fluids.

- This study has investigated how one igneous intrusion affected intrusion-proximal sandstone laminas in shales. More quantified studies of porosity and permeability in host rocks with different lithologies (i.e. shales, sandstones, carbonates) are needed to better understand fluid flow in volcanic basins.

- This study has contributed to a better understanding of fracturing related to igneous intrusions. However, the emplacement of thicker intrusives, such as the Grønsteinfjellet sill and the Hatten feeder complex, which are subaerially exposed 15-20 km north of the injection site, must have caused host rock damage on a much larger scale than the thinner intrusions investigated in this study. How these intrusions affect fluid flow may be an important factor for understanding fluid flow within the targeted reservoir.

- As regional vertical pressure barriers are shown to exist (Senger et al., 2013b), studies of vertical sealing features such as faults, pinch-outs and igneous intrusions need to be combined in order to understand the possible compartmentalization of the reservoir.

/7

Conclusions

This study has integrated outcrop and borehole data in order to investigate the effect that the Early Cretaceous intrusions of the Diabasodden Suite have on local and regional fluid flow. On the basis of the descriptions, analyses and discussions of the intrusions and their host rocks, the following conclusions can be drawn:

- Digital geology has provided a much larger dataset than what would have been possible in the same amount of time during traditional fieldwork.

- The investigated intrusions are inferred to belong to the Diabasodden Suite, and it is likely that they have developed during different episodes of intrusion emplacement.

- A decrease in precipitated calcite, and an increase in porosity in the host rocks of the DH4 intrusion is documented to occur somewhere between 4.82 m and 17.64 m from the intrusion contacts. Calcite cement is also present in fractures within the dolerites and in faults that are cross-cutting dolerites. It is therefore suggested that extensive cementation in and around the dolerites has occurred both related to hydrothermal activity during magma emplacement and cooling in Early Cretaceous, and during subsidence in Late Paleogene.

- Several fracture sets are identified both within the intrusions and the host rocks, reflecting the orientation of the intrusions, and are interpreted to either have formed related to paleostress during emplacement in the Early Cretaceous, or during transpression in Paleogene.

- Fracture frequencies in both dykes and sills increase towards the intrusion contact.

- Fracture frequencies in the host rocks of dykes increase towards the intrusion contact. For sills, an increased fracture frequency in the host rocks towards the intrusion contact is not documented due to a limited vertical outcrop extent and general high rates of bedding-parallel fractures present in shales and fine grained sandstones.

- Despite the occurrence of calcite within fractures, porosity and permeability are inferred to be restricted to fractures due to the low porosities of the intrusion-proximal host rocks.

- Schematic wireline logs was produced in order better identify igneous sills within the subsurface.

- Due to highly cemented fractures within the intrusions, and increased fracture frequencies in both the intrusions and the host rocks towards the intrusion contact, the igneous intrusions are suggested to act as impermeable barriers to fluid flow, and provide high-permeability pathways along the intrusion-host rock interface.

- Abundant calcite along the dyke-host rock interface and no chilled margins of dykes indicate restricted vertical fluid flow along the dyke margins. In contrast, the absence of calcite at the sill-host rock interface and the presence of highly fractured chilled margins of sills, indicate more efficient horizontal fluid flow along the intrusion-host rock interface.

- Based on the obtained dataset and the current state-of-the-art, a time-transgressive conceptual model with three different scenarios for rock evolution and fracture development in and around igneous intrusions within the Triassic-Jurassic strata in central Spitsbergen has been presented.

- The time-transgressive model has been incorporated into three possible 2D scenarios of regional fluid flow related to hypothetical igneous intrusions.

Appendices

/A

Trace elements

Trace element results from this study (Table A.1, Fig. A.1) indicate that the Botneheia dyke and the Rotundafjellet sill were emplaced in a continental intra-plate setting, due to their similarity to results obtained by Shipilov & Karyakin (2010) and Nejbert et al. (2011, Fig. A.1).

Table A.1: Minor (ppm) concentrations of samples from the Botneheia dyke (sample B_01) and the Rotundafjellet sill (sample R_b_01).

					Trace elements (ppm)					
Sample	Sc	V	Cr	Co	Ni	Cu	Zn	Ga	Rb	Sr
B_01	39,8	375,9	146	35,5	64,1	246	118,7	23,7	5,8	433,6
R_b_01	37,8	388,3	236,6	47	90,6	246,4	119,1	24	31,1	285,9

Sample	Y	Zr	Nb	Cs	Ba	Pb	Th	La	Ce	Nd
B_01	43,2	209,4	11	2,4	250,4	2,9	2,8	19,7	43,5	23,5
R_b_01	45,5	209,4	10,7	2,4	228	5	5,6	20,9	38,5	21,2
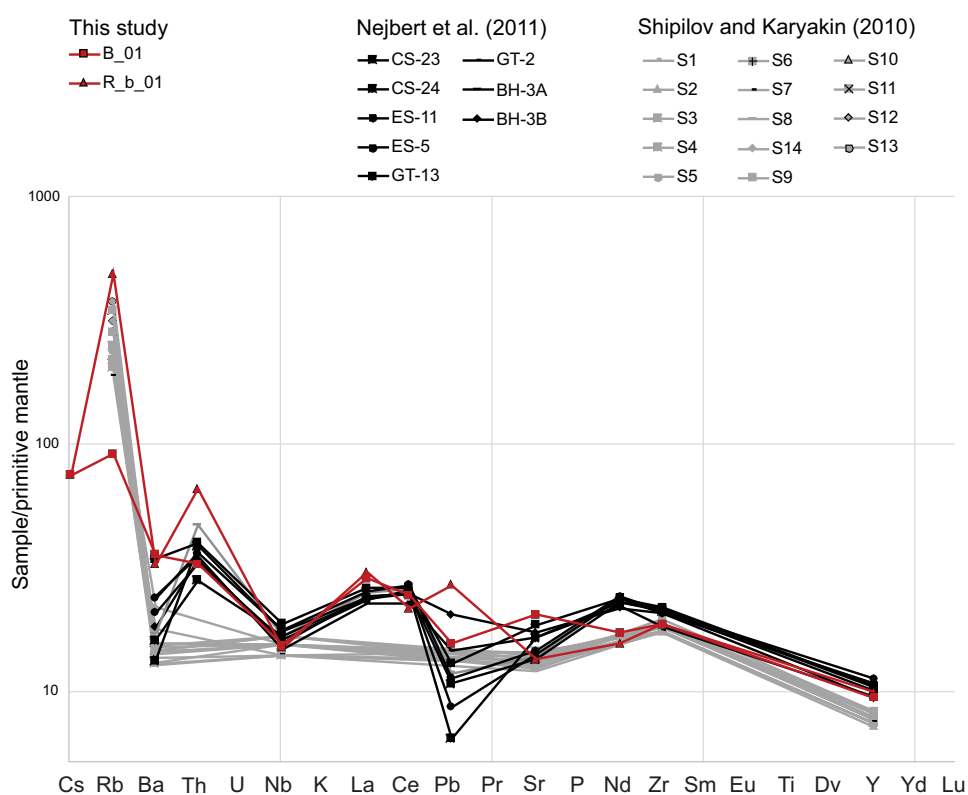
Figure A.1: Trace element data from this study and from different areas in Svalbard from previous studies, plotted in a primitive mantle normalized trace element diagram. Data from Shipilov & Karyakin (2010, gray), Nejbert et al. (2011, black) and this study (red). Normalization factors are from Sun & McDonough (1989).

/B

Virtual outcrop models

Parts of the 3D virtual outcrop models are exported as pdf's (see links below) and can be viewed by downloading the file and opening it in Adobe Acrobat Reader. The pdf's are decimated, meaning that the high resolution mesh is exported as a low resolution mesh in order to be viewed in most conventional software. The resolution of the models is thereby largely reduced, both with respect to mesh and texture.

Beach c sills (Bc)
Grønsteinfjellet sill (Gf_c)
Hatten valley sills (Hv)
Rotundafjellet dyke (R_a)
Studentdalen dyke east (Sd_e)
Wallenbergfjellet sill (Wf_e)

/C

Virtual outcrop reports

Comprehensive reports, generated by Agisoft Photoscan for each virtual outcrop model, can be downloaded from the links below. For an introduction to the different parts of the reports, see to Agisoft (2014).

Beach c sills (Bc)
Grønsteinfjellet sill (Gf_c)
Hatten valley sills (Hv)
Rotundafjellet dyke (R_a)
Studentdalen dyke east and west (Sd_e)
Wallenbergfjellet sill (Wf_e)

/D

Analyzed planes from PlaneDetect

Planes that were analyzed by the software PlaneDetect are presented below. No color bar was provided by the program, however, similar colors of the planes indicate similar orientations. The figures are shown in order to give an introduction to how the software works.
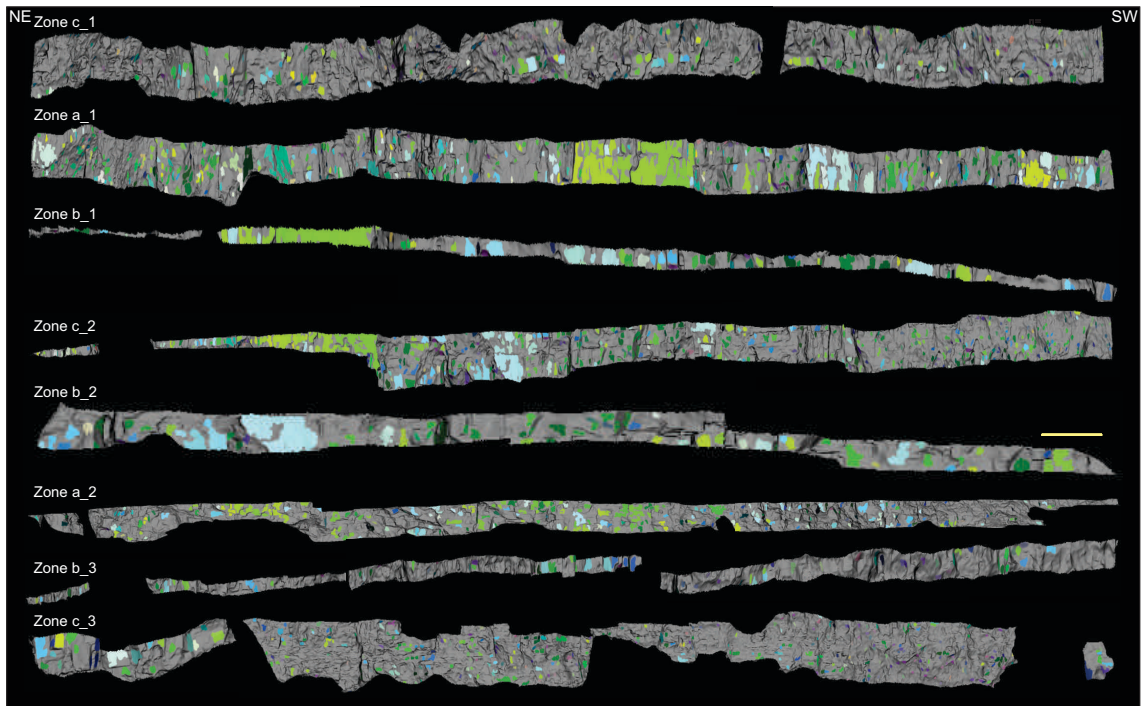
Figure D.1: Beach C sills (Bc). Planes analyzed by PlaneDetect. The zones are vertically exaggerated and not to scale. See Fig. 4.10 for zone interpretations.
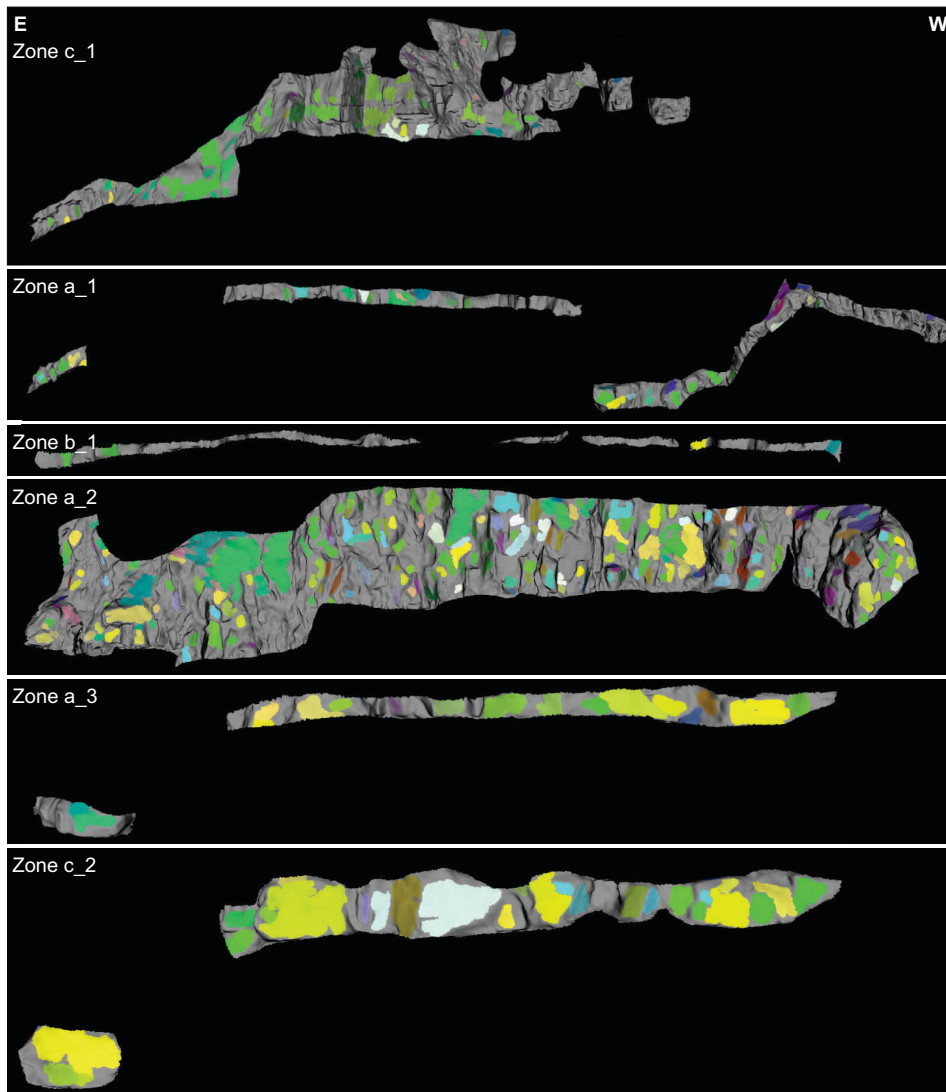
Figure D.2: Hatten valley sills (Hv). Planes analyzed by PlaneDetect. The zones are vertically exaggerated and not to scale. See Fig. 4.16 for zone interpretations.
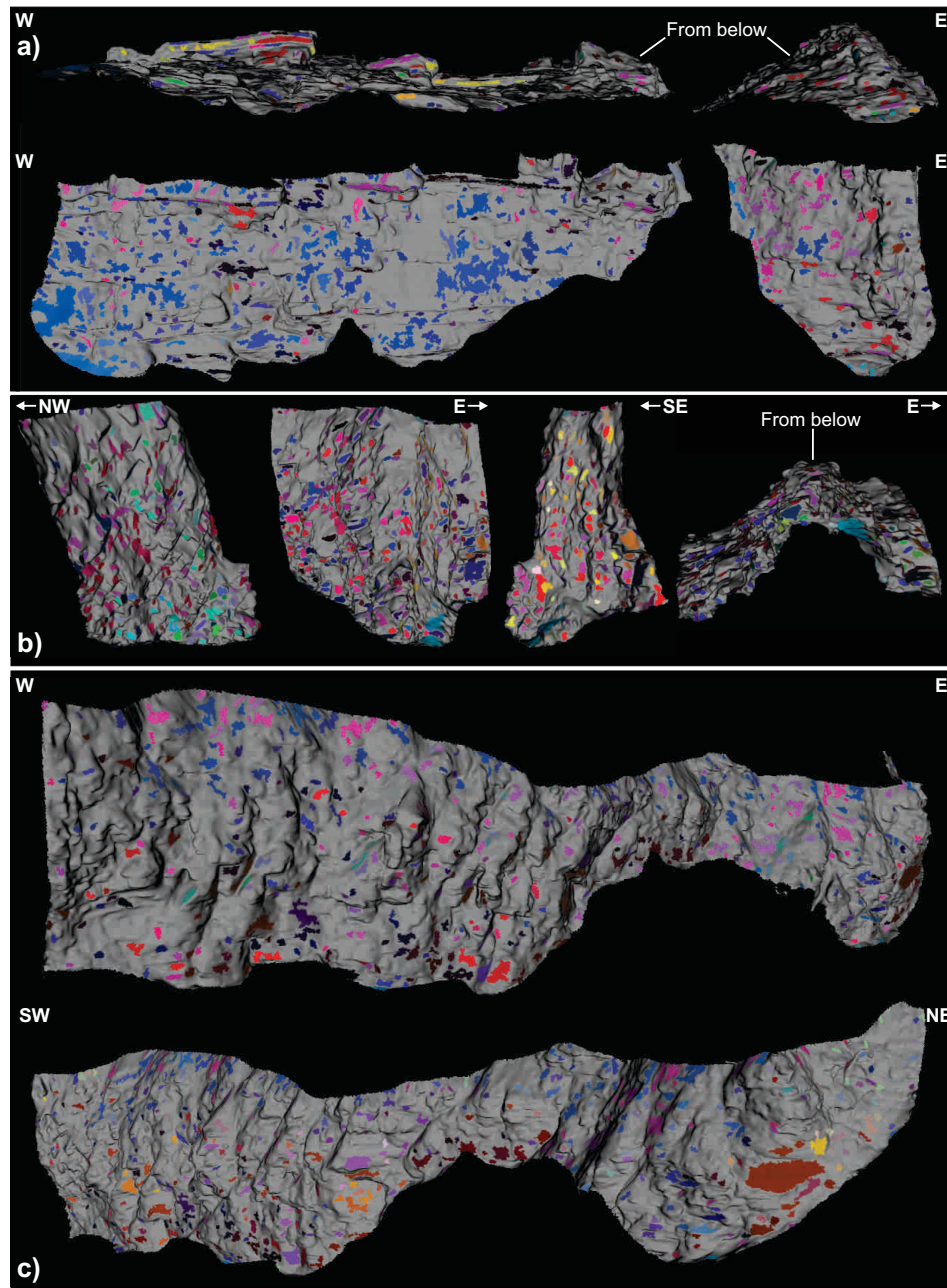
Figure D.3: Rotundafjellet dyke (R_a). Planes analyzed by PlaneDetect. Includes different view angles of the virtual outcrop. (a) Western host rock = zone "C_w" and "D_w", (b) dolerite = zone "A", "B_e" and "B_w", and (c) eastern host rock = zone "C_e" and "D_e". See Fig. 4.3 for zone interpretations.
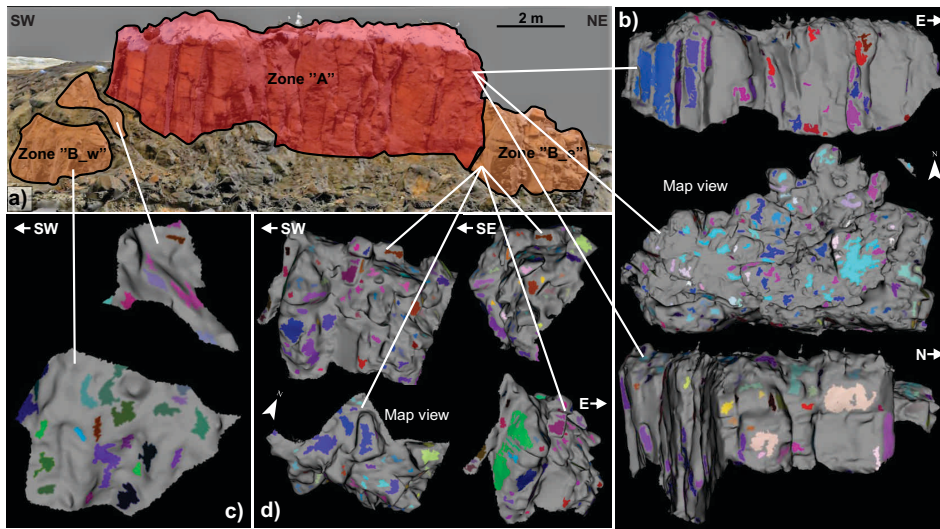
Figure D.4: Studentdalen dyke east (Sd_e). (a) Zone interpretations, with different view angles of the planes analyzed by PlaneDetect of (b) central dolerite, (c) western contact-proximal dolerite, and (d) eastern contact proximal dolerite.
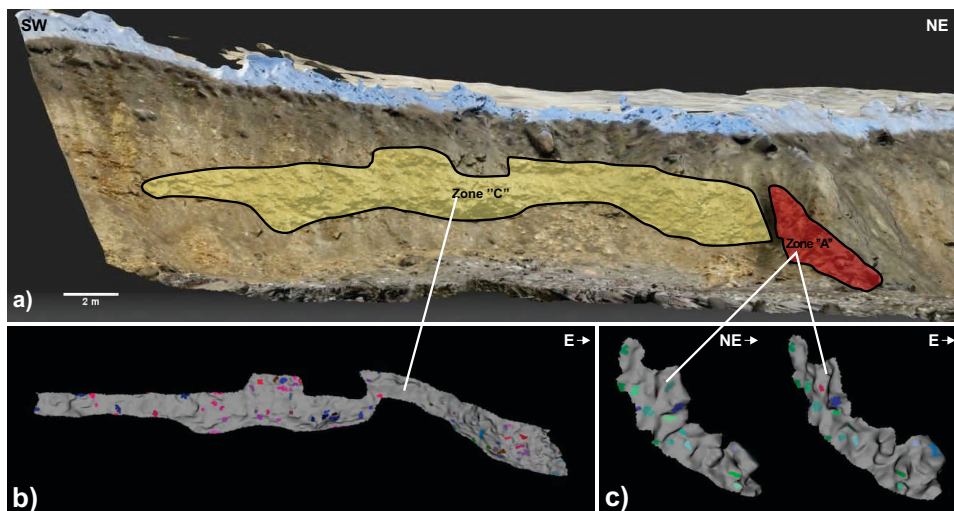
Figure D.5: Studentdalen dyke west (Sd_w). (a) Zone interpretations, with different view angles of the planes analyzed by PlaneDetect of (b) western contact-proximal host rocks, and (c) central dolerite.
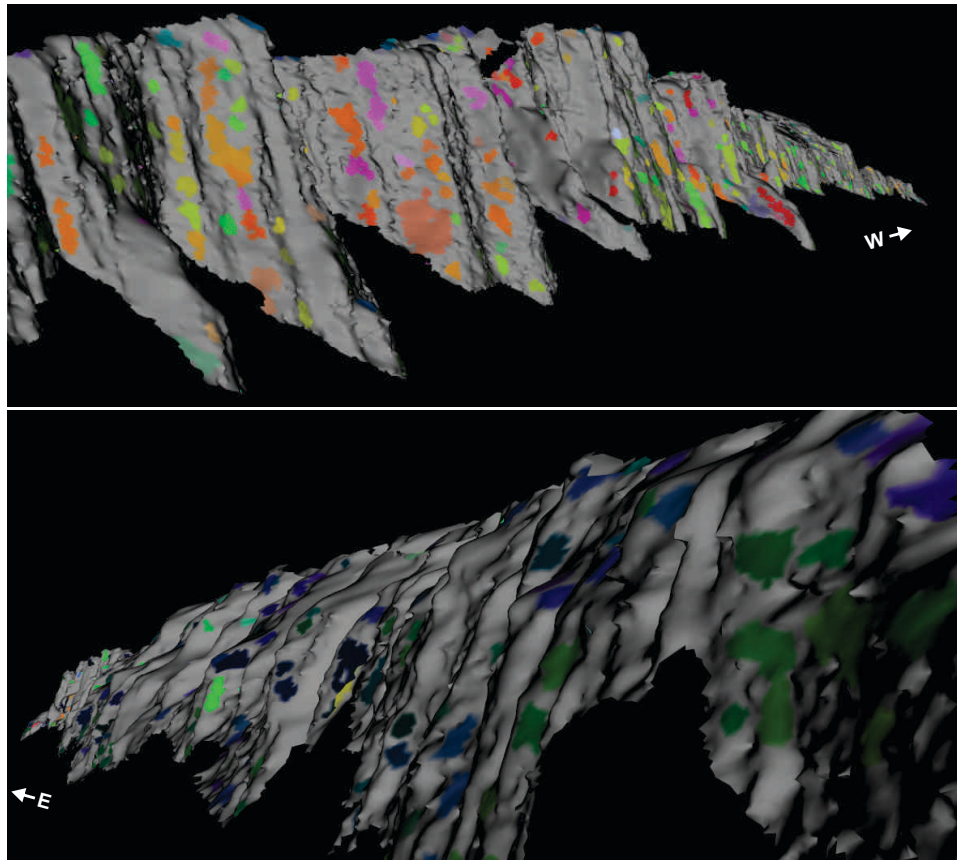
Figure D.6: Wallenbergfjellet sill (Wf_e). Analyzed planes of the sill illustrated with two different view angles.

/E

Making the Arctic accessible

A poster that this study has contributed to, used on the 2nd Virtual Geoscience Conference, Sep. 2016, Bergen, Norway.

Making the Arctic accessible: the use of digital outcrops in research and education at 78°N

Kim Senger[1,*], Mark Mulrooney,[1] Aleksandra Smyrak-Sikora [1,2], Snorre Olaussen[1,2], Maria Jensen,[1] Alvar Braathen [1,2], Simon J. Buckley[3,4] and Marte Festøy[5]

[1] Department of Arctic Geology, UNIS, Longyearbyen, Norway
[2] Department of Geosciences, University of Oslo, Oslo, Norway
[3] Centre for Integrated Petroleum Research, Uni Research AS, Bergen, Norway
[4] Department of Earth Science, University of Bergen, Norway
[5] Department of Geology, University of Tromsø, Norway

[*] corresponding author: kim.senger@unis.no, +47 95291592

2nd Virtual Geosciences Conference
21-23 Sep 2016, Bergen, Norway

Overall goal and objectives

Improve student learning by active use of virtual outcrops in education and outreach:
a. Active hands-on learning
b. Acquisition of key virtual outcrops
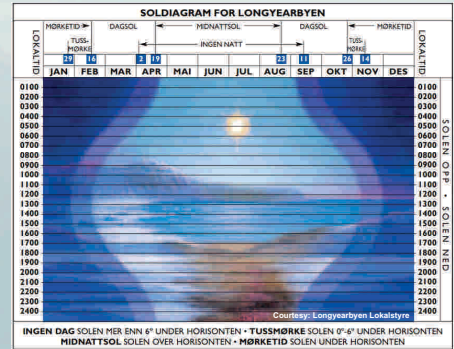c. Multi-scale interpretation in a variety of geological settings
d. Onshore-offshore correlations by e.g., using synthetic seismic modelling
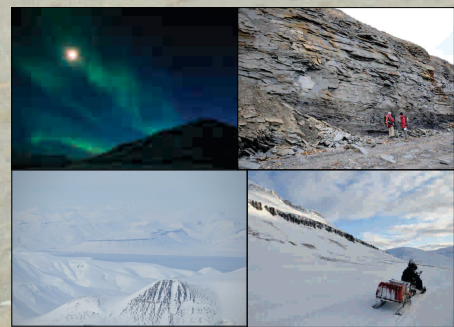
Why do we need virtual outcrops in the Arctic?

SOLDIAGRAM FOR LONGYEARBYEN
Courtesy: Longyearbyen Lokalstyre

1. Extending the "field season"
· Many outcrops are snow-covered for 10 months of the year and only well exposed from mid-July to mid-September
· The polar night from mid-October to mid-February prohibits any extensive geological fieldwork
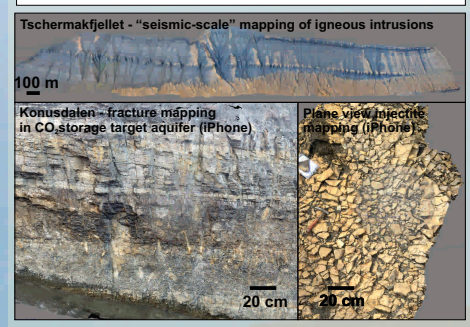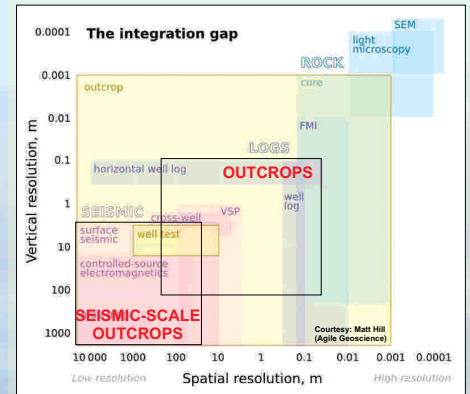
2. Multi-scale outcrops
· Both "seismic-scale", "well-scale" and "core plug-scale" outcrops are present and can be used to quantify the geometry of geological features
· World-class examples of "seismic-scale" outcrops allow the construction of synthetic seismic profiles

3. Logistics
· Many relevant outcrops are in remote locations, accessible only during parts of the season and at a high cost (e.g., Edgeøya)
· Many relevant outcrops lie in protected areas where access and sampling permission is required prior to each field campaign
· Svalbard outcrops are typically only cost-efficiently accessible in late winter on snowmobile (inland outcrops), on boat during summer (coastal outcrops) or by helicopter to select localities

4. Safety
· Many outcrops are too steep and prone to rock fall to allow detailed mapping without compromising safety
· Polar bears and at times challenging weather conditions make fieldwork in the Arctic in general more demanding than in more temperate latitudes
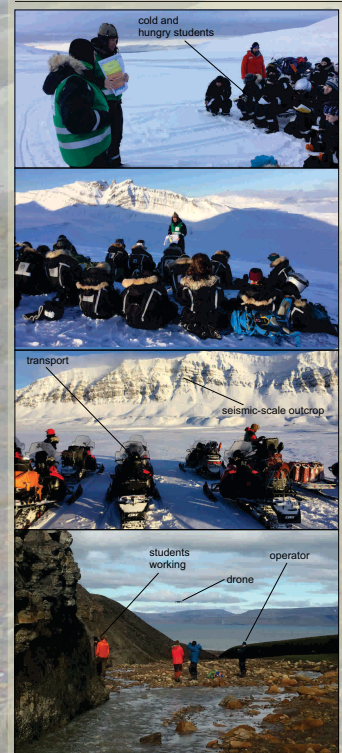
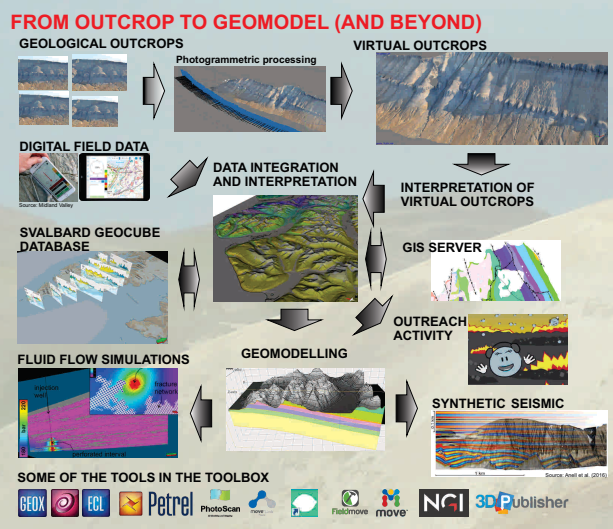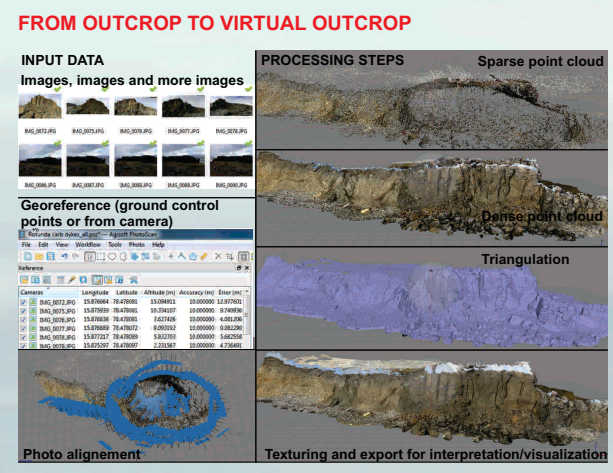## The issue of the right scale

The integration gap

OUTCROPS
SEISMIC-SCALE OUTCROPS
Courtesy: Matt Hill (Agile Geoscience)

Tschermakfjellet - "seismic-scale" mapping of igneous intrusions
100 m

Konusdalen – fracture mapping in CO₂ storage target aquifer (iPhone)
Plane view injectite mapping (iPhone)
20 cm · 20 cm

Student learning at heart

Phase	Requirements	Purpose	Tools presently used
Pre-course	No hardware requirements, easy access with "standard" PCs	Pre-course assignments, familiarization with outcrops	3D pdf, web-viewers
Pre-fieldwork	Detailed virtual outcrop interaction	Fieldwork planning, some interpretation	Lime, Petrel, Move, Google Earth
During fieldwork	Visualization of virtual outcrops in the field	Seeing the "big" picture, maintaining overview	3D pdf apps, FieldMove
Post-fieldwork	Detailed interpretation and processing of new data	Detailed interpretation, processing and integration	Lime, Agisoft, Petrel
Post-course	No hardware requirements, easy access with "standard" PCs	Outreach to general public	3D pdf, web-viewers

cold and hungry students
transport
seismic-scale outcrop
students working · drone · operator

Workflows and techniques

FROM OUTCROP TO VIRTUAL OUTCROP

INPUT DATA
Images, images and more images

Georeference (ground control points or from camera)

PROCESSING STEPS
Sparse point cloud
Dense point cloud
Triangulation
Photo alignement
Texturing and export for interpretation/visualization

FROM OUTCROP TO GEOMODEL (AND BEYOND)

GEOLOGICAL OUTCROPS
Photogrammetric processing
VIRTUAL OUTCROPS
DIGITAL FIELD DATA *Source: Midland Valley*
DATA INTEGRATION AND INTERPRETATION
INTERPRETATION OF VIRTUAL OUTCROPS
SVALBARD GEOCUBE DATABASE
GIS SERVER
OUTREACH ACTIVITY
FLUID FLOW SIMULATIONS
GEOMODELLING
SYNTHETIC SEISMIC *Source: Anell et al. (2016)*

SOME OF THE TOOLS IN THE TOOLBOX
GEOX · ECL · Petrel · PhotoScan · move · Fieldmove · move · NGI · 3D Publisher

The Svalbard Geocube "all-in-one" concept

INPUT DATA

SURFACE DATA
- MAPS: Geological, Structural, Paleogeographic etc.
- TERRAIN MODEL
- PSEUDO-WELLS: Stratigraphic logs
- GPS DATA: Tracks, key localities, sample locations etc.
- VIRTUAL OUTCROPS: Aerial and ground based at a range of scales and resolutions
- SATELLITE DATA: Remote sensing, time-lapse etc.
- PUBLISHED DATA: Digitized uplift maps, maturity trends, key references for specific areas etc.
- SAMPLE DATABASE: Location and result (e.g., core plugs, outcrop samples, thin section of key features)
- BATHYMETRY
- GIS MAP SERVICES: Satellite images, Public-domain data sets, Topographic maps etc.
- DIGITAL FIELD DATA: Structural measurements

SUBSURFACE DATA
- SEISMIC DATA: Onshore and offshore, real and synthetic
- WELLS: Exploration and research boreholes
- WELL TOPS: Chrono- and Lithostratigraphic boundaries
- GEOPHYSICAL DATA: Electrical resistivity profiles, regional grav-mag, published profiles
- CROSS-SECTIONS: Published geological cross-sections, geophysical profiles, interpreted seismic profiles etc.
- WELL LOGS: Digital or image logs

SVALBARD GEOCUBE DATABASE
DEPTH DOMAIN
PETREL-MOVE-ARCGIS LINK
TIME DOMAIN
VELOCITY MODEL

OUTPUT PRODUCTS
COURSE-BASED PROJECTS FOR STUDENTS: All relevant material in single Petrel project, partly available as 3D pdf
OUTREACH PRODUCTS: 3D printed models of Svalbard, interactive displays at UNIS/museums
RESEARCH PROJECT DATABASE: "Packages" for various MSc/PhD/research projects
BASIS FOR REGIONAL STUDIES: Standardised database of subsurface data at numerous scales

midland valley · NORSAR · cegal · Schlumberger · Badleys

/F

Effects of igneous intrusions on the petroleum system

The abstract of a review paper that this study has contributed to is presented below.

Effects of igneous intrusions on the petroleum system: a review

Kim Senger[1], John Millett[2,3], Sverre Planke[2,4], Kei Ogata[5], Christian Haug Eide[6], Marte Festøy[7], Olivier Galland[8] and Dougal A. Jerram[9,4]

Abstract

Igneous intrusions feature in many sedimentary basins where hydrocarbon exploration and production is continuing. Due to distinct geophysical property contrasts with siliciclastic host rocks (e.g., higher V_p, density and resistivity than host rocks), intrusions can be easily delineated within data sets including seismic and CSEM profiles, provided igneous bodies are larger than the detection limit of the geophysical methods. On the other hand, igneous bodies affect geophysical imaging in volcanic basins. Recent analyses of 3D seismic data, supported by field observations and lab-based experiments, have provided valuable insights into the prevailing geometries of intrusions, i.e. (1) layer-discordant dykes, (2) layer-parallel sills and (3) saucer-shaped intrusions. Where emplaced, intrusive bodies affect all five principal components of a given petroleum system: (1) Charge, (2) Migration, (3) Reservoir, (4) Trap and (5) Seal. Magmatic activity may positively or adversely affect any of these individual components, for instance by locally enhancing maturation within the thermal aureoles, typically 30-250% of the intrusion thickness, or by causing regional overmaturation. Site-specific evaluations, including the timing and duration of the magmatic event are needed to evaluate the overall effect of intrusions on a given sedimentary basin's petroleum system, and these are highlighted by case studies from different volcanic basins.

Bibliography

Aarnes, I., Svensen, H., Connolly, J. A., & Podladchikov, Y. Y. (2010). How contact metamorphism can trigger global climate changes: Modeling gas generation around igneous sills in sedimentary basins. *Geochimica et Cosmochimica Acta*, 74(24), 7179–7195.

Abdelmalak, M. M., Mourgues, R., Galland, O., & Bureau, D. (2012). Fracture mode analysis and related surface deformation during dyke intrusion: Results from 2D experimental modelling. *Earth and Planetary Science Letters*, 359, 93–105.

Agisoft, L. (2014). Agisoft PhotoScan User Manual: Professional Edition, Version 1.2. (pp. 1–97).

Allmendinger, R. (2005). Stereonet. *Program for stereographic projection*.

Andresen, A., Haremo, P., Swensson, E., & Bergh, S. G. (1992). Structural geology around the southern termination of the Lomfjorden Fault Complex, Agardhdalen, east Spitsbergen. *Norsk Geologisk Tidsskrift*, 72(1), 83–91.

Babiker, M. & Gudmundsson, A. (2004). The effects of dykes and faults on groundwater flow in an arid land: the Red Sea Hills, Sudan. *Journal of Hydrology*, 297(1), 256–273.

Bælum, K. & Braathen, A. (2012). Along-strike changes in fault array and rift basin geometry of the Carboniferous Billefjorden Trough, Svalbard, norway. *Tectonophysics*, 546, 38–55.

Bailey, J. C. & Rasmussen, M. H. (1997). Petrochemistry of Jurassic and Cretaceous tholeiites from Kong Karls Land, Svalbard, and their relation to Mesozoic magmatism in the Arctic. *Polar Research*, 16(1), 37–62.

Barclay, S., Worden, R., Parnell, J., Hall, D., & Sterner, S. (2000). Assessment of fluid contacts and compartmentalization in sandstone reservoirs using fluid inclusions: an example from the Magnus oil field, North Sea. *AAPG bulletin*, 84(4), 489–504.

Baresel, B., Bucher, H., Bagherpour, B., Brosse, M., Guodun, K., & Schaltegger, U. (2017). Timing of global regression and microbial bloom linked with the Permian-Triassic boundary mass extinction: implications for driving mechanisms. *Scientific Reports*, 7.

Barker, C. & Bone, Y. (1995). The minimal response to contact metamorphism by the Devonian Buchan Caves Limestone, Buchan Rift, Victoria, Australia. *Organic Geochemistry*, 22(1), 151–164.

Barlet-Gouédard, V., Rimmelé, G., Goffé, B., & Porcherie, O. (2007). Well technologies for CO_2

geological storage: CO2-resistant cement. *Oil & Gas Science and Technology-Revue de l'IFP*, 62(3), 325–334.

Bergh, S. G., Braathen, A., & Andresen, A. (1997). Interaction of basement-involved and thin-skinned tectonism in the Tertiary fold-thrust belt of central Spitsbergen, Svalbard. *AAPG bulletin*, 81(4), 637–661.

Bermúdez, A. & Delpino, D. H. (2008). Concentric and radial joint systems within basic sills and their associated porosity enhancement, Neuquén Basin, Argentina. *Geological Society, London, Special Publications*, 302(1), 185–198.

Birkenmajer, K., Krajewski, K., Pécskay, Z., & Lorenc, M. (2010). K-Ar dating of basic intrusions at Bellsund, Spitsbergen, Svalbard. *Polish Polar Research*, 31(1), 3–16.

Birkenmajer, K. & Morawski, T. (1960). Dolerite intrusions of Wedel-Jarlsberg Land, Vestspitsbergen. *Studia Geologica Polonica*, 4, 103–123.

Bjørlykke, K. (2015). Introduction to Petroleum Geology. In *Petroleum Geoscience* (pp. 1–29). Springer.

Bjørlykke, K. & Jahren, J. (2010). *Sandstones and sandstone reservoirs*. Springer.

Blinova, M., Inge Faleide, J., Gabrielsen, R., & Mjelde, R. (2012). Seafloor expression and shallow structure of a fold-and-thrust system, Isfjorden, west Spitsbergen. *Polar Research*, 31(1), 11209.

Blinova, M., Thorsen, R., Mjelde, R., & Faleide, J. I. (2009). Structure and evolution of the Bellsund Graben between Forlandsundet and Bellsund (Spitsbergen) based on marine seismic data. *Seismic study along the west Spitsbergen continental margin and adjacent area of the West Spitsbergen Fold and Thrust Belt (Isfjorden)*.

Blomeier, D., Dustira, A., Forke, H., & Scheibner, C. (2011). Environmental change in the early permian of ne svalbard: from a warm-water carbonate platform (Gipshuken Formation) to a temperate, mixed siliciclastic-carbonate ramp (Kapp Starostin Formation). *Facies*, 57(3), 493–523.

Boike, J., Roth, K., & Ippisch, O. (2003). Seasonal snow cover on frozen ground: Energy balance calculations of a permafrost site near Ny-ålesund, Spitsbergen. *Journal of Geophysical Research: Atmospheres*, 108(D2).

Bowman, S. J., Pe-Piper, G., Piper, D. J., Fensome, R. A., & King, E. L. (2012). Early Cretaceous volcanism in the Scotian Basin. *Canadian Journal of Earth Sciences*, 49(12), 1523–1539.

Braathen, A., Bælum, K., Christiansen, H. H., Dahl, T., Eiken, O., Elvebakk, H., Hansen, F., Hanssen, T. H., Jochmann, M., Johansen, T. A., Johnsen, H., Larsen, L., Lie, T., Mertes, J., Mørk, A., Mørk, M. B., Nemec, W., Olaussen, S., Oye, V., Rød, K., Titlestad, G. O., Tveranger, J., & Vagle, K. (2012). The Longyearbyen CO2 Lab of Svalbard, Norway– initial assessment of the geological conditions for co2 sequestration. *Norwegian Journal of Geology*, 92, 353–376.

Braathen, A., Bergh, S. G., & Maher, H. D. (1999). Application of a critical wedge taper model to the Tertiary transpressional fold-thrust belt on Spitsbergen, Svalbard. *Geological Society of America Bulletin*, 111(10), 1468–1485.

Bray, R., Lawrence, S., Swart, R., et al. (1998). Source rock, maturity data indicate potential off Namibia. *Oil and Gas Journal*, 96(32), 84–88.

Bryan, S. E. & Ernst, R. E. (2008). Revised definition of large igneous provinces (LIPs). *Earth-Science Reviews*, 86(1), 175–202.

Buchan, K. L. & Ernst, R. (2006). Giant dyke swarms and the reconstruction of the Canadian Arctic islands, Greenland, Svalbard and Franz Josef Land. *Dyke swarms: time markers of crustal evolution*, (pp. 27–37).

Buckley, S. J., Howell, J., Enge, H., & Kurz, T. (2008). Terrestrial laser scanning in geology: data acquisition, processing and accuracy considerations. *Journal of the Geological Society*, 165(3), 625–638.

Cartwright, J., Huuse, M., & Aplin, A. (2007). Seal bypass systems. *AAPG bulletin*, 91(8), 1141–1166.

Casini, G., Hunt, D., Monsen, E., & Bounaim, A. (2016). Fracture characterization and modeling from virtual outcrops. *AAPG Bulletin*, 100(1), 41–61.

Chevallier, L., Gibson, L., Nhleko, L., Woodford, A., Nomquphu, W., & Kippie, I. (2004). Hydro-geology of fractured-rock aquifers and related ecosystems within the Qoqodala dolerite ring and sill complex, Great Kei catchment, Eastern Cape. *Water Res. Com., S. Afr*, 1238, 127.

Chevallier, L. & Woodford, A. (1999). Morpho-tectonics and mechanism of emplacement of the dolerite rings and sills of the western Karoo, South Africa. *South African Journal of Geology*, 102(1), 43–54.

Comte, J.-C., Wilson, C., Ofterdinger, U., & González-Quirós, A. (2017). Effect of volcanic dykes on coastal groundwater flow and saltwater intrusion: A field-scale multiphysics approach and parameter evaluation. *Water Resources Research*.

Corfu, F., Polteau, S., Planke, S., Faleide, J. I., Svensen, H., Zayoncheck, A., & Stolbov, N. (2013). U–Pb geochronology of Cretaceous magmatism on Svalbard and Franz Josef Land, Barents Sea large igneous province. *Geological Magazine*, 150(06), 1127–1135.

Crane, K., Eldholm, O., Myhre, A. M., & Sundvor, E. (1982). Thermal implications for the evolution of the spitsbergen transform fault. *Tectonophysics*, 89(1-3), 1–32.

Cukur, D., Horozal, S., Kim, D. C., Lee, G. H., Han, H. C., & Kang, M. H. (2010). The distribution and characteristics of the igneous complexes in the northern East China Sea Shelf Basin and their implications for hydrocarbon potential. *Marine Geophysical Researches*, 31(4), 299–313.

Cuvier, B. G. (1825). Discourse on the revolutionary upheavals on the surface of the globe and on the changes which they have produced in the animal kingdom.

Dahlgren, S., Riis, F., Hø y, T., & Hansen, S. (1992). Basaltvulkanismen på Kong Karls Land og tilgrensende områder.

Dallmann, W. K. (1999). *Lithostratigraphic lexicon of Svalbard: review and recommendations for*

nomenclature use: Upper Palaeozoic to Quaternary bedrock. Norsk Polarinstitutt.

Dallmann, W. K. (2015). *Geoscience Atlas of Svalbard*. Norsk Polarinstitutt.

Dawes, P. R. (2009). Precambrian–Palaeozoic geology of Smith Sound, Canada and Greenland: key constraint to palaeogeographic reconstructions of northern Laurentia and the North Atlantic region. *Terra Nova*, 21(1), 1–13.

DeGraff, J. M. & Aydin, A. (1987). Surface morphology of columnar joints and its significance to mechanics and direction of joint growth. *Geological Society of America Bulletin*, 99(5), 605–617.

Delaney, P. T. & Pollard, D. D. (1981). *Deformation of host rocks and flow of magma during growth of minette dikes and breccia-bearing intrusions near Ship Rock, New Mexico*. Technical report, USGPO,.

Delaney, P. T., Pollard, D. D., Ziony, J. I., & McKee, E. H. (1986). Field relations between dikes and joints: emplacement processes and paleostress analysis. *Journal of Geophysical Research: Solid Earth*, 91(B5), 4920–4938.

Delpino, D. H. & Bermúdez, A. M. (2009). Petroleum systems including unconventional reservoirs in intrusive igneous rocks (sills and laccoliths). *The Leading Edge*, 28(7), 804–811.

Dimakis, P., Braathen, B. I., Faleide, J. I., Elverhøi, A., & Gudlaugsson, S. T. (1998). Cenozoic erosion and the preglacial uplift of the Svalbard–Barents Sea region. *Tectonophysics*, 300(1), 311–327.

Dörr, N., Lisker, F., Clift, P., Carter, A., Gee, D. G., Tebenkov, A., & Spiegel, C. (2012). Late Mesozoic–Cenozoic exhumation history of northern Svalbard and its regional significance: Constraints from apatite fission track analysis. *Tectonophysics*, 514, 81–92.

Døssing, A., Jackson, H., Matzka, J., Einarsson, I., Rasmussen, T., Olesen, A. V., & Brozena, J. (2013). On the origin of the Amerasia Basin and the High Arctic Large Igneous Province-results of new aeromagnetic data. *Earth and Planetary Science Letters*, 363, 219–230.

Drachev, S. & Saunders, A. (2006). The Early Cretaceous Arctic LIP: its geodynamic setting and implications for Canada Basin opening. In *Proc. Fourth Int. Conf. on Arctic Margins, Dartmouth, Nova Scotia*, volume 30 (pp. 216–223).

Dustira, A. M., Wignall, P. B., Joachimski, M., Blomeier, D., Hartkopf-Fröder, C., & Bond, D. P. (2013). Gradual onset of anoxia across the Permian–Triassic boundary in Svalbard, Norway. *Palaeogeography, Palaeoclimatology, Palaeoecology*, 374, 303–313.

Dypvik, H. (1979). Major and minor element chemistry of Triassic black shales near a dolerite intrusion at Sassenfjorden, Spitsbergen. *Chemical Geology*, 25(1-2), 53–65.

Dypvik, H. (1984). Jurassic and Cretaceous black shales of the Janusfjellet formation, Svalbard, Norway. *Sedimentary Geology*, 41(2-4), 235–248.

Eide, C. H., Schofield, N., Jerram, D. A., & Howell, J. A. (2016). Basin-scale architecture of deeply

emplaced sill complexes: Jameson Land, East Greenland. *Journal of the Geological Society*, 174(1), 23–40.

Einsele, G., Gieskes, J. M., Curray, J., Moore, D. M., Aguayo, E., Aubry, M.-P., Fornari, D., Guerrero, J., Kastner, M., Kelts, K., et al. (1980). Intrusion of basaltic sills into highly porous sediments, and resulting hydrothermal activity. *Nature*, 283(5746), 441–445.

Elvevold, S., Dallmann, W., & Blomeier, D. (2007). *Geology of Svalbard*.

Embry, A. F. & Osadetz, K. G. (1988). Stratigraphy and tectonic significance of Cretaceous volcanism in the Queen Elizabeth Islands, Canadian Arctic Archipelago. *Canadian Journal of Earth Sciences*, 25(8), 1209–1219.

Enslin, J. (1955). Some applications of geophysical prospecting in the union of South Africa. *Geophysics*, 20(4), 886–912.

Estrada, S. & Henjes-Kunst, F. (2004). Volcanism in the Canadian High Arctic related to the opening of the Arctic Ocean. *Zeitschrift der Deutschen Geologischen Gesellschaft*, 154(4), 579–603.

Faleide, J. I., Gudlaugsson, S. T., & Jacquart, G. (1984). Evolution of the western Barents Sea. *Marine and Petroleum Geology*, 1(2), 123IN1129IN5137–128IN4136IN8150.

Farokhpoor, R., Torsater, O., Baghbanbashi, T., Mork, A., Lindeberg, E. G., et al. (2010). Experimental and numerical simulation of CO_2 injection into upper-Triassic sandstones in Svalbard, Norway. In *SPE International Conference on CO2 Capture, Storage, and Utilization*: Society of Petroleum Engineers.

Feden, R., Vogt, P., & Fleming, H. (1979). Magnetic and bathymetric evidence for the "Yermak hot spot" northwest of Svalbard in the Arctic Basin. *Earth and Planetary Science Letters*, 44(1), 18–38.

Fialko, Y. A. & Rubin, A. M. (1999). Thermal and mechanical aspects of magma emplacement in giant dike swarms. *Journal of Geophysical Research: Solid Earth*, 104(B10), 23033–23049.

Flood, B., Nagy, J., & Winsnes, T. S. (1971). The triassic succession of Barentsøya, Edgeøya, and Hopen (Svalbard).

Francis, E. H. (1982). Emplacement mechanism of late Carboniferous tholeiite sills in northern Britain Presidents anniversary address 1981. *Journal of the Geological Society*, 139(1), 1–20.

Fuller, R. E. (1938). Deuteric alteration controlled by the jointing of lavas. *American Journal of Science*, (207), 161–171.

Gabrielsen, R. H., Kløvjan, O. S., Haugsbø, H., Midbøe, P. S., Nøttvedt, A., Rasmussen, E., & Skott, P. H. (1992). A structural outline of Forlandsundet Graben, Prins Karls Forland, Svalbard. *Norsk Geologisk Tidsskrift*, 72(1), 105–120.

Gallagher, J. W. & Dromgoole, P. W. (2008). Seeing below the basalt-offshore Faroes. *Geophysical Prospecting*, 56(1), 33–45.

Galland, O. & Scheibert, J. (2013). Analytical model of surface uplift above axisymmetric flat-lying magma intrusions: Implications for sill emplacement and geodesy. *Journal of Volcanology and Geothermal Research*, 253, 114–130.

Gao, Z., Tian, W., Wang, L., Shi, Y., & Pan, M. (2017). Emplacement of intrusions of the Tarim Flood Basalt Province and their impacts on oil and gas reservoirs: A 3D seismic reflection study in Yingmaili fields, Tarim Basin, northwest China. *Interpretation*, 5(3), SK51–SK63.

Gill, R. (2010). *Igneous rocks and processes: a practical guide*. John Wiley & Sons.

Gillespie, P., Monsen, E., Maerten, L., Hunt, D., Thurmond, J., & Tuck, D. (2011). Fractures in carbonates: From digital outcrops to mechanical models. *Outcrops revitalized-Tools, techniques and applications: Tulsa, Oklahoma, SEPM Concepts in Sedimentology and Paleontology*, 10, 137–147.

Gjelberg, J. & Steel, R. J. (1995). Helvetiafjellet Formation (Barremian-Aptian), Spitsbergen: characteristics of a transgressive succession. *Norwegian Petroleum Society Special Publications*, 5, 571–593.

Gradstein, F. M., Anthonissen, E., Brunstad, H., Charnock, M., Hammer, O., Hellem, T., & Lervik, K. S. (2010). Norwegian offshore stratigraphic lexicon (NORLEX). *Newsletters on Stratigraphy*, 44(1), 73–86.

Grasemann, B., Fritz, H., & Vannay, J.-C. (1999). Quantitative kinematic flow analysis from the Main Central Thrust Zone (NW-Himalaya, India): implications for a decelerating strain path and the extrusion of orogenic wedges. *Journal of Structural Geology*, 21(7), 837–853.

Grasemann, B. & Stüwe, K. (2001). The development of flanking folds during simple shear and their use as kinematic indicators. *Journal of Structural Geology*, 23(4), 715–724.

Grogan, P., Nyberg, K., Fotland, B., Myklebust, R., Dahlgren, S., & Riis, F. (2000). Cretaceous magmatism south and east of Svalbard: evidence from seismic reflection and magnetic data. *Polarforschung*, 68, 25–34.

Grossenbacher, K. A. & McDuffie, S. M. (1995). Conductive cooling of lava: columnar joint diameter and stria width as functions of cooling rate and thermal gradient. *Journal of volcanology and geothermal research*, 69(1-2), 95–103.

Grundvåg, S.-A., Johannessen, E. P., Helland-Hansen, W., & Plink-Björklund, P. (2014). Depositional architecture and evolution of progradationally stacked lobe complexes in the Eocene Central Basin of Spitsbergen. *Sedimentology*, 61(2), 535–569.

Gudmundsson, A. & Løtveit, I. F. (2014). Sills as fractured hydrocarbon reservoirs: examples and models. *Geological Society, London, Special Publications*, 374(1), 251–271.

Gürer, D., Galland, O., Corfu, F., Leanza, H. A., & Sassier, C. (2016). Structure and evolution of volcanic plumbing systems in fold-and-thrust belts: A case study of the Cerro Negro de Tricao Malal, Neuquén Province, Argentina. *Geological Society of America Bulletin*, 128(1-2), 315–331.

Haave, C. (2005). Metamorphic and petrophysical effects of sill intrusions in sedimentary strata:

the Karoo Basin, South Africa. *Unpublished MSc Thesis, University of Oslo, Norway Thesis*.

Hansen, D. M. & Cartwright, J. (2006). The three-dimensional geometry and growth of forced folds above saucer-shaped igneous sills. *Journal of Structural Geology*, 28(8), 1520–1535.

Hansen, J., Jerram, D., McCaffrey, K., & Passey, S. (2011). Early cenozoic saucer-shaped sills of the Faroe Islands: an example of intrusive styles in basaltic lava piles. *Journal of the Geological Society*, 168(1), 159–178.

Haremo, P. & Andresen, A. (1988). Tertiary movements along the Billefjorden Fault Zone and its relation to the Vest-Spitsbergen Orogenic Belt. *Tertiary tectonics of Svalbard. Norsk Polarinstitutt Rapportserie*, 46, 71–74.

Haremo, P., Andresen, A., & Dypvik, H. (1993). Mesozoic extension versus Tertiary compression along the Billefjorden Fault Zone south of Isfjorden, central Spitsbergen. *Geological Magazine*, 130(06), 783–795.

Harland, W. B. & Ay, P. A. D. (1997). Northwestern Spitsbergen. *Geological Society, London, Memoirs*, 17(1), 132–153.

Harland, W. B., Cutbill, J., Friend, P. F., Gobbett, D. J., Holliday, D., Maton, P., Parker, J., & Wallis, R. H. (1974). The Billefjorden Fault Zone, Spitsbergen: the long history of a major tectonic lineament.

Henriksen, E., Ryseth, A., Larssen, G., Heide, T., Rønning, K., Sollid, K., & Stoupakova, A. (2011). Tectonostratigraphy of the greater Barents Sea: implications for petroleum systems. *Geological Society, London, Memoirs*, 35(1), 163–195.

Hetényi, G., Taisne, B., Garel, F., Médard, É., Bosshard, S., & Mattsson, H. B. (2012). Scales of columnar jointing in igneous rocks: field measurements and controlling factors. *Bulletin of volcanology*, 74(2), 457–482.

Hoel, A. (1914). Nouvelles observations sur le district volcanique du spitsbergen du nord. (New observations in the volcanic district of northern Spitsbergen.) Viden skaps Selskapet Skrifter I. Matematisk–Naturvitenskapelig Klasse 9.

Hofmann, A. W. (1988). Chemical differentiation of the Earth: the relationship between mantle, continental crust, and oceanic crust. *Earth and Planetary Science Letters*, 90(3), 297–314.

Holford, S., Schofield, N., Jackson, C., Magee, C., Green, P., & Duddy, I. (2013). Impacts of igneous intrusions on source and reservoir potential in prospective sedimentary basins along the Western Australian continental margin. In *West Australian Basins Symposium. Proceedings of the Petroleum Exploration Society of Australia Symposium, Perth, WA* (pp. 1–12).

Holmes, A. (1918). The basaltic rocks of the Arctic region. *Mineral. Mag*, 18, 180–223.

Hubred, J. H. (2006). Thermal effects of basaltic sill emplacement in source rocks on maturation and hydrocarbon generation. Master's thesis.

Hüneke, H., Joachimski, M., Buggisch, W., & Lützner, H. (2001). Marine carbonate facies in

response to climate and nutrient level: the Upper Carboniferous and Permian of Central Spitsbergen (Svalbard). *Facies*, 45(1), 93–135.

Huppert, H. E. & Sparks, R. S. J. (1988). The generation of granitic magmas by intrusion of basalt into continental crust. *Journal of Petrology*, 29(3), 599–624.

Huppert, H. E. & Sparks, R. S. J. (1989). Chilled margins in igneous rocks. *Earth and Planetary Science Letters*, 92(3-4), 397–405.

Irvine, T. & Baragar, W. (1971). A guide to the chemical classification of the common volcanic rocks. *Canadian journal of earth sciences*, 8(5), 523–548.

Jackson, H., Marcussen, C., Funck, T., Jakobsson, M., & Hell, B. (2010). The structure of the Lomonosov Ridge, Arctic Ocean. In *AGU Fall Meeting Abstracts*.

Jackson, M. D. & Pollard, D. D. (1990). Flexure and faulting of sedimentary host rocks during growth of igneous domes, Henry Mountains, Utah. *Journal of Structural Geology*, 12(2), 185–206.

Jaeger, J. (1959). Temperatures outside a cooling intrusive sheet. *American Journal of Science*, 257(1), 44–54.

Jaeger, J. (1968). Cooling and solidification of igneous rocks. *Basalts*, 2, 503–536.

Jakobsson, M., Mayer, L., Coakley, B., Dowdeswell, J. A., Forbes, S., Fridman, B., Hodnesdal, H., Noormets, R., Pedersen, R., Rebesco, M., Schenke, H.-W., Zarayskaya, Y., Acettella, D., Armstrong, A., Anderson, R. M., Bienhoff, P., Camerlenghi, A., Church, I., Edwards, M., Gardner, J. V., Hall, J. K., Hell, B., Hestvik, O. B., Kristoffersen, Y., Marcussen, C., Mohammad, R., Mosher, D., Nghiem, S. V., Pedrosa, M. T., Travaglini, P. G., & Weatherall, P. (2012). The international bathymetric chart of the Arctic Ocean (IBCAO) version 3.0. *Geophysical Research Letters*, 39(12).

Jerram, A., Single, R. T., Hobbs, E. W., & E, N. C. (2009). Understanding the offshore flood basalt sequence using onshore volcanic facies analogues: an example from the Faroe–Shetland basin. *Geological Magazine*, 146.

Jin, Q., Xiong, S., & Lu, P. (1999). Catalysis and hydrogenation: volcanic activity and hydrocarbon generation in rift basins, eastern China. *Applied Geochemistry*, 14(5), 547–558.

Johannessen, E. & Steel, R. (1992). Mid-Carboniferous extension and rift-infill sequences in the Billefjorden Trough, Svalbard. *Norsk geologisk tidsskrift*, 72(1), 35–48.

Johansen, S., Ostisty, B., Birkeland, Ø., Fedorovsky, Y., Martirosjan, V., Christensen, O. B., Cheredeev, S., Ignatenko, E., & Margulis, L. (1992). Hydrocarbon potential in the Barents Sea region: play distribution and potential. *Arctic Geology and Petroleum Potential, Norwegian Petroleum Society (NPF), Special Publication*, 2, 273–320.

Jones, M. T., Eliassen, G. T., Shephard, G. E., Svensen, H. H., Jochmann, M., Friis, B., Augland, L. E., Jerram, D. A., & Planke, S. (2016). Provenance of bentonite layers in the Palaeocene strata of the Central Basin, Svalbard: implications for magmatism and rifting events around the onset of the North Atlantic Igneous Province. *Journal of Volcanology and Geothermal*

Research, 327, 571–584.

Kato, S., Hashimoto, K., & Watanabe, K. (2012). Microbial interspecies electron transfer via electric currents through conductive minerals. *Proceedings of the National Academy of Sciences*, 109(25), 10042–10046.

Kattenhorn, S. A. & Schaefer, C. J. (2008). Thermal–mechanical modeling of cooling history and fracture development in inflationary basalt lava flows. *Journal of Volcanology and Geothermal Research*, 170(3), 181–197.

Kelsey, C. (1965). Calculation of the CIPW norm. *Mineralogical Magazine*, 34(268), 276–282.

Kjeldstad, A., Langtangen, H., Skogseid, J., & Bjørlykke, K. (2003). Simulation of sedimentary basins. In *Advanced Topics in Computational Partial Differential Equations* (pp. 611–658). Springer.

Knies, J., Mattingsdal, R., Fabian, K., Grøsfjeld, K., Baranwal, S., Husum, K., De Schepper, S., Vogt, C., Andersen, N., Matthiessen, J., et al. (2014). Effect of early Pliocene uplift on late Pliocene cooling in the Arctic–Atlantic gateway. *Earth and Planetary Science Letters*, 387, 132–144.

Koevoets, M., Abay, T., Hammer, Ø., & Olaussen, S. (2016). High-resolution organic carbon–isotope stratigraphy of the Middle Jurassic–Lower Cretaceous Agardhfjellet Formation of central Spitsbergen, Svalbard. *Palaeogeography, Palaeoclimatology, Palaeoecology*, 449, 266–274.

Kurz, T., Buckley, S., Howell, J., & Schneider, D. (2008). Geological outcrop modelling and interpretation using ground based hyperspectral and laser scanning data fusion. *International Archives of the Photogrammetry, Remote Sensing and Spatial Information Sciences*, 37, 1229–1234.

La Terra, E., Vital, L., Santos, I., Miquelutti, L., & Fontes, S. (2016). Mapping of basement relief and volcanic intrusions of parecis basin in brazil based on 3d magnetotelluric imaging and potential field data. In *International Conference and Exhibition, Barcelona, Spain, 3-6 April 2016* (pp. 172–172).: Society of Exploration Geophysicists and American Association of Petroleum Geologists.

Ladygin, V., Frolova, J. V., & Genshaft, Y. S. (2003). Petrophysical properties of Quaternary lavas of Spitsbergen. *Russian Journal of Earth Sciences*, 5(4), 291–298.

Lato, M. & Vöge, M. (2012). Automated mapping of rock discontinuities in 3D lidar and photogrammetry models. In *ISRM International Symposium-EUROCK 2012*: International Society for Rock Mechanics.

Le Bas, M. (2000). IUGS reclassification of the high-Mg and picritic volcanic rocks. *Journal of Petrology*, 41(10), 1467–1470.

Le Bas, M. J., Le Maitre, R., Streckeisen, A., Zanettin, B., et al. (1986). A chemical classification of volcanic rocks based on the total alkali-silica diagram. *Journal of petrology*, 27(3), 745–750.

Le Maitre, R. W. B., Dudek, P., Keller, A., Lameyre, J., Le Bas, J., Sabine, M., Schmid, P., Sorensen, R., Streckeisen, H., Woolley, A., et al. (1989). *A classification of igneous rocks and glossary*

of terms: Recommendations of the International Union of Geological Sciences, Subcommission on the Systematics of Igneous Rocks. Number 552.3 CLA. International Union of Geological Sciences.

Lechler, P. & Desilets, M. (1987). A review of the use of loss on ignition as a measurement of total volatiles in whole-rock analysis. *Chemical Geology*, 63(3-4), 341–344.

Lillesand, T., Kiefer, R. W., & Chipman, J. (2014). *Remote sensing and image interpretation*. John Wiley & Sons.

Lister, J. R. & Kerr, R. C. (1991). Fluid-mechanical models of crack propagation and their application to magma transport in dykes. *Journal of Geophysical Research: Solid Earth*, 96(B6), 10049–10077.

Livsic, J. (1974). Palaeogene deposits and the platform structure of Svalbard.

Lundschien, B. A., Høy, T., & Mørk, A. (2014). Triassic hydrocarbon potential in the northern Barents Sea; integrating Svalbard and stratigraphic core data. *Norwegian Petroleum Directorate Bulletin*, 11, 3–20.

Machel, H. (2005). Geological and hydrogeological evaluation of the Nisku Q-Pool in Alberta, Canada, for H2S and/or CO2 storage. *Oil & gas science and technology*, 60(1), 51–65.

Magee, C., Briggs, F., & Jackson, C. A. (2013). Lithological controls on igneous intrusion-induced ground deformation. *Journal of the Geological Society*, 170(6), 853–856.

Maher, Jr, H. D. (2001). Manifestations of the Cretaceous High Arctic large igneous province in Svalbard. *The Journal of Geology*, 109(1), 91–104.

Maher, J., Senger, K., Ogata, K., Braathen, A., Mulrooney, M., Smyrak-Sikora, A., & Osmundsen, P. T. (2016). Mesozoic regional stress field evolution in Svalbard [PowerPoint slides]. *Retrieved from https://gsa.confex.com/gsa/2016AM/webprogram/Paper281384.html*.

Matter, J. M., Broecker, W., Gislason, S., Gunnlaugsson, E., Oelkers, E., Stute, M., Sigurdardóttir, H., Stefansson, A., Alfreðsson, H., Aradóttir, E., et al. (2011). The CarbFix Pilot Project–storing carbon dioxide in basalt. *Energy Procedia*, 4, 5579–5585.

Matter, J. M., Goldberg, D., Morin, R. H., & Stute, M. (2006). Contact zone permeability at intrusion boundaries: new results from hydraulic testing and geophysical logging in the Newark Rift Basin, New York, USA. *Hydrogeology Journal*, 14(5), 689.

McCarthy, K., Rojas, K., Niemann, M., Palmowski, D., Peters, K., & Stankiewicz, A. (2011). Basic petroleum geochemistry for source rock evaluation. *Oilfield Review*, 23(2), 32–43.

McGlone, C., Mikhail, E., & Bethel, J. (1980). Manual of photogrammetry.

Menand, T. (2008). The mechanics and dynamics of sills in layered elastic rocks and their implications for the growth of laccoliths and other igneous complexes. *Earth and Planetary Science Letters*, 267(1), 93–99.

Mencher, E., Fichter, H., Renz, H. H., Wallis, W., Renz, H., Patterson, J., & Robie, R. (1953). Geology of Venezuela and its oil fields. *AAPG Bulletin*, 37(4), 690–777.

Mériaux, C., Lister, J. R., Lyakhovsky, V., & Agnon, A. (1999). Dyke propagation with distributed damage of the host rock. *Earth and Planetary Science Letters*, 165(2), 177–185.

Michelsen, J. K. & Khorasani, G. K. (1991). A regional study on coals from Svalbard; organic facies, maturity and thermal history. *Bulletin de la Société Géologique de France*, 162(2), 385–397.

Minakov, A., Yaryshina, V., Faleide, J. I., Krupnova, N., Sakoulina, T., Dergunov, N., & Glebovsky, V. (2017). Dyke emplacement and crustal structure within a continental large igneous province - northern Barents Sea. *Geological Society London Special Publications*.

Monreal, F. R., Villar, H., Baudino, R., Delpino, D., & Zencich, S. (2009). Modeling an atypical petroleum system: a case study of hydrocarbon generation, migration and accumulation related to igneous intrusions in the Neuquen Basin, Argentina. *Marine and Petroleum Geology*, 26(4), 590–605.

Moran, K., Backman, J., Brinkhuis, H., Clemens, S. C., Cronin, T., Dickens, G. R., Eynaud, F., Gattacceca, J., Jakobsson, M., Jordan, R. W., Kaminski, M., King, J., Kac, N., Krylov, A., Martinez, N., Matthiessen, J., McInroy, D., Moore, T. C., Onodera, J., O'Regan, M., Pälike, H., Rea, B., Rio, D., Sakamoto, T., Smith, D. C., Stein, R., St John, K., Suto, I., Suzuki, N., Takahashi, K., Watanabe, M., Yamamoto, M., Farrell, J., Frank, M., Kubik, P., Jokat, W., & Kristoffersen, Y. (2006). The cenozoic palaeoenvironment of the arctic ocean. *Nature*, 441(7093), 601–605.

Mørk, A., Elvebakk, G., Forsberg, A. W., Hounslow, M. W., Nakrem, H. A., Vigran, J. O., , & Weitschat (1999). The type section of the Vikinghogda Formation: a new Lower Triassic unit in central and eastern Svalbard. *Polar Research*, 18(1), 51–82.

Mørk, A., Embry, A. F., & Weitschat, W. (1989). Triassic transgressive-regressive cycles in the Sverdrup Basin, Svalbard and the Barents Shelf. In *Correlation in hydrocarbon exploration* (pp. 113–130). Springer.

Mørk, A., Knarud, R., & Worsley, D. (1982). Depositional and diagenetic environments of the Triassic and Lower Jurassic succession of Svalbard.

Mork, M. B. E. (1999). Compositional variations and provenance of Triassic sandstones from the Barents Shelf. *Journal of Sedimentary Research*, 69(3), 690–710.

Mørk, M. B. E. (2013). Diagenesis and quartz cement distribution of low-permeability Upper Triassic–Middle Jurassic reservoir sandstones, Longyearbyen CO_2 lab well site in Svalbard, Norway. *AAPG bulletin*, 97(4), 577–596.

Mørk, M. B. E. & Duncan, R. A. (1993). Late Pliocene basaltic volcanism on the Western Barents Shelf margin: implications from petrology and 40 Ar-39 Ar da ting of volcaniclastic de bris from a shallow drill core. *Norsk Geologisk Tidsskrift*, 73, I993.

Murashov, L., Pcelina, T., & Semevskij, D. (1983). New data on manifestations of volcanism in Lower Devonian and Upper Triassic Formations of the island of West Spitsbergen, Geology of Spitsbergen. *Collection of Scientific Papers. PGO Sevmorgeologija, Leningrad*, (pp. 96–101).

Nejbert, K., Krajewski, K. P., Dubińska, E., & Pécskay, Z. (2011). Dolerites of Svalbard, north-west Barents Sea Shelf: age, tectonic setting and significance for geotectonic interpretation of the High-Arctic Large Igneous Province. *Polar Research*, 30.

Nelson, C. E., Jerram, D. A., & Hobbs, R. W. (2009). Flood basalt facies from borehole data: implications for prospectivity and volcanology in volcanic rifted margins. *Petroleum Geoscience*, 15(4), 313–324.

Nelson, R. (2001). *Geologic analysis of naturally fractured reservoirs*. Gulf Professional Publishing.

Newell, N. D. (1967). Revolutions in the history of life. *Geological Society of America Special Papers*, 89, 63–92.

Nøttvedt, A., Cecchi, M., Gjelberg, J., Kristensen, S., Lønøy, A., Rasmussen, A., Rasmussen, E., Skott, P., & Van Veen, P. (1993). Svalbard-Barents Sea correlation: a short review. *Arctic Geology and Petroleum Potential, Norwegian Petroleum Society (NPF), Special Publication*, 2, 363–375.

Nøttvedt, A. & Kreisa, R. (1987). Model for the combined-flow origin of hummocky cross-stratification. *Geology*, 15(4), 357–361.

Novakova, L. & Pavlis, T. L. (2017). Assessment of the precision of smart phones and tablets for measurement of planar orientations: A case study. *Journal of Structural Geology*, 97, 93–103.

Ntaflos, T. & Richter, W. (2003). Geochemical constraints on the origin of the continental flood basalt magmatism in Franz Josef Land, Arctic Russia. *European journal of mineralogy*, 15(4), 649–663.

O'Brien, J., Lerche, I., et al. (1986). The preservation of primary porosity through hydrocarbon entrapment during burial. *SPE Formation Evaluation*, 1(03), 295–299.

Ogata, K., Senger, K., Braathen, A., Tveranger, J., & Olaussen, S. (2012). The importance of natural fractures in a tight reservoir for potential CO_2 storage: a case study of the upper Triassic–middle Jurassic Kapp Toscana Group (Spitsbergen, Arctic Norway). *Geological Society, London, Special Publications*, 374(1), 395–415.

Ogata, K., Senger, K., Braathen, A., Tveranger, J., & Olaussen, S. (2014). Fracture systems and meso-scale structural patterns in the siliciclastic Mesozoic reservoir-caprock succession of the longyearbyen CO_2 Lab project: implications for geologic CO_2 sequestration on Central Spitsbergen, Svalbard. *Norwegian Journal of Geology*, 94(2-3), 121–154.

Ohta, Y. (1985). Geochemistry of Precambrian basic igneous rocks between St. Jonsfjorden and Isfjorden, central western Spitsbergen, Svalbard. *Polar Research*, 3(1), 49–67.

Olariu, M. I., Ferguson, J. F., Aiken, C. L., & Xu, X. (2008). Outcrop fracture characterization using terrestrial laser scanners: Deep-water Jackfork sandstone at Big Rock Quarry, Arkansas. *Geosphere*, 4(1), 247–259.

Orchard, N., Braathen, A., & Mørk, A. (2010). Permeability of sandstones in drill core from well Dh2/Dh1a of Longyearbyen CO_2 lab. *Unis CO2 lab AS*.

Park, Y.-R. & Ripley, E. M. (1999). Hydrothermal flow systems in the Midcontinent Rift: oxygen and hydrogen isotopic studies of the North Shore Volcanic Group and related hypabyssal sills, Minnesota. *Geochimica et cosmochimica acta*, 63(11), 1787–1804.

Petford, N. (2003). Controls on primary porosity and permeability development in igneous rocks. *Geological Society, London, Special Publications*, 214(1), 93–107.

Planke, S., Alvestad, E., & Eldholm, O. (1999). Seismic characteristics of basaltic extrusive and intrusive rocks. *The Leading Edge*, 18(3), 342–348.

Planke, S., Rasmussen, T., Rey, S., & Myklebust, R. (2005). Seismic characteristics and distribution of volcanic intrusions and hydrothermal vent complexes in the Vøring and Møre basins. In *Geological Society, London, Petroleum Geology Conference series*, volume 6 (pp. 833–844).: Geological Society of London.

Pollard, D. D. (1973). Derivation and evaluation of a mechanical model for sheet intrusions. *Tectonophysics*, 19(3), 233–269.

Polteau, S., Hendriks, B. W., Planke, S., Ganerød, M., Corfu, F., Faleide, J. I., Midtkandal, I., Svensen, H. S., & Myklebust, R. (2016). The Early Cretaceous Barents Sea Sill Complex: Distribution, 40 Ar/39 Ar geochronology, and implications for carbon gas formation. *Palaeogeography, Palaeoclimatology, Palaeoecology*, 441, 83–95.

Polteau, S., Mazzini, A., Galland, O., Planke, S., & Malthe-Sørenssen, A. (2008). Saucer-shaped intrusions: Occurrences, emplacement and implications. *Earth and Planetary Science Letters*, 266(1), 195–204.

Prestvik, T. (1978). Cenozoic plateau lavas of Spitsbergen-a geochemical study. *Arbok. Norsk Polarinstituitt*, (pp. 129–143).

Prestvik, T. (1982). Basic volcanic rocks and tectonic setting. A discussion of the Zr-Ti-Y discrimination diagram and its suitability for classification purposes. *Lithos*, 15(3), 241–247.

Pringle, J., Howell, J., Hodgetts, D., Westerman, A., & Hodgson, D. (2006). Virtual outcrop models of petroleum reservoir analogues: a review of the current state-of-the-art. *First break*, 24(3), 33–42.

Ramberg, I. B., Bryhni, I., & Nøttvedt, A. (2007). *Landet blir til: Norges geologi*. Norsk geologisk forening.

Rateau, R., Schofield, N., & Smith, M. (2013). The potential role of igneous intrusions on hydrocarbon migration, West of Shetland. *Petroleum Geoscience*, 19(3), 259–272.

Reed, S. J. B. (2005). *Electron microprobe analysis and scanning electron microscopy in geology*. Cambridge University Press.

Riis, F., Lundschien, B. A., Høy, T., Mørk, A., & Mørk, M. B. E. (2008). Evolution of the Triassic shelf in the northern Barents Sea region. *Polar Research*, 27(3), 318–338.

Rocchi, S., Mazzotti, A., Marroni, M., Pandolfi, L., Costantini, P., Giuseppe, B., Biase, D. d.,

Federici, F., & Lo, P. G. (2007). Detection of Miocene saucer-shaped sills (offshore Senegal) via integrated interpretation of seismic, magnetic and gravity data. *Terra Nova*, 19(4), 232–239.

Rød, R. S., Hynne, I. B., & Mørk, A. (2014). Depositional environment of the Upper Triassic De Geerdalen Formation-an EW transect from Edgeøya to Central Spitsbergen, Svalbard. *Norwegian Petroleum Directorate Bulletin*, 11, 21–40.

Roeder, P. & Emslie, R. (1970). Olivine-liquid equilibrium. *Contributions to mineralogy and petrology*, 29(4), 275–289.

Salas, G. P. (1968). Petroleum evaluation of north-central Mexico. *AAPG Bulletin*, 52(4), 665–674.

Saltus, R., Miller, E., Gaina, C., & Brown, P. (2011). Regional magnetic domains of the Circum-Arctic: a framework for geodynamic interpretation. *Geological Society, London, Memoirs*, 35(1), 49–60.

Savary-Sismondini, B., Monsen, E., Bounaim, A., Larsen, A. L., Nickel, M., Sonneland, L., Hunt, D., Gillespie, P., & Thurmond, J. (2008). Fracture population of carbonate geological models using digital outcrop data. In *GEO 2008*.

Schaaf, N. W., Senger, K., Mulrooney, M., Ogata, K., Braathen, A., & Olaussen, S. (2017). Towards characterization of natural fractures in a caprock shale: an integrated borehole-outcrop study of the Agardhfjellet Formation, Svalbard. *NGF Winter Conference 2017: 9th to 11th of January 2017, Oslo, Norway*.

Schaefer, C. J. & Kattenhorn, S. A. (2004). Characterization and evolution of fractures in low-volume pahoehoe lava flows, eastern Snake River Plain, Idaho. *Geological Society of America Bulletin*, 116(3-4), 322–336.

Schiffer, C., Tegner, C., Schaeffer, A. J., Pease, V., & Nielsen, S. B. (2017). High Arctic geopotential stress field and implications for geodynamic evolution. *Geological Society, London, Special Publications*, 460, SP460–6.

Schofield, N., Holford, S., Millett, J., Brown, D., Jolley, D., R Passey, S., Muirhead, D., Grove, C., Magee, C., Murray, J., Malcom, H., Jackson, C., & Stevenson, C. (2015). Regional magma plumbing and emplacement mechanisms of the Faroe-Shetland Sill Complex: implications for magma transport and petroleum systems within sedimentary basins. *Basin Research*.

Schutter, S. R. (2003). Hydrocarbon occurrence and exploration in and around igneous rocks. *Geological Society, London, Special Publications*, 214(1), 7–33.

Selley, R. C. & Sonnenberg, S. A. (2014). *Elements of petroleum geology*. Academic Press.

Senger, K., Buckley, S. J., Chevallier, L., Fagereng, Å., Galland, O., Kurz, T. H., Ogata, K., Planke, S., & Tveranger, J. (2015). Fracturing of doleritic intrusions and associated contact zones: implications for fluid flow in volcanic basins. *Journal of African Earth Sciences*, 102, 70–85.

Senger, K., Millett, J., Planke, S., Kei, O., Eide, C., Festøy, M., Galland, O., & Jerram, D. (2017). Effects of igneous intrusions on the petroleum system: a review. *First Break*.

Senger, K., Mulrooney, M., Braathen, A., Ogata, K., & Olaussen, S. (2016a). Integrated Characterization of an Organic-rich Caprock Shale, Svalbard, Arctic Norway. In *Fifth EAGE Shale Workshop*.

Senger, K., Mulrooney, M., Smyrak-Sikora, A., Olaussen, S., Jensen, M., Braathen, A., Buckley, S., & Festøy, M. (2016b). Making the Arctic accessible: the use of digital outcrops in research and education at 78 degrees N. *2nd Virtual Geoscience Conference, Bergen, Norway*.

Senger, K., Planke, S., Polteau, S., Ogata, K., & Svensen, H. (2014a). Sill emplacement and contact metamorphism in a siliciclastic reservoir on Svalbard, Arctic Norway. *Nor. J. Geol.*, 94, 155–169.

Senger, K., Roy, S., Braathen, A., Buckley, S. J., Bælum, K., Gernigon, L., Mjelde, R., Noormets, R., Ogata, K., Olaussen, S., Planke, S., Ruud, B. O., & Tveranger, J. (2013a). Geometries of doleritic intrusions in central Spitsbergen, Svalbard: an integrated study of an onshore-offshore magmatic province with implications for CO_2 sequestration. *Geological controls on fluid flow and seepage in western Svalbard fjords, Norway. An integrated marine acoustic study*.

Senger, K., Tveranger, J., Ogata, K., Braathen, A., & Olaussen, S. (2013b). Reservoir characterization and modeling of a naturally fractured siliciclastic CO_2 sequestration site, Svalbard, Arctic Norway. *UNIS CO2 lab AS/Uni CIPR report, Longyearbyen, Norway*.

Senger, K., Tveranger, J., Ogata, K., Braathen, A., & Planke, S. (2014b). Late Mesozoic magmatism in Svalbard: A review. *Earth-Science Reviews*, 139, 123–144.

Shipilov, E. & Karyakin, Y. V. (2010). The Barents sea magmatic province: Geological-geophysical evidence and new 40Ar/39Ar dates. In *Doklady Earth Sciences*, volume 439 (pp. 955).: Springer.

Simoneit, B. R., Brenner, S., Peters, K., & Kaplan, I. (1978). Thermal alteration of Cretaceous black shale by basaltic intrusions in the Eastern Atlantic. *Nature*, 273, 501–504.

Simpson, M. P., Palinkas, S. S., Mauk, J. L., & Bodnar, R. J. (2015). Fluid inclusion chemistry of adularia-sericite epithermal Au-Ag deposits of the southern Hauraki Goldfield, New Zealand. *Economic Geology*, 110(3), 763–786.

Singhal, B. B. S. & Gupta, R. P. (2010a). *Applied hydrogeology of fractured rocks*. Springer Science & Business Media.

Singhal, B. B. S. & Gupta, R. P. (2010b). *Applied hydrogeology of fractured rocks*. Springer Science & Business Media.

Skjelkvåle, B.-L., Amundsen, H., O'Reilly, S. Y., Griffin, W., & Gjelsvik, T. (1989). A primitive alkali basaltic stratovolcano and associated eruptive centres, northwestern Spitsbergen: volcanology and tectonic significance. *Journal of Volcanology and Geothermal Research*, 37(1), 1–19.

Skogseid, J., Planke, S., Faleide, J. I., Pedersen, T., Eldholm, O., & Neverdal, F. (2000). NE Atlantic continental rifting and volcanic margin formation. *Geological Society, London, Special Publications*, 167(1), 295–326.

Smallwood, J. R. & Maresh, J. (2002). The properties, morphology and distribution of igneous

sills: modelling, borehole data and 3d seismic from the Faroe-Shetland area. *Geological Society, London, Special Publications*, 197(1), 271–306.

Smith, D., Harland, W., Hughes, N., & Pickton, C. (1976). The geology of Kong Karls Land, Svalbard. *Geological Magazine*, 113(03), 193–232.

Spry, A. (1962). The origin of columnar jointing, particularly in basalt flows. *Journal of the Geological Society of Australia*, 8(2), 191–216.

Stearns, D. W. (1978). Faulting and forced folding in the Rocky Mountains foreland. *Geological Society of America Memoirs*, 151, 1–38.

Steel, R., Gjelberg, J., Helland-Hansen, W., Kleinspehn, K., Nøttvedt, A., & Rye-Larsen, M. (1985). The Tertiary strike-slip basins and orogenic belt of Spitsbergen.

Steel, R. J. & Worsley, D. (1984). Svalbard's post-Caledonian strata-an atlas of sedimentational patterns and palaeogeographic evolution. In *Petroleum geology of the North European margin* (pp. 109–135). Springer.

Stemmerik, L. & Worsley, D. (2005). 30 years on-Arctic Upper Palaeozoic stratigraphy, depositional evolution and hydrocarbon prospectivity. *Norwegian Journal of Geology/Norsk Geologisk Forening*, 85.

Støen, S. J. (2016). Late Triassic sedimentology and diagenesis of Barentsøya, Wilhelmøya and eastern Spitsbergen. Master's thesis, NTNU.

Sun, S.-S. & McDonough, W. F. (1989). Chemical and isotopic systematics of oceanic basalts: implications for mantle composition and processes. *Geological Society, London, Special Publications*, 42(1), 313–345.

Sundvor, E. & Eldholm, O. (1979). The western and northern margin off Svalbard. *Tectonophysics*, 59(1-4), 239–250.

Talwani, M. & Eldholm, O. (1977). Evolution of the Norwegian-Greenland sea. *Geological Society of America Bulletin*, 88(7), 969–999.

Tarduno, J. A., Brinkman, D. B., Renne, P. R., Cottrell, R. D., Scher, H., & Castillo, P. (1998). Late Cretaceous Arctic volcanism: tectonic and climatic consequences. In *AGU Spring Meeting*.

Taylor, H. (1974). The application of oxygen and hydrogen isotope studies to problems of hydrothermal alteration and ore deposition. *Economic geology*, 69(6), 843–883.

Tebenkov, A. & Sirotkin, A. (1990). A new occurrence of Cenozoic (?) basalt from Manbreen, Ny Friesland, northeastern Spitsbergen. *Polar Research*, 8(2), 295–298.

Tegner, C., Storey, M., Holm, P. M., Thorarinsson, S., Zhao, X., Lo, C.-H., & Knudsen, M. F. (2011). Magmatism and Eurekan deformation in the High Arctic Large Igneous Province: 40 Ar–39 Ar age of Kap Washington Group volcanics, North Greenland. *Earth and Planetary Science Letters*, 303(3), 203–214.

Thórarinsson, S. B., Söderlund, U., Døssing, A., Holm, P. M., Ernst, R. E., & Tegner, C. (2015). Rift magmatism on the Eurasia basin margin: U-Pb baddeleyite ages of alkaline dyke swarms in North greenland. *Journal of the Geological Society*, 172(6), 721–726.

Tugrul, A. & Gürpinar, O. (1997). The effect of chemical weathering on the engineering properties of Eocene basalts in northeastern Turkey. *Environmental & Engineering Geoscience*, 3(2), 225–234.

Twiss, R. J. & Moores, E. M. (1992). *Structural geology*. Macmillan.

Tyrrell, G. W. & Sandford, K. S. (1933). *Geology and petrology of the dolerites of Spitsbergen*, volume 53. R. Grant & Son.

Vågnes, E. & Amundsen, H. E. F. (1993). Late Cenozoic uplift and volcanism on Spitsbergen: Caused by mantle convection? *Geology*, 21(3), 251–254.

Van Wyk, W. L. (1963). Ground-water studies in northern Natal, Zululand and surrounding areas.

Vaughan, A., Collins, N., Krus, M., & Rourke, P. (2014). Recent Development of an Earth Science App - FieldMove Clino. In *EGU General Assembly Conference Abstracts*, volume 16 of *EGU General Assembly Conference Abstracts* (pp. 14751).

Vogt, P., Taylor, P., Kovacs, L., & Johnson, G. (1979). Detailed aeromagnetic investigation of the Arctic Basin. *Journal of Geophysical Research: Solid Earth*, 84(B3), 1071–1089.

Wærum, G. O. (2011). Bruddmønstre i øvre triaslagrekken ved Vindodden på Svalbard: opptreden, geometri og dannelsesmekanismer samt betydning for CO_2 lagring. Master's thesis, Universitetet i Tromsø.

Wangen, M., Souche, A., & Johansen, H. (2015). A model for underpressure development in a glacial valley, an example from Adventdalen, Svalbard. *Basin Research*, 28(6), 752–769.

Weigand, P. W. & Testa, S. M. (1982). Petrology and geochemistry of Mesozoic dolerites from the hinlopenstretet area, Svalbard. *Polar Research*, 1982(1), 35–52.

Wilkes, S. M., Clement, T. P., & Otto, C. J. (2004). Characterisation of the hydrogeology of the Augustus River catchment, Western Australia. *Hydrogeology Journal*, 12(2), 209–223.

Winkler, H. G. (1949). Crystallization of basaltic magma as recorded by variation of crystal size in dikes. *Mineral Mag*, 28, 557–574.

Witte, J., Bonora, M., Carbone, C., & Oncken, O. (2012). Fracture evolution in oil-producing sills of the Rio Grande Valley, northern Neuquén basin, Argentina. *AAPG bulletin*, 96(7), 1253–1277.

Wolela, A. (2002). Effects of heat flow and hydrothermal fluids from volcanic intrusions on authigenic mineralization in sandstone formations. *Bulletin Chemical Society of Ethiopia*, 16, 37–52.

Woodford, A. & Chevallier, L. P. (2002). *Regional Characterization and Mapping of Karoo Fractured Aquifer Systems: An Integrated Approach Using a Geographical Information System and Digital Image Processing*. Water Research Commission.

Worsley, D. (2008). The post-Caledonian development of Svalbard and the western Barents sea. *Polar Research*, 27(3), 298–317.

Worsley, D., Aga, O., Dalland, A., Elverhøi, A., & Thon, A. (1986). Evolution of an Arctic archipelago. the Geological History of Svalbard. *Den norske stats oljeselskap as, Stavanger, Norway*, (pp. 121).

Wu, C., Gu, L., Zhang, Z., Ren, Z., Chen, Z., & Li, W. (2006). Formation mechanisms of hydrocarbon reservoirs associated with volcanic and subvolcanic intrusive rocks: Examples in Mesozoic-Cenozoic basins of eastern china. *AAPG bulletin*, 90(1), 137–147.

Yoder, H. S. & Tilley, C. E. (1962). Origin of basalt magmas: an experimental study of natural and synthetic rock systems. *Journal of Petrology*, 3(3), 342–532.

Zhang, S.-l., Song, X.-z., Lu, Z.-x., YANG, X., & Qing, Y.-h. (2016). Reservoir characteristics and controlling factors in the 4th member of the xujiahe formation in the Xinchang structural zone, western Sichuan. *Sedimentary Geology and Tethyan Geology*, 1, 013.